Mechanics and Materials Center
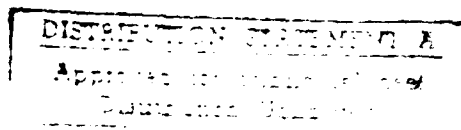**TEXAS A&M UNIVERSITY**
College Station, Texas

AD-A225 789

STUDIES OF MODE I AND MODE II DELAMINATION USING A J-INTEGRAL ANALYSIS AND IN-SITU OBSERVATIONS OF FRACTURE IN THE SEM

Final Technical Report

W.L. Bradley
C.R. Corleto
D.P. Goetz

DTIC
ELECTE
AUG 27 1990
D

MM 5021-90-7   July 1990

90 08 27 008

REPORT DOCUMENTATION PAGE

Form Approved
OMB No. 0704-0188

1a. REPORT SECURITY CLASSIFICATION	1b. RESTRICTIVE MARKINGS
unclassified	

2a. SECURITY CLASSIFICATION AUTHORITY	3. DISTRIBUTION/AVAILABILITY OF REPORT
2b. DECLASSIFICATION/DOWNGRADING SCHEDULE	unlimited

4. PERFORMING ORGANIZATION REPORT NUMBER(S)	5. MONITORING ORGANIZATION REPORT NUMBER(S)
MM-5021-90-7	AFOSR-TR· 90 0874

6a. NAME OF PERFORMING ORGANIZATION	6b. OFFICE SYMBOL (If applicable)	7a. NAME OF MONITORING ORGANIZATION
Mechanics and Materials Center Texas A&M University		AFOSR/NA

6c. ADDRESS (City, State, and ZIP Code)	7b. ADDRESS (City, State, and ZIP Code)
College Station, TX 77843	Building 410 Bolling AFB, DC 20332-6448

8a. NAME OF FUNDING/SPONSORING ORGANIZATION	8b. OFFICE SYMBOL (If applicable)	9. PROCUREMENT INSTRUMENT IDENTIFICATION NUMBER
AFOSR	NA	Grant No. AFOSR-84-0064

8c. ADDRESS (City, State, and ZIP Code)	10. SOURCE OF FUNDING NUMBERS			
Building 410 Bolling AFB, DC 20332-6448	PROGRAM ELEMENT NO.	PROJECT NO.	TASK NO.	WORK UNIT ACCESSION NO.
	61102F	2302	B2	

11. TITLE (Include Security Classification)
Studies of Mode I and Mode II Delamination Using a J-integral Analysis and In-situ Observations of Fracture in SEM (u)

12. PERSONAL AUTHOR(S)
W.L. Bradley, C.R. Corleto, D.P. Goetz

13a. TYPE OF REPORT	13b. TIME COVERED	14. DATE OF REPORT (Year, Month, Day)	15. PAGE COUNT
Final	FROM 2-01-84 TO 12-31-89	90/07/16	145

16. SUPPLEMENTARY NOTATION

17.	COSATI CODES		18. SUBJECT TERMS (Continue on reverse if necessary and identify by block number)
FIELD	GROUP	SUB-GROUP	

19. ABSTRACT (Continue on reverse if necessary and identify by block number)

The mode I and mode II delamination of multi-directional composite laminates have been studied using a J-integral approach. The analytical and experimental formalism to apply the J-integral to delamination have been developed and verified on three different composite material systems with matrix toughness varying from very brittle to very tough. Large deflections and rotations, midplane straining and distributed damage are taken into account in the methodology. The experimental conditions under which a path independent J may be measured have been established. The effect of several variables including specimen geometry, stacking sequence, and material constitutive behavior on the J-Moment-at-the-crack-tip relationship have been determined. Multidirectional composite laminates are both more susceptible to far field damage in the off-axis plies and less stiff than unidirectional layups. These two factors cause a greater tendency to geometric and material nonlinearity in delamination testing. The use of a traditional G approach to characterize fracture behavior of such laminates gives artificially high indications of the delamination resistance.   (see over)

20. DISTRIBUTION/AVAILABILITY OF ABSTRACT	21. ABSTRACT SECURITY CLASSIFICATION
☑ UNCLASSIFIED/UNLIMITED ☑ SAME AS RPT. ☐ DTIC USERS	(u)

22a. NAME OF RESPONSIBLE INDIVIDUAL	22b. TELEPHONE (Include Area Code)	22c. OFFICE SYMBOL
George K. Haritos	(202) 767-0463	NA

DD Form 1473, JUN 86   Previous editions are obsolete.   SECURITY CLASSIFICATION OF THIS PAGE

(u)

19. Continued

However, the use of the J approach developed in this research program satisfies in general the requirements of geometry independence. If the plies bounding the delamination plane are unidirectional, the mode I and mode II delamination resistance as measured by J are the same as that measured for delamination of a unidirectional composite laminate. The use of G for such a comparison gives the erroneous indication that delamination resistance for a multidirectional composite is greater than for a unidirectional composite Delamination of multidirectional laminates with off axis plies bounding the initial delamination starter crack always resulted in the growth of the delamination crack into the adjacent ply. For mode I delamination, the crack would move into the ply several fiber diameters and then grow at the same elevation thereafter. For mode II delamination, the crack tended to migrate further from the original delamination plane as it grew along the length of the specimen. For both mode I and mode II delamination, the critical J for crack growth was greater for multidirectional (delamination planes) laminates than for unidirectional laminates. In the case of mode I delamination, the delamination resistance did not seem to vary with fiber orientation whereas it monotonically increased with increasing with increasing fiber orientation for the mode II case. The use of a mode I induced precrack gave artificially low initial values for mode II delamination crack growth which soon increased to a steady-state value. Since fiber bridging does not play a significant role in mode II delamination, the R-curve like behavior is thought to be an artifact of the use of a mode I crack to begin mode II delamination, rather than representing some meaningful description of material behavior. Strain field around the tip of growing cracks for neat resin and delamination have been made. The critical strain to failure at the crack tip is typically 3x to 10x the elongation observed in a tensile test. This indicates that tensile tests on brittle systems are truncated by propagation of incipient flaws. On ductile systems, tensile tests must have some significant degree of strain localization prior to fracture. The large crack tip strain fields measured in brittle systems are exaggerated in part by the inclusion in the displacement, measures of microcracking induced displacements in addition to resin strain. A highly complex strain state has been measured for mode II delamination of multidirectional laminates.

TABLE OF CONTENTS

I. RESEARCH OBJECTIVES

The objectives of this study have been (1) to develop analytical and experimental procedures for determining the mode I and mode II delamination fracture toughness of unidirecional and multidirectional fiber reinforced composites using a J integral approach; and (2) to acquire a better understanding of the fracture physics for mode I and mode II delamination of these materials, including the study of strain fields ahead of the crack tips for unidirectional and multidirectional delamination crack growth. The investigation of a physically based fracture criteria that can be of significance to better understand delamination and could be incorporated into mathematical models of delamination will also be considered.

II. RESEARCH SUMMARY

INTRODUCTION

One of the most attractive features of fiber reinforced composite materials, is that they outperform their metal counterparts in stiffness-to-weight and strength-to-weight ratios. This is particularly important in aerospace applications where considerable weight savings can be very significant. Other significant features of composites include the possibility of tailoring their mechanical and thermal properties. Such capabilities are useful in the design of complex and sophisticated components that could not be made of existing metals or alloys (e.g., components with a zero or negative coefficient of thermal expansion; aircraft wings with aeroelastic tailoring).

1. Delamination of Fiber Reinforced Composites

An appropriate use of composites in service applications demands an adequate understanding and knowledge of composite behavior, including mechanical properties, thermal properties, chemical stability, and failure modes and characteristics. One which is particularly important and of major concern is their delamination fracture resistance in the presence of cracks. Delamination involves virtual separation of adjacent plies in the thickness direction of the composite for which the material is not reinforced. Fig 1.1a illustrates a schematic of a fiber reinforced composite material showing the laminated structure which makes it susceptible to delamination. Under service conditions, delamination can develop from several sources, including fabrication flaws such as matrix cracks and voids, free edges, holes or notches, ply drop-offs, bonded joints, and any load-path discontinuity (Fig. 1.1b) [1].

Delaminations can occur under three modes, mode I or opening mode, mode II or shearing mode, and mode III or tearing mode (see Fig. 1.2). Delaminations can grow under any single or combination of these modes. However, most of the research has been concentrated in mode I and mode II delamination. In fact, a recent review of delamination done by Sela and Ishai [1], includes eighty of the most relevant publications done on mode I and mode II delamination. The study of mode III delamination has been much more limited [2-6].

Delamination can be affected by several intrinsic as well as extrinsic factors. These factors include loading rate [3,7], fatigue loading [7-8], and environmental exposure to temperature, moisture, and radiation [7,9,10,11]. The nature of the resin has been found to have a considerable effect on delamination behavior. Composites made with brittle resins have lower delamination resistance than composites made with tougher resins [9,12-14]. Delamination resistance has also been found to increase going from mode I to mode II delamination [14,15,16]. However, the increase seems to be smaller with composites made with toughened resins and sometimes not significant at all [14].

Another factor influencing delamination is the fiber/matrix interfacial strength. Poor fiber/matrix interfaces can limit taking full advantage of matrix toughness, particularly for mode I delamination [10,17,18]. Other factors affecting delamination include resin and fiber volume content [12], void content [19], creation of starter cracks [30], and angle of reinforcement [16,21,22,23].

Figure 1.2 Three modes of crack face displacement. a) mode I, opening mode b) mode II, in-plane shear mode c) mode III, anti-plane shear mode.
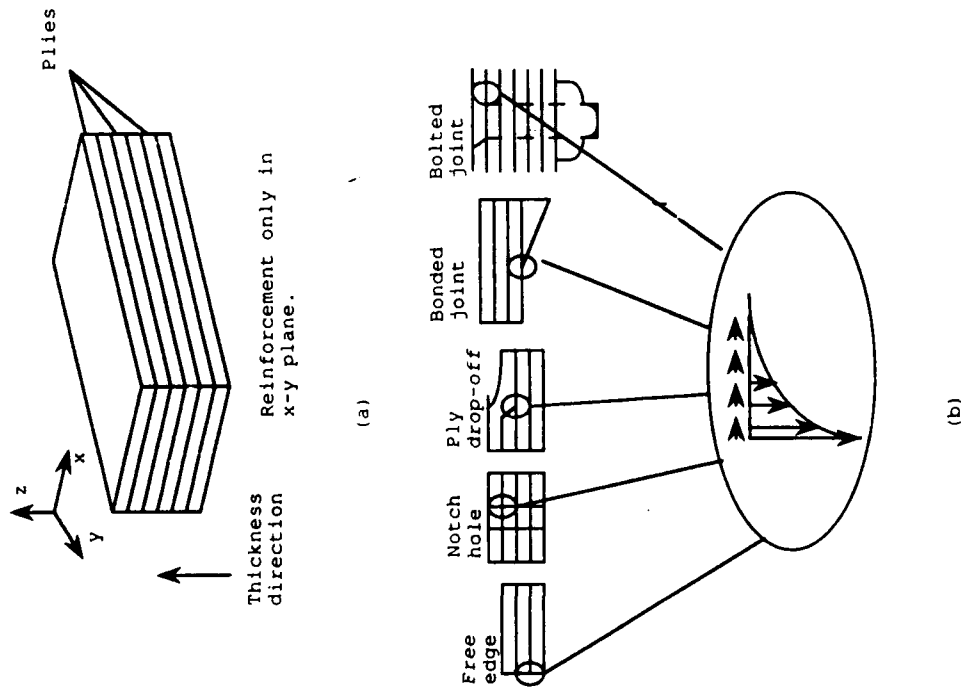

Figure 1.1 (a) A schematic of a fiber reinforced composite showing laminated structure. (b) Potential delamination sources due to load-path discontinuity.
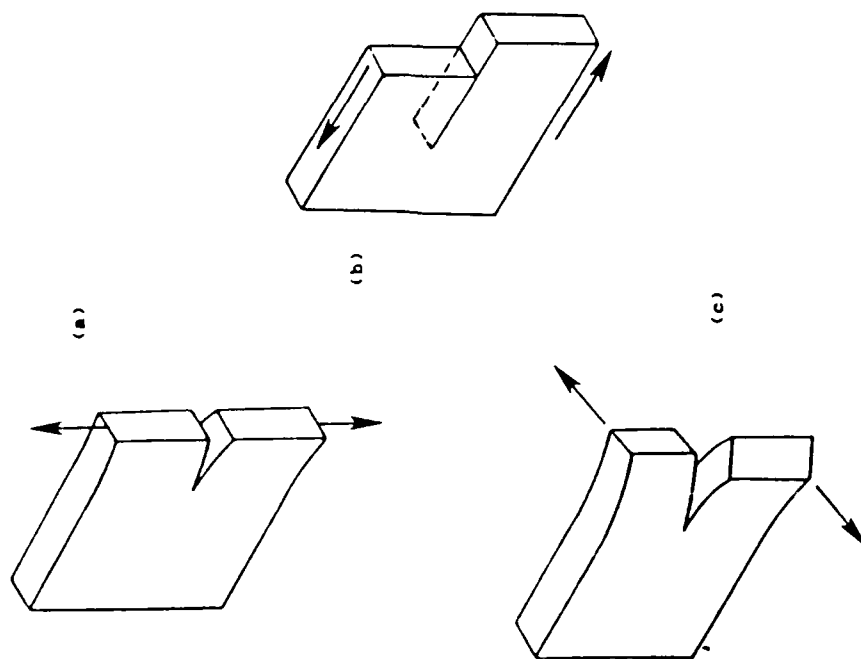
2. Delamination Fracture Characterization

In view of the complexity and importance of delamination in composites, a proper characterization of this fracture phenomenon is of paramount importance. In general, characterization of delamination involves the development of analyses and experimental techniques to measure delamination fracture toughness, the study of the fracture physics through in-situ and postmortem observations of the fracture process, and ideally, micromechanics based analyses of the fracture process. The information gathered through this process can be useful in several ways. First, the screening of composites can be accomplished in terms of their resistance to delamination fracture. Second, delamination testing can be used to develop, improve, and optimize materials with respect to their delamination performance. Third, delamination characterization is needed in the design and analysis of structural composite components.

The usefulness of delamination fracture characterization mentioned in the previous paragraph assumes analyses and experimental techniques used to measure delamination fracture toughness are capable of revealing intrinsic material fracture behavior, free from test configurations, methos of data reduction, or any other artifact related to the test method. Some examples include specimen geometry (i.e. crack length, specimen size), and/or material response (i.e., ductile or brittle behavior, damage development, etc). If the test method meets these requirements, then the variables which affect delamination can be controlled in the test and their influence established. In addition, by means of the study of delamination fracture physics through in-situ and postmortem observations of the fracture process, a better understanding can be achieved between the macroscopically measured fracture parameters and the micromechanics of fracture. In general, delamination fracture characterization of composites using fracture mechanics and fracture physics, is needed to be able to develop reliable structural components made of composite materials.

2.1 Delamination Fracture Parameters

2.1.1 The Energy Release Rate G

Determination of the delamination fracture toughness of fiber reinforced composites has been mostly done using G, an energy release rate parameter approach to fracture [1-4,6-16,19-22]. Considering the cracked body shown in Fig. 1.3, G is defined by the change in total potential energy Π per unit area of crack extension A and represented by,

$$G = -\frac{\partial \Pi}{\partial A} \tag{1.1}$$

More convinient forms of this expression are often obtained in terms of the compliance C of the loaded body [24]. This is useful since C is defined as the ratio of displacement δ and load P. Often, a closed form solution of C is derived based on specimen geometry or when this is not possible, experimentally determined compliance information can be used.
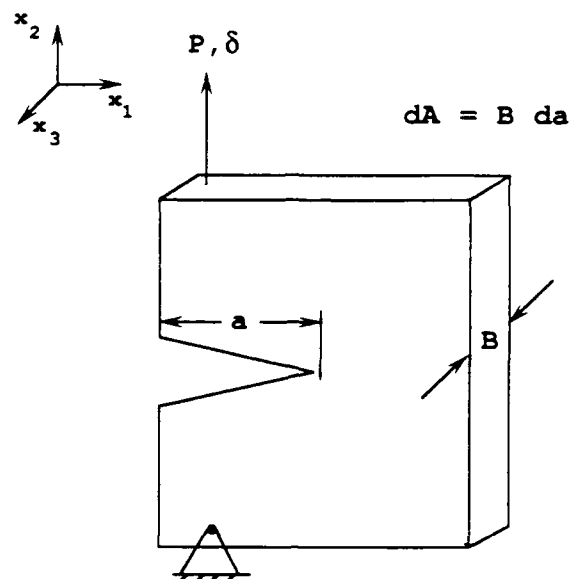
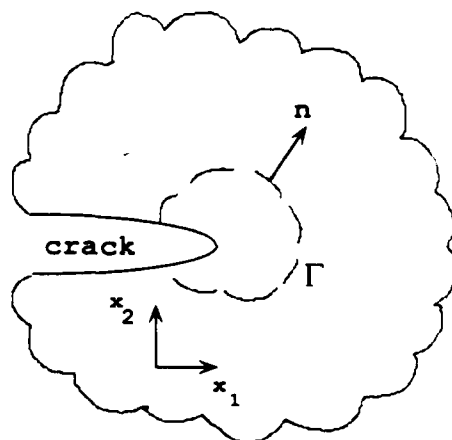Figure 1.3 A linear elastic cracked body

Figure 1.4 Homogeneous body of a linear or nonlinear
elastic material subjected to a two dimen-
sional deformation field

One of the advantages of using G in fracture characterization is that it is a global parameter. It is based on a global energy balance approach to fracture. The energy available for crack growth equals the change in strain energy stored in the body and external work done on it with respect to crack extension. For crack growth the energy available to produce crack growth (the crack driving force), must equal or be greater than the energy required to propagate the crack (crack resistance force). This criterion can be expressed as

$$G \geq G_c \tag{1.2}$$

G_c then is an intrinsic property of the material which measures the materials intrinsic resistance to crack growth. G represents the crack driving force for crack growth, which depends on loading and geometry of the cracked body.

The use of G as a fracture characterization parameter assumes all the energy available was used to create a new crack surface. Therefore, eq.(1.1) applies only to elastic bodies. This means that crack extension is the only process in the body which consumes energy. If other processes such as plasticity or distributed damage (often in the form of microcracking in multidirectional composite laminates) develop as well, G will most likely not be a valid fracture parameter.

Originally, the derivation of this fracture parameter was done by Griffith [25] when he approached the fracture of an ideally brittle material from a thermodynamics point of view, though the modern nomenclature was introduced by Irwin.

2.1.2 The J Integral

The other fracture parameter that has been used to characterize delamination fracture toughness of composites is the J integral [7,26-34]. The original derivation of this integral was done by Eshelby [35], but the first to recognize its potential use as a fracture parameter was Rice [36]. The application of the J integral in fracture was originally intended for characterization of nonlinear elastic materials and latter for elastic-plastic materials.

The J integral expression as originally introduced by Rice is given by [36],

$$J = \int_\Gamma (W dx_2 - \mathbf{T}\frac{\partial \mathbf{u}}{\partial x_1}ds) \tag{1.3}$$

Γ is a counterclockwise contour path surrounding the crack shown in the body in Fig. 1.4, u is the displacement vector, ds is an element of arc length along Γ. T is the traction vector, and W is the strain-energy density. A unique feature of this integral is that regardless of the integration path chosen, the J integral is an invariant for identical loading conditions. This path independence can be used to show that for an elastic material, J is equal to the rate of decrease of the total potential energy and therefore synomymous to G [36],

$$J = -\frac{\partial \Pi}{\partial A} \tag{1.4}$$

$$J = G \tag{1.5}$$

This energy release rate interpretation of J can be useful in determining J values from experimental load-deflection records and for component fracture predictions.

The J integral has been also applied to fracture of elastic-plastic materials when deformation plasticity (actually a nonlinear elasticity theory) is used to idealize elastic-plastic behavior. The restrictions to this application are in conditions of proportional loading such as is the case prior and up to crack initiation. In the case of a growing crack of an elastic-plastic material, elastic unloading and nonproportional loading around the crack tip takes place. Under this conditions, the J integral is no longer path independent and its usefulness is restricted.

An important feature of this integral derives from its path independence. That is, it can be conveniently evaluated so as to use global or far field quantities to approximate it. This is the case when the integration path is taken through specimen boundaries where displacements and tractions are known. When the path is taken in the vicinity of the crack tip, near field information can be obtained. Therefore, global far field quantities provide a measure of the near field state of the cracked body.

A new adaptation of the J integral has been made by Schapery [37] to characterize crack growth in inelastic media with large deformations. The source of inelasticity can be due to several factors including microcracking, microslipping, plasticity, and rate processes (viscoelasticity). In the absence of body forces this adaptation of J yields [37].

$$J = \int_{\Gamma} (\Phi n_1 - T_i u_i) dL \tag{1.6}$$

Φ in this case is a strain-energy like function called a work potential that describes material constitutive behavior in the presence of inelastic behavior. n_1 is the unit outward normal in the x_1 direction. The tractions T_i are defined using the piola stresses.

$$\sigma_{ij} = \frac{\partial \Phi}{\partial(u_{i,j})} \tag{1.7}$$

dL is along Φ. All quantities are in reference to the undeformed configuration. The body is assumed homogeneous in the x_1 direction and the crack parallel to this axis (x_1 axis).

Schapery has also shown that the energy release rate interpretation approach to fracture still holds if Φ is used instead of the strain energy W in eqs. (1.1) and (1.4) to define the potential energy Π [34].

2.2 Delamination Testing

2.2.1 Test Configurations

Several specimen configurations have been proposed and used to characterize delamination fracture toughness experimentally. By far, the most-used specimen for mode I delamination is the double cantilever beam (DCB) specimen (Fig. 1.5a). A modified DCB specimen is the width-tapered DCB commonly refer to as (WTDCB) and shown in Fig. 1.5b [38,39]. The effect of the taper yields an expression of G which for an

applied load is independent of crack length. Therefore, crack measurements are not necessary. For steady state crack growth, an average value of G_c is calculated using the average value of load during this state. Another modification that can be made to the standard DCB specimen is by stiffening the arms of the DCB when stiff beams are adhered to them (See Fig. 1.5c) [39]. The motivation for doing this is to ensure geometrically linear behavior of thin laminates.

Another configuration that can be used to study mode I delamination is the Arcan-type specimen [40]. As seen in Fig. 1.5d, when the loading angle $\alpha = 90°$, mode I loading is induced at the crack tip. However, mixed mode ($0° < \alpha < 90°$) as well as mode II ($\alpha = 0°$) can be achieved with this configuration. The versatility of loading from mode I to mode II obtained with this specimen has been used to develop a failure criterion for combined mode I and mode II delamination [41].

Several other specimen configurations have been proposed and used to study mixed mode I/II delamination (e.g., [42-46]) and mode III delamination (e.g., [32-36]) testing. These are of peripheral interest in this study. However, it should be noted that the wide variety of specimen configurations available allows the study of delamination fracture criteria for loading varying from mode I to mode II and mode III. Mode I and mode II are of primary interest in this research effort; they provide an extreme point in the failure envelope. This indicates accurate mode I and mode II test methods are essential. Also, the phenomenology of delamination that can be revealed through mode I and mode II testing can be expected to be found to varying extents for mixed-mode tests. Therefore, the knowledge obtained is not necessarily limited to the pure mode I and mode II cases. Also, the results of mixed-mode may be useful in interpreting the results from pure mode I and mode II tests.

Mode II delamination test configurations, besides the Arcan-type specimen, are the end-notched flexure test (ENF) [47], the center-notched flexure test (CNF) [48], and the end-loaded split laminate test (ELS) [44]. Figure 1.6 shows these test configurations. By far, most of the mode II delamination testing has been done with the ENF [8-11,15,16,19,21,47,49-51] and the ELS tests [23,44,52-56]. One of the most significant features for the use of the ENF test for mode II delamination has been its relatively simple configuration. It is basically a three-point bend test setup (see Fig. 1.6a). On the other hand, an attractive feature of the ELS test is its ability to allow the study of stable crack growth. Nevertheless, it requires a somewhat more complicated setup.

2.2.2 Data Analysis Procedures

Data analysis procedures for delamination testing can be classified into several groups. These groups are primarily divided upon the assumptions and limitations of each method and are therefore of special concern. Most data analysis procedures involve the fundamental assumption that composite mechanical behavior is essentially linear elastic. Therefore, the delamination fracture parameter measured with these tests is G. Generally, this assumption is valid for composite laminates with unidirectional layups. However, multidirectional layups may undergo inelastic processes which cause nonlinear behavior that invalidate this assumption.

The first group of data analysis assumes that test specimens are beam structures that can be modelled using linear beam theory. As a result, closed form solutions
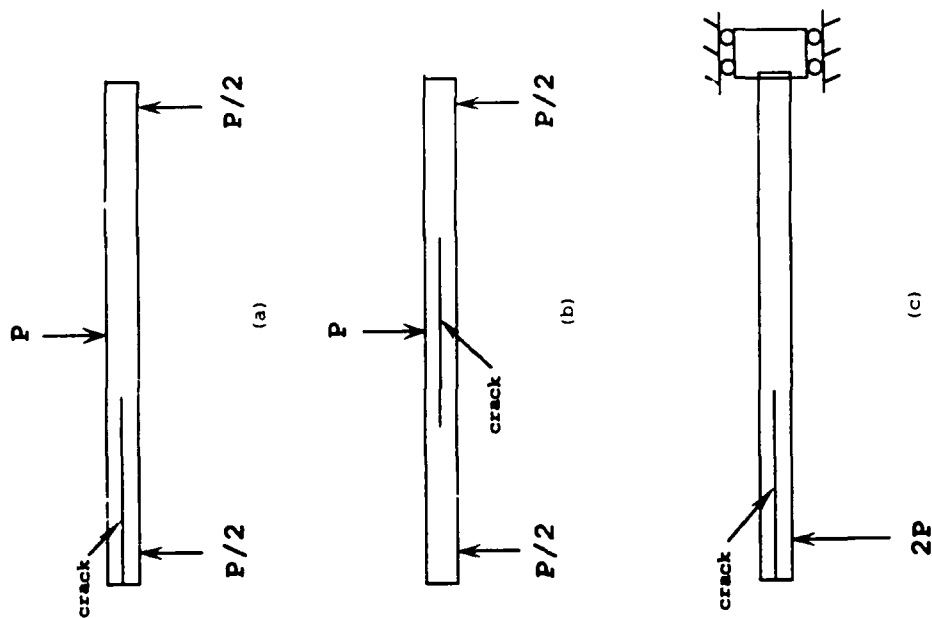
Figure 1.6 Typical Mode II Delamination Test Configurations. (a) ENF; (b) CNF; (c) ELS tests.
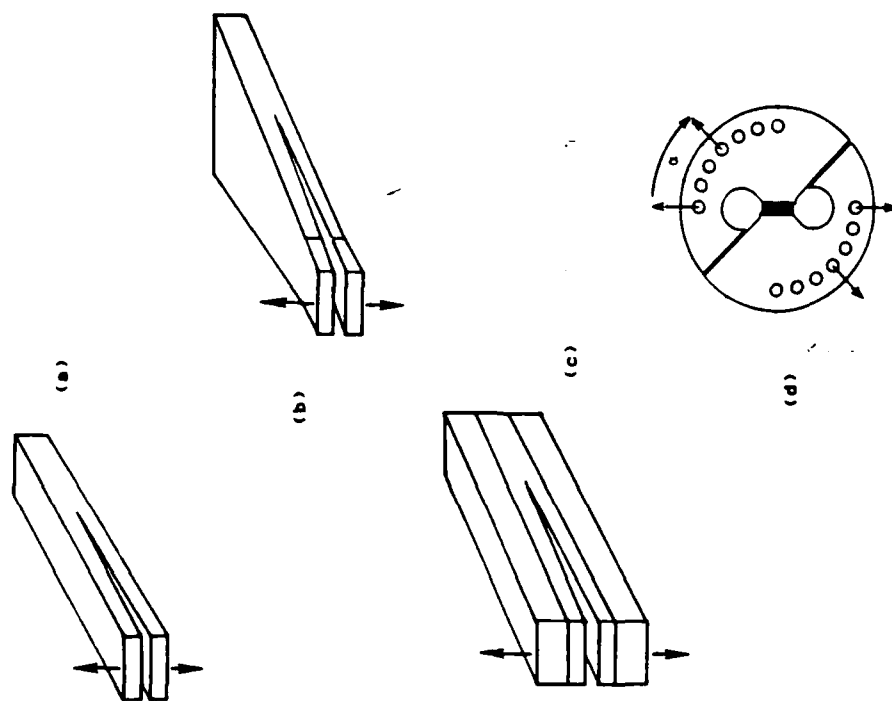

Figure 1.5 Specimens for mode I delamination. a) double cantilever beam (DCB) specimen b) width-tapered DCB specimen (WTDCB) c) DCB with support beams d) Arcan-type specimen.

of G can be obtained in terms of the load applied, crack length, and other specimen dimensions and moduli. Also, if displacements are used, the moduli can be eliminated from the solutions. Shear deformation corrections can also be incorporated through the use of the shear modulus. This has been a common practice with the ENF test [50,55]. A typical P-δ during delamination under linear beam theory and linear elastic conditions is shown in Fig. 1.7a.

A second group of data analysis schemes use experimental approximations of compliance versus crack length (e.g., [30,36,39,50,56,57]). These approximations are determined by loading and unloading a specimen at various crack lengths. Curve fitting is then used to approximate the compliance-crack length relationship.

Analyses which attempt to account for geometric nonlinearities comprise the third group of data analyses methods (e.g., [58,59]). Geometric nonlinearities occur when large displacements and rotations develop with thin (highly compliant layups) or with tough composites that require large loads to delaminate. Fig. 1.7b shows a P-δ record during delamination of a geometrically nonlinear case. Typically, nonlinear beam theory is used as the basis of these analyses. Also, analyses that account for geometric nonlinearities from large rotations of the tabs used to load the DCB and ELS specimens have been developed [59,60].

All the previous data analyses procedures that have been reviewed assume linear elastic material behavior. A fourth general approach removes this assumption and allows for material and geometric nonlinearities. Fig. 1.7c shows delamination of a nonlinear elastic material (material nonlinear behavior). In this case, the area method is the approach used [7,19,39,52,56,61]. Basically, with the area method, G_c is approximated for a finite increment of crack growth Δa, and it can be defined as the energy required to create a new crack surface area,

$$G = \frac{1}{B}\frac{U}{\Delta a} \tag{1.8}$$

where U is the area shown in Fig. 1.7 under the P-δ delamination plots. There are several advantages with this method. First, it is applicable to linear and nonlinear material behavior as well as linear and nonlinear geometric response. Second, since the method uses directly the P-δ diagrams, eq.(1.8) is valid for all test configurations. Third, no knowledge of moduli is required. However, the area method can not be used when composite laminates undergo inelastic material response since it implicitly assumes that all the energy consumed is used to create the new crack area. Inelastic composite response may develop in the form of plastic deformation and microcracking (distributed damage).

The last group of data analyses and reduction methods are the ones that precisely attempt to differentiate between the energy consumed in energy dissipating processes and macroscopic crack growth. They allow for limited inelasticity and material nonlinear behavior as well. Fig. 1.8 shows typical P-δ record of delamination with inelastic behavior. The most significant procedure that has been developed in this group of analyses is the one by Schapery. He used multi-valued work potentials to account for inelastic material behavior in the calculation of G and J for the DCB (mode I delamination) specimen [34,37]. His analysis resulted in an expression of J in terms of the

Figure 1.8   Load-displacement relation indicating inelastic material behavior
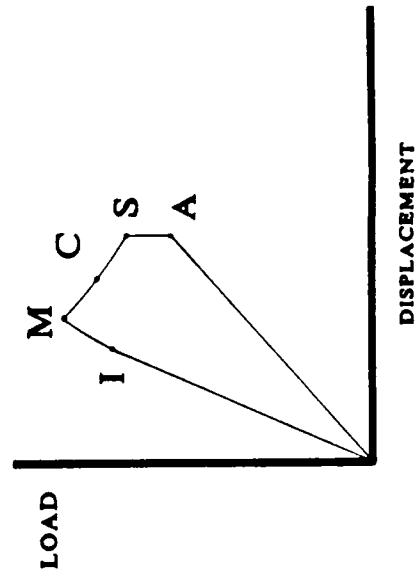
Figure 1.9   Five points on a DCB load-displacement record for a single load-unload cycle.
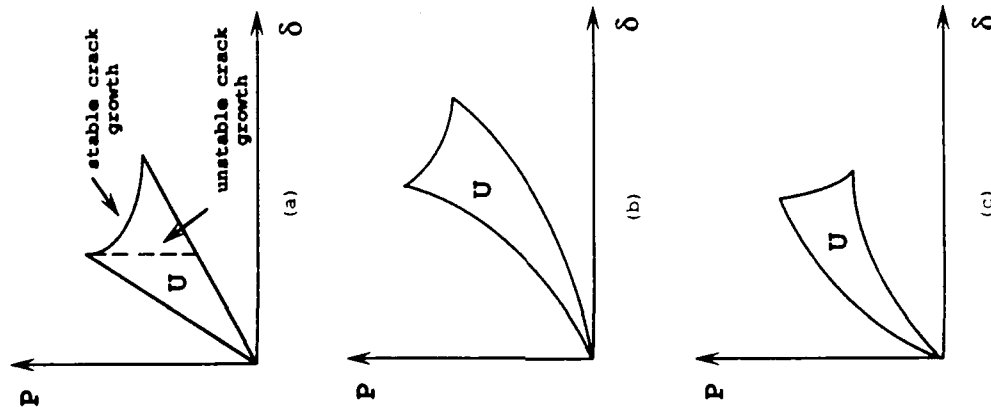

Figure 1.7   Load-displacement relations indicating (a) linear elastic, (b) geometrically non-linear elastic, and (c) non-linear elastic material behavior.
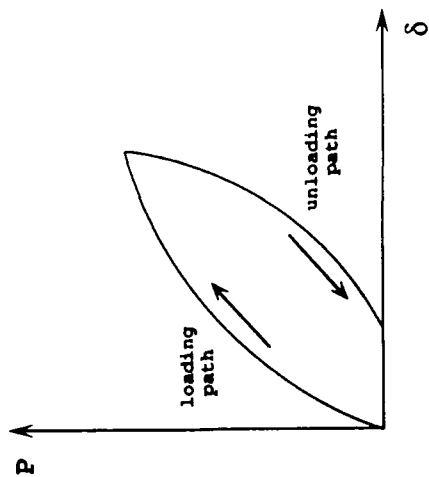
moment-curvature relationship of the DCB legs but was limited to overall small rotations and displacements. He noted that the path-independence of J could be maintained even in the case of crack propagation, as long as crack advance occurs at a constant crack tip moment. For mode II delamination, no successful approach has been established. An attempt to correct for nonlinear P-δ curves obtained using the ENF specimen has been reported by Carlsson et al [49]. However, their proposed correction to G can only account for non-linear effects caused by subcritical crack growth (slow stable crack growth prior to maximum load) and does not account for inelastic effects such as resin yielding and damage. In the case of the ELS test, Ilcewicz and co-workers [7] attempted to use the energy release rate interpretation of J along with a technique employed for testing of metals by Landes and Begley [62,63]. Their approach was not successful for mode II delamination but they reported critical values of J for mode I delamination of unidirectional specimens that underwent permanent deformation.

2.3 Results of Delamination Testing

As it has been already pointed out, mode I and mode II delamination have been the subject of most of the reserach in the past years [1]. This research has been limited for the most part to unidirectional composites. A variety of investigations have been done to understand the effect intrinsic and extrinsic factors on delamination (see section 1). However, for the scope of this study, the validity of fracture parameters and test procedures are of major concern.

2.3.1 Unidirectional Composites

Characterization of unidirectional delamination behavior has been performed with relative success. G has been commonly used to characterize delamination [1-4,6-16,19-22]. With the exception of very tough composites, G has been found to be a valid delamination fracture parameter. Very tough composites often show nonlinear behavior that limits the use of G. Some studies have identified nonlinear P-δ curves as that shown in Fig. 1.9 [39,52]. Point I indicates the onset of nonlinearity, and in some systems has been identified with the beginning of crack propagation [49,54,64]. G associated with point I has been observed to be as much as 16% lower than G for stable crack growth [64]. Point M denotes the point of maximum load during delamination. C is a point during crack propagation. The point at which displacement is no longer increased is S. If the displacement is not immediately reversed, the load may drop off to a point A at virtually constant displacement. When the data reduction method uses particular P-δ pairs, the point which is chosen can be significant. Typically investigators do not specify their practice, which often leads to discrepancies when comparisons from different sources are made. The behavior shown in Fig. 1.9 represents stable crack growth. If unstable crack growth occurs, point S would be the point when unstable growth begins and A would be associated with dynamic rather than quasi-static crack arrest.

For some unidirectional systems the P-δ curves do not return to the origin upon unloading, displaying permanent deflection [30,52]. This has been observed for both mode I and mode II delamination. Processes such as matrix cracking and fiber-resin pullout (in the case of mode I delamination) were identified as probable causes. When

this is the case, G in not a valid fracture parameter. For mode I delamination, a successful formulation using work potentials and the J integral with the DCB specimen have been developed to approach this inelastic behavior [37]. The approach is limited to linear beam theory. This might not always be appropriate since tougher composites tend to undergo large rotations and deflections.

2.3.2 Multidirectional Composites

In most actual composite structure applications, laminate layups are multidirectional instead of unidirectional. The use of unidirectional data to screen materials or in structural design and analysis can only be justified if unidirectional response reflects multidirectional behavior. There are at least two reasons to expect multidirectional behavior to differ from unidirectional behavior. First, the character of the matrix material may have much more effect on composite behavior for the multidirectional case. Viscoelasticity or inelasticity of the matrix is more likely to be reflected in multidirectional than unidirectional layups. Second, the complex stress state that develops within multidirectional laminates may induce responses that are unlikely to occur in unidirectional ones.

Relatively few investigations have been done to study mode I or mode II delamination of multidirectional composites [38,44,45,65-69]. There exists an incomplete understanding of how their behavior differs from that of unidirectional ones. Of particular interest to this investigation is what special problems must be addressed in their testing, and what variables determine their toughness.

Some investigators have reported a two to three fold increase in G_{Ic} going from unidirectional to multidirectional delamination planes [67]. However, others have measure similar delamination fracture toughness for unidirectional and multidirectional laminates [38]. Ply jumping, crack deviation, and branching have been observed [38,65,66], and are believed to be the result of edge effects (width). As a result, a wide range of fracture toughness values were observed as a function of crack length. There is therefore reason to consider how to interpret the results in a way that is relevant to analysis for crack growth in structures. Another study of mode I delamination of multidirectional layups has found that tests performed using layups with $0°$ plies except at the fracture plane at which there was a $\pm 10° or \pm 45°$ interface, the stiffness of the composites were similar to that of the unidirectional layup, and the toughness values were also similar. However, as the percentage of off-axis plies was increased and the modulus decreased, the size of the zone of microcracking at the crack tip increased, as did the amount of damage in the specimen away from the crack tip. Analysis methods which did not account for the effect of far field damage gave results showing a large increase in apparent fracture toughness. However, when data analysis was performed using a damage-dependent J integral, the intrinsic fracture energy was found to be comparable to that for the unidirectional composite in three of the four systems tested. This suggests that there exists an intrinsic fracture energy which is independent of interface angle. However, it should be noted that this conclusion is based on limited data.

With regard to mode II delamination, only composites with woven reinforcement have been studied [16,21]. It has been reported that G_{IIc} increases as the angle of reinforcement goes from being parallel up to $45°$ with delamination direction. These

tests were done using the ENF test and nonlinear P-δ records were obtained. No explanation was provided to explain this behavior and its effect on G_{IIc} was not addressed. Whether far field damage development took place or not, it was not mentioned. If this is the case, an analysis that distinguishes energy used in the creation of the crack and far field damage is needed for mode II delamination.

Determination of mode I and mode II delamination fracture toughness of multidirectional composites poses numerous questions that do not arise when studying unidirectional ones. When delamination tests are done, one seeks a geometry-independent material fracture parameter. The question of geometry-independence has not been adequately addressed for multidirectional testing of mode I or mode II specimens. Studies of the multidirectional DCB specimens have shown that the fracture energy of a specimen can vary widely with crack length if fracture mode transitions (e.g., ply jumping) develop. This poses a problem and a challenge in interpreting and reporting data. One can always use the lowest bound for the delamination fracture toughness measured. This at least provides information of the lowest energy fracture mechanisms that take place. However, it does not provide insight into the full range of material behavior. In fact, material development and improvement can be optimized if higher toughness behavior can be properly studied. If this is desired, the choice of data analysis methods is limited since most methods are inapplicable when geometric, material nonlinearity, and inelasticity take place as it occurs with multidirectional layups. There is a need to develop data analysis methods which are capable of revealing the details of the various fracture processes.

It has been reported both that in some instances mode I multidirectional fracture toughness is similar to the unidirectional value and in some it is not. In particular, the effect of stacking sequence on delamination resistance is not clear. The usefulness of a correlation between unidirectional and multidirectional laminate toughness is very great, since it would permit to perform a simple test to obtain information for many complex layups.

The development of far-field damage has been reported to be a complicating factor in delamination testing. Particular care must be taken to discriminate between the energy available for fracture and the energy dissipated in the generation of far-field damage (e.g., microcracking). As it has been noted, very few investigators have attempted to develop analyses and tests that properly account for damage [26,30,34,37]. Far-field damage is associated with stacking sequence. Matrix dominated layups and layups with large differences in interface angles generate more damage. However, in test specimens such as the DCB and ELS, damage can be due not only to bending stresses but also due to tensile stresses in the legs where the angle of rotation of the legs is large.

In addition to the introduction of far-field damage, the stacking sequence can potentially affect the delamination process by inducing a local three dimensional stress state leading to local mixed mode I/II/III, even if globally only pure mode I or pure mode II are applied.

3. Delamination Fracture Physics

One of the most significant aspects of delamination fracture physics is the valuable

knowledge provide through observations of the mechanics of delamination. Observing the way in which delamination takes place is not only of mere academic interest but is also valuable for understanding test results, material response, screening of materials, and development of new materials and test methods.

Among the most common practices to study delamination fracture physics is post-mortem observations of the cracked surfaces. Typically, the fracture surfaces are observed with the naked eye, through optical microscopy, or with more advance methods such as scanning electron mircoscopy (SEM). Several important findings are worth mentioning. For example, the differences in the fracture mechanisms of mode I and mode II delamination of unidirectional composites correlate well with their delamination fracture resistance. It is widely accepted that for brittle composites, mode II fracture toughness is larger than its mode I counterpart because the hackled surface (jagged appearance) formed during mode II delamination [14,52,70,71] reflects a more tortous crack path than the almost featureless fracture appearance of mode I fracture surfaces [52]. Therefore, more energy is required to propagate the crack in mode II than mode I delamination. On the other hand, in the case of very tough unidirectional composites, where the increase in delamination fracture toughness going from mode I to mode II delamination is almost nonexistant, a comparison of their fracture surfaces indicated no significant differences. Instead, both showed resin yielding and deformation as the primary process preceeding fracture [14].

Understanding the importance of the fiber/matrix interface has been also revealed through postmortem fracture surface observations. Often, the poor fiber/matrix interfaces are revealed by bare fibers with little or no resin adhered to them [23,52]. It seems that extracting all the resin toughness is restricted if the fiber/matrix interface is weak, although for tough systems, the fibers are also believed to limit G_c by not allowing it to fully deform [12]. Also, the fiber/matrix interface is more critical for mode I than mode II delamination [21].

The study of the fracture physics of delamination via in-situ observations has been also helpful in understanding composite delamination behavior [23,51,71]. In a study in which delamination growth was observed for mode I and mode II delamination, it was observed that damage zones develop ahead of crack tips. Further, the damage zone for mode II loading was considerably larger than for mode I. This information further substantiated the increase in fracture toughness going from mode I to mode II loading. The damage zones were characterized by microcracking of the resin. In the case of a composite with a tough resin, the damage zone also showed extensive resin yielding and was found to be at least 10 times larger than the one of a brittle composite [52].

As discussed in the previous paragraphs, most of the effort in understanding delamination frcture physics has been limited to microfractographic studies of fracture mechanisms (i.e., microcracking, hackle formaton, size of damage zones ahead of crack tips, fiber/matrix interfaces) by means of in-situ and postmortem observations in the SEM. These findings have been very useful in correlating measured delamination fracture toughness with loading modes (mode I, mode II), and fiber/resin systems (tough and brittle) combinations. An additional application of delamination fracture physics that is currently emerging is in the efforts to define an appropriate physically based

fracture criterion. Such criterion can be of significance to better understand delamination fracture physics. Also, it can be incorporated into simple analytical or numerical models and is essential in the development of micromechanics based analysis of the delamination fractue process. Ideally, delamination fracture toughness should be predicted from constitutive properties of the resin and fiber. Perhaps one of the most important contributions in accomplishing this task is the measurement of strain fields in the neighborhood of the crack tip. Hibbs and Bradley [72] have utilized a stereoimaging technique originally developed for metals by Davidson and Langford [73] to measure the surface displacement field around the crack tip from which the strain field field was calculated. Their results were encouraging. However, the technique is limited in resolution since the photographs taken of the specimen loaded in the SEM must be at a sufficiently low magnification so that a zero displacement reference point is in the field of view.

More recently, Hibbs, Bradley and Burghart [74] have developed a new technique in which a very fine pattern of regularly spaced points may be placed in the neighborhood of the crack tip on the specimen surface at intervals as small as 2.5 μ. Then the specimen may be loaded in the SEM and the new positions of the dots determined, allowing the relative displacement to be measured and the strain field around the growing crack to be calculated. One of the major advantages of this technique is that a higher resolution around the crack tip can be obtained by working at a higher magnification. In this way, local strain to failure can be determined with considerable precision. In fact, an important question to be addressed in establishing a physically based local fracture criterion is whether a critical local strain achieved over some critical volume (or distance ahead of the crack tip) can be used as a failure criterion.

4. Objectives of this Study

The objectives of this study have been (1) to develop analytical and experimental procedures for determining the mode I and mode II delamination fracture toughness of unidirecional and multidirectional fiber reinforced composites using a J integral approach; and (2) to acquire a better understanding of the fracture physics for mode I and mode II delamination of these materials, including the study of strain fields ahead of the crack tips for unidirectional and multidirectional delamination crack growth. The investigation of a physically based fracture criteria that can be of significance to better understand delamination and could be incorporated into mathematical models of delamination will also be considered.

ANALYSIS OF DELAMINATION: A J-INTEGRAL APPROACH

1. Motivation

The primary motivation for the use of the J-integral for mode I and mode II fracture toughness characterization is its ability to be a valid fracture parameter when nonlinear elastic and some inelasticity is undergone by the material being tested. In the previous chapter, it was noted that the J-integral is capable of accounting for distributed damage [34,37]. Also, the J-integral as proposed by Schapery includes the development of a failure/damage zone ahead of the crack tip [37]. As reviewed in Chapter I, damage zones characterized by extensive resin yielding (in the case of tough composites) and microcracking develop ahead of mode II delamination crack tips.

Another feature of the J-integral which makes it suitable for delamination fracture toughness characterization is that it can be used to account for geometric and material nonlinearities. Geometric nonlinearities arise with thin composites or highly toughened ones. Multidirectional composites, which are typically more compliant than their unidirectional counterparts are also subject to geometric nonlinearities.

The evaluation of the J-integral requires the knowledge of the stresses and displacements in the body where it is being evaluated. Often, closed form solutions are not available which forced the use numerical analyses. This requires knowledge of the constitutive behavior. Since nonlinear material behavior may develop with nonhomogenous, anisotropic composites, the analyses can become very complicated. The use of the DCB and ELS specimens for mode I and mode II delamination studies, respectively, leads to a less complicated problem. In the following analysis, simple beam theory has been used to derive approximate J expressions for the DCB and ELS specimens and then extended to nonlinear beam theory. Derivation of an approximate expression of J for the DCB has already been performed under linear beam theory conditions [26,34]; however, experimental data is limited. Methods to evaluate the derived J expressions are also outlined, particularly when nonlinear beam theory is applicable.

2. Approximate J Analysis of Delamination (Linear Theory)

The DCB and ELS specimens have been chosen in this study to characterize mode I and mode II delamination, respectively. Essentially, a split laminate beam is used for both specimens; however, by changing the loading configuration, the delamination mode is changed. The ELS loading configuration is obtained by reversing one of the loads in the arms of the DCB specimen such that instead of having opposite loads on the beam arms, both loads are applied in the same direction (See Figs. 1.5 and 1.6).

Prior to the evaluation of the J-integral for the DCB and ELS specimen, let us consider some preliminary concepts of beam theory. Consider an elastic, homogeneous in the x_1 direction, orthotropic beam as that shown in Fig. 2.1a. Beam theory states that under the application of a constant bending moment M, the curvature K of the beam is defined as $\frac{1}{R}$. Under small strains assumptions, K can also be found to be related to the applied moment M, the flexural modulus E_b (not necessarily the same as the axial modulus E), and the moment of inertia I_m of the cross-section,
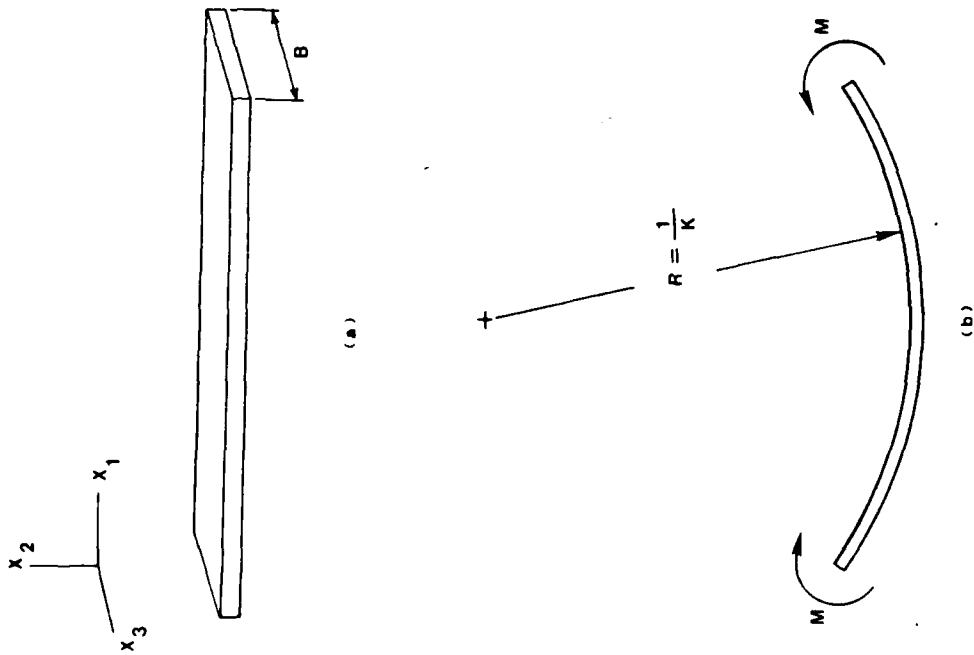
Figure 2.2 DCB loaded by points loads showing integration path for calculating J

Figure 2.1. Beam of uniform cross-section. a) Undeformed configuration b) Deformed configuration under constant moment.

$$K = \frac{M}{E_b I_m} \tag{2.1}$$
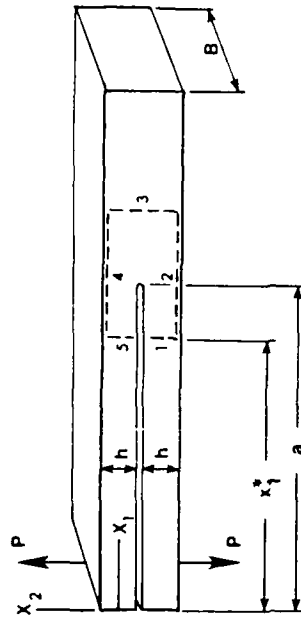
The midplane curvature can also be described by

$$K = \frac{\frac{\partial^2 u_2}{\partial x_1^2}}{[1 + (\frac{\partial u_2}{\partial x_1})^2]^{3/2}} \tag{2.2}$$

where u_1 and u_2 are the displacements in the x_1 and x_2 directions, respectively. Further, if $\frac{\partial u_2}{\partial x_1}$ (the slope) is small compared to 1, linear beam theory states that an adequate approximation of K is

$$K = \frac{\partial^2 u_2}{\partial x_1^2} \tag{2.3}$$

With linear beam theory then, it is assumed that plane sections remain plane and normals to the midplane remain normal, even when shear loading is present. When the length L of the beam is much larger than the thickness h, shear effects are negligible. These effects can also be neglected in the calculation of the strain energy since most of the energy is due to bending of the beam.

2.1 Mode I DCB Specimen (Linear Theory)

A DCB specimen is shown in Fig. 2.2 loaded by points loads. A counterclockwise path is taken such that rotations are small and linear beam theory applies. The evaluation of the J-integral for the DCB will be denoted by J_I ; likewise, for the ELS, J_{II}

Beginning with equation (1.6), a two dimensional form of J is given by

$$J = \int_{\Gamma} (\Phi n_1 - T_i u_{i,1}) dL \tag{2.4}$$

No contribution to the J-integral comes from paths 1,3,5,7 since at these locations, $T_i = 0$ and $n_1 = 0$. At path 4, $\Phi = 0$ and $T_i = 0$ as long as it is far enough away from the crack tip to be in the unstressed region. The only contribution to J comes from path segments 2 and 6 where $n_1 = -1$ and $dL = -dx_2$. Further, due to symmetry, the contribution to J from paths 2 and 6 are equal. Therefore,

$$\frac{J_I}{2} = \int_{(2)} (\Phi + T_i u_{i,1}) dx_2 \tag{2.6}$$

The tractions T_i are,

$$T_1 = S_{11}n_1 + S_{12}n_2 = -S_{11}$$
$$T_2 = S_{21}n_1 + S_{22}n_2 = -S_{21} \tag{2.7}$$

Due to the symmetry of the stress tensor, $S_{12} = S_{21}$. The strain energy like potential, in the context of negligible shear effects (small deformations) is given by

$$\Phi = \int_0^{\epsilon_{11}} S_{11} d\epsilon_{11}'$$ (2.8)

S_{11} and ϵ_{11} are the Eulerian stress and the strain due to bending. The prime superscript denotes a dummy variable of integration. Upon subtition of eqs. (2.7) and (2.8) and noting that in the context of linear beam theory $u_{1,1} = \epsilon_{11} = -x_2 K$ and the slope $u_{2,1}$ does not depend on x_2, it can be shown that,

$$\frac{J_I}{2} = -\int_0^K [\int_{\frac{h}{2}}^{-\frac{h}{2}} S_{11} x_2 dx_2] dK' + K \int_{\frac{h}{2}}^{-\frac{h}{2}} S_{11} x_2 dx_2 - u_{2,1} \int_{\frac{h}{2}}^{-\frac{h}{2}} S_{12} dx_2$$ (2.9)

Noting that

$$\int_{-\frac{h}{2}}^{\frac{h}{2}} S_{11} x_2 dx_2 = -\frac{M}{B}$$ (2.10)

$$\int_{-\frac{h}{2}}^{\frac{h}{2}} S_{12} dx_2 = -\frac{P}{B}$$ (2.11)

and substituting this equations into (2.9), integrating by parts, and simplifying

$$J_I = \frac{2}{B} \int_0^M K dM' - \frac{2P}{B} u_{1,2}$$ (2.12)

Since $u_{2,1i} = K$, the slope $u_{2,1}$ can be expressed by

$$u_{2,1} = \int_a^{x_1^*} K dx_1$$ (2.13)

where x_1^* is the location of the path and a is the crack length (cf. Fig. 2.4). Making a change of variables using $M = Px_1$ and inverting the limits of integration, substitution of eq. (2.13) into (2.12) gives

$$J_I = \frac{2}{B} \int_0^{M_{tip}} K dM$$ (2.14)

where $M_{tip} = Pa$. This result was derived by Schapery [34]. Graphically, the integral is the area to the left of the moment-curvature, curve as shown in Fig. 2.3.

For an orthotropic, linear elastic material with material axes aligned with the beam axes, eq. (2.14) combined with (2.1) can be shown to reduce to

$$J_I = \frac{M_{tip}^2}{BE_bI_m} = \frac{P^2a^2}{BE_bI_m} \tag{2.15}$$

Comparing this equation with the expression of G_I [44] based on linear beam theory assumptions confirms that $G = J$ for the conditions assumed.

Equation (2.15) indicates the crack driving force is only dependent on the moment at the crack tip, M_{tip}, when shear deformation is negligible. Thus, when deflections of the DCB are large enough that the load-line to crack tip distance, a_p, is significantly less than the crack length, a, in the undeformed configuration,

$$J_I = \frac{P^2a_p^2}{BE_bI_m} \tag{2.16}$$

This result was derived by Williams using nonlinear beam theory with G [59].

The ability of the J approach just derived to characterize steady state crack growth beyond initiation when damage develops in the arms of the DCB, is possible since as argued by Schapery [34], as long as continuous crack growth reaches a steady state value, a constant maximum crack tip moment is reached. This critical moment is the maximum moment which any section of the arm of the DCB will experience as the crack passes. Thus, as the crack grows, all material elements to the right of the original crack tip will undergo identical unloading paths. This will assure the path independence of J_I even when unloading takes place as the crack grows.

The $M - K$ relationship in eq.(2.14) has to be dependent only on M (thus, independent of x_1) in order for this equation to be valid. Furthermore, bending-twisting, bending-stretching, and bending shearing coupling are neglected.

2.2 Mode II ELS Specimen (Linear Theory)

An ELS specimen is shown in Fig 2.4. In the same manner as done for the DCB, a counterclockwise path is taken such that rotations are small and linear beam theory applies. Starting with eq. (2.4), it can be seen that the contributions to J around the path are only those due to path 2,6 and 4. For the other paths, $T_i = 0$ and $n_1 = 0$. Note that in order for $T_i = 0$ in paths 1 and 7, friction effects are assumed to be negligible. Further, paths 2 and 6 are the same as in the DCB case; therefore, the superscript (^{c}) will be used to indicate the contribution to J from the cracked portion of the ELS (paths 2 and 6) in eq. (2.12) to get

$$J_{II}^c = \frac{2}{B} \int\limits_0^{M^c} K^c dM' - \frac{2P}{B} u_{1,2}^c \tag{2.17}$$

Evaluation of the contribution of the uncracked portion of the ELS (path segment 4) can be done starting with eq. (2.4). Since $n_1 = 1$, $n_2 = 0$, and $dL = dx_2$,

contour
Γ

2P
PL

L

a

x₁

B - width

Figure 2.4 An ELS specimen loaded by points loads and showing integration path used to evaluate the J integral.

M

K

$$Area = \int_0^M K \, dM'$$

$$J = \frac{2}{B} \int_0^M K \, dM'$$

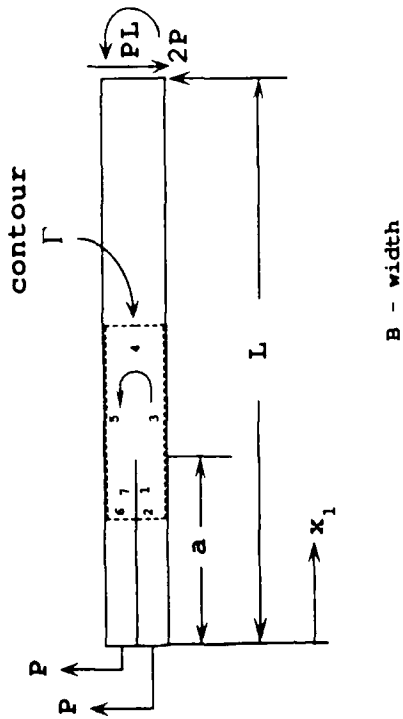Figure 2.3 Relationship of J to the moment-curvature curve for a DCB loaded by moments.

$$J_{II}^u = \int\limits_{(4)} (\Phi - T_i u_{i,1}) dx_2 \qquad (2.18)$$

Proceeding in a similar fashion as before, the tractions are

$$T_1 = S_{11}n_1 + S_{12}n_2 = S_{11}$$
$$T_2 = S_{21}n_1 + S_{22}n_2 = S_{21} \qquad (2.19)$$

Again due to symmetry $S_{12} = S_{21}$. Substitution of eqs. 2.19 and 2.8 into 2.18 and under linear beam theory assumptions, it can be shown that

$$J_{II}^u = -\int\limits_0^{K} [\int\limits_{-\frac{3h}{2}}^{\frac{h}{2}} S_{11}x_2 dx_2] dK' - K \int\limits_{-\frac{3h}{2}}^{\frac{h}{2}} S_{11}x_2 dx_2 + u_{2,1} \int\limits_{-\frac{3h}{2}}^{\frac{h}{2}} S_{12} dx_2 \qquad (2.20)$$

The boundary conditions are now

$$\int\limits_{-\frac{3h}{2}}^{\frac{h}{2}} S_{11}x_2 dx_2 = -\frac{M}{B} \qquad (2.21)$$

$$\int\limits_{-\frac{3h}{2}}^{\frac{h}{2}} S_{12} dx_2 = -\frac{2P}{B} \qquad (2.22)$$

Substituting this equations into (2.20), intergrating by parts, and simplifying,

$$J_{II}^u = -\frac{2}{B} \int\limits_0^{M^u} K^u dM' + \frac{2P}{B} u_{1,2}^u \qquad (2.23)$$

The total contribution to J for the ELS can now be simply found by adding equations (2.23) and (2.17) to get

$$J_{II} = \frac{2}{B} \int\limits_0^{M^c} K^c dM' - \frac{2P}{B} u_{1,2}^c - \frac{2}{B} \int\limits_0^{M^u} K^u dM' + \frac{2P}{B} u_{1,2}^u \qquad (2.24)$$

This equations can be simplified since the slopes can be expressed by

$$u_{2,1}^c = \int\limits_L^a K^u dx_1 + \int\limits_a^{x_1^c} K^c dx_1 \qquad (2.25)$$

$$u_{2,1}^u = \int_L^{x_1^u} K^u dx_1 \tag{2.26}$$

where x_1^c and x_1^u are shown in Fig. 2.4 and represent the location of the paths on the cracked and uncracked portions of the ELS. Since the moments at those locations are $M^c = Px_1^c$ and $M^u = 2Px_1^u$, making a change of variables, substitution of eqs. (2.25) and (2.26) into (2.24) will yield,

$$J_{II} = \frac{2}{B} \int_0^{M_{tip}^c} K^c dM - \frac{1}{B} \int_0^{M_{tip}^u} K^u dM \tag{2.27}$$

where $M_{tip}^c = Pa$ and $M_{tip}^u = 2Pa$ represents the crack tip moment for the cracked and uncracked portion of the ELS specimen. Note that J_{II} is independent of where the paths are originally taken. Equation (2.27) has been derived assuming linear beam theory applies but inelastic material behavior is allowed. However, for an orthotropic, linear elastic composite with homogeneity in the x_1 direction, the $M - K$ relationships can be evaluated using eq. (2.1) to obtain,

$$J_{II} = \frac{6(M_{tip}^c)^2}{BE_bI_m^u} = \frac{6P^2a^2}{BE_bI_m^u} \tag{2.28}$$

This result is the same as that derived by Vanderkeley using G and linear beam theory [44], which confirms that $J = G$ for the conditions assumed.

Equation (2.28) indicates that similar to the mode I case, mode II delamination depends only on the moment at the crack tip if shear deformation is neglected. Therefore this equation applies for geometric nonlinearities as long as the load-line to crack tip distance, a_p is used instead of a,

$$J_{II} = \frac{6P^2a_p^2}{BE_bI_m^u} \tag{2.29}$$

This result was also derived by Williams using nonlinear beam theory [59].

With regard to the ability of J to be a valid fracture parameter to characterize steady state crack growth in the presence of damage away from the crack tip of the ELS specimen, it should be noted that contrary to the DCB configuration, the crack tip moment during crack growth is not the maximum moment seen throughout the ELS. In fact, at any section to the right of the crack tip (uncracked portion of beam), the moment will always be larger than the crack tip moment. Therefore, as the crack grows, if inelastic behavior is experienced in these sections, the unloading paths will not be the same. If this is the case, J_{II} will not be path independent. However, the independence of the J can be maintained if the uncracked sections behave elastically and inelasticity does not develop until the crack grows into these sections. Under these conditions, all unloading paths for a constant crack tip moment will be the same.

Similar to the mode I derivation of J , the analysis for mode II does not take into account include bending-twisting, bending-stretching, and bending-shearing coupling.

For a more detailed derivation of the previous analyses, references [22] and [75] are provided. These are Ph.D. dissertations of two of the students that worked for this research project.

3. Approximate J Analysis of Delamination (Nonlinear Theory)

In the previous J-integral analyses of the DCB and ELS, the use of linear beam theory required that rotations were small throughout the specimen or at least a path could be found where this condition would be met, in addition this path would be far enough away from the crack tip that linear beam theory applied. Also, no mid-plane straining occurred. Finally, the moment curvature relationships were independent of the position along the beam. For the next analyses, all these restrictions are removed.

3.1 Mode I DCB Specimen (Nonlinear Theory)

Consider the DCB specimen of Fig. 2.5a where large rotations develop. Once more, start with eq. (1.6) which defines the J-integral . Because large deformations are now allowed, all quantities are referred to the undeformed configuration (Fig 2.5b). As before, the only contribution to J comes from paths 2 and 6, Thus,

$$J_I = \int_{\frac{h}{2}}^{-\frac{h}{2}} (\Phi + T_i u_{i,1}) dx_2 \tag{2.30}$$

Assuming negligible through-thickness strains have a negligible effect on the displacement gradients and negligible shear deformation effects, Goetz [22] has derived expressions of these gradients when large rotations are undergone by the DCB legs,

$$u_{1,1} = -1 + cos\theta(1 + \epsilon^\circ) - x_2 K^* cos\theta$$
$$u_{2,1} = -sin\theta(1 + \epsilon^\circ) + x_2 K^* sin\theta \tag{2.31}$$

θ is the slope angle at the path location as shown in Fig 2.5a. ϵ° is the midplane strain. K^* is the curvature of a plane in the beam which does not strain and is given by

$$K^* = (1 + \epsilon^\circ)K \tag{2.32}$$

K is the curvature of the midplane. When no midplane straining develops (as assumed with linear theory) K^* will become K.

The stresses will be expressed in terms of components which are due to the moment, axial, and shear forces acting on the cross-section. This separation allows an easier simplification of the results using the force and moment resultants. Consider first the notation that will be used from the free body diagram of the portion of one leg on the specimen from the path to the end where the point load is applied. See Fig. 2.6a. The resultant of the forces normal to the cross-section is denoted by H. The resultant of the forces transverse to the cross-section (i.e., shear resultant on the section) is denoted by V. From force equilibrium,

(a) Free body diagram of part of one leg of a DCB specimen

(b) Stresses on a material element of a DCB or ELS specimen loaded by points loads.
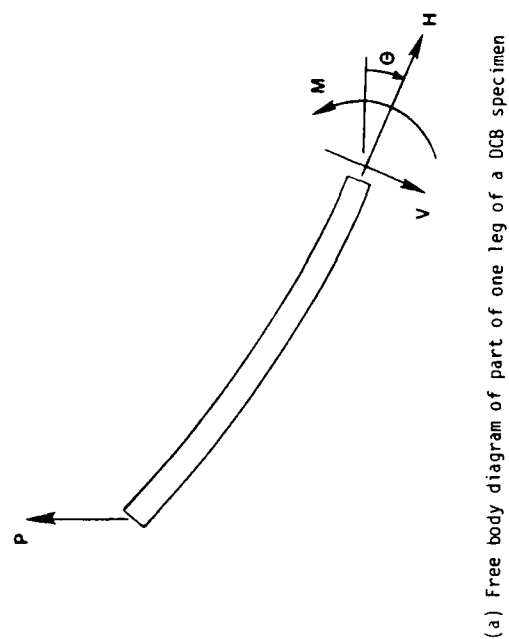
Figure 2.6

(a) DCB showing large rotations in the legs.
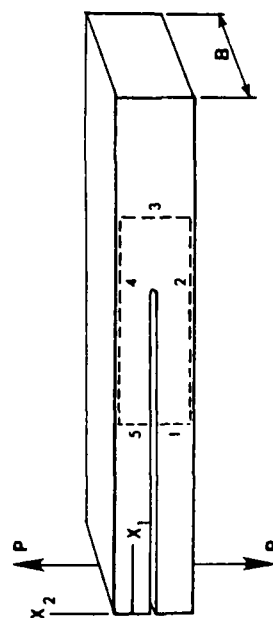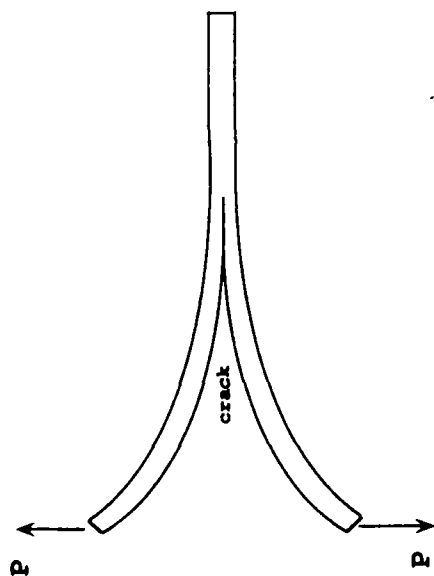
(b) DCB in undeformed configuration showing integration path.

Figure 2.5

$$V = P\cos\theta$$
$$H = P\sin\theta \tag{2.33}$$

Now consider an elemental cube at a point along the path (Fig. 2.6b). The S^H is the stress due to the axial force H, S^M is the stress due to the moment M, and τ^V is the shear stress due to the shear force V. Transformation of the stresses from the $x_\alpha - x_\beta$ coordinate system to the $x_1 - x_2$ system gives

$$S_{11} = (S^H + S^M)\cos^2\theta - 2\tau^V\sin\theta\cos\theta$$
$$S_{22} = (S^H + S^M)\sin^2\theta - 2\tau^V\sin\theta\cos\theta$$
$$S_{12} = -(S^H + S^M)\sin\theta\cos\theta - \tau^V(\cos^2\theta - \sin^2\theta) \tag{2.34}$$
$$S_{21} = S_{12}$$

Since evaluation of eq. (2.4) is now made using the undeformed configuration due to large deformations (rotations) along the beam, the Eulerian stresses (with respect to the deformed configuration), S_{ij}, need to be converted to Piola stresses σ_{ij} (with respect to the undeformed configuration). The transformation is done using the relationship,

$$\sigma_{ij}n_j dA_o = S_{ij}n_j^d dA \tag{2.35}$$

where n_j are the components of the outward normal to the surface element in the undeformed configuration; n_j^d are the components of the outward normal to the surface element in the deformed configuration; dA_o is the area of the face of the material element associated with n_j in the undeformed configuration; and dA is the area of the face of the material element associated with n_j^d in the deformed configuration. The Piola stresses are now found substituting eq.(2.34) into (2.35) and since $n_1 = -1$, $n_2 = 0$, $n_1^d = -\cos\theta$, and $n_2^d = \sin\theta$, assuming $dA_o = dA$,

$$\sigma_{11} = (S^H + S^M)\cos\theta - \tau^V\sin\theta$$
$$\sigma_{21} = -(S^H + S^M)\sin\theta - \tau^V\cos\theta \tag{2.36}$$

Evaluation of the work potential function Φ will be done as before assuming negligible shear deformation such that each point along the path is in an state of uniaxial stress, and can be calculated with

$$\Phi = \int_0^\epsilon \sigma d\epsilon' \tag{2.37}$$

where σ is the nonzero principal stress and ϵ the nonzero principal strain. The strain can be written in terms of the curvature and midplane strain, and is given by [22]

$$\epsilon = \epsilon^o - x_2 dK^* \tag{2.38}$$

From Fig. 2.6b, the principal stress is

$$\sigma = S^H + S^M \tag{2.39}$$

Differentiating eq.(2.38) and substituting it along with eq.(2.39) into eq.(2.37), the first term of eq.(2.30) can be expressed as

$$\int\limits_{\frac{h}{2}}^{-\frac{h}{2}} \Phi dx_2 = \int\limits_{\frac{h}{2}}^{-\frac{h}{2}} \int\limits_{0}^{\epsilon^o} (S^H + S^M) d(\epsilon^o)' dx_2 - \int\limits_{\frac{h}{2}}^{-\frac{h}{2}} \int\limits_{0}^{K^*} (S^H + S^M) x_2 d(K^*)' dx_2 \tag{2.40}$$

From the definition of S^H and S^M,

$$\int\limits_{\frac{h}{2}}^{-\frac{h}{2}} S^H dx_2 = \frac{-H}{B} \qquad \int\limits_{\frac{h}{2}}^{-\frac{h}{2}} S^H x_2 dx_2 = 0$$

$$\tag{2.41}$$

$$\int\limits_{\frac{h}{2}}^{-\frac{h}{2}} S^M dx_2 = 0 \qquad \int\limits_{\frac{h}{2}}^{-\frac{h}{2}} S^H x_2 dx_2 = \frac{-M}{B}$$

substituting these into eq.(2.40)

$$\int\limits_{\frac{h}{2}}^{-\frac{h}{2}} \Phi dx_2 = -\epsilon^o \frac{P}{B} sin\theta - \frac{1}{B} \int\limits_{0}^{K^*} M d(K^*)' \tag{2.42}$$

With the first term of eq. (2.30) calculated, the second is now evaluated. Expansion of the traction gives

$$\int\limits_{\frac{h}{2}}^{-\frac{h}{2}} T_i u_{i,1} dx_2 = \int\limits_{-\frac{h}{2}}^{\frac{h}{2}} (\sigma_{11} u_{1,1} + \sigma_{12} u_{2,1}) dx_2 \tag{2.43}$$

The shear force resultant on the cross-section is (Fig. 2.6b)

$$\int\limits_{-\frac{h}{2}}^{\frac{h}{2}} \tau^V dx_2 = \frac{V}{B} \tag{2.44}$$

Now, eq.(2.31) and (2.3) can be now be used along with eq.(2.41) and eq.(2.44) to give

$$\int\limits_{-\frac{h}{2}}^{\frac{h}{2}} (\sigma_{11} u_{1,1} + \sigma_{12} u_{2,1}) dx_2 = (1 + \epsilon^o) \frac{P}{B} sin\theta + \frac{MK^*}{B} \tag{2.45}$$

Using this result with (2.42) in (2.30)

$$\frac{J_I}{2} = -\epsilon^o \frac{P}{B} sin\theta - \frac{1}{B} \int\limits_0^{K^*} M d(K^*)' + (1 + \epsilon^o) \frac{P}{B} sin\theta + \frac{M K^*}{B} \qquad (2.46)$$

Simplification by integrating by parts give the final result

$$J_I = \frac{2}{B} \int\limits_0^M K^* dM' + \frac{2P}{B} sin\theta \qquad (2.47)$$

This expression indicates J depends on the moment-curvature relationship, local moment, slope angle, and load.

Equation (2.47) is analogous to (2.12); it is more general since it allows for midplane straining, large rotations, and large strains along the beam provided the change in the area of the cross-section is negligible $(dA_o = dA)$. Further, if the integration path is taken near the crack tip, where the slope angle is essentially zero, eq. (2.47) is analogous to eq. (2.14). When no midplane straining occurs, $K^* = K$ and J is given by (2.14), the result for the geometrically nonlinear case.

J can also be calculated if the path is chosen at the loaded end so that $M = 0$ and

$$J_I = \frac{2P}{B} sin\theta \qquad (2.48)$$

The effect of midplane straining is implicit in the slope angle θ. Devitt et al. and Williams have calculated G for the DCB using nonlinear beam theory for a linear elastic material without midplane straining. Their relationship is basically the same as that in (2.48), indicating that their results are more general than originally thought. However, they did not show this because their analysis assumed midplane inextensibility.

3.2 Mode II ELS Specimen (Nonlinear Theory)

Consider an ELS specimen as shown in Fig. 2.7., where large rotations develop at the path locations. Similar to the geometric linear case, it can be shown that the only contribution to J comes from paths 2,6, and 4. Further, 2 and 6 are the same as the mode I DCB geometry. Therefore, their contribution to J , starting with (1.6) is given by

$$J_{II}^c = \frac{2}{B} \int\limits_0^{M^c} (K^*)^c dM' + \frac{2P}{B} sin\theta^c \qquad (2.49)$$

Evaluation of the contribution of the uncracked portion of the ELS (path segment 4) can be done in the same way in which it was done for the DCB except that now, the direction of integration and sign of the outward normal are opposite to those of the cracked portion. Thus,

STRAIN GAGES

P

a_e

l_g

(a) Schematic of J-M_{II} specimen.

P

θ_{load}

θ_x

x
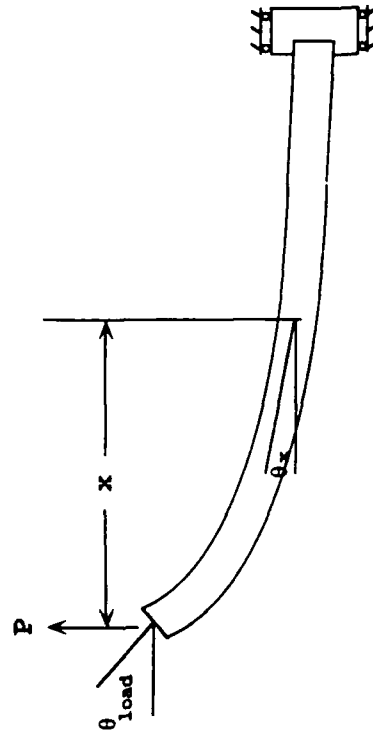
(b) Cantilever test used to evaluate moment-curvature relationships of the cracked and uncracked portions of ELS specimen.

Figure 2.8

P
P

Figure 2.7 End-loaded split laminate specimen for mode II delamination testing.

$$J_{II}^u = \int\limits_{-\frac{3h}{2}}^{\frac{h}{2}} (\Phi - T_i u_{i,1}) dx_2 \tag{2.50}$$

The resultant forces will now be

$$V = 2P\cos\theta$$
$$H = 2P\sin\theta \tag{2.51}$$

and the limits of integration will be from $\frac{-3h}{2}$ to $\frac{h}{2}$ since the origin of x_2 is at the midplane of the upper cracked leg. Proceeding in the same manner as for the DCB leg, the first term of eq.(2.50) will be given by

$$\int\limits_{-\frac{3h}{2}}^{\frac{h}{2}} \Phi dx_2 = \epsilon^o \frac{2P}{B}\sin\theta^u + \frac{1}{B}\int\limits_0^{K^*} M^u d(K^*)' \tag{2.52}$$

Expanding the second term of eq.(2.50)

$$\int\limits_{-\frac{3h}{2}}^{\frac{h}{2}} T_i u_{i,1} dx_2 = \int\limits_{-\frac{3h}{2}}^{\frac{h}{2}} (\sigma_{11} u_{1,1} + \sigma_{12} u_{2,1}) dx_2 \tag{2.53}$$

and using eq.(2.36) and (2.31) along with the boundary conditions,

$$\int\limits_{-\frac{h}{2}}^{\frac{h}{2}} (\sigma_{11} u_{1,1} + \sigma_{12} u_{2,1}) dx_2 = (1 + \epsilon^o)\frac{P}{B}\sin\theta^u + \frac{(MK^*)^u}{B} \tag{2.54}$$

Substitution of this equation and (2.52) into (2.50),

$$J_{II}^u = \epsilon^o \frac{2P}{B}\sin\theta^u + \frac{1}{B}\int\limits_0^{K^*} M^u d(K^*)' - (1 + \epsilon^o)\frac{2P}{B}\sin\theta^u + \frac{(MK^*)^u}{B} \tag{2.55}$$

simplyfying and integrating by parts,

$$J_{II}^u = -\frac{1}{B}\int\limits_0^{M^u} (K^*)^u dM' - \frac{2P}{B}\sin\theta^u \tag{2.56}$$

The final result is obtained adding eq. (2.56) and (2.49) to get

$$J_{II} = \frac{2}{B} \int_{0}^{M^c} (K^*)^c dM' + \frac{2P}{B} sin\theta^c - \frac{1}{B} \int_{0}^{M^u} (K^*)^u dM' - \frac{2P}{B} sin\theta^u \qquad (2.57)$$

This expression indicates that J depends on the moment-curvature relationship, local moment, slope angle, and load of the cracked and uncracked segments of the ELS specimen.

Similar to the DCB case, this equation is analogous to (2.24) for the linear case. Furthermore, if the paths are chosen close to the crack tip, the slope angle terms cancel each other to get

$$J_{II} = \frac{2}{B} \int_{0}^{M^c_{tip}} (K^*)^c dM - \frac{1}{B} \int_{0}^{M^u_{tip}} (K^*)^u dM$$

$$J_{II} = \frac{2}{B} I_c - \frac{1}{B} I_u \qquad (2.58)$$

This equation is analogous to (2.27) except that K^* replaces K. This indicates that equation (2.27) is more comprehensive than what it was previously derived for; it will account for geometrically nonlinear behavior (large rotations).

The analyses for mode I and mode II delamination using the J-integral and work potential theory derived do not treat bending-twisting or bending-shearing coupling (particularly in the $x_1 - x_3$ plane). The complexities of the state of stress near the crack tip which changes in the x_3 direction (plane stress-plane strain transitions) are not explicitly accounted for and are incorporated by calculating an average J which is done away from the complexities of the crack tip. Poisson effects which can lead to concavity of the beam (anticlastic curvature) are not accounted for in the J_I and J_{II} expressions. However, using moment-curvature relationships that have been obtained from specimens having the same width and thickness of the delaminating specimen will account for this behavior implicitly.

4. Methods to Evaluate the J-integral for Delamination Testing

4.1 Mode I Delamination

Evaluation of J_I in its most general form would be for an arbitrary path away from the crack tip and the end of the DCB legs, by measuring the load, P, the slope angle, θ, the load-line to path distance (to measure the local moment), and the moment- K^* relationship. In general, the M-k* relationship will be unique to the path since k* depends on midplane strain. However, if the midplane strain is small, K^* is approximately equal to K and the moment- curvature relationship will be essentially independent of position along the beam.

Determination of the value of J_I for crack growth requires making all the afore-mentioned measurements on a DCB specimen at the onset of crack growth. Also, the complete M- K^* relationship at the path location needs to be recorded. This approach is not practical, and when material behavior behaves inelastically , those measurements on the DCB specimen cannot be used to find J_I . An alternate method is one in which a delamination test is performed to determine the critical value of the moment at the crack tip, M_{tip} , together with an auxiliary test to evaluate the J vs M_{tip} relationship. This follows from consideration of (2.48), when the path is taken near the crack tip such that J_I is given by the first term of equation (2.47) with the M_{tip} as the upper limit of integration.

For the delamination test, point loaded DCB specimens are loaded in displacement control to the point of crack extension. During advance, the load and load-line to crack tip distance, a_e, are measured. The position of the crack tip is marked to correlate J with crack length, a. M_{tip} is given by the load times a_e.

A specimen similar to one leg of the DCB is used in the auxiliary test to deter-mine the J_I -M_{tip} relationship. It is a beam with the same width and layup which is cantilevered at one end and loaded with a point load at the other. Strain gages are mounted on the top and bottom of the specimen to measure the longitudinal strain. Figure 2.8 illustrates this test. A J_I vs M_{tip} plot is generated when as the specimen is loaded, at successive loads the load, P, the slope angle, θ, the load-line to path distance, l_g load-line to fixed end distance a_e, and the strain gage outputs are measured. The moment at the strain gages, M_g (where the integration path is evaluated) and the moment at the fixed end (corresponding gage readings are used to calculate K^* since the strains on the top and bottom surfaces, ϵ_T and ϵ_B and the thickness h are related to K^* by [22],

$$K^* = \frac{\epsilon_B - \epsilon_T}{h} \qquad (2.59)$$

With this equation, the data from this test, P, θ, M_g, K^* , and M_{tip} is used to calculate J for a given M_{tip} using (2.47). Due to path indendence , the position of the strain gages does not matter although, as it will be shown latter, they can not be placed too close from the cantilevered end. Because of the unique relationship of J_I and M_{tip} , one equation can be used to reduce data taken from the DCB when the crack was at various lengths.

The results of the two type of tests described are a set of M_{tip} values corresponding to crack growth and the J_I -M_{tip} relationship. Combining the data gives a set of critical J_I values for crack growth.

Evaluation of J_I requires consideration of material which is loading rather than unloading when inelastic behavior develops. Therefore, the material used for the J_I -M_{tip} test must be previously unloaded. When the material is elastic the unloading behavior and the loading behavior are the same and J_I can be found without the auxiliary test. Particularly, (2.48) can be used where the paths are taken at the ends of the legs of the DCB. Since only the load and the slope angle are needed, it is possible to automate the angle measurement by using rotational potentiometers or some other rotational transducer. J_I can then be determined continuously during crack growth.

In the case of inelastic behavior, equation (2.48) can be used for the auxiliary test. A particular attraction of this procedure is that strain gages are not necessary. Another alternative to evaluate the J_I - M_{tip} relationship is to chose the paths close to the crack tip such that slope angle measurements are not necessary. However, this would require the placement of strain gages at or very close to the fixed end. The problem with this approach is that the constraint of the fixed end could affect the strain gage readings in an unanticipated way. Experimental results concerning these effects will be presented later.

4.2 Mode II Delamination

Evaluation of J_{II} with the ELS, for the more general case, equation (2.56),requires the measurement of the load P, the load-line to crack and uncracked path distances l_c, l_u, their corresponding slope angles, θ_c and θ_u, and the $M^c - (K_c^*)$ and $M^u - (K_u^*)$ relationships. During the mode II delamination test, the aforementioned quantities would have to be measured during crack growth. Unfortunately, this is an impractical procedure. Furthermore, when inelasticity develops, the measured J_{II} would not be valid due to unloading behavior taking place as the crack advances.

An alternate method to evaluate J_{II} is one in which the paths are taken close to the crack tip such that J_{II} is given by equation (2.58). During a delamination test, under displacement controlled conditions, the load P, the load-line to crack tip distance a_e , and the slope angle θ_{tip} at the crack tip during crack advance are monitored. Also, the location of the crack tip a is located using pencil marks on the edge of the specimen to correlate it to J_{II} . From the load P and load-line to crack tip distance, the critical moments at the crack tip for the cracked and uncracked segments of the ELS are calculated. Even though θ_{tip} does not explicitly appear in (2.58), it is needed to evaluate the moment-curvature relationships for the cases when midplane straining occurs, which affect these relationships. When crack growth is relatively stable, several sets of M_{tip} (for cracked and uncracked portions of ELS), θ_{tip}, and a can be output for crack growth.

With the information obtained during the mode II delamination test, similar to the DCB case, the moment-curvature relationship is evaluated using an auxiliary test. However, in this case, in addition to the auxiliary test for the legs of the ELS, another one is needed for the uncracked portion. Also, the effect of θ_{tip} needs to be assessed on the moment-curvature relationships. A convenient way of accomplishing this task derives from the path-independence of the J_I . From (2.47), it can be seen that for one leg of the DCB, equivalent to the auxiliary test shown in Fig. 2.8b, its contribution to the total J is given by

$$\frac{J}{2} = \frac{1}{B} \int_{0}^{M_x} K^* dM' + \frac{P}{B} sin\theta_x \qquad (2.60)$$

where M_x is the moment at a distance x form the load line and θ_x is the slope angle at the x location. Evaluation of the moment-curvature relationships at different fixed slope angles can be done by equating the results of(2.60) when the path is taken at the load line (x=0), and taken at any location x away from it. Therefore,

$$\frac{J}{2} = \frac{P}{B}sin\theta_{load} = \frac{1}{B} \int\limits_{0}^{M_x} K^* dM' + \frac{P}{B}sin\theta_x \tag{2.61}$$

where θ_{load} is the slope angle at the load-line. Then, solving for the $M - K$ relationship one obtains

$$\int\limits_{0}^{M_x} K^* dM' = P(sin\theta_{load} - sin\theta_x) \tag{2.62}$$

The moment-curvature relationships for the cracked and uncracked portion of the ELS test can now be determined by conducting the test shown in Fig. 2.8b using beams identical to these portions, using the measured moments and slope angles at the crack tip during crack growth. An advantage of this procedure is that it is not necessary to measure surface strains. Only by means of the load P, the load-line to path distance x are the moment-curvature relationships evaluated. Furthermore, these can be measured at any desired slope angle such as is the case of the slope angle during actual crack growth θ_{tip} during mode II delamination of the ELS.

Once the moment-curvature relationships are measured, they can be used in (2.58) to obtain values between J_{II} for crack growth and a.

DELAMINATION TESTING

The main objective of this section is to investigate variables which are anticipated to be of importance in determining the mode I and mode II delamination fracture toughness of composites, particularly multidirectional ones, using the J theory outlined in the previous chapter.

The effect of stacking sequence on toughness is of primary interest. Essentially there are two questions: First, what is the effect of particular combinations of ply angles at the delamination plane? Second, what is the effect of a high percentage of off-axis plies? The first question deals mostly with the effect of layup near the crack tip; the second with more general specimen behavior, such as far-field damge and viscoelasticity. To investigate these effects, tests were conducted using several layups:unidirectional specimens (to form a baseline for comparison), specimens with various ply angles at the delamination plane, but with a high percentage of 0° fibers, and full angle-ply specimens.

Another concern is possible geometry dependence of delamination resistance on crack length. For mode I delamination, the dependence of delamination resistance on crack length was performed using specimens with very short crack lengths; for mode II delamination, this dependance was assessed by means of varying the slope angle at the crack tip which changes with crack length. The dependence of toughness on the crack-length-to-width aspect ratio is an intimately linked issue. Tests were conducted on specimens of different widths for the angle-ply layup. Tests were also conducted on specimens of different thicknesses to check the possible dependence of J on number of plies.

Rate effects on mode I delamination were addressed through a series of experiments to determine the correlation between J and crack speed. Unidirectional, fiber-dominated, and angle-ply specimens were tested.

To study the possible influence on delamination of matrix damage due to in-plane loading, a few experiments were conducted on material which had been predamaged by inplane fatigue loading. Also, the effect of very tough matrices on the ability of the proposed J-integral to characterize delamination is addressed in the case of mode II delamination.

3.1 Materials and Procedures

The composite materials used in this investigation were AS4/3502, T2C145/F155, and T6T145/F185. The former is manufactured by Hercules Inc. whereas the latter two are manufactured by Hexcel Corporation. The AS4 graphite fibers have an average tensile strength of 520 ksi [52]. The T2C145 and T6T145 graphite fibers have an average tensile modulus of 34 msi [22,52]. The 3502 epoxy is a highly cross-linked brittle resin with a tensile elongation of only 1.5% and a fracture toughness of approximately 0.4 lb/in [54]. The F155 is a medium cross-linked rubber toughened epoxy with about 6% elastomer by weight. Approximately 4% is liquid carboxy-terminated solid particles (Picar 1472). It has a tensile elongation of 5.2% and a fracture toughness of 4.18 lb/in

[22]. Finally, the F185 epoxy resin, the most ductile resin of the three, contains 8.1% by weight of the liquid CTBN and 5.41472 particles. It has a strain to failure of 8-15% and a fracture toughness of 34 to 46 lb/in [52].

All laminates were made from 12 inch prepreg tape of the three type of materials used. The laminates were cured according to the cycles recommended by the manufacturer. The curing procedures were done in an open-cavity press at the Materials and Structures Laboratory at Texas A&M University. The layups used for the mode I and mode II delamination studies are shown in Tables 3.1 and 3.2, respectively. The starting crack at the midplane of the DCB and ELS specimens were introduced on all panels by means of a teflon insert 0.001 in. thick. The same material was used to separate part of the laminate (during hand layup prior to curing) into two half laminates. These half laminates were used to obtain specimens from which to evaluate the contribution of the cracked legs of the DCB and ELS specimens in J_I and J_{II}. For the ELS, uncracked specimens were used to evaluate the contribution of the uncracked segment of the ELS into J_{II}.

DCB, ELS, and J_I -M_{tip} and I_c -M_{tip}, I_u -M_{tip} specimens approximately 1 inch wide and 10 inch long were cut from the cured plates using a diamond blade cutter. Some 0.5 inch and 2 inch wide specimens were also cut. The DCB specimens were cut out of the plates so that the starter crack was generally 2 inches long. The starter crack for the ELS specimens was typically at least 3 to 5 inches long. However, this varied from plate to plate.

Aluminum and brass tabs were bonded to the cracked end of the specimens using an M-bond 200 adhesive and 200 catalyst made by MM Measurements Group, Inc, Raleigh, NC.

350 ohm nominal resistance strain gages were bonded to the J_I -M_{tip} specimens using the MM measurements Group AE-15 adhesive system. The adhesive was cured in an oven at 140 °F for two hours. Gages were mounted in pairs–one on top and one opposite it on the bottom of the specimen. Gages were centered with respect to the width. The strain gages had effective gage lengths of either 0.0625, 0.125, or 0.25 inches. Matched gages were used for each specimen. The different gage lengths did not appear to give different results. The gages were all self-compensating for a thermal expansion coefficient of 6×10^{-6} in/in/°F.

3.1.1 DCB and ELS Testing

The DCB tests (see Fig. 3.1) were performed for this study using three different MTS closed-loop servo-hydraulic testing machine with load capacities of 5, 20, and 100 thousand pounds. The testing procedure was the same in each case. The tests were run in displacement control; displacements were measured by means of a linear voltage differential transducer (LVDT) mounted on each ram. Loads were measured using load cells of either 100 or 750 pounds capacity. In the latter case, the full scale calibration was for 100 pounds.

ELS testing (mode II delamination) was done with a mode II fixture attached to one of the closed-loop servo-hydraulic MTS machines (see Fig. 3.2). During testing, this fixture prevents the uncracked beam end from any rotation, while allowing free longitudinal movement to keep the concentrated load perpendicular at the loaded end.
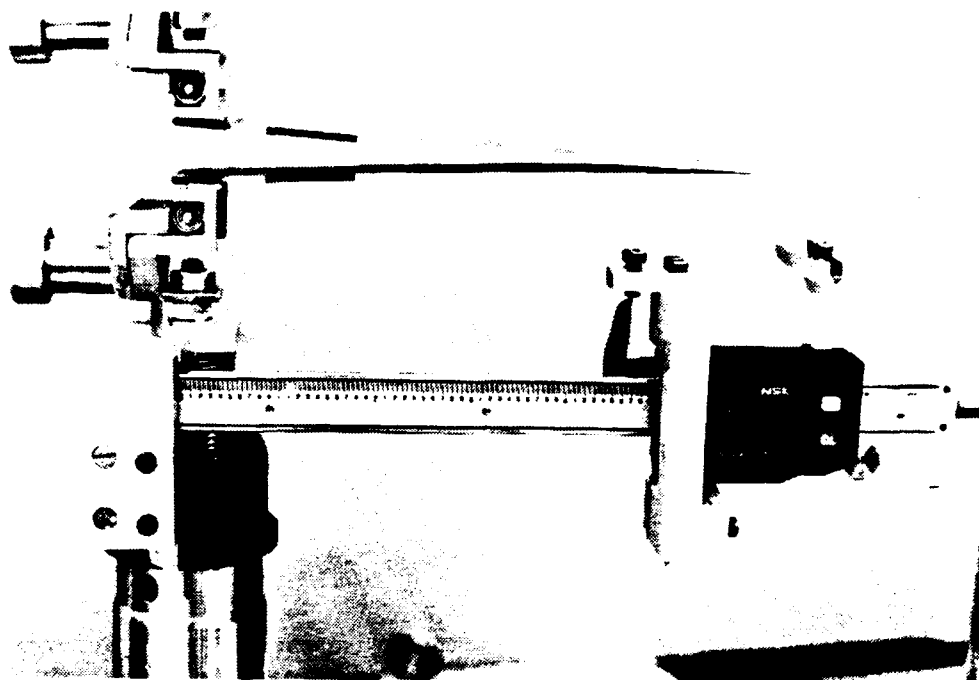
Figure 3.1 DCB test configuration (mode I)
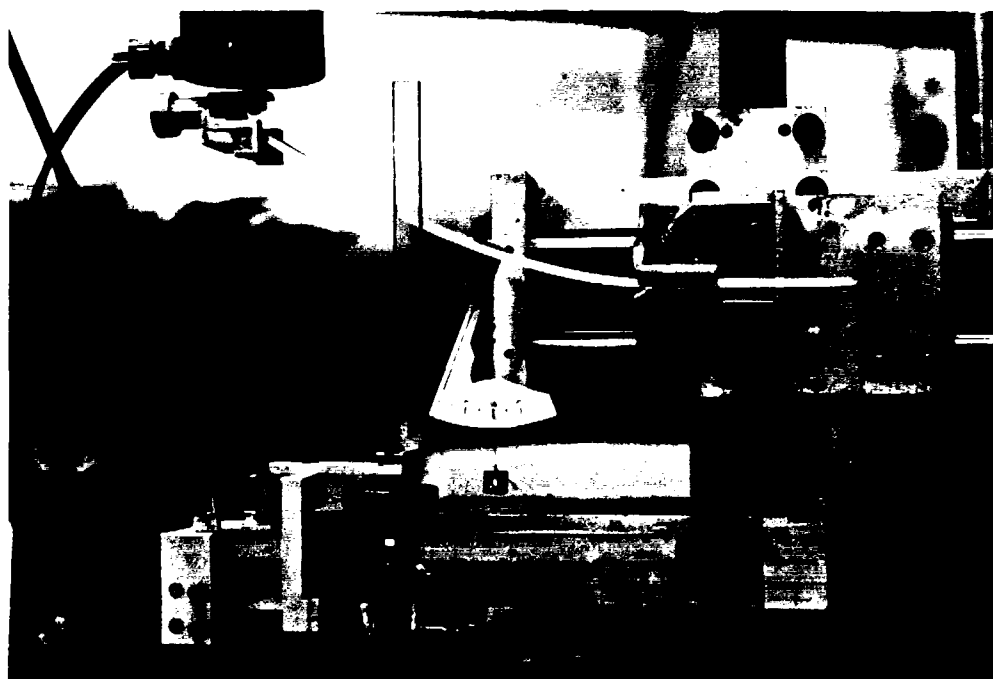
Figure 3.2 ELS test configuration (mode II)

Table 3.1 Laminate layups used to study mode I delamination

Designation	Layup
Unidirectional	$[O_{24}]$
+-45 fiber-dominated	$[+-45/O_8/-+45]_{anti}$
+-45 angle-ply	$[+-45/(-+45)_2/(+-45)_2/+45]_{anti}$
+-45 angle-ply (16 ply)	$[+-45/(-+45)_2/-+45]_{anti}$
+-45 angle-ply (16 ply) (antisymmetric legs)	$[(+-45)_8]$
+-10 fiber-dominated	$[+-10/O_8/-+10]_{anti}$
+-30 fiber-dominated	$[+-30/O_8/-+30]_{anti}$

Notes:
1. Subscripts indicate repeated plies or subsequences.
2. "anti" indicates antisymmetry about the midplane.
3. Layups are 24 plies unless noted.
4. Material: T2C145/F155

Table 3.2 Laminate layups used to study mode II delamination

AS4/3502	T2C145/F155	T6T145/F185
$[O_8]$	$[O_8]$	$[O_8]$
$[O_{24}]$	$[O_2,+-30]_{anti}$	$[O_{24}]$
	$[O_2,+-45]_{anti}$	
	$[O_{16}]$	
	$[O_{24}]$	
	$[O_{32}]$	
	$[0,(+-45)_2,O_2,(-+45)_2,0]_s$	
	$[(-+30)_2,-30,O_2,(-+30)_2,-30]_{anti}$	
	$[(-+45)_2,-45,O_2,(-+45)_2,-45]_{anti}$	

ELS specimens were clamped such that most of the specimens were 8 inch gage length. Some were 6 inch long. A mode I precrack was introduced to all the ELS specimens to sharpen the initial crack created by the teflon insert and to provide an initial crack-length-to-beam-length (a/L) ratio of approximately 0.55. At this ratio and larger, stable crack growth is expected for this test configuration.

Load-displacement records were made during each test using an X-Y recorder. In addition, computer data acquisition was sometimes used to gather digital load and displacement data. A Hewlett-Packard 3497A data acquisition unit was connected to either a Hewlett-Packard 9845B or 9816 computer for this purpose. The digital data was useful for production of scaled graphs and data reduction using the area method.

Most crack length measurements for the DCB and ELS were made using one of two methods. (Other methods were used to measure crack length for high displacement-rate tests). In both methods, the crack tip was first located visually on the painted specimen edge using a magnifying glass. The position was then marked using a fine pencil mark. The load-line to crack tip distance was then measured. In the early tests, this measurement was made using a ruler marked 0.01 inch increments. The precision of these measurements was limited to an estimated 0.05 inch (about 1 to 3% of the crack length for the range of crack lengths in a typical test). In order to improve the precision of the projected crack length measurements, a special device was designed for use in the later tests. This device is shown in Fig. 3.1 which also illustrates the DCB test. It consists of a digital caliper mounted on the ram below the lower loading grip and a transparent plastic piece scribed with a line. During the test, after the location of the crack tip was marked the sighting line was moved to the crack tip. The load-line to crack tip distance was then read directly from the caliper. To avoid error due to parallax , the device was adjustable so that the sighting piece could be moved close to the specimen edge. The resolution of the digital caliper was 0.0005 inches. The overall measurement precision is estimated to be no better than 0.02 inches (less than 1 test). After completion of the test, the actual crack lengths measured during the test were measured. This was done after unloading the specimen using the digital caliper to measure the distance from the load-line to the pencil marks made during the test.

Crack lengths measurements for the DCB test with high crack speeds were done using two methods. The first used Micro-Measurement crack propagation gages (TK-09-CPC03-003/DCP) which were mounted in parallel on the edge of the specimen using the M-bond 200 adhesive. A specimen is shown in Fig. 3.3. Basically, as a crack grows into the stranded gage, the strands are broken sequentially. During loading, the specimen was videotaped which allowed the measurement of the load-line to crack tip distance which was correlated to the the load by timing the experiment. Actual crack length was determined by the position of the strand on the specimen. Crack speeds were determined by dividing the increment of crack advance by the time elapsed between previously determined points. For a more detailed explanation of this procedure see reference [22].

After construction of the digital caliper fixtures, an alternate technique was used. Tests were conducted in the normal manner, but no actual record was made of the load-line to crack tip distance or load. Instead, the test was videotaped. A digital voltmeter
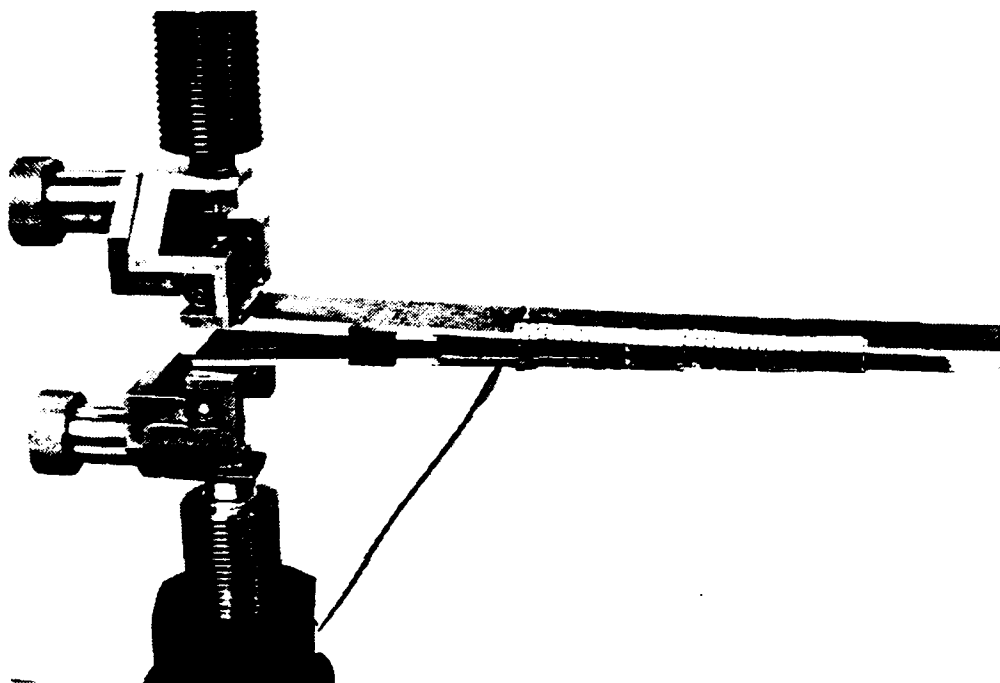
Figure 3.3 DCB specimen with crack propagation gages

showing the load and a digital stopwatch were placed in the view of the video camera. The position of the crack tip was marked using a fine pencil mark in the usual way, so the crack length for each reading could be measured after the test. The corresponding load-line to crack tip distance, load, and time could be read from the videorecord.

With the exception of the high crack speed tests, most tests were conducted at displacement rates of 0.1 inch/min. However, in some were run between 0.005 and 0.1 inch/min.

During the course of a DCB test, load and projected crack length were measured periodically based on the load-displacement of the specimen. Measurements were made during crack advance, except for some instances just after sudden increment of crack growth followed by arrest. Arrest values are specially noted in the discussion of results.

For the ELS test, the load, the slope angle at the crack tip, and the projected crack length (load line to crack tip distance) were measured periodically. The angles were measured by means of a simple protractor with a weighted thread to indicate the vertical. Brass mounts were used to attach the protractor to the specimen. For most of the ELS tests, the slope angle at the crack tip during crack growth was measured at the beginning and end of overall crack growth to establish the range at which crack growth occurred.

3.1.2 Tests to Determine the J_I -M_{tip} and J_{II} -M_{tip} Relationships

The set-up for a typical J -M_{tip} test is shown in Fig. 3.4. The specimen is loaded as a cantilever beam (top leg). The lower leg is an identical beam, without strain gages. This set-up allows the clamped end of the cantilever to move horizontally.

Tests were conducted by loading the specimen in displacement control in increments. For each increment the curvature, slope, load, and two load-line distances were measured. The curvatures were measured using the strain gage readings of the top and bottom surfaces and equation (2.59). A Hewlett-Packard 3497A data acquisition unit connected to a Hewlett-Packard 9845B or 9816 computer was used to monitor the strain gage output and reduce the data. The slope of the beam at the location of the strain gages was measured using a simple protractor having a weighted thread to indicate the vertical (see Fig. 3.4). A second protractor was used to measure the angle at the loaded end of the beam. Spring steel clips were used to attach the protractor to the specimen. The load-line distances were measured with the digital caliper and manually entered into the computer to calculate the moments. The load was increased until measurements were taken for moments at the clamp corresponding to crack tip moments observed in the DCB tests.

A limited number of four point bend test were performed to obtain the J_I -M_{tip} relationship when no midplane straining develops (as when using equation 2.14). Fig. 3.5 shows an schematic of this test. The strain gages can be located anywhere in the constant moment region between the interior loading points. The advantage of this method is that it is not necessary to measure the load-line to strain gage distance. In order to avoid friction at the loading points the center loading pins were mounted on bearings. Teflon film was also placed over the outer loading pins to minimize friction.
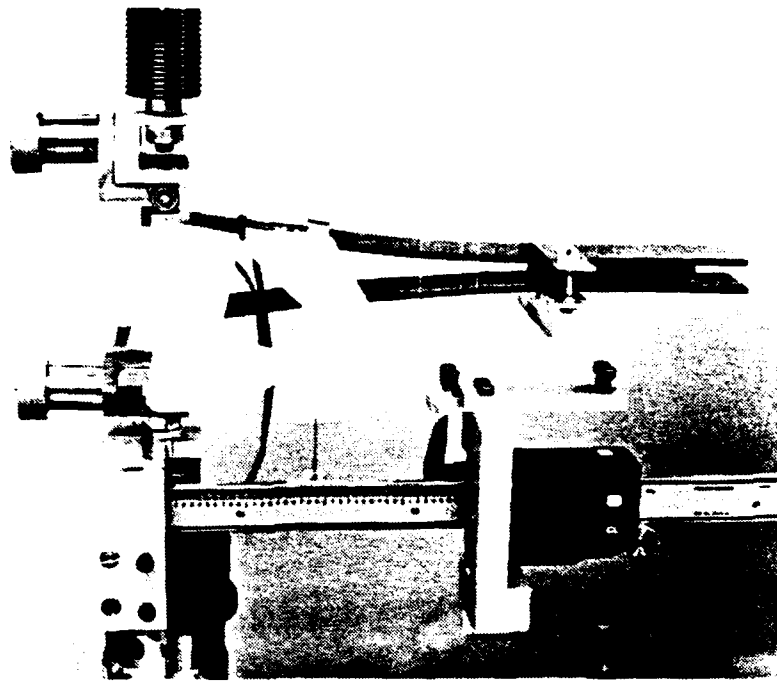
Figure 3.4 Setup to determine the J-M_{tip} relationships
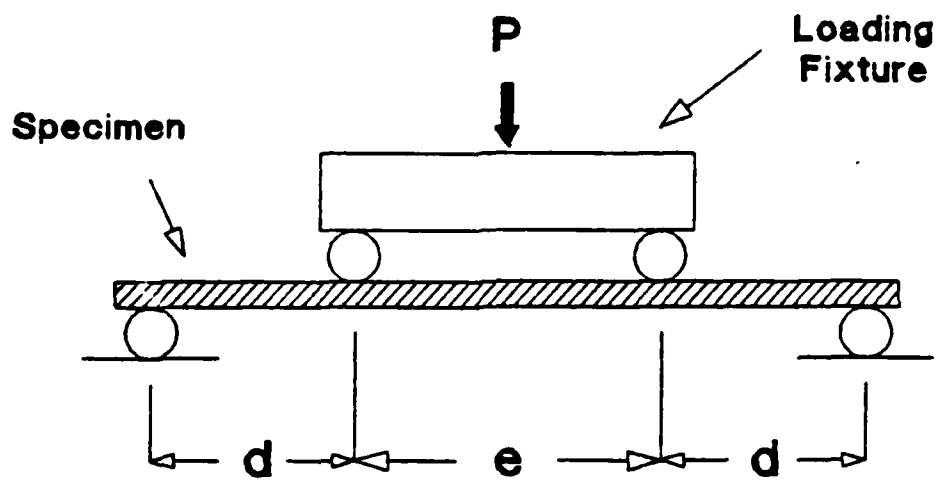
Figure 3.5 Schematic of four point bend test set-up

Determination of the J_{II} -M_{tip} relationship was done by performing a variation of the cantilever beam test used to compute the J_I -M_{tip} relationship on beams representing the cracked and uncracked portions of the ELS specimen. The test generated data to evaluate the I_c -M_{tip} and I_u -M_{tip} relationships that define the J_{II} integral (equation 2.58). For this test, instead of using strain gages, only the angle at the path location where the moment-curvature is evaluated is monitored. Therefore, the moment-curvature relationships were indirectly measured by means of equation (2.62). The protractor used for this slope measurement was moved along the beam to obtain variable moments at constant slope angles. This allowed the generation of moment-curvature relationships at constant slope angle.

During the test, for a fixed load, the movable protractor was typically placed at three slope angle locations. At each location, the distance from the loaded end was measured with the digital caliper described earlier. During each load step, the load, slope angle at the loaded end, and the three locations from the loaded end of the slope angles along the beam were recorded. The range of slope angles was determined from the slope angles at which crack growth took place and determined during the ELS test for each layup. The range of moments tested were also determined from the moment at which crack growth occurred. These cantilever beam tests were performed with beams identical to the cracked and uncracked portions of the ELS specimens.

The data obtained was used with (2.62) to evaluate I_c -M_{tip} and I_u -M_{tip} relationships as a function of slope angle. In turn these relationships were used to evaluate J_{II} -M_{tip} curves for all layups tested. The slope angles represent indirectly crack growth and thus crack length. Therefore, with these relationships it was possible to evaluate any dependence of the J_{II} -M_{tip} curves with crack length.

The length of the beams representing the uncracked portion of the ELS specimen was 8 inches whereas the ones for the cracked portion was 6 inches. The choice of lengths was made to facilitate measuring the required moments and slope angles.

3.1.3 Tensile Fatigue Predamage tests

Three monotonic tensile tests were perfomred to determine the average ultimate tensile stress for 24 ply angle-ply DCB specimens. This stress was used to set the maximum load levels for the cyclic loading. Load and grip displacement were recorded on an X-Y recorder. The specimens were 0.5 inch wide and 6 inches long. Flat aluminum tabs were bonded to the specimen ends to prevent crushing in the grips.

Three DCB and two J_I -M_{tip} specimens were predamaged before delamination testing. High elongation strain gages (Micro-Measurement EP-08-125AC-350) were bonded to either side of each specimen using the AE-15 adhesive system. Each specimen was then subjected to ten tensile load cycles. Specimens were cycled to 75% and 60% of the ultimate stress. During cycling the strain gages and load were read by a Hewlett-Packard 3497A data acquisition unit and a Hewlett-Packard 9816 computer. After predamaging, the tensile loading tabs were cut off and the usual DCB loading tabs were attached. New strain gages were installed on the J_I -M_{tip} specimens, since the old gages had experienced significant permanent strain.

3.2 Mode I Results

3.2.1 Verification of Procedure to Evaluate J_I

This section documents tests done which verify tne testing and data reduction procedures. The objective here is to demonstrate two characteristics of the behavior necessary for the procedure to be useful; namely, (1) the J_I -M_{tip} curves for a particular layup must be identical for any path chosen to evaluate J_I , and (2) the length of the specimen should not affect the J_I -M_{tip} curve. In other words, the J_I -M_{tip} relationship should not depend of crack length.

The first characteristic is demostrated by Figs. 3.6-8. The J_I -M_{tip} relationships are shown for specimens with unidirectional, ±45 fiber-dominated, and ±45 angle -ply layups, respectively. Curves are shown as derived from different paths for calculation of J_I . J(end) was calculated using the load and angle at the loaded end of the beam through (2.48). Strain gage data was used with equation (2.47) to calculate J_I for other paths, designated as J(g1) and J(g2). Note the agreement of the curves which confirms the path-independence of the approximation of J_I derived in Chapter II. It should be noted that this verification of the path-independence of the approximate J_I relation is only valid for the conditions assumed in these tests.

Figure 3.9 illustrates that the length of the specimen used to calculate the J_I - M_{tip} relationship does not affect it. One should be able to use a specimen of arbitraty length to determine it. Therefore, the agreement of these curves for the ±45 fiber-dominated specimen which has been clamped to give different free lengths, is a check on the independence of the J_I -M_{tip} relationship from beam length (i.e. crack length).

3.2.1 Effect of Stacking Sequence on J_I -M_{tip}

The effect of stacking sequence on J_I -M_{tip} is shown in Fig. 3.10. All specimens were one inch wide. The layups associated with curves 1-6 had 24 plies total (so these specimens were 12 plies thick); for specimens 7 and 8, the total thickness was 16 plies (giving 8 ply specimens). The primary characteristic of the curves is that to apply a given J_I , stiffer layups require higher crack tip moments. In the case of curves for the unidirectional and ±10° fiber-dominated layups (numbers 1 and 2), one sees that the general trend does not hold. However, this is due to the actual thickness of the specimens. The latter plate was thicker than the unidirectional plate. Therefore using the measured thicknesses of the specimens, laminate theory predicts that the ±10° fiber-dominated specimen would be stiffer than the unidirectional one. The same type of difference in stiffness is seen for curves 4 and 5 which are for identical stacking sequences. The discrepancy is again due to variations in thickness for the two different plates. The same is true for curves 7 and 8 which are for specimens with similar stacking sequences. The variation of the J_I -M_{tip} behavior due to thickness is practically significant for the testing method. It emphasizes the importance of using specimens of the J_I -M_{tip} tests which are taken from the same plate of the material as the DCB specimens.

Figure 3.8 J_1 versus crack tip moment from two paths for the +- 45 angle-ply layup. Specimen length: 4.962 in. Distance of gages from loaded end: 2.390 in.

Figure 3.9 J_1 versus crack tip moment from two specimens of different lengths. Length of no. 1 = 4.008 in. Length of no. 2 = 5.987 in. Gages were 1.974 in. from the loaded end in each case.
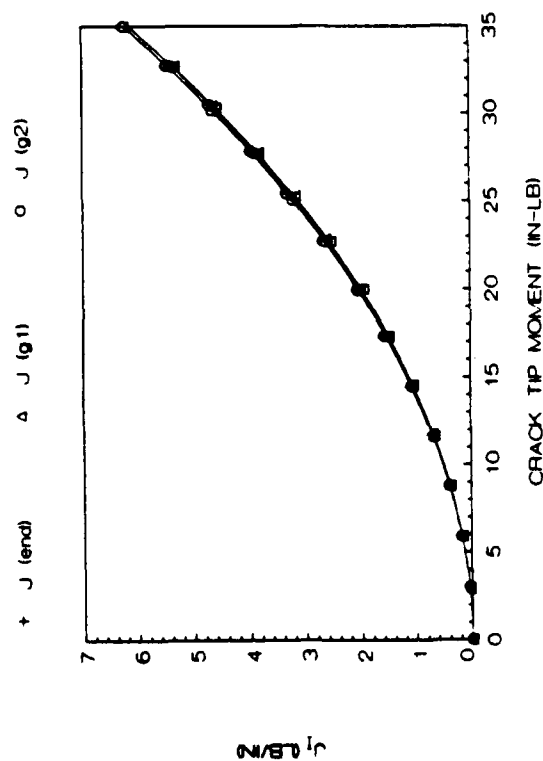
Figure 3.6 J_1 versus crack tip moment from three paths for the +-45 fiber-dominated layup. Specimen length: 5.963 in. Distance of gages from loaded end: 2.477 in. and 4.198 in.
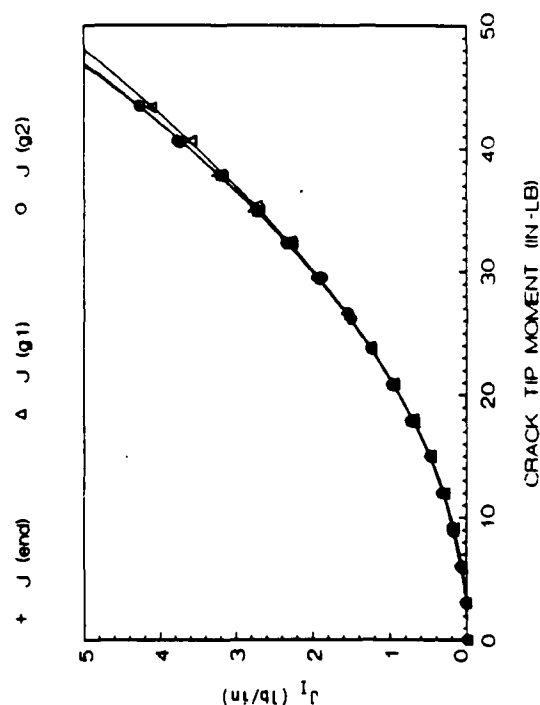
Figure 3.7 J_1 versus crack tip moment from three paths for the unidirectional layup. Specimen length: 6.005 in. Distance of gages from loaded end: 2.515 in. and 4.127 in.

3.2.3 Effect of Width on J_I -M_{tip}

Figure 3.11 shows the J_I versus M_{tip} curves for angle-ply specimens with widths of 0.5, 1 and 2 inches. The crack tip moment (i.e. moment at the clamp) is normalized by the specimen width. Because the curves are distinct , it is clear that one must use a J_I -M_{tip} specimen which has the same width as the DCB specimen used to determine the M_{tip} for crack advance. It should be noted that in order to completely assess a possible geometry-dependence of J_I on width, J_I -M_{tip} tests should be combined with M_{tip} from DCB tests of varying width.

3.2.4 Moment-Curvature Behavior

Figure 3.12 illustrates specimen behavior via moment-curvature relationships of a unidirectional and two fiber dominated layups with $\pm30^o$ and $\mp45^o$ plies. Contrary to the unidirectional curves, the angle-ply fiber dominated layups show an apparent stiffening for high moments. This is due to midplane compression since from (2.32), $K^* = (1 + \epsilon^o)K$. Fig. 3.13 supports this interpretation since it shows that for bending without midplane straining, the absolute value of the strains measured on the top and bottom of the beams would be the same. Note that the compressive strain is larger for the more compliant specimens. It appears that rather than experiencing a tensile strain due to the axial tensile force generated when large rotations develop, these specimens go into compression at the midplane due to a difference between the compression and tension moduli. Thus, any would-be stretching of the midplane is overwhelmed. The *effect of the difference in moduli* is to produce stretching-bending-coupling. even for nominally symmetric laminates. Another feature of the curves in Fig. 3.12 is the very small hysteresis for loading and unloading of these fiber-dominated layups.

The moment-curvature relationship of a ±45 angle-ply specimen exhibits a different type of behavior, as seen in Fig. 3.14. The apparent stiffening of the fiber-dominated laypus has been replaced by a strong softening. The hysteresis is also large. The specimen was also seen to experience permanent deformation upon unloading which did not recover with time. Therefore, damage took place during loading. The strain gage data for these layup indicates midplane compression (Fig. 3.15) which was not apparent from the $M - K^*$ plot because the softening due to damage conceals it. It is clear from the $M - K^*$ plots of fiber dominated and angle-ply laminates that the most significant aspect of the behavior of the angle-ply is that they experience damage which leads to permanent deformation.

The placement of the strain gages to determine the $M - K^*$ relationship that defines the J_I -M_{tip} curves can be critical for some cases. Figs. 3.16-18 provide evidence of the errors introduced in the J_I -M_{tip} plots derived from gage placement; unidirectional, fiber-dominated, and angle-ply layups are shown, respectively. Two paths were used, away from the clamp (between 2 to 3 inches from clamp) and near the clamp (between 0.36 to 0.22 inches from clamp). It is rather obvious that as one goes from the more fiber-dominated layups to angle-ply layups, the error in J_I becomes larger for a fixed M_{tip} when the gages are placed near the clamped end. To avoid this problem, gage placement was always done at no less than 2 inches from the clamped end, which has also been suggested in [76]. In conclusion, it seems that for angle-ply layups,

Figure 3.12 Moment-curvature relationship for three fiber-dominated specimens. a) unidirectional b) +-30 fiber-dominated c) +-45 fiber-dominated.
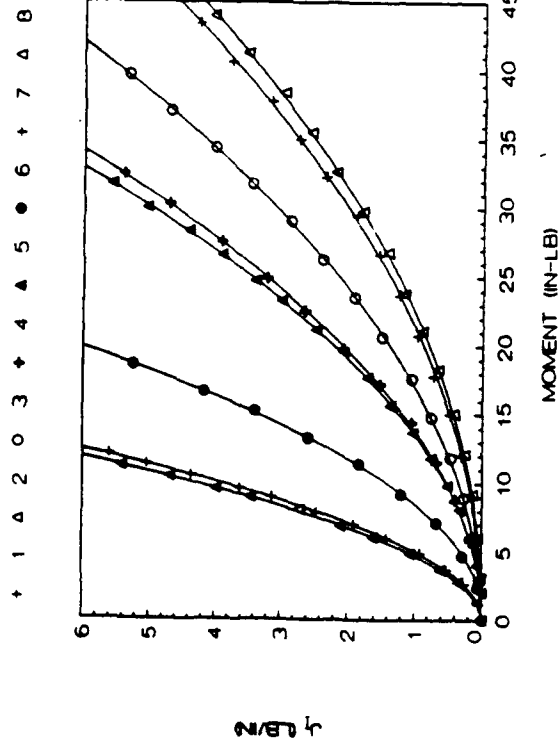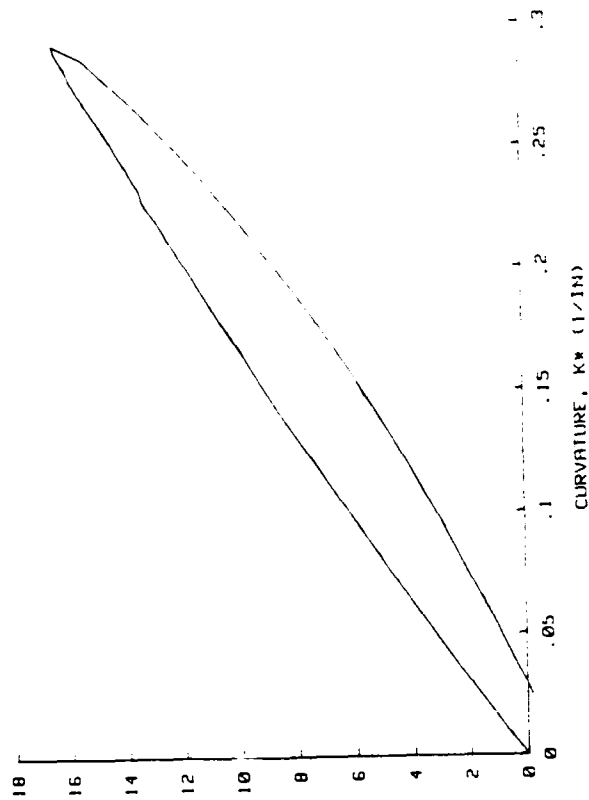

Figure 3.10 J_I versus crack tip moment for eight layups. 1) +-45 angle-ply (16 plies, antisymmetric) 2) +-45 angle-ply (16 plies, symmetric) 3) +-30 fiber-dominated 4) +-45 fiber-dominated 6) +-45 angle-ply 7) unidirectional 8) +-10 fiber-dominated.
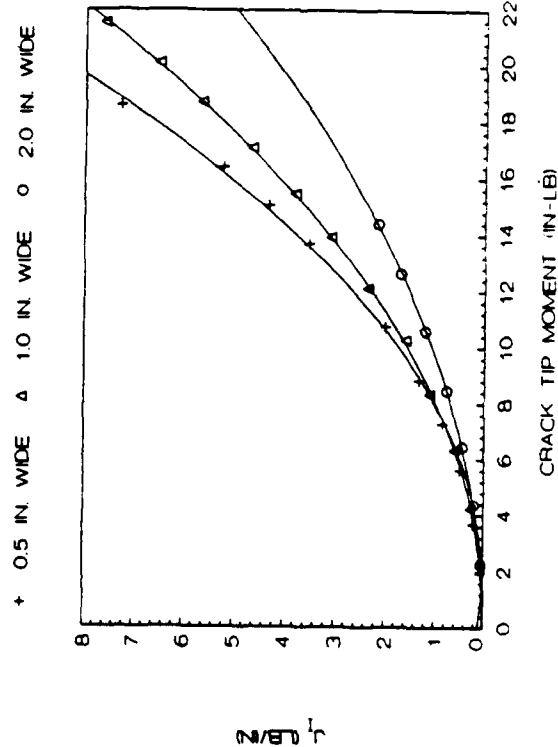
Figure 3.11 J_I versus crack tip moment for +-45 angle ply specimens of three different widths.

Figure 3.14 Moment curvature relationship for a +-45 angle-ply specimen.

MOMENT (IN-LB)

GAGE IN TENSION

GAGE IN COMPRESSION
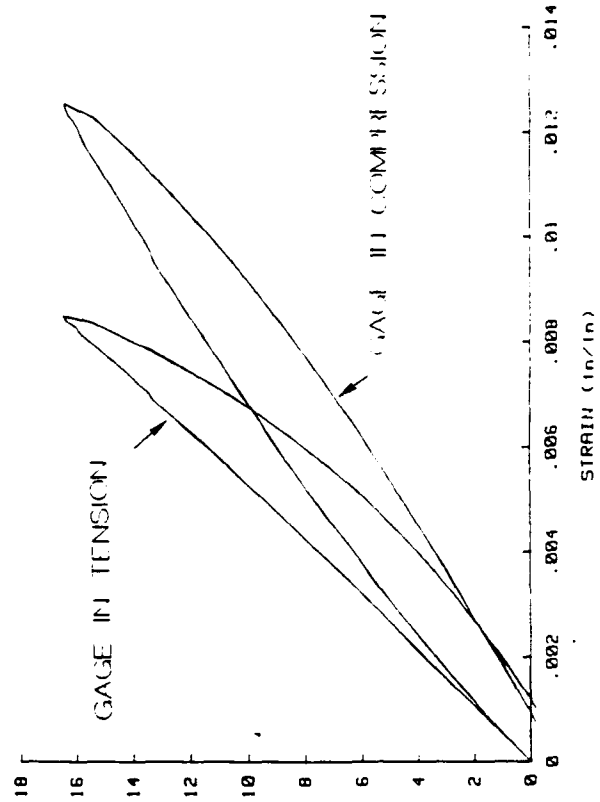
Figure 3.15 Strain gage readings for a +-45 angle-ply moment curvature specimen.

MOMENT (in-lbs)

GAGE IN TENSION

GAGE IN COMPRESSION

(a)

MOMENT (in-lbs)

GAGE IN TENSION

GAGE IN COMPRESSION

(b)

MOMENT (in-lbs)
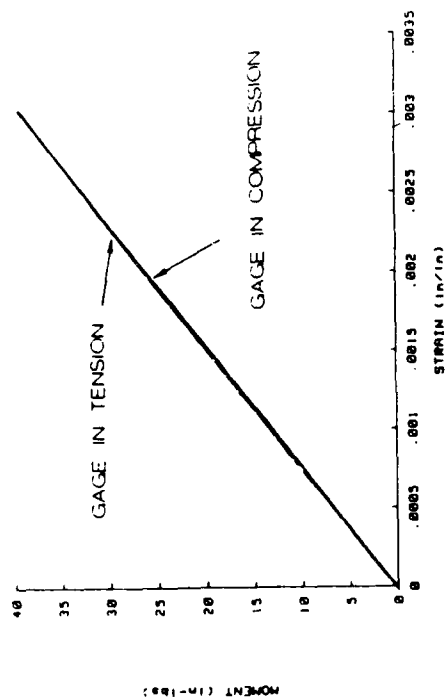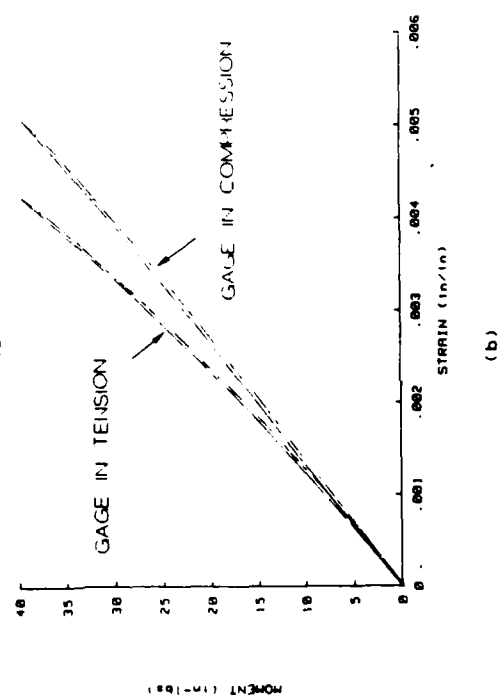
Figure 3.13 Strain gage readings for two moment-curvature specimens. a) unidirectional b) +-30 fiber-dominated. The +-45 fiber-dominated specimen was similar to (b).

+ GAGES AND
ANGLE

△ GAGES NEAR
CLAMP

CRACK TIP MOMENT (IN-LB)

Figure 3.18 J versus crack tip moment from two methods
for a ±45 angle-ply specimen.

+ GAGES AND
ANGLE

△ GAGES NEAR
CLAMP

CRACK TIP MOMENT (IN-LB)
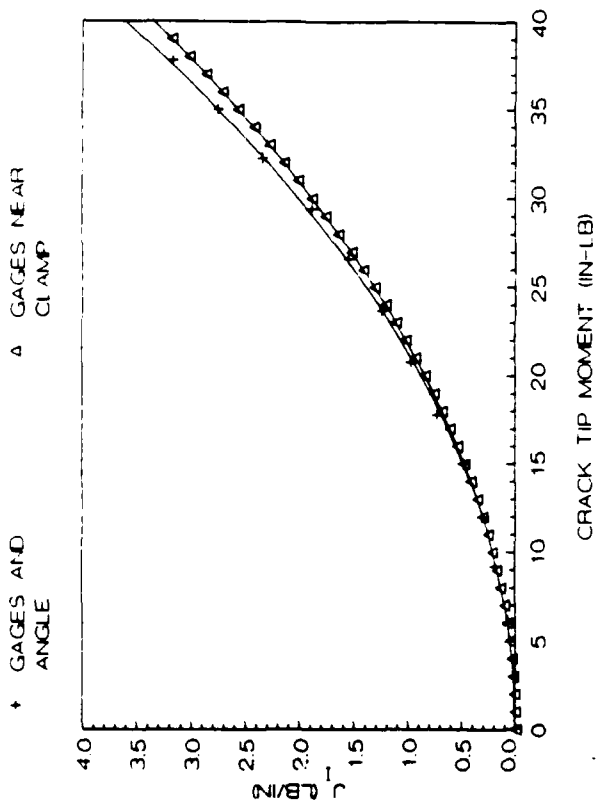
Figure 3.16 J versus crack tip moment from two methods
for a unidirectional specimen.

+ GAGES AND
ANGLE

△ GAGES NEAR
CLAMP

CRACK TIP MOMENT (IN-LB)
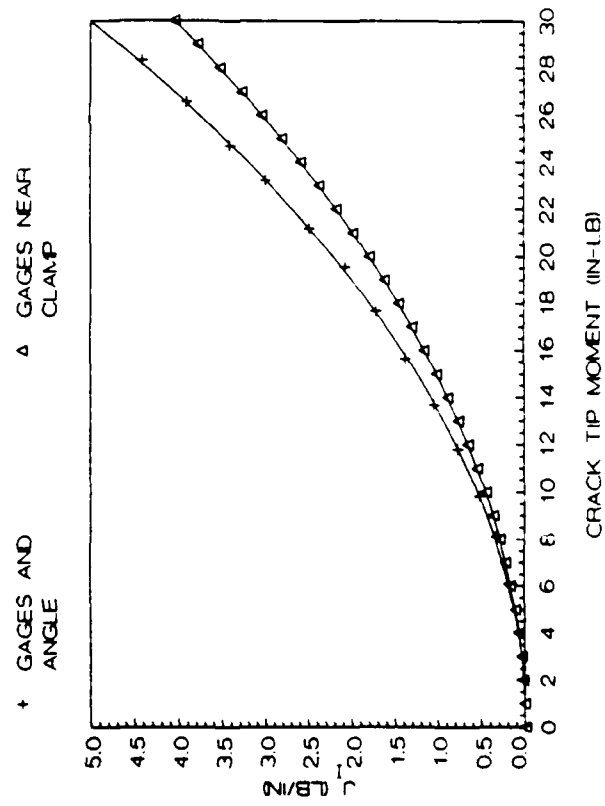
Figure 3.17 J versus crack tip moment from two methods
for a ±45 fiber-dominated specimen.

determination of the $M - K^*$ relationship can not be done near the clamp where the slope angle need not be measured.

An alternate method of determining the $M - K^*$ relationship for calculating J_I with a near-tip path is by using four-point bend specimens as described in section 3.1.2. The procedure is simpler than using cantilever beam specimens since only the load needs to be measured during the test. Therefore, data reduction can be fully automated. Figs. 3.19 and 20 show representative $M - K^*$ plots from four-point bend tests compared with plots of cantilever type tests. All specimens were 1 inch wide. Significant differences can be seen between the two methods, with the greatest differences for the more flexible layups. The difference is primarily from large deflections which invalidate the simple beam analysis of the four-point bend test. Reduction of the span between loading points effectively restricts deflections but the distance from the strain gage to the loading points becomes smaller than that recommended in [77]. Midplane straining, as has already been discussed, is the result of changing geometry of loading for large deflections which gives compressive axial stress at the gages and differing tensile and compressive moduli.

In summary, the four-point bend method can only be used for relativley stiff layups. The significance of this is limited, however, since such layups tend to undergo little or no distributed damage, thereby obviating the need to use the J-integral approach.

3.2.5 Mode I Delamination of Unidirectional Layups

Figure 3.21 shows the load-displacement record of a unidirectional specimen tested with periodic unloading. The behavior is clearly linear elastic. There is some waviness in the trace during crack growth, probably the result of fiber bridging which was noted during the test. Fiber bridging was generally periodic in nature; a tie zone would develop, then break down. Then a new zone would form and break down, and so forth. The sudden drops in load are from unstable crack growth followed by an arrest.

Both J_I and G_I (calculated by the area method) are plotted as a function of crack length in Fig. 3.22. The two methods give similar results as is to be expected, since the unidirectional laminate experiences no significant distributed damage. However, the comparison is not a direct one, since the J_I values reflect instantaneous toughness while G_I from the area method gives an average toughness over the prior increment of crack growth. The plot clearly illustrates the effect of inherent averaging of the area method.

J_I versus crack length is plotted for several specimens tested at various displacement rates in Fig. 3.23. Arrest values are included. The DCB data for these specimens was redured using the same J_I -M_{tip} relationship since the unidirectional layup did not display significant time-depedence in the J_I -M_{tip} tests. There is not a discernable trend in the data for overall specimen response except for specimen 1. However, there are increases and decreases in resistance which can be seen for shorter increments of crack growth. The decreases tend to be in the form of sudden drops, while the increases are gradual. In part this can be associated with the tie zone phenomena explained before.

Figure 3.24 shows J_I versus crack speed using logarithmic axes. One very significant fact which can be seen is that for any one specimen, there is no trend (an exception
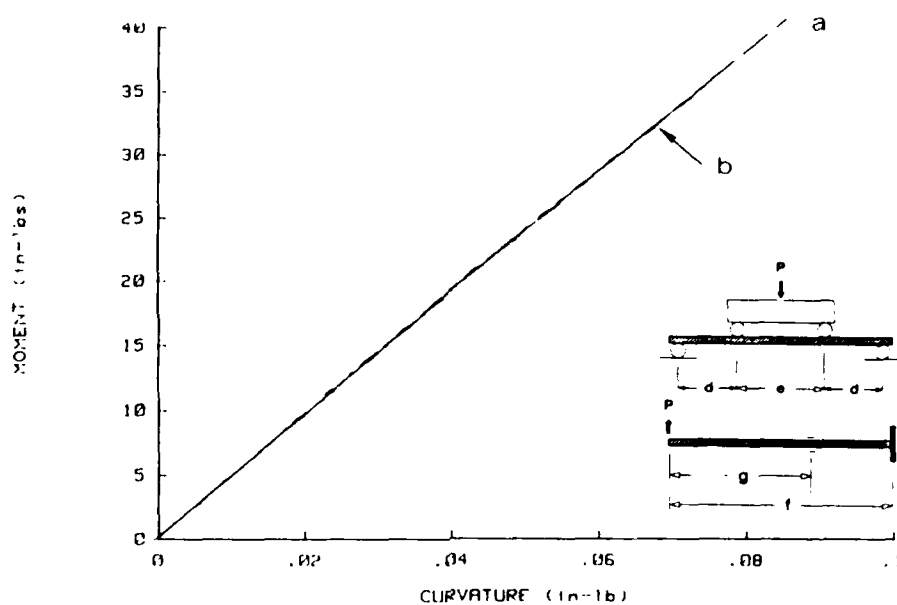
Figure 3.19 Moment-curvature relationship for the
unidirectional layup from a) cantilever-type specimen and
b) four-point bend specimen. d=2, e=4, f=3.931, g=1.931.
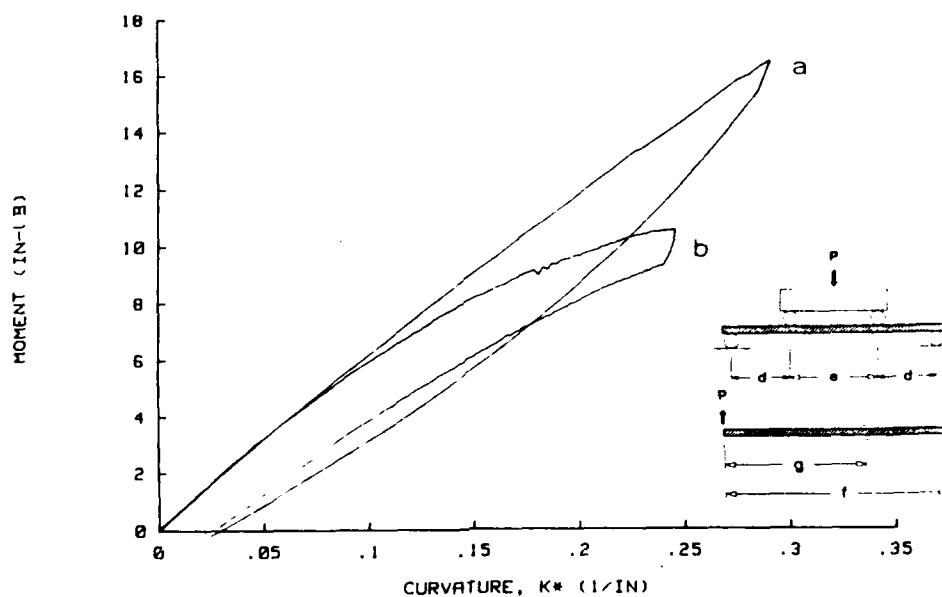

Figure 3.20 Moment-curvature relationship for the +-45
angle-ply layup from a) cantilever-type specimen and b)
four-point bend specimen. d=3, e=2, f=3.980, g=1.980.

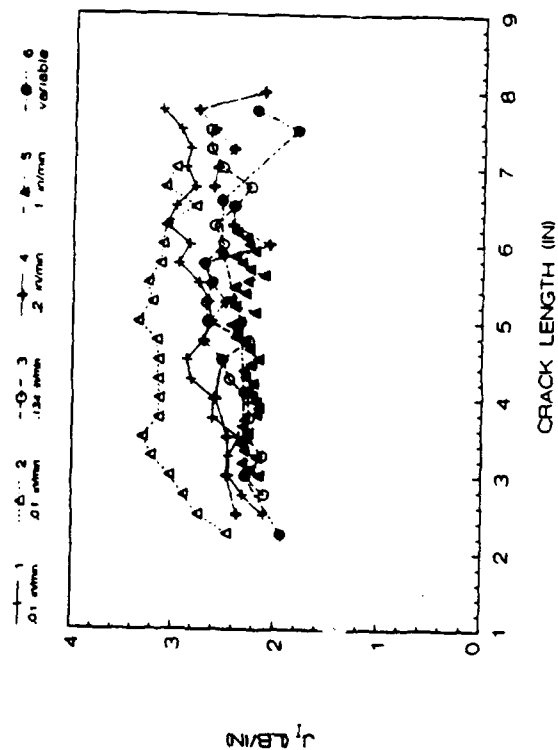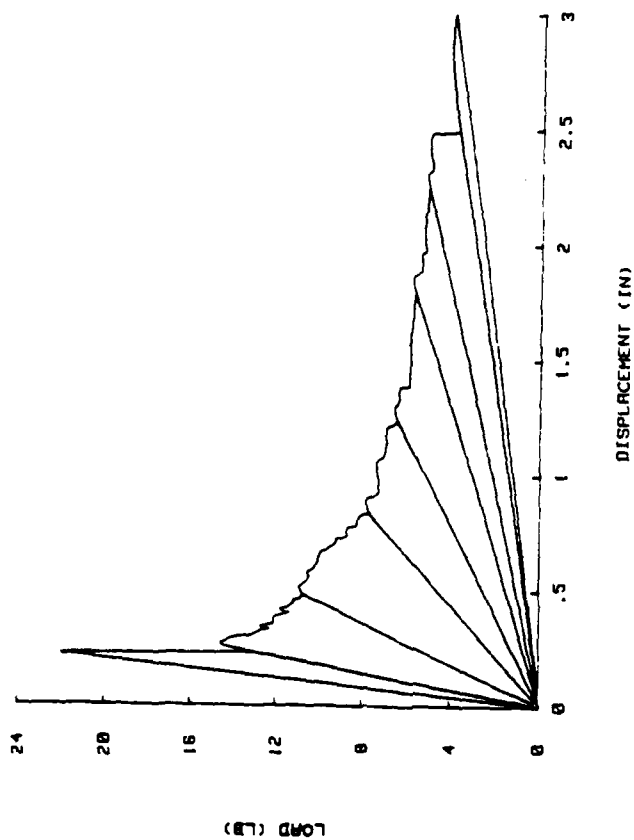Figure 3.21 Load-displacement record for a unidirectional specimen.
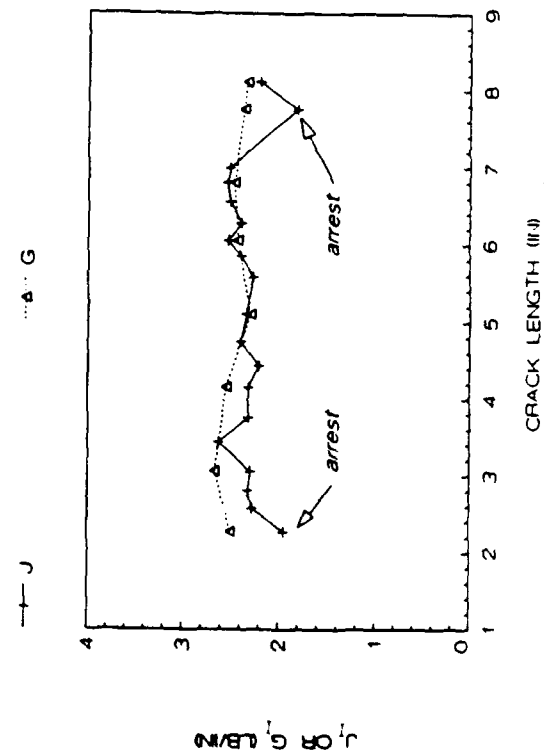
Figure 3.22 J_I and G_I versus crack length for a unidirectional DCB specimen.

Figure 3.23 J_I versus crack length for unidirectional DCB specimens tested at various rates.

Figure 3.24 J_I versus crack speed for unidirectional DCB specimens tested at various displacement rates.

53

is specimen 1, but the trend is not replicated for specimen 2). Overall it appears that there is a slight decreasing trend in J_I with increasing crack speed. Smiley and Pipes observed a decrease in toughness with increasing crack speed for a composite with an unmodified epoxy matrix. In the range of displacement rates in this study, the trend was relatively slight, but became pronounced at high rates. The response here could be similar; however, in the range of rates tested, the trend was not strong.

Specimens 1 and 2 (which were run at the lowest displacement rate) are the most influential in establishing the apparent trend. Considering Fig. 3.23, these two specimens show different behaviors. Specimen 2 starts with a value of J_I comparable to the other specimens but rapidly increases to a higher overall J_I level. Specimen 1 also starts in the same way as 2, but it slowly increases the level of J_I until almost at the end of the test reaches the level of 2. Considering the fracture surfaces of these specimens, the fracture surface of specimen 2 shows a high degree of fiber waviness relative to the waviness seen on the other fracture surfaces. For specimen 1, waviness is seen to increase from the normal amount to an amount comparable to that seen in specimen 2. Inspection of the fracture surfaces of other specimens did not reveal the unusual degree of waviness seen in specimens 1 and 2. As a result, fiber waviness seems to better correlate with J_I than with crack speed.

Although the significance of the decreasing trend seen in Fig. 3.24 is clouded by the presence of fiber waviness, other evidence suggests that the trend cannot be dismissed. Frassine [77] observed a power law decrease in toughness with increasing crack speed for transverse fracture of uinidirectional graphite/F155 composite. Comparison with DCB test results revealed a similar relationship between tougness and crack speed, though the toughness for transverse fracture was appreciably higher than for delamination fracture.

3.2.6 Mode I Delamination of Fiber-dominated Layups

This section reports and discusses the results of DCB tests of layups for which two thirds of the plies are at $0°$. The plies at the delamination plane are at various angles. The primary variable of interest in this test series is the effect of ply angles at the delamination plane on toughness in the absence of significant distributed damage.

Figure 3.25 shows the $J_I - a$ behavior of a $± 10°$ fiber-dominated laminate. All specimens were tested using monotonic loading (no unloading) at a displacement rate of 0.1 inch/minute. The load-displacement records from the DCB tests were similar to those for the unidirectional cases. The specimens were unloaded to zero load at zero displacement; little nonlinearity could be seen in the unloading curve. Dramatic variations in fracture behavior from specimen to specimen are seen in Fig. 3.25. Specimen 1 fractures at a significantly lower range of J_I values than the unidirectional range. Specimen 2 starts out in the unidirectional range, then climbs to nearly twice the initial toughness. Specimen 3 starts out similar to specimen 2, but remains in the unidirectional range throughout the test. These different behaviors can be clearly associated with the characteristics of the fracture surfaces shown in Fig. 3.26. Considering the fracture surface of the specimen which gave the relatively low value of J_I , the fracture surface is homogeneous with few loose fibers. Essentially, the $± 10°$ ply interface has prevented fiber bridging due to fiber nesting, as shown by Johnson and Magalgiri

55
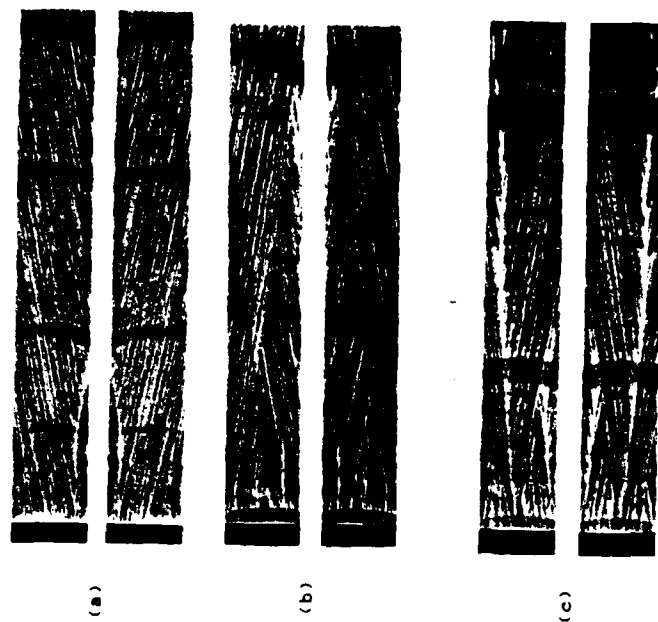

Figure 3.26. Fracture surfaces of the +-10 fiber-dominated DCB specimens. a) Specimen 1 b) Specimen 2 c) Specimen 3.
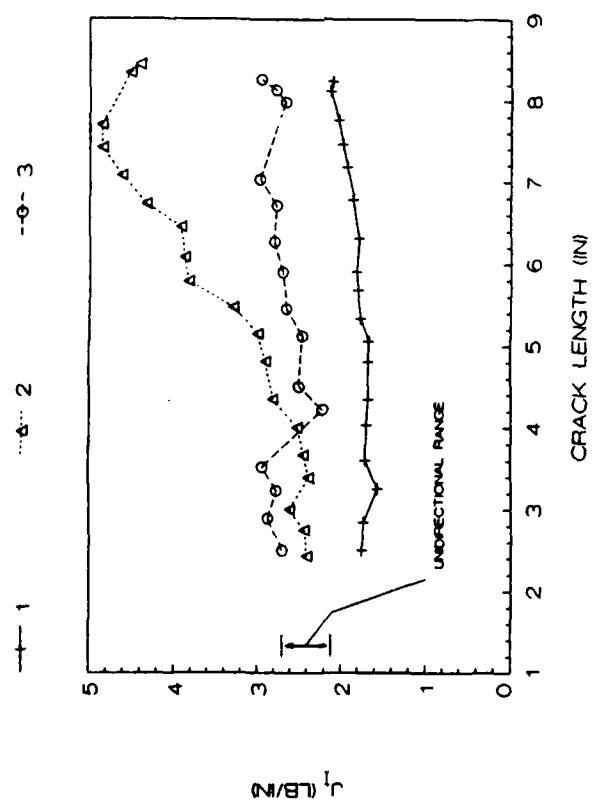

Figure 3.25. J_1 versus crack length for +-10 fiber-dominated DCB specimens.

[78]. As they found, the elimination of bridging leads to lower toughness than for the unidirectional case.

In contrast, the fracture surfaces of specimens 2 and 3 (Figs. 3.26a and 3.26b) are in general much rougher. The crack front was on more than one plane at a time, so there are transition zones from one ply to another. Fiber bridging was noted during the tests. Fiber bridging due to nesting did not occur but crack growth occurred in a complex manner involving ply transitions (such as seen by Nicholls and Gallager [67]) with the attendant fiber bridging and breakage. In addition, the transitions forced at least a portion of the crack front to advance through resin away from the fibers, which would have higher toughness. The very high toughness exhibited by specimen 2 was the result of crack propagation on two planes simultaneously. The result of this fracture behavior is to effectively increase the delamination surface area and increase the fracture energy.

Another significant observation from Fig. 3.26 is that the crack did not grow at the $\pm 10^\circ$ ply interface, but within a ply. The fibers on both halves of each specimen are oriented in the opposite direction when they are laid side by side; they are in the same direction when the halves are put together. Thus the character of delamination is intraply rather than between plies. Only over small regions on the fracture surface was true interlaminar fracture seen. These were usually regions where the crack plane was changing between plies.

The load-displacement record for delamination of a $\pm 30^\circ$ fiber-dominated DCB is seen in Fig. 3.27. In comparison to the unidirectional and $\pm 10^\circ$ fiber-dominated layups, this one shows many more sudden load drops and the load sometimes increased during crack growth. The specimens displayed a wide variety of fracture behavior, as shown in Fig. 3.28. Unstable crack growth typically occur after an increase in resistance. A saw-tooth pattern formed both in the load-displacement and J_I versus crack length records. In contrast to the ± 10 fiber-dominated laminate, none of the J_I values were below the unidirectional range. Only the arrest values were in this range.

Again the variations in toughness could be related to features on the fracture surfaces. The surfaces are shown in Fig. 3.29. Observations of these surfaces essentially indicate that smooth regions correlate with low toughness values and high toughness values with high surface roughness. The specific reasons for the different behaviors are not clear but they must be localized in nature or it would affect all of the specimens.

A feature of the fracture surfaces which is more prominent for these specimens than the earlier ones is the contrast between periods of stable and unstable crack growth. The former show up on the fracture surfaces as light regions; the latter appear as dark bands. However, no difference in the two regions is apparent when inspected using the scanning electron microscope (SEM). This obvious difference in the appearance of the surfaces when veiwed with the unaided eye suggests that there is some rate-dependence on the material, though it is not clear how that particular dependence is related to toughness.

The arrest marks indicate the shape of the crack front. Note that the front is generally not straight, but convex in the direction of crack growth. More will be said about the crack front curvature later in the discussion of the $\pm 45^\circ$ angle-ply specimens.
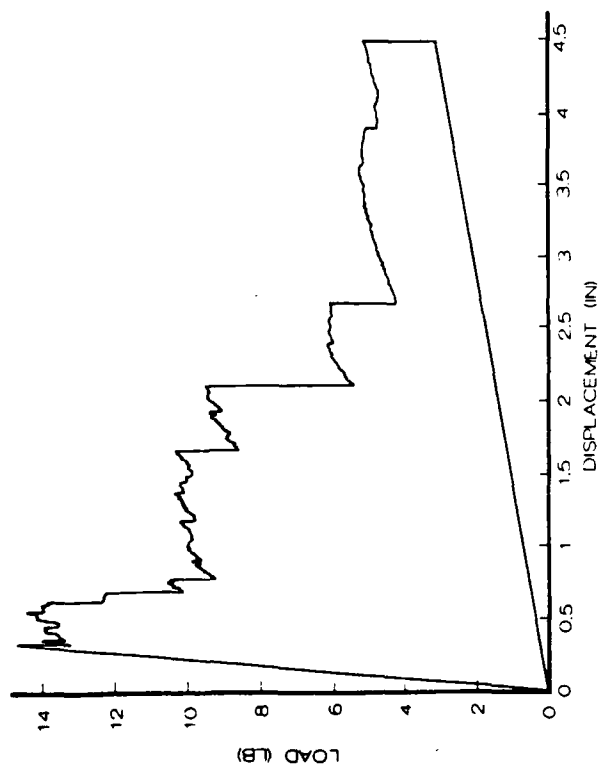
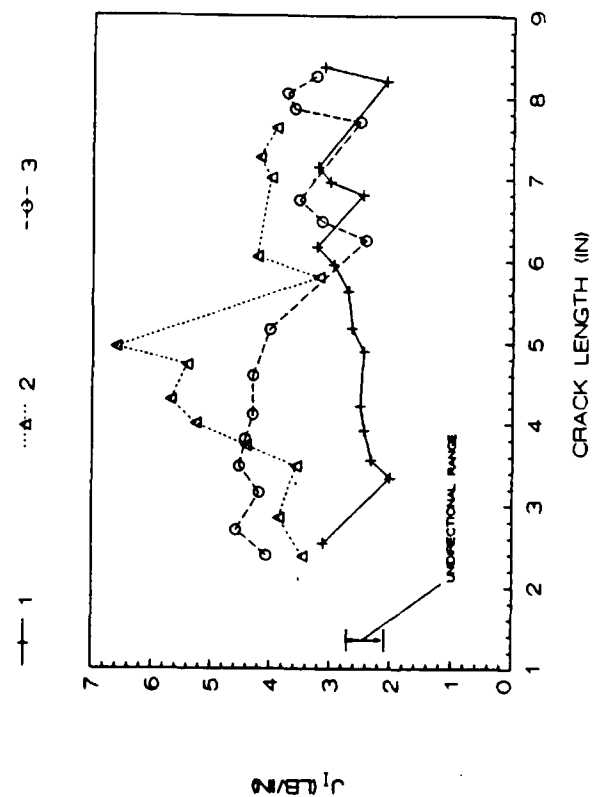Figure 3.29. Fracture surfaces of the +-30 fiber-dominated DCB specimens. a) Specimen 1 b) Specimen 2 c) Specimen 3.

(a)

(b)

(c)

Figure 3.27. Load-displacement record for a +-30 fiber-dominated specimen.

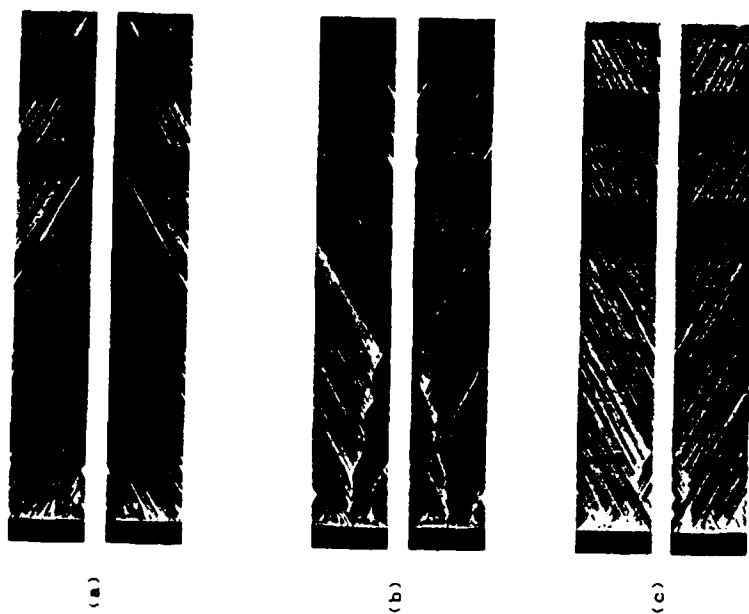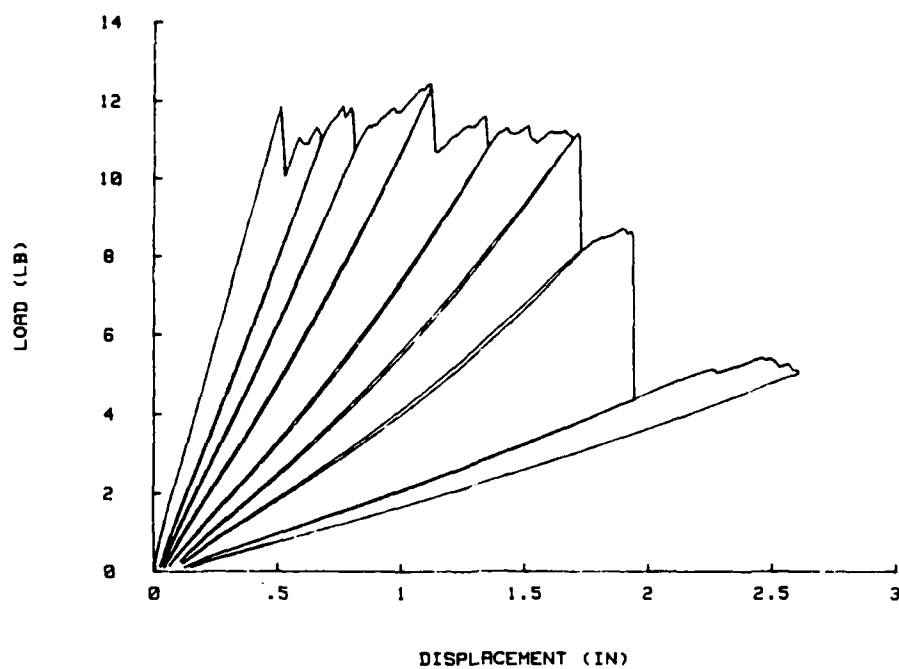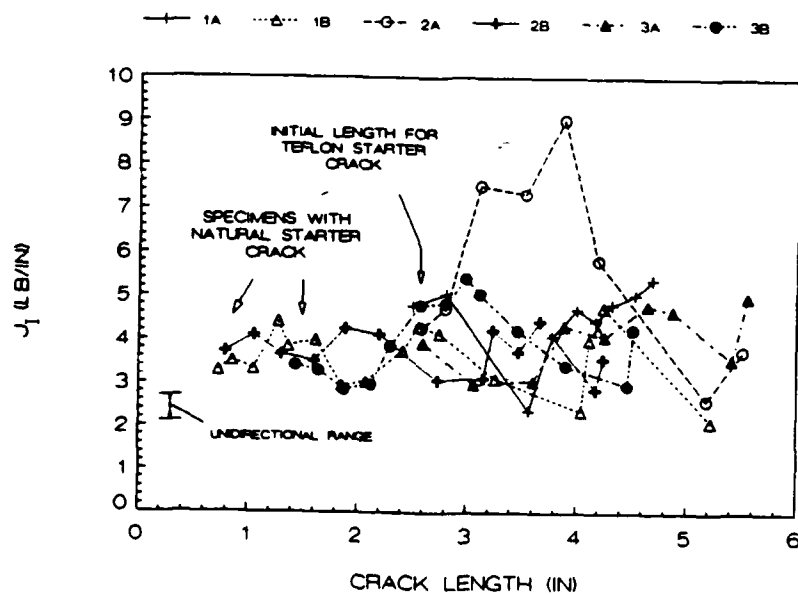Figure 3.28. J versus crack length for +-30 fiber-dominated DCB specimens.

Figure 3.30. Load-displacement record for a +-45 fiber-dominated specimen.

Figure 3.31. J_I versus crack length for +-45 fiber-dominated DCB specimens with natural and artificial starter cracks.

The trends which were established for increasing ply angles at the interface were continued in the $\pm 45^\circ$ fiber-dominated specimens. Figure 3.30 is an example of a load-deflection record for a specimen tested with periodic unloading, which became more jagged, having more sudden load drops. The behavior is elastic, as for the other fiber-dominated layups. One difference with the other laminates is that there is some nonlinearity in the load-unload curves.

There was considerable scatter in the toughness measurements; some of the scatter is associated with initial crack growth from the teflon starter crack. Figure 3.31 is a plot of $J_I - a$ for two sets of three specimens. One set (labeled with "A") had a teflon starter crack about 2.5 inches long. The other set (labeled with "B") had natural starter cracks about 0.7 to 1.4 inches long. The specimens with the natural crack were actually specimens which had originally 2 inch starter cracks, except that after some considerable amount of crack growth, upon completion of the test, most of the cracked legs were cut and new tabs were bonded to the remaining part of the DCB. There is no discernible difference in the quality of the early data from the specimens with the short natural crack from the other data. The fracture surfaces of the two sets of specimens do show a significant difference for the initial growth. The specimens with teflon inserts generally have a very complex fracture surface for short crack lengths, as the crack is trying to establish on which plane it will grow. This has been already been established for the specimens with natural starter cracks. Typical fracture surfaces for the two sets of specimens are shown in Fig. 3.32.

The J values were generally above the basic range of unidirectional values. Except for arrest points, the lowest values were at 3 lb/in. This is comparable to the upper values which were observed for the unidirectional case. As for the tests discussed earlier, the toughness varied widely. The pattern of increasing scatter with increasing ply angle was continued. The multiplanar fracture surfaces and intraply crack growth were also similar to that seen in the other tests.

A plot of $J_I - a$ is shown in Fig. 3.33 also for a ± 45 fiber-dominated layup at various displacement rates. The variations in J_I are again very large. Local minima are generally arrest points. Figure 3.34 plots J_I versus crack speed. As for the unidirectional case, there is an overall trend to lower J_I for higher crack speed. The tremendous scatter makes judging the degree of rate-dependence very difficult; however, compared to the unidirectional case in Fig. 3.24, the variation in J_I over three decades of crack speed is significantly greater. One reason for some of the scatter is that instantaneous J_I values are being plotted against average crack speed over the crack growth increment since the previous measurement. Also as for the unidirectional case, no correlation can be seen for data from an individual specimen.

3.2.7 Mode I Delamination of Angle-ply Layups

Figure 5.35 shows a typical load-displacement record of a $\pm 45^\circ$ angle-ply laminate. Generally there is some increase in load during crack extension, indicating that the delamination resistance is increasing. A review of all the load-displacment records reveals that load drops are slightly less frequent than for the $\pm 45^\circ$ fiber-dominated laminate. The load-unload curves are nonlinear, and the reloading curves do not quite retrace the unloading curves. Also permanent deformation upon unloading to zero

Figure 3.33. J_I versus crack length for +-45 fiber-dominated DCB specimens tested at various displacement rates.

Figure 3.34. J_I versus crack speed for +-45 fiber-dominated DCB specimens tested at various displacement rates.

Figure 3.32. Fracture surfaces of two +-45 fiber-dominated DCB specimens showing difference between crack growth from a) artificial and b) natural starter cracks. Both specimens are one inch wide.
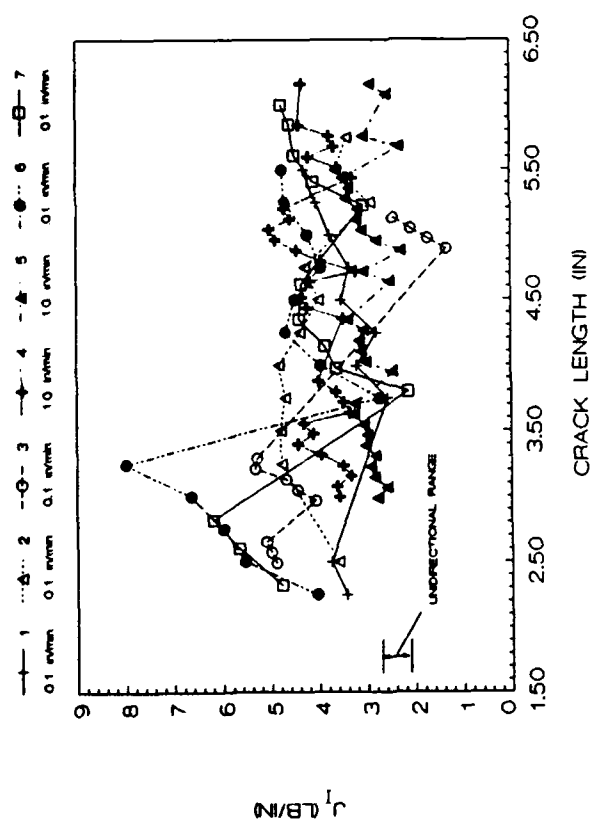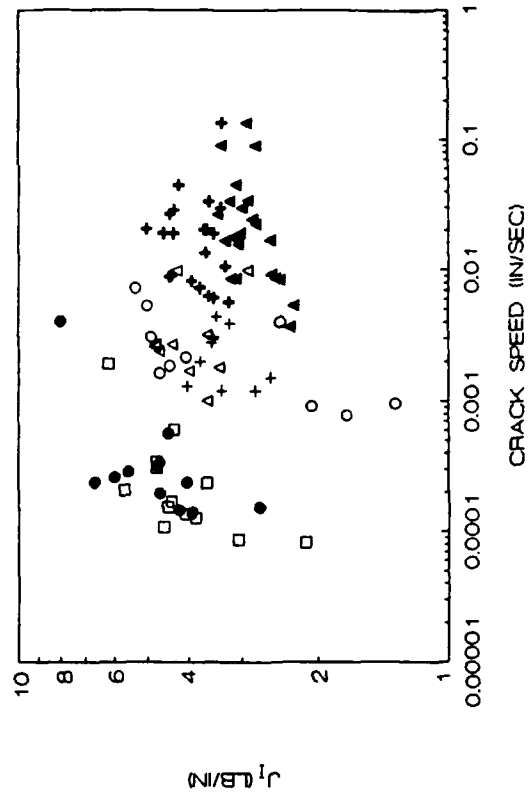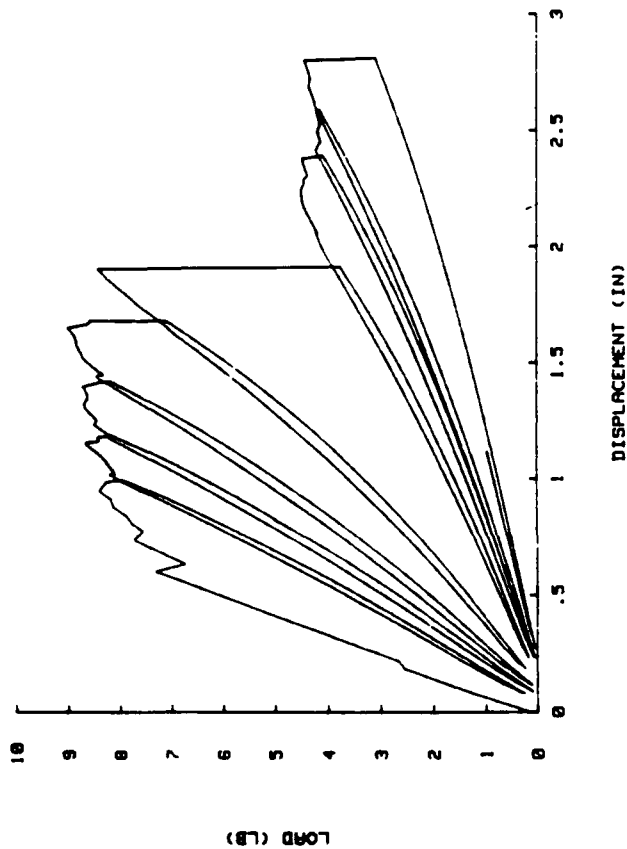
Figure 3.37. J_I versus crack length for +-45 angle-ply DCB specimens with natural and artificial starter cracks.

Figure 3.38 J_I versus crack speed for +-45 angle-ply DCB specimens tested at various displacement rates.

Figure 3.35. Load-displacement record for a +-45 angle-ply specimen.
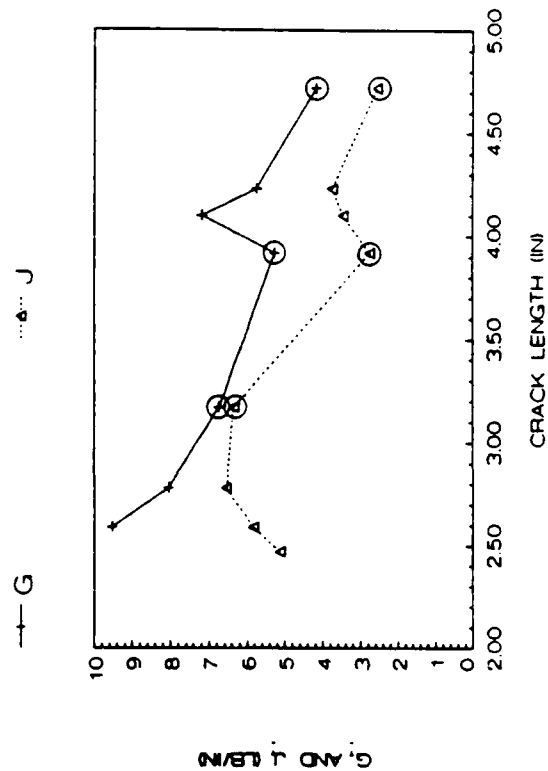
Figure 3.36. G and J versus crack length for a +-45 angle-ply DCB specimen. Arrest points are marked.

load is observed. Observation of the DCB legs after the test showed they were curved, indicating the permanent deformation is due to distributed damage (inelasticity in the legs or slow to recover viscoelasticity).

The J_I and G_I (from the area method) for the specimen referred in Fig. 3.35 are shown plotted against crack length in Fig. 3.36. The plot indicates J_I to be in general lower than G_I which is consistent with the fact that the area method does not account for the energy going to produce distributed damage. Fig. 3.37 shows the results of $J_I - a$ for a series of tests using teflon and natural starter cracks. Note that the values for short crack lengths are not different in character than the data for longer cracks. A basic premise of the J method used here is that the delamination behavior is completely determined by the conditions at the crack tip which seems to be supported by this finding.

Similarly to the previous layups tested, correlation of the toughness with fracture morphology for the $\pm 45^\circ$ angle-ply specimens indicates that complex fracture surfaces correspond to high toughness. The homogeneous surfaces correspond to the lower energy mechanisms.

Figure 3.38 shows J_I versus crack speed for the $\pm 45^\circ$ angle-ply specimens. No strong correlation of J_I with crack speed can be seen. However, the data displays an apparent maximum at the mid-range of crack speed. Because of the inherent variability of J_I for this material, a rigorous examination of the possible correlation would require a sizable data base. At least one can say that the crack speed need not be considered when interpreting the data from an individual specimen.

3.2.8 Effect of Width on Mode I Delamination

The effect of width was explored by testing 24 ply angle-ply DCB specimens 0.5, 1, and 2 inches wide. Six representative specimens were chosen for comparison, two for each of the widths tested. They were picked because they displayed the most consistent lower-bound behavior for each group. Fig. 3.39 shows that comparison. For this particular set of data, the wider specimens appear to tend to give slightly lower values. Of course, the amount of data is very limited and somewhat biased beacuse of the way it was chosen. The only solid statement which can be made (especially when considering all the data available) is that the J_I values given by the specimens of different widths are generally comparable. No pronounced trend can be seen for this range of widths.

Unlike unidirectional composites, multidirectional laminates exhibit significantly curved crack fronts in DCB tests [79,80,81]. The curvature depends on the width of the specimen. Fig. 3.40 shows, for comparison purposes, normalized crack front profiles associated with several superimposed crack lengths on the same specimen for 1/2, 1, and 2 inch wide specimens. The general trend appears to be decreasing curvature with increasing crack length, but there is considerable scatter in the behavior. The differences between the shapes of the three plots are plain. The curvature associated with edge effects is dominant for the 0.5 inch specimen, but becomes less significant for increasing widths. Apparently the large variations in toughness have overshadowed the effect of width reflected in these different crack fronts. The stress state along the
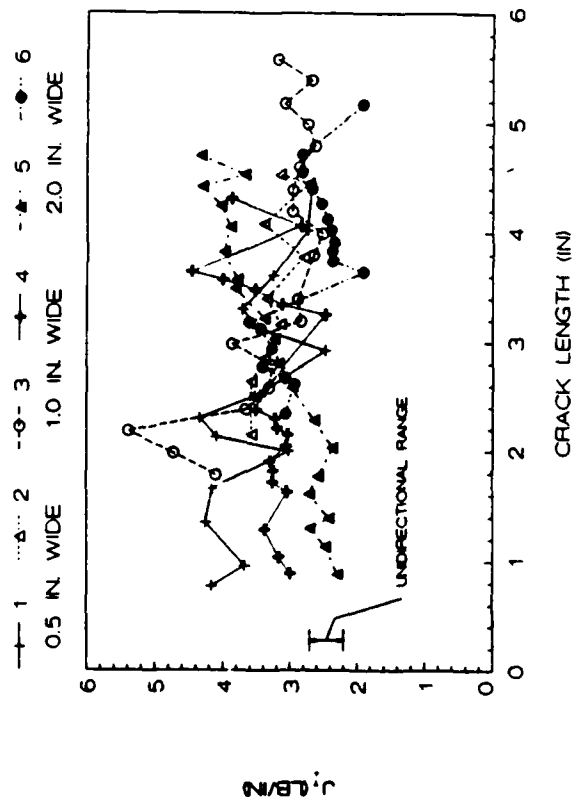
1 INCH WIDE SPECIMEN

CRACK LENGTH/WIDTH

2.99
3.15
3.90
4.77

(DELTA a)/WIDTH

DISTANCE FROM EDGE/WIDTH

2 INCH WIDE SPECIMEN

CRACK LENGTH/WIDTH

1.665
1.860
2.445
2.640
2.770

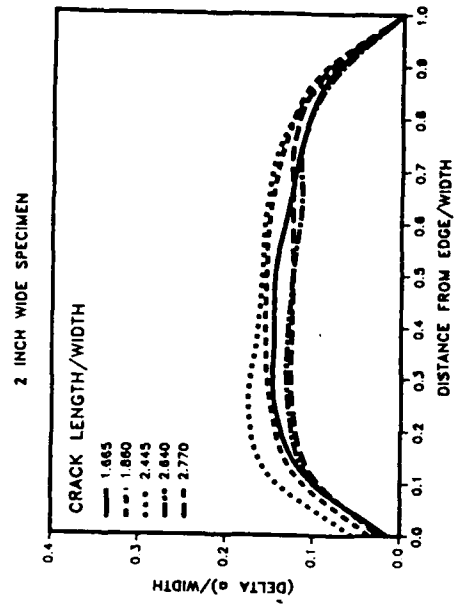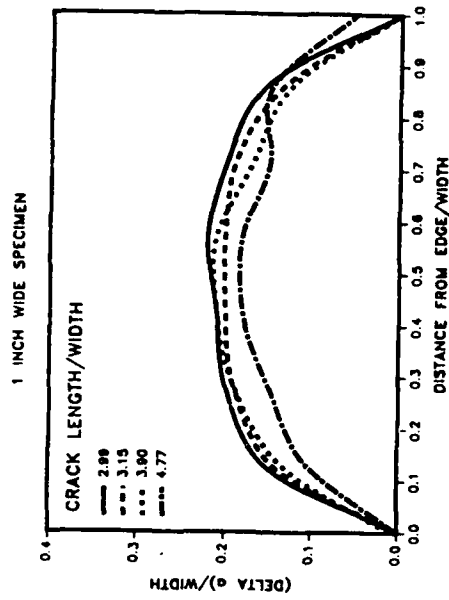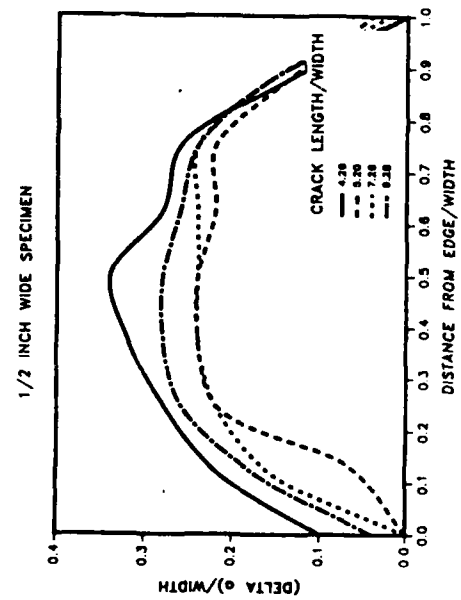(DELTA a)/WIDTH

DISTANCE FROM EDGE/WIDTH

Figure 3.40 Normalized crack front profiles for three +-45 angle-ply DCB specimens of different widths. The profiles for various crack lengths have been superimposed.

1   2   3   4   5   6
0.5 IN. WIDE   1.0 IN. WIDE   2.0 IN. WIDE

UNIDIRECTIONAL RANGE

CRACK LENGTH (IN)

J, LB/IN

Figure 3.39 J_i versus crack length for +-45 angle-ply DCB specimens of three widths.

1/2 INCH WIDE SPECIMEN

CRACK LENGTH/WIDTH

4.36
5.30
7.28
6.38

(DELTA a)/WIDTH

DISTANCE FROM EDGE/WIDTH

crack front of wider specimens is more uniform over a larger portion of the crack front and edge effects are minimized.

3.2.9 Effect of Thickness on Mode I Delamination

Tests were conducted to investigate the potential effect of specimen thickness on apparent toughness. The results of these tests do not seem to be definitive in light of the scatter of the data. A $J_I - a$ plot for a 16 ply layup with balanced legs is shown in Fig. 3.41. The relative uniformity of the data is partly attributable to the small range of crack lengths with which is is associated. The amount of crack growth is limited because of the high compliance of the specimens and the limitation of the maximum displacement of the loading ram. These limited tests give J_I values which are generally at the upper edge of the range of J_I for the 24 ply angle-ply. See Fig. 3.37 for comparison. Note that if the toughness were affected by the thickness through its effect on fiber bridging, the thinner laminate would have less bridging and thus a lower toughness.

Another $J_I - a$ plot for a 16 ply laminate is shown in Fig. 3.42. The stacking sequence for this laminate was asymmetric: $[(\pm 45)_8]$. Twisting of the DCB legs was coupled to bending. The crack front was seen to be mostly symmetric across the width of the specimen; twisting did not cause one side to grow ahead of the other. The behavior is comparable to the behavior of the 24 ply angle-ply, and generally lower than the other 16 ply layup.

The preliminary result from these tests is that within the range of variability of the behavior, the number of plies does not significantly affect the toughness as measured using J . Further, the effect of twisting-bending coupling was not apparent.

3.2.10 Effect of Fatigue Predamaged on Mode I Delamination

As described Chapter IV, several specimens were loaded cyclically in tension to induce damage prior to J_I -M_{tip} and delamination testing. The laminate used was the 24 ply $\pm$ 45 angle-ply layup. The ultimate strength was determined to be 33,700 psi by averaging the results from the tensile tests. Figure 3.43 shows the stress-strain record for a typical specimen during cyclic loading. Due to clarity, only 4 of the 10 cycles experienced by the specimens are shown. Upon initial loading and inelastic strain of a few percent was induced which increased with subsequent cycling. Also, the stiffness of the specimen increased slightly during successibe cycles. Poursartip et al.[82] have attributed this behavior to realignment of off-axis fibers. An x-ray made of one of the specimens showed that fibers scissored approximately 3° (changing from $\pm$ 45° to $\pm$ 42°) to align themselves with the load. Extensive transverse cracking of the matrix was the major form of damage, which was observed from a replica of a specimen edge made using acetate replicating tape. Axial predictions based on lamination theory also indicated that indeed fiber realigment caused significant stiffening, qualitatively confirming the role of fiber realignment.

The J_I -M_{tip} relationships for the two predamage levels (loaded to 60% and 75% of the ultimate stress) and the unconditioned laminate are shown in Fig. 3.44. The amount of predamage makes a difference, but since the predamage specimens were
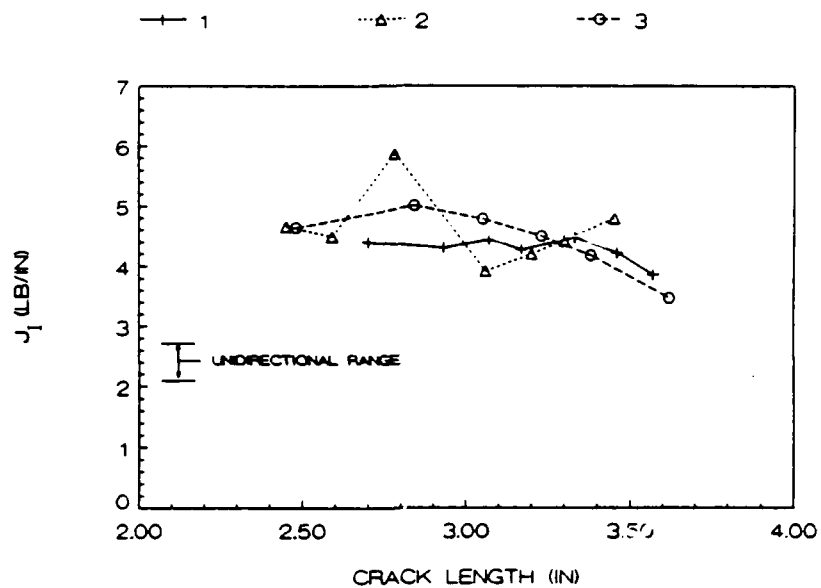
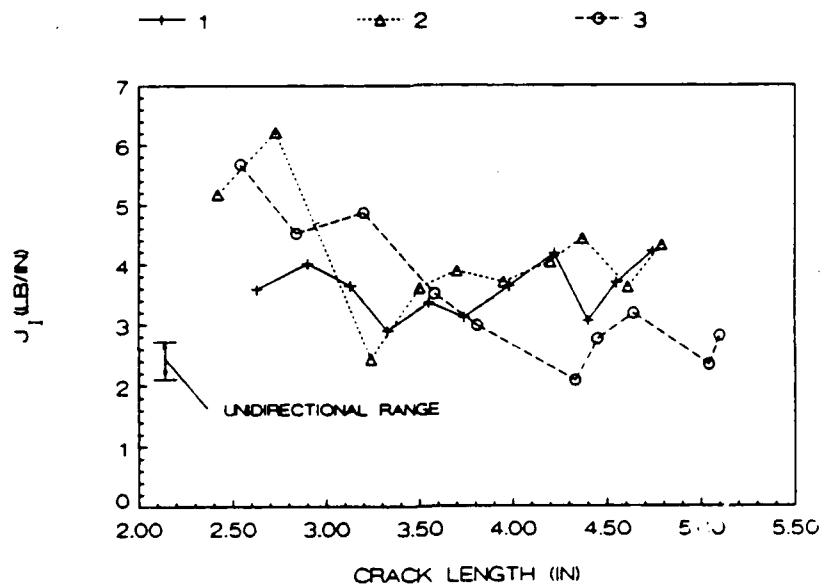Figure 3.41 J_I versus crack length for 16-ply +-45 angle-ply DCB specimens with symmetric legs.

Figure 3.42 J_I versus crack length for 16-ply +-45 angle-ply DCB specimens with asymmetric legs.
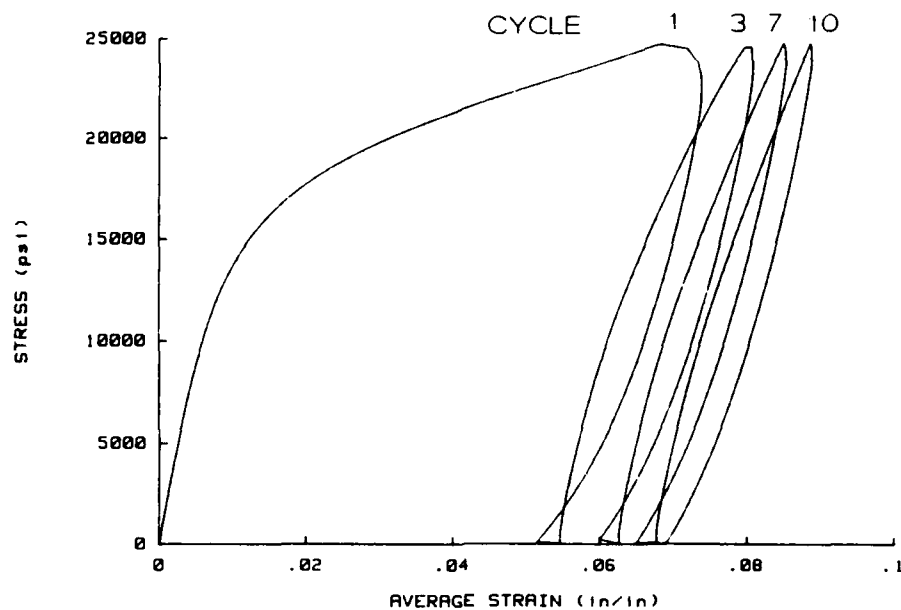
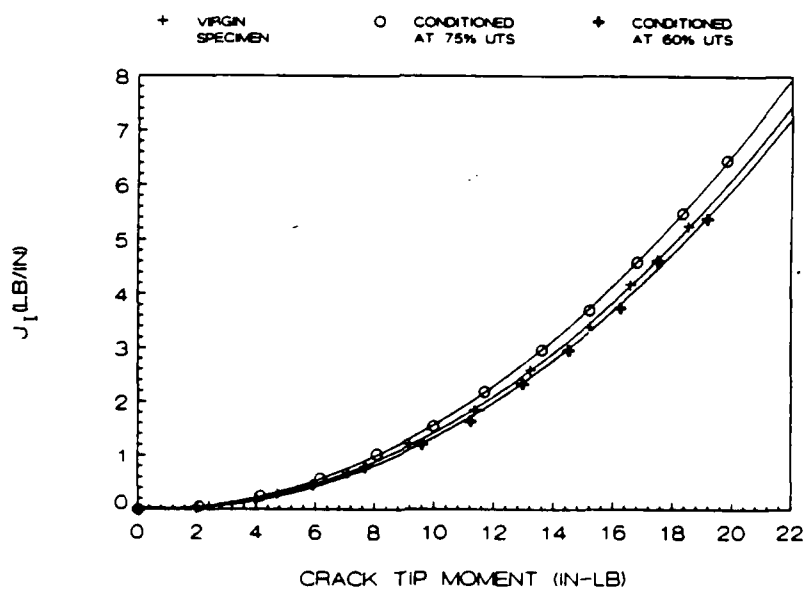Figure 3.43 Stress-strain record for a +-45 angle-ply DCB specimen during tensile fatigue loading.

Figure 3.44 J_1 versus crack tip moment for +-45 angle-ply specimens with and without tensile predamage.
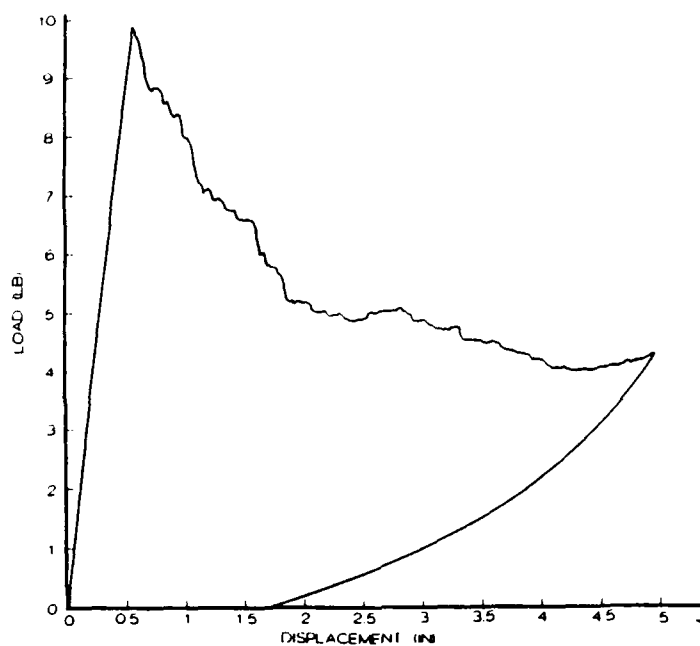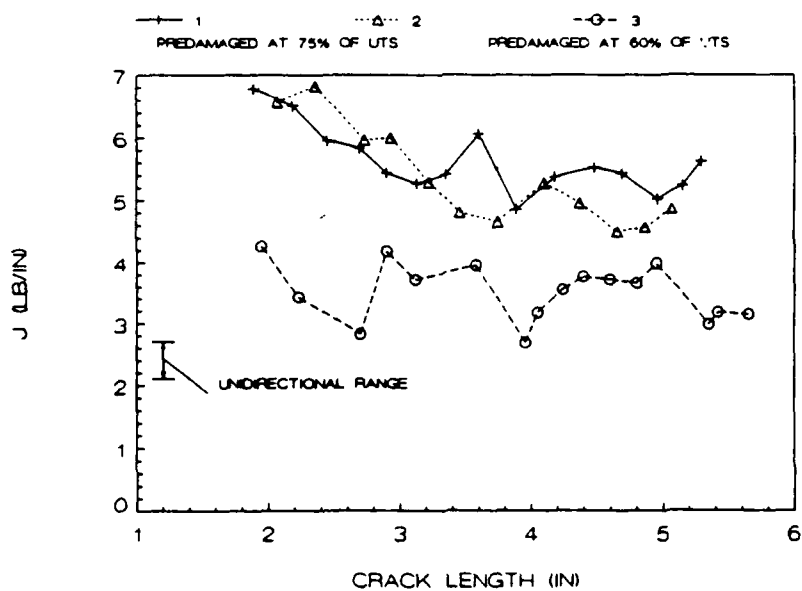
Figure 3.45 Load-displacement record for a predamaged +-45 angle-ply DCB specimen.

Figure 3.46 J_I versus crack length for +-45 angle-ply DCB specimens after fatigue predamage.

taken from a different plate than the unconditioned one, plate-to-plate variations in material seems to also have an effect, blurring the trend.

Figure 3.45 shows the load-displacement record for a DCB specimen which had been predamaged at 75% of the ultimate stress. Note how the permanent deflection upon unloading is very large relative to the unconditioned angle ply specimens. Also, the sudden load drops associated with bursts of crack growth which are typical for multidirectional laminates are not present. J_I versus crack length is shown in Fig. 3.46. The specimen damage at 60% level is in the range of the unconditioned specimens (cf. Fig. 3.37), while the specimens predamage at about the 75% level showed significantly higher toughness. The fracture surfaces of these specimens were very rough.

These exploratory tests indicate that fatigue predamage can significantly increase the delamination fracture toughness. Also, crack growth tends to be more stable for predamaged specimens.

3.3 Mode II Results

3.3.1 Verificaton of Procedure to Evaluate J_{II}

Due to the path independence of the J-integral , the choice of paths to evaluate it for the ELS configuration can be done at will, or for mere convinience, or to avoid complex states of stress such as crack tips, clampled ends, etc. As explained in Chapter 2, the paths at the cracked and uncracked portions of the ELS specimen were chosen very close to the crack tip such that only the applied load P and the projected crack length a_p should be monitored during a delamination test. However, during delamination, crack growth takes place at different slope angles θ_{ct}. At short crack lengths the angle is larger than at longer crack lengths. Therefore, in order to maintain the path inpendence of J_{II} , and thus, the validity of the proposed procedure to evaluate it, the effect of θ_{ct} on J_{II} -M_{tip} has to be investigated. Specifically, it is needed to to determine if a different J_{II} -M_{tip} curve is needed for each angle θ_{ct} during crack growth. This verification indirectly determines the invariability of J_{II} with crack length.

The effect of θ_{ct} on J_{II} -M_{tip} can be established by determining the effect of θ_{ct} on the I_c -M_{tip} and I_u -M_{tip} relationships that through (2.58) define J_{II} as a function of crack tip moment.

The results of I_c -M_{tip} for three of the unidirectional 24 ply laminates are seen in Figs. 3.47-49. The laminates are for AS4/3502, T2C145/F155, and T6T145/F185, respectively, and are in order of increasing material toughness. Since these relationships represent the cracked portion of the ELS, they are from 12 ply cantilever beams. These results indicate there appears to be little dependance of I_c -M_{tip} for the range of θ_{ct} tested. In the case of AS4/3502, a small variation between the I_c -M_{tip} at 5° with curves for 10° and 15° is seen for moments as low as 20 lb-in. A similar but smaller variation is seen for T6T145/F185 (Fig. 3.49) at moments between 70 and 120 lb-in. However, the curves seem to collapse at moments higher than 120 lb-in. It can be argued that because the measurement of θ_{ct} defining a moment location on the beam is done moving a protractor along the beam obtaining increasing moments at constant θ, error associated with this procedure can explain the small variation seen in this I_c -M_{tip} curves. Note how in the case of T2C145/F155, I_c -M_{tip} is completely invariant
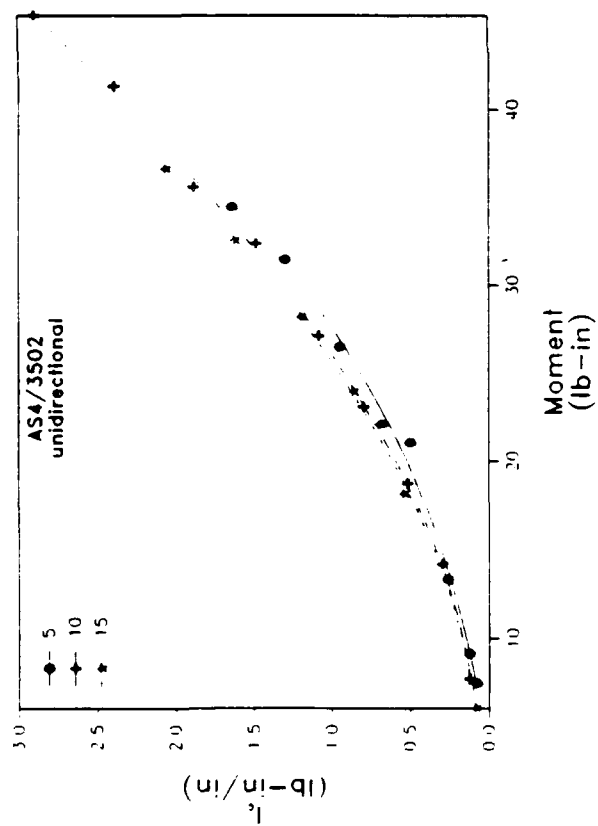
Figure 3.47 I_c-M relationship of AS4/3502
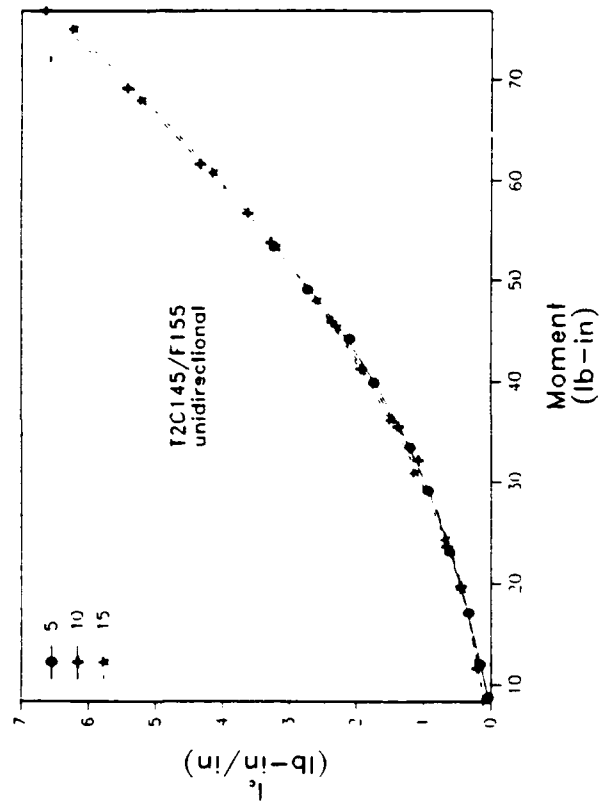
Figure 3.48 I_c-M relationship of T2C145/F155
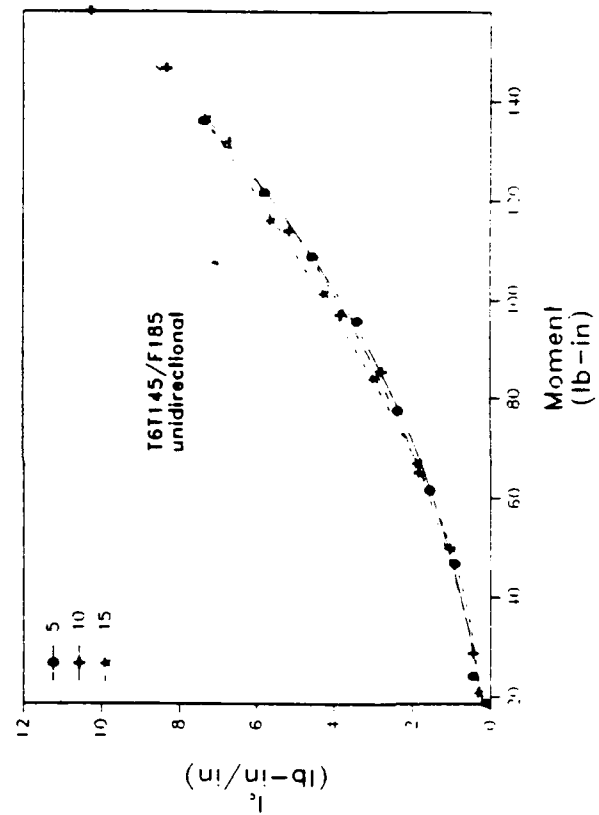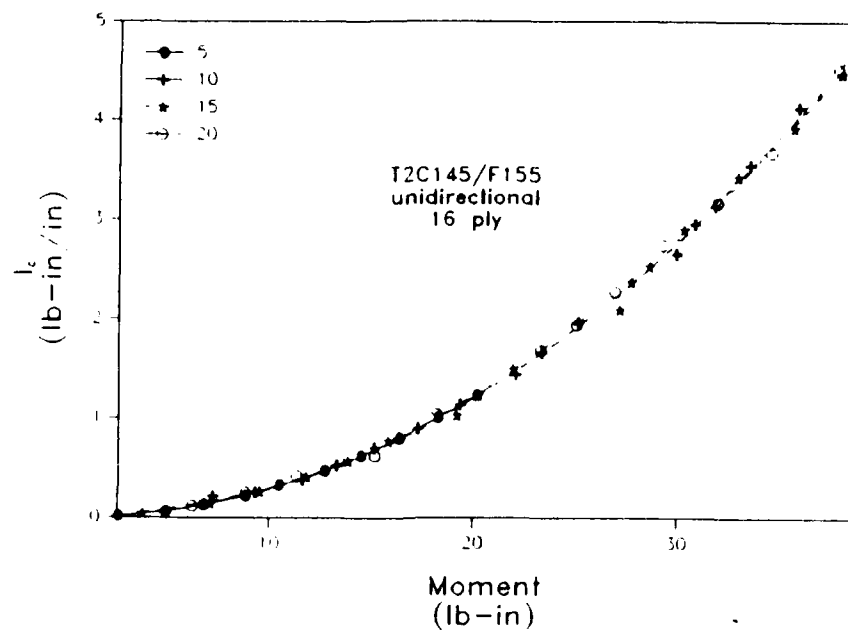

Figure 3.49 I_c-M relationship of T6T145/F185

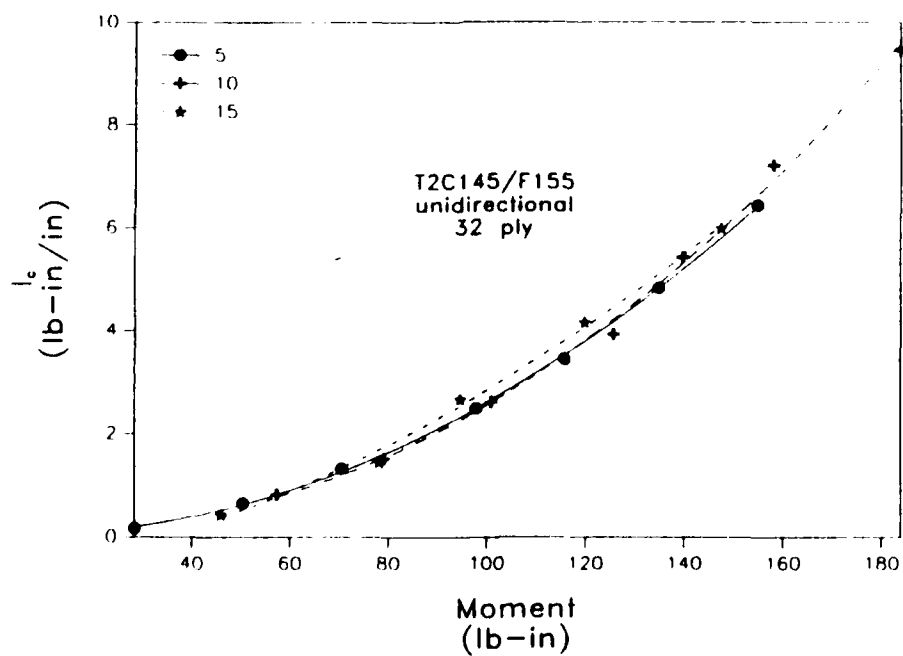Figure 3.50 I_c-M relationship of 16 ply T2C145/F155

Figure 3.51 I_c-M relationship of 32 ply T2C145/F155

with respect to the range of slopes angles tested.

Figs. 3.50-51 show the I_c -M_{tip} curves for 16 and 32 ply laminates of T2C145/F155. The relationships are therefore from 8 and 16 ply beams, respectively. Both curves show independence with θ_{ct} . For the 16 ply beam, tests were also performed at 20° . The agreement is definite for the former one.

The last set of I_c -M_{tip} curves are seen in Figs. 3.52-54. These correspond to multidirectional layups. The relationships are clearly independent of θ. They are for a fiber dominated layup with $\pm$ 45° and $\pm$ 0° plies, and the matrix dominated $\pm$ 30° and $\pm$ 45° layups of T2C145/F155, respectively. The significance of these findings is that even in the presence of considerable damage, as in the case of the matrix dominated layups, the I_c -M_{tip} curves are independent of θ_{ct} , and therefore, of crack length. Evidence for damage development is illustrated by the increasing hysterisis of the load-deflection records obtained as these tests were performed (see Figs. 3.55-56). Viscoelastic effects were discarded since the permanent deformation did not recover with time after the tests were completed. These results are in agreement with the results of the J_I -mtip curves previously discussed.

Figs. 3.57-58 show I_u -M_{tip} at varying slope angles for the AS4/3502 and T6T145/F185 laminates, respectively. The number of plies for the beams tested to generate this data is 24 since they represent the behavior of the uncracked portion of the ELS specimen. For these cases there appears to be some difference between the I_u -M_{tip} curves at the angles tested. In the case of AS4/3502, at low moments, the 5° curve predicts lower I_u values than the curves for 10° , and 15° . At moments higher than 100 lb-in, all three curves are coincident. This behavior is unexpected, and it is probably the result of experimental errors. For a unidirectional laminate subjected to higher slope angles, the beam should be stiffened provided no strain softening develops (damage). Such stiffening would make I_u to be lower as θ_{ct} increases for fixed moment values. The same behavior seen for the I_u -M_{tip} for AS4/3502 is observed for T6T145/F185.

A possible explanation for this unexpected behavior can be associated with the method used to measure the slope angles, and therefore, the moment corresponding to the slope angles. The resolution of the protractor used to measure the angles is at most $\pm$ 1° . If small angle changes occur over a long length section of the beam, which is the case for the higher angles, an underestimation of the location of the higher angles from the loaded end will take place if the protractor is slided from the loaded end towards the clamped end. Therefore, the moment is also underestimated. The effect on the I_u -M_{tip} relationship is that for a given moment, the measured I_u will be higher that the actual value. This is precisely what the relationships in Figs. 3.57-58 indicate.

Once the location of the higher angles approaches the clamped end (larger loads and deflections), steeper angle changes occur for small distances along the beam. Therefore, I_u -M_{tip} relationships should be free from significant errors associated with the measurement method. In fact, it can be seen that the I_u -M_{tip} curves shown are in closer agreement at the higher moments.

A possible procedure to minimize these measurement errors is by using digital inclinometers or rotational tranducers with a resolution capability in the order of $\pm$
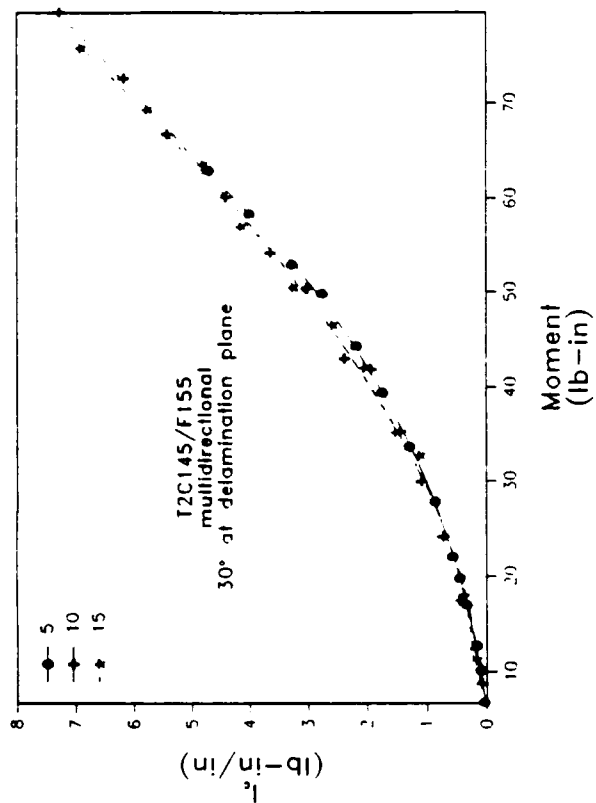
Figure 3.52 I_c–M relationship of multidirectional
T2C145/F155 with 0° plies bounding the delam-
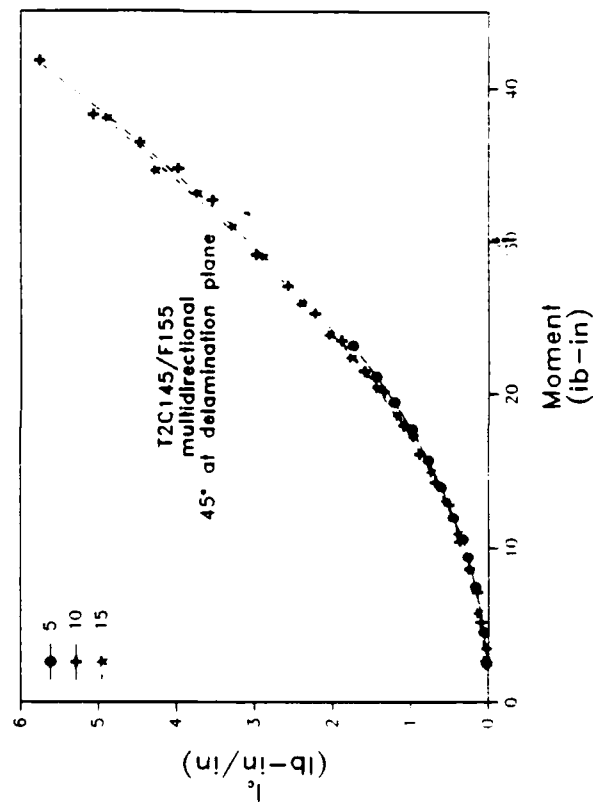ination plane

Figure 3.53 I_c–M relationship of multidirectional
T2C145/F155 with ±30° plies bounding the delam-
ination plane

Figure 3.54 I_c M relationship of multidirectional
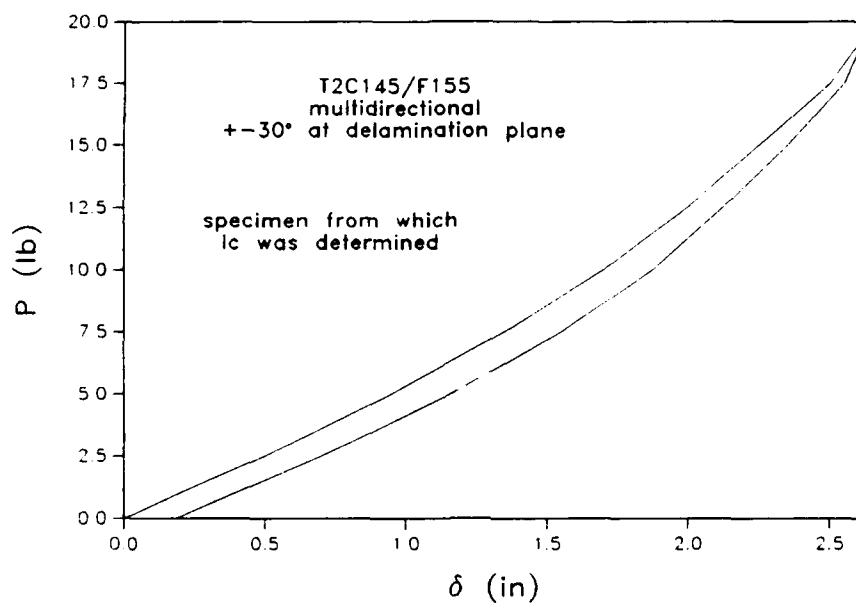T2C145/F155 with ±45° plies bounding the delam-
ination plane

Figure 3.55 Load-deflection record of beam where I_c-M for
multidirectional T2C145/F155 with $\pm30°$ plies
was measured. Note the amount of permanent defor-
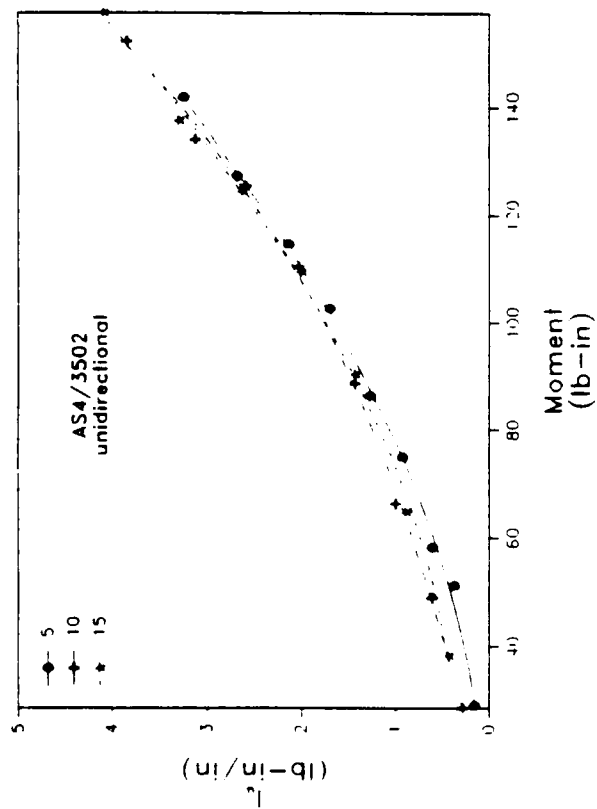mation due to far field damage development
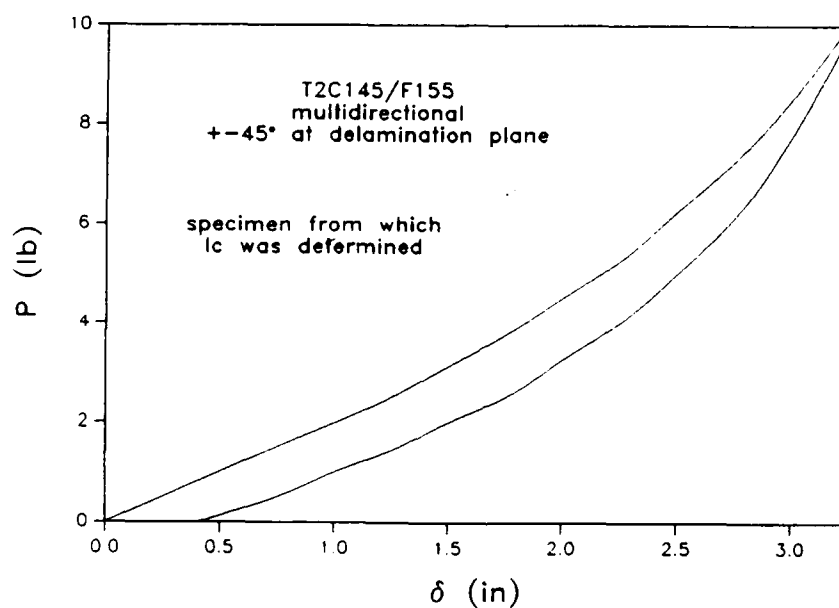
Figure 3.56 Load-deflection record of beam where I_c-M for
multidirectional T2C145/F155 with $\pm45°$ plies
was measured. Note the amount of permanent defor-
mation due far field damage development
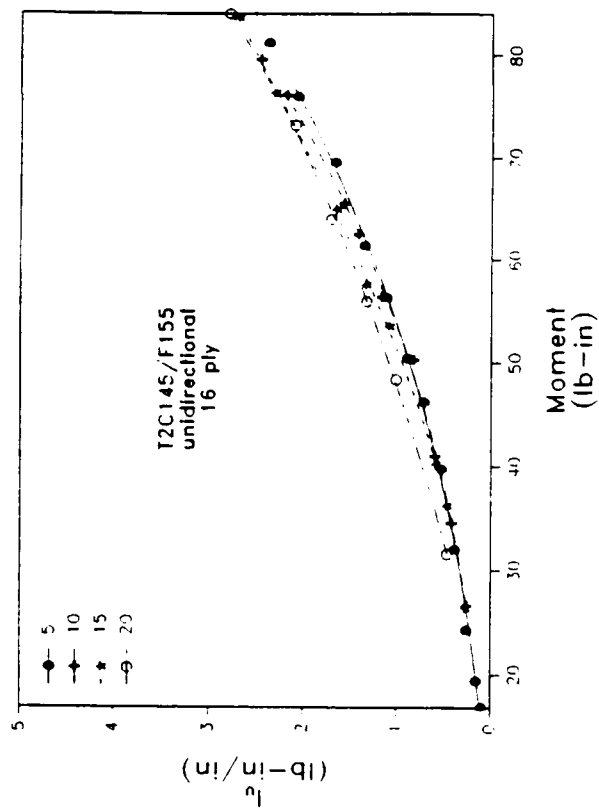
Figure 3.59 I_u-M relationship of 16 ply T2C145/F155
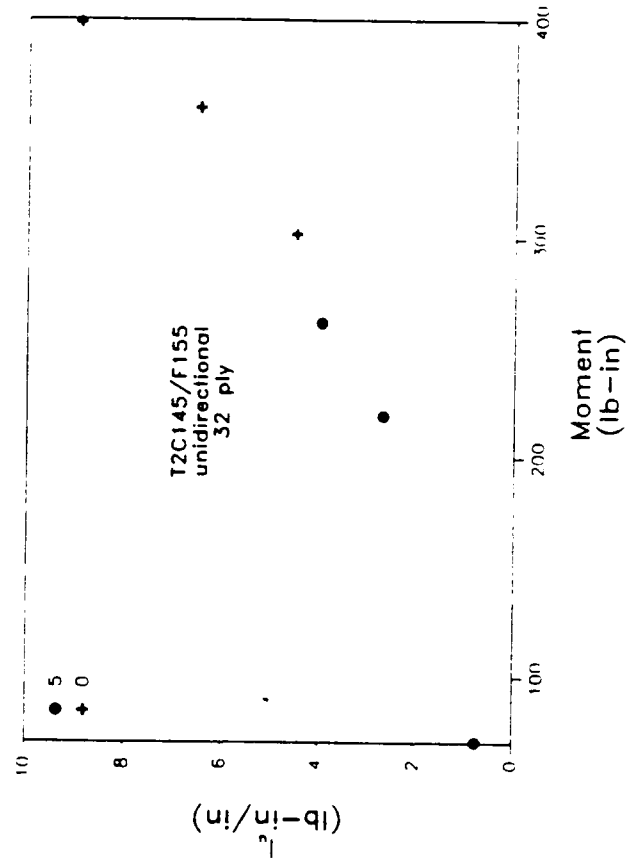
Figure 3.60 I_u-M relationship of 32 ply T2C145/F155

Figure 3.57 I_u-M relationship of AS4/3502
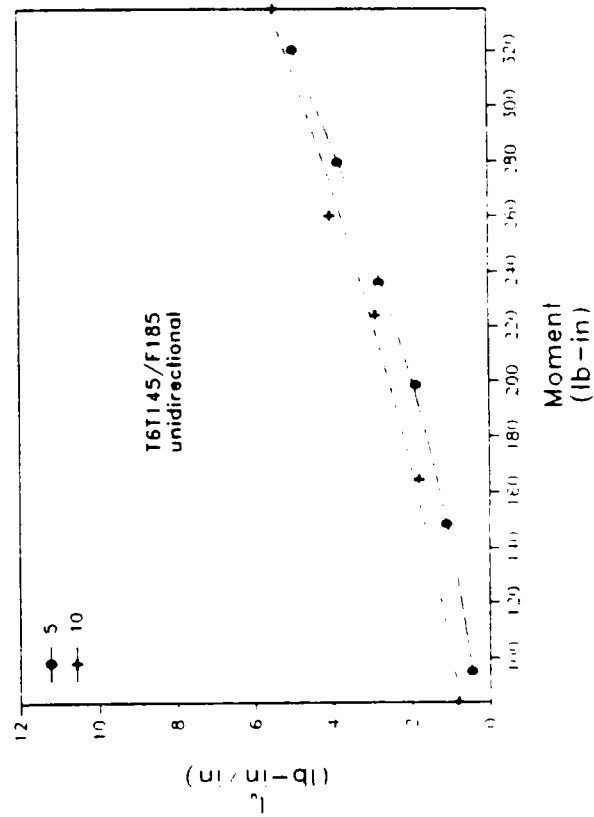
Figure 3.58 I_u-M relationship of T6T145/F185

0.1° . Another approach would by videotaping the tests and then use image analysis devices to measure the slope and momemt arm.

Figs. 3.59-60 show the I_u -M_{tip} relationships of the uncracked beams of the 16 and 32 ply lamintes of T2C145/F155. In the case of the former, only the curve measured at 20° predicts higher values at low moments until it collapses with the 10° and 15° curve at higher moments. This behavior is similar to the one observed in the laminates discussed above and is most likely due to the measurement error explained already. Difficulty in constructing an adequate curve for 5° and 0° for the 32 ply laminate was experienced. This was a very stiff specimen compared to the previous ones presented. Very early in the test, the moments at which crack growth takes place for this layup developed and the angles along the beam were generally 5° including very close to the loaded end. However there is an indication that the 5° curve would have predicted higher I_u values than the 0° at the low moment level. Based on the explanation previously given to account for this apparent behavior, it indeed should be more clearly seen with this thick and stiff beam since slope changes are very small at the moments at which crack growth occurred with this specimens.

The I_u -M_{tip} relationships for the multidirectional layups of T2C145/F155 are seen in Figs 3.61-63. The curves show a small discrepancy at lower moments but are nearly identical at higher moments. The same trend is observed for the matrix dominated $\pm$ 30 and $\pm$ 45 layups. However, the I_u -M_{tip} curve at 15° does not merge with the 5° and 10° ones in the range of moments tested. Yet the difference is small in both cases. Further, it is unlikely that the discrepancy is real and the result of more damage development for the higher angles. In fact, no discrepancy was seen in the I_c -M_{tip} curves when the development of damage is very much greater than these 24 ply layups. In fact, the hysterisis was were small as seen in the load-deflection records of the beams used to determine these I_u -M_{tip} relationships.

A final comment with regard to the I_u -M_{tip} relationships is that the value of I_u is typically one half times its corresponding I_c . Therefore, since the contribution of I_c in the J_{II} (2.58) is multiplied by a factor of two, the aforementioned errors associated with measuring I_u will most likely be negligible on J_{II} .

Summarizing the results of the I_c -M_{tip} and I_u -M_{tip} at different θ_{ct} , it can be stated that considering the errors involved in the measurement of data, these relationships are invariant. Therefore, having established the independence of the I_c -M_{tip} and I_u -M_{tip} with θ_{ct} , the J_{II} -M_{tip} will also be independent of θ_{ct} and crack length. It needs to be emphasized that the uniqueness of the J_{II} -M_{tip} has only been demostrated for the conditions tested.

The independence of the I_c -M_{tip} and I_u -M_{tip} curves with crack length allows the construction of only one J_{II} -M_{tip} relationship. Further, this independence indicates it is not necessary to monitor θ_{ct} during each increment of crack growth. The verification has been done for a wide range of composite behavior and specimen dimensions including brittle, toughened, damaged, stiff and compliant laminates.

3.3.2 J_{II} -M_{tip} Results of Unidirectional Laminates

J_{II} -M_{tip} curves as a function of material toughness from brittle to toughnened composites are seen in Fig. 3.65. They correspond to 24 ply AS4/3502, T2C145/F155,
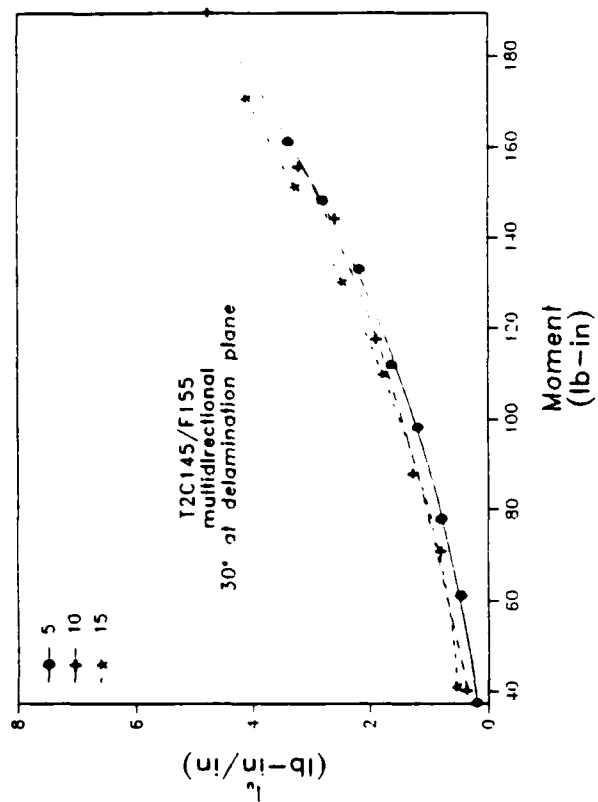
Figure 3.61 I$_u$-M relationship of multidirectional
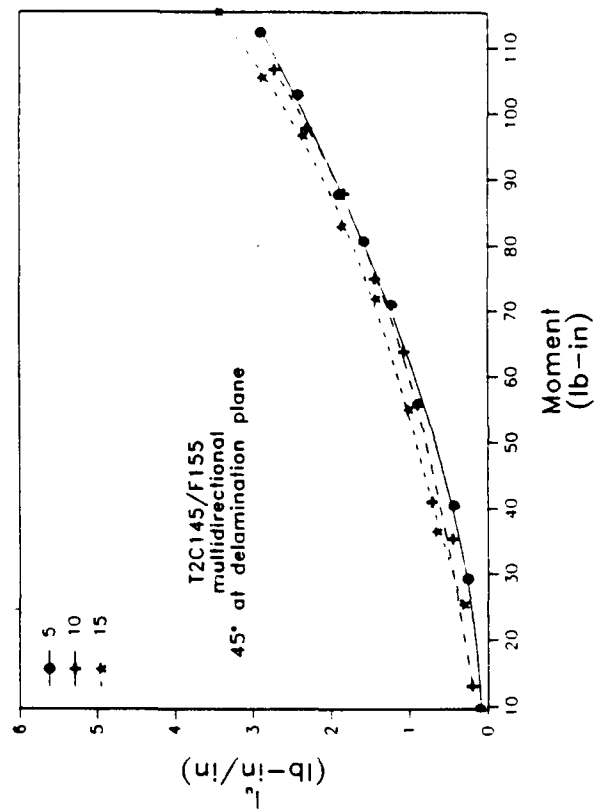T2C145/F155 with 0° plies bounding the delam-
ination plane

Figure 3.62 I$_u$-M relationship of multidirectional
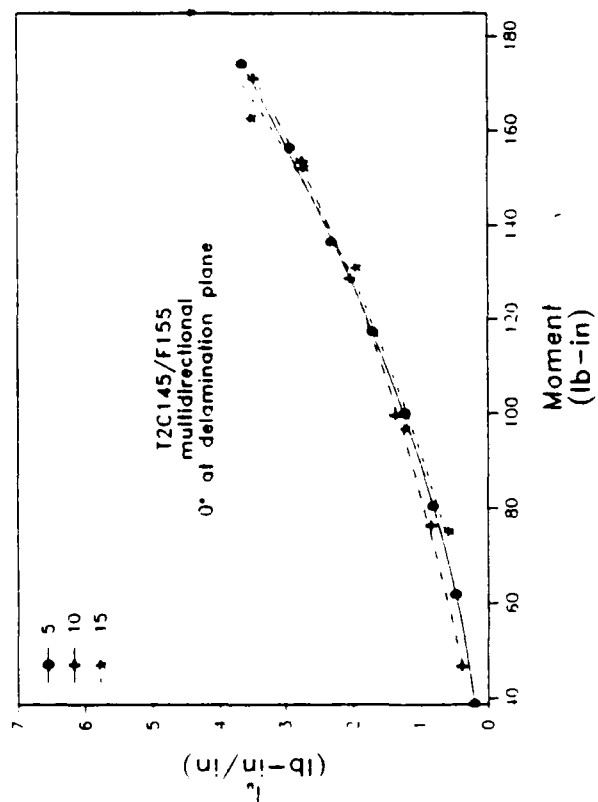T2C145/F155 with ±30° plies bounding the delam-
ination plane

Figure 3.63 I$_u$-M relationship of multidirectional
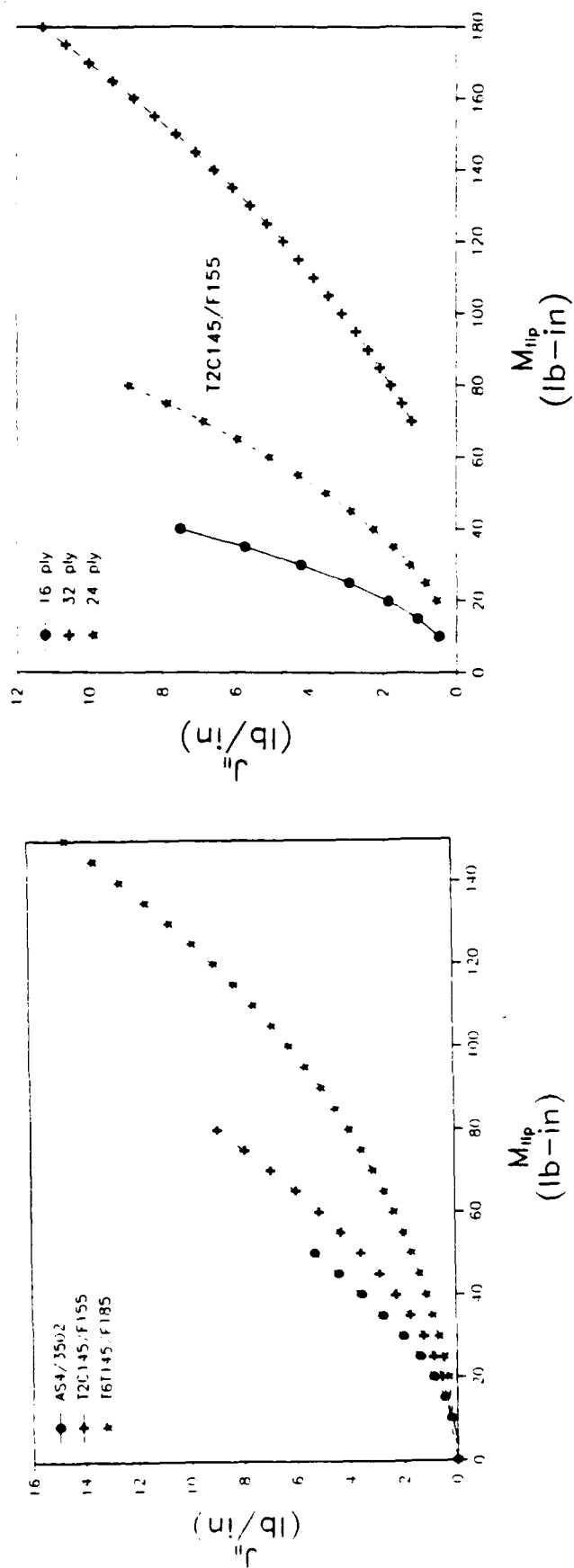T2C145/F155 with ±45° plies bounding the delam-
ination plane

T2C145/F155

16 ply
32 ply
24 ply

M_{tip}
(lb-in)

J_{II}
(lb/in)

Figure 3.65 J_{II}-M_{tip} relationships of unidirectional 16 ply, 24 ply, and 32 ply T2C145/F155 composite

AS4/3502
T2C145/F155
T6T145/F185

M_{tip}
(lb-in)

J_{II}
(lb/in)

Figure 3.64 J_{II}-M_{tip} relationships of unidirectional 24 ply composites

T2C145/F155

0
30
45
unidirectional

M_{tip}
(lb-in)

J_{II}
(lb/in)

Figure 3.66 J_{II}-M_{tip} relationships of unidirectional and

and T6T145/F185 unidirectional composites. The major characteristics of these rela-
tionhips is that for a fixed value of M_{tip} , the corresponding J_{II} decreases as a function
of material increasing toughness. This trend seems to be in contradiction of an expected
increase in J_{II} going from a tougher (more compliant) to a brittle (stiffer) laminate.
However, since tougher composites are thicher than brittle ones for a fixed number of
plies, this increase in thickness is enough to overshadow any tendency of J_{II} to increase
with material increasing toughness. (Fig. 3.65).

Another feature of the J_{II} -M_{tip} curves is that the moment at the crack tip is
observed to increase as specimen thickness increases for a fixed value of J_{II} . See
Figure 3.65. Therefore, if J_{II} for initiation or steady state crack growth is a material
property, increasing specimen thickness should only require higher moments to reach
the same J_{II} . If this is not the case, J_{II} -M_{tip} would be dependent on specimen
geometry, thickness in this case. Such dependence would most likely predict higher
J_{II} during crack growth for thinner specimens, with J_{II} progressively decreasing as
the number of plies increases to an adequate thickness that provides the constraint
necessary to evaluate J_{II} during crack growth.

Varying the thickness of the ELS specimens also provides an indirect assessment of
the effect of neglecting shear deformation in the derivation of J_{II} . ELS specimens are
typically long and slender. Therefore, deformation due to bending should be dominat
over shear deformation. However, as the ratio of beam length to its thickness and
flexural modulus to shear modulus decrease, shear deformation might no longer be
negligible.

### 3.3.3 J_{II} -M_{tip} Results of Multidirectional Laminates

The effect of stacking on the J_{II} -M_{tip} relationships is shown in Fig 3.66. The
curves represent an increasing number of angle plies and increasing magnitude of the
angle in the plies from 0° to $\pm 45^o$. A unidirectional layup is shown as a reference point.
The general trend is that as the stacking sequence goes from a more fiber dominated
to the increasingly matrix dominated layups, J_{II} will increase for a constant moment.
This is similar to the J_I -M_{tip} results previously discussed. Note that an apparent
contradiction to this trend is observed for the layups with 0° at the delamination plane
but with angle plies away from the midplane. This, as it was also found in the J_I -M_{tip}
curves, is because the tendency of J_{II} to increase as one goes from a fiber dominated to
a matrix dominated layup, is offset be the tendency of J_{II} versus moment to decrease
for thicker specimens (Fig. 3.65).

Another consideration with regard to the effect of stacking sequence on J_{II} -M_{tip} is
that for increasingly matrix dominated layups, damage development is observed. This
behavior is primarily experienced by the cracked portion of the ELS.

The effects of width on J_{II} -M_{tip} is essentially expected to be as it was found for
the J_I -M_{tip} curves. Therefore, the width of the specimens to evaluate the J_{II} -M_{tip}
curve should be matched with the width of the ELS specimen as well.

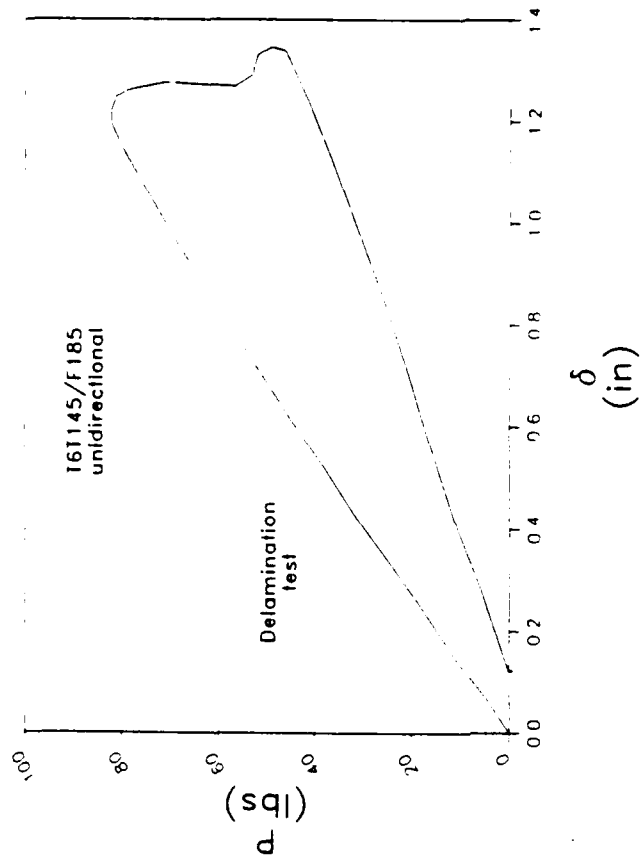### 3.3.4 Mode II Delamination of Unidirectinal Layups

Typical load-deflection curves of AS4/3502, T2C145/F155, and T6T145/F185
composites are illustrated in Fig. 3.67. For AS4/3502, material linear elastic response

(c) Mode II delamination load deflection record of T6T145/F185 composite
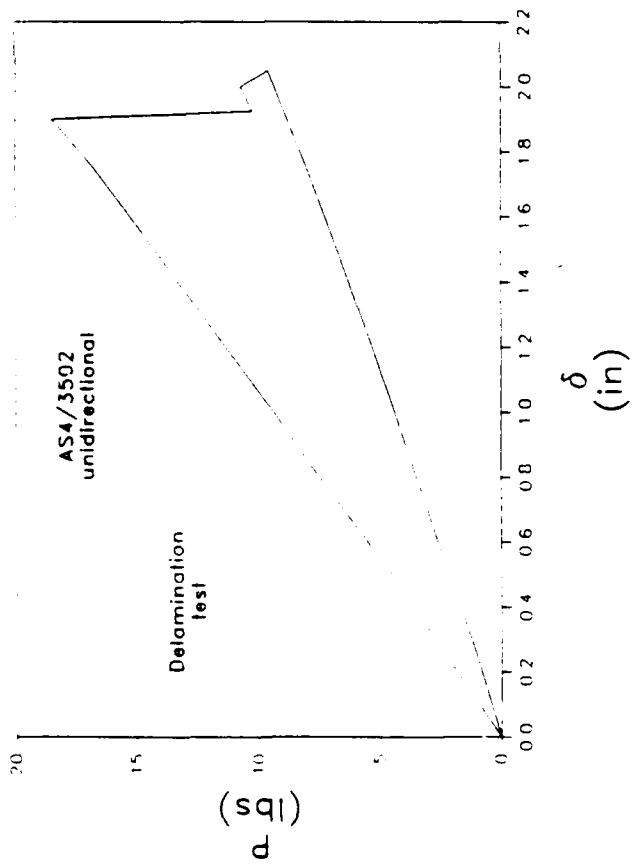
(a) Mode II delamination load deflection record of AS4/3502 composite
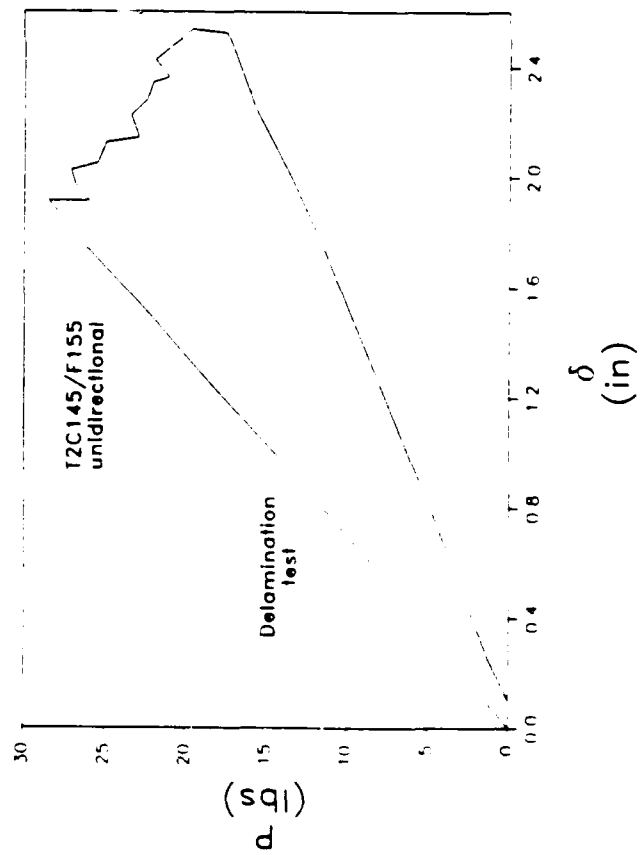
(b) Mode II delamination load deflection record

Figure 3.67

is observed with some evidence of stiffening due to shortening of the moment arm is seen as the load increases. Crack growth was unstable at the beginning of delamination. This crack growth behavior was consistently observed , even when the ratio of crack length to ELS length was greater than 0.55, the required ratio to obtain stable crack growth from geometric considerations. Hashemi and co-workers have also observed this instabilities with the ELS test [54]. The angle at which crack propagation occurred was between $5°$ and $10°$. Crack growth for T2C145/F155 was more stable than AS4/3502. However, periodic sudden crack growth intervals were followed by stable regions. Upon unloading, a small amount of permanent deflection is seen. The load-deflection record of T6T145/F185, the tougher composite reveals nonlinearities early in the test. Stable crack growth was seen prior and up to maximum load. Unstable crack extension then followed until stability was reached. Upon unloading, some permanent deflection is observed indicating some form of energy dissipation took place besides crack growth.

The $J_{II} - a/L$ plots for the composites of Fig. 3.67 are shown in Fig. 3.68. In addition to J_{II} , G_{II} values based on beam theory are shown. G in this case allows for large deflections. The results for AS4/3502 indicate that J_{II} and G_{II} are basically identical, which is expected since material response is linear elastic. The small discrepancy (less than 10%) is most likely related to differences in specimen behavior between the ELS specimen and the beams used to evaluate the I_u -M_{tip} relationships. Such discrepancies may be observed even if the specimens used to evaluate J_{II} are from the same panel as the ELS specimen. Composite panels are not completely uniform. For example, thickness variations in the laminate between the edges and the core were observed in all panels made for this investigation. The resistance to delamination for initiation and steady state propagation are basically the same for AS4/3502.

The crack growth behavior noticed in the load-deflection curve of T2C145/F155 is reflected in the variability of J_{II} during crack growth (Fig. 3.68b). The lower J_{II} values correspond to arrest values after the small unstable crack growth increments. The value of J_{II} at initiation is clearly different than the steady state one. However, this value should be taken with caution due to the difficulty in detecting the precise time when crack growth initiates. The mode I precrack done on the specimens to sharpen the crack tip may alter initition as well as due to the damage introduced during precracking. A dramatic decrease in J_{II} steady state was observed with one of the specimens tested. There seem to be a change in fracture mechanism induced by the large unstable crack increment. This phenomenon will be addressed in the next chapter. The similarity of J_{II} with G_{II} suggests the material behaves in an essentially linear elastic fashion.

The $J_{II} - a/L$ behavior of T6T145/F185 indicates a definite raising J_{II} with crack length until steady state was reached. This indicates part of the nonlinearity in the load-deflection record of this material is due to crack growth prior to maximum load, often referred as subcritical crack growth. The same behavior was shown by T2C145/F155. This behavior has been observed by other investigators for tough composites [9,15,21,49,52-54]. Carlsson et al. [49] have determined through the use of a travelling microscope that the onset of the type of nonlinear behavior observed in Fig. 3.67c can be correlated with onset of subcritical crack growth. However , they also concluded that viscoelastic effects. or matrix yielding, may contribute significantly to

the nonlinear behavior. Other investigators have also found that nonlinearity in the load-deflection records is not always associated with subcritical crack growth.

Extensive resin yielding and microcracking has been observed by Corleto and Bradley to develop in the failure zone ahead of the crack tip of T6T145/F185 under mode II SEM observations [52]. This indicates that inelastic energy has been consumed in the creation of this failure zone. The nonlinearity in the load-deflection curves can therefore be not only to the result of subcritical crack growth but also the formation of this failure zone.

A comparison between G_{II} and J_{II} for T6T145/F185 shows a difference of approximately 30% between the two, G_{II} being larger. The pemanent deflection observed in the load-deflection record during delamination of this material suggests some inelastic energy was dissipated away from the damage zone such in the legs of the ELS. Since the unloading line in Fig. 3.67c should have the same slope, with or without permanent deformation (damage), a comparison of G_{II} using the area, method including the permanent deformation, and not including it (assuming the unloading line returned to the origin but with the same slope), indicates a discrepancy in the order of 30%. The value of G_{II}, assuming no permanent deflection, is lower and comparable to that predicted by J_{II}. Therefore, this seems to also indicate that inelastic energy was dissipated in the legs of the ELS.

3.3.5 Effect of Thickness on Mode II Delaminaion

$J_{II} - a/L$ plots of 16 and 32 ply laminates of T2C145/F155 are shown in Fig. 3.69. The load-deflection record for the 16 ply layup is similar to the one for AS4/3502 (Fig. 3.67a), and the 32 ply similar to the 24 ply of the T2C145/F155 (Fig. 3.67b). However, the nonlinearity prior to maximum load was slightly larger for the 32 ply than the 24 ply specimens, The J_{II} values for the 16 ply specimens show an increasing trend at the early stable crack growth during the test. The maximum value obtained was approximately 7 lb/in followed by an average steady state value of 5 lb/in after unstable crack extension. Comparison between the steady state J_{II} for the 24 ply of the same material (Fig. 3.68b) indicates its value is nearly the same as the maximum measured for the 16 ply.

The trend found for the 16 ply and 24 ply can be seen for the 32 ply specimens. The level of crack propagation for this layup is also similar to the former ones. However, after the large unstable crack extension, J_{II} for the 32 ply was somewhat higher. It is evident that no significant thickness effects can be found on mode II delamination for the range of thicknesses studied for this layups.

The importance of this finding is twofold. First, sufficient constraint at the crack tip is obtained for 16 ply specimens, since the toughness measured with thicker laminates is comparable to the one predicted by this layup. Second, the assumption that shear deformation is negligible is indeed confirmed at least with respect to the thickness. In other words, the thickness to length ratios used for this study are adequate to provide shear deformation that is negligible in magnitude. This is of course strictly true only for T2C145/F155.
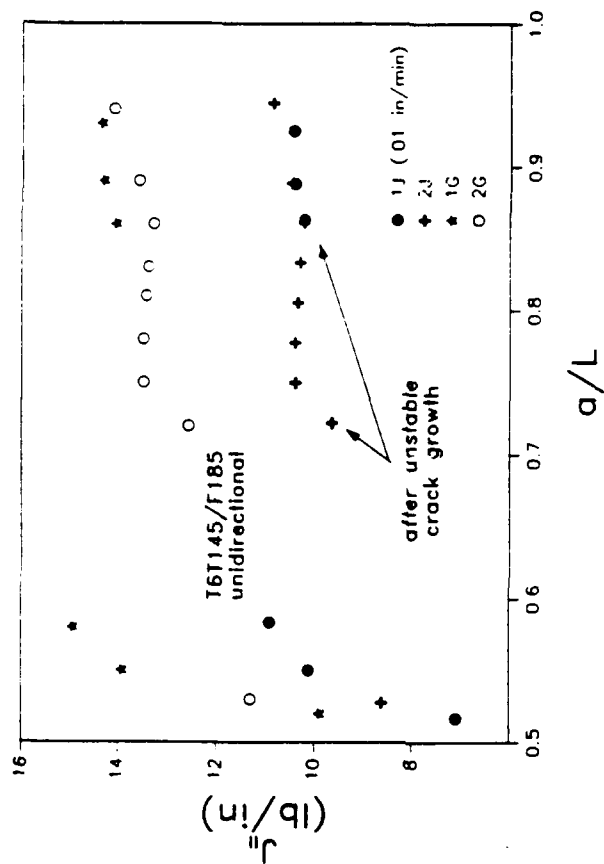
Finally, as shown in Figs. 3.68b and 3.69, the specimens were tested at different displacement rates (crosshead speed of testing machine). The results indicate indepen-
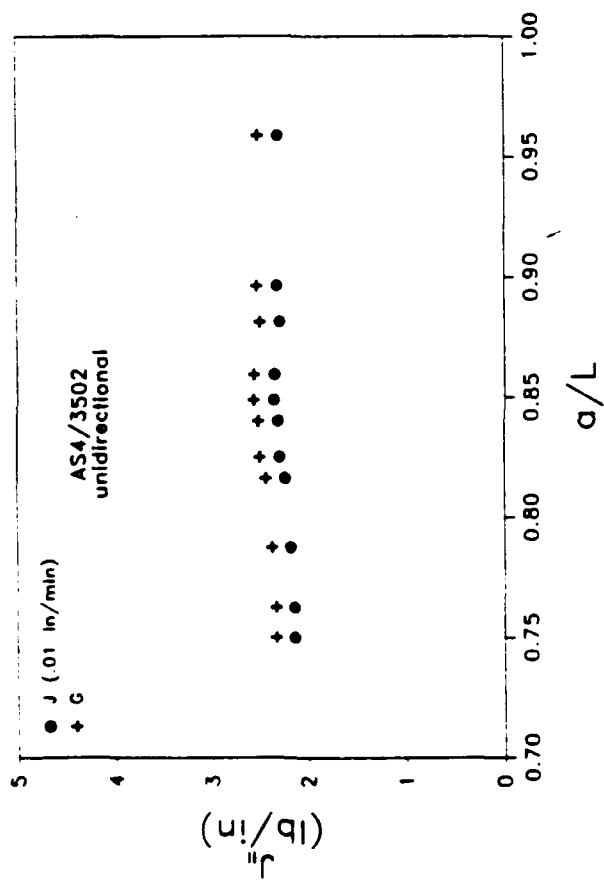
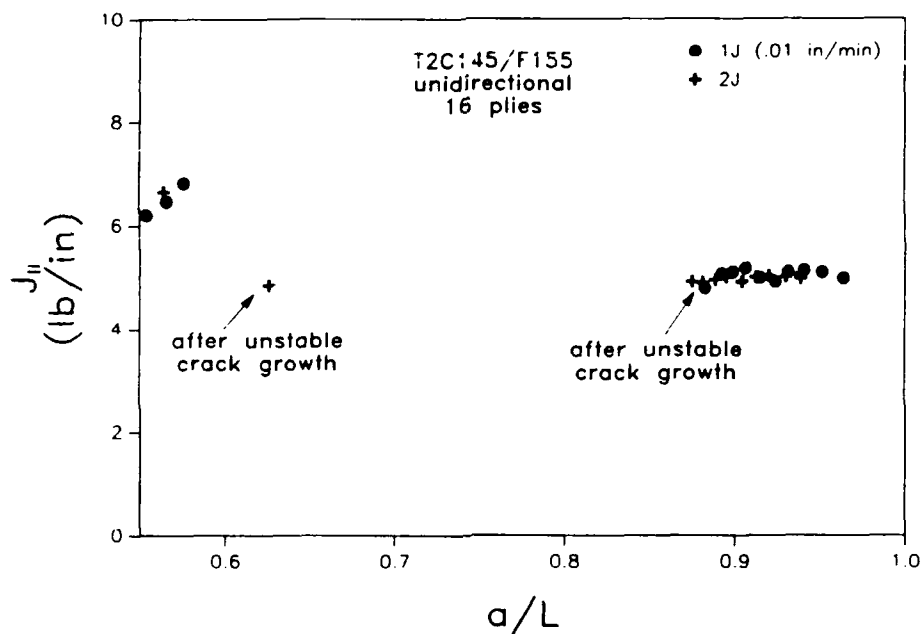(a) $J_{II}-a/L$ plot of AS4/3502 composite during mode II delamination
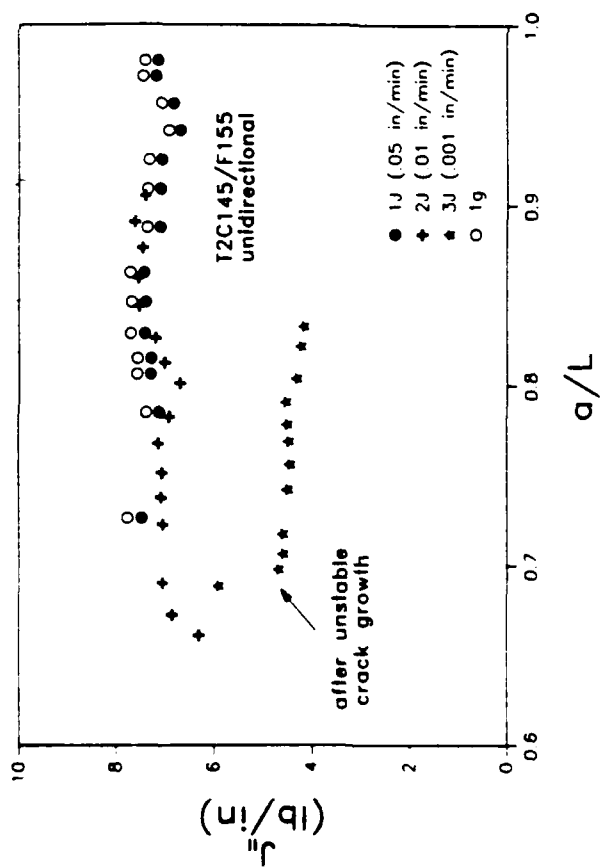
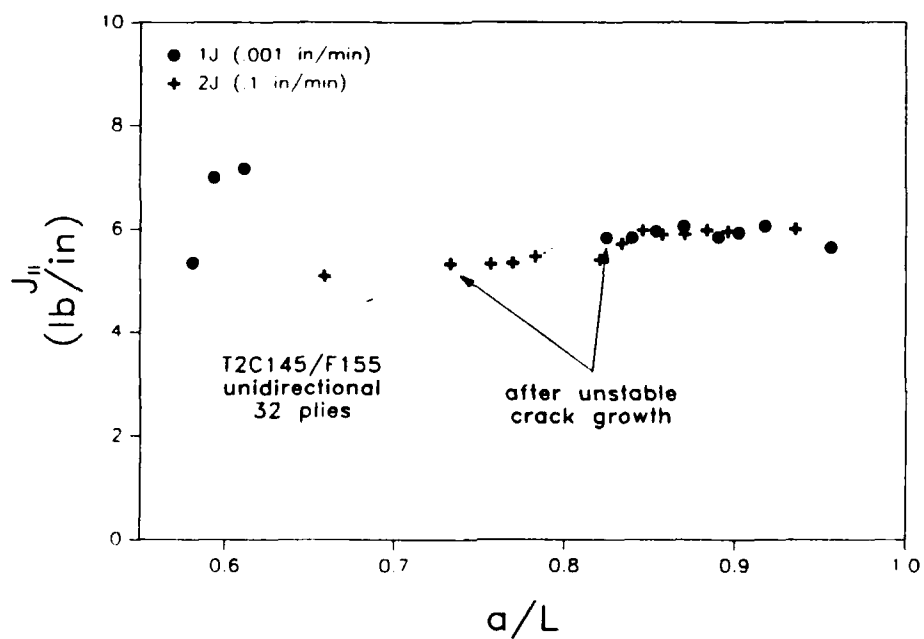(b) $J_{II}-a/L$ plot of T2C145/F155 composite during mode II delamination

(c) $J_{II}-a/L$ plot of T6T145/F185 composite during mode II delamination

Figure 3.68

82

(a) J_{II}-a/L plot of 16 ply T2C145/F155 composite during mode II delamination

(b) J_{II}-a/L plot of 32 ply T2C145/F155 composite during mode II delamination

Figure 3.69

dence between the J_{II} and the range of rates tested (0.1-0.001 in/min). Therefore, no significant viscoelasticity is evident for this composite tested over this range of rates. This indicates the adequacy of using the same J_{II} -M_{tip} relationship for the ELS data generated at different rates.

3.3.6 Mode II Delamintion of Fiber Dominated and Angle-Ply Layups

A typical load-deflection record of a composite with two-thirds of the plies at $\pm$ 45° and one-third 0° plies is shown in Fig. 3.70a. The delamination plane was 0° . The location of the 0° plies along the beam have inhibited the formation of any considerable damage development (see stacking sequence in Table 2.).This is seen by the very small permanent deflection upon unloding. The curve is mostly linear and similar to the one of the 24 ply unidirectional of the same material (Fig. 3.68b). Crack growth occurred at θ_{ct} between 5° and 12° . A tendency to more stability was obtained throughout the test with respect to crack growth. Some small geometric nonlinear response can be seen as well.

The $J_{II} - a/L$ results for this layup (Fig. 3.70b) clearly indicates scatter in J_{II} as much as $\pm$ 15%. This is similar to the trend found in mode I delamination earlier were multidirectional layups gave more scatter in toughness than unidirectional ones.

G_{II} predicts higher toughness than J_{II} (compare 3J and 3G in Fig. 3.70b). This difference is probably the result of a difference between the flexural modulus in tension and compression at higher moments, as was shown in the moment-curvature behavior of fiber dominated layups (section 3.2.4).

Initiation values of tougheness are significantly lower that the steady state value (3 lb/in compared to 6.5-7 lb/in). This increased resistance to delamination observed can be due to the formation of an increasingly large damage zone ahead of the crack tip until a maximum size for steady state is reached. However, since a mode I precrack was always introduced into the specimens to create a sharp crack tip, a damage zone is artificially introduced , the meaning of the initiation toughness is therefore dubious.

A slight trend towards a decrease in crack growth resistance can be seen at higher a/L ratios. However, on average, the steady state J_{II} remains similar to the value of the unidirectional layup of this composite. The significance of this finding is that stacking sequence effects (placing angle plies surrounding a unidirectional delamination plane) appear to be negligible.

A load-deflection curve of the matrix dominated layup with a $\pm$ 30° delamination plane is shown in Fig 3.71a. Crack growth took place at crack tip slope angles between 6° and 14° . Propagation was relatively stable throughout the a/L range tested. Note the amount of permanent deformation upon unloading. This deformation did not recover with time as observed in the permanent set in the specimen legs after completing the tests. This permanent deflection is similar in magnitude to the permanent deflection of the beam used to measure the I_c -M_{tip} relationship (Fig. 3.55).

Scatter in the $J_{II} - a/L$ plot is seen from specimen to specimen in Fig. 3.71b. The initiation value of fracture resistance is very low (1 lb/in). However, an examination of the fracture surface of one of these specimens (Fig. 3.72) indicates that as the mode I precrack is performed, the crack moves from the resin rich region between plies into an adjacent ply. This was also observed with the mode I fracture surfaces of angle-ply
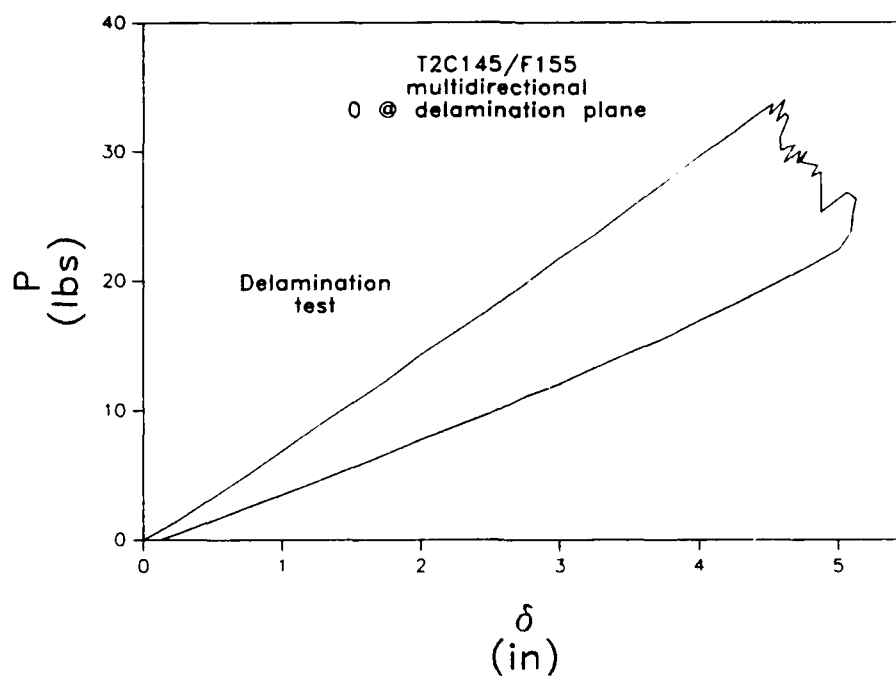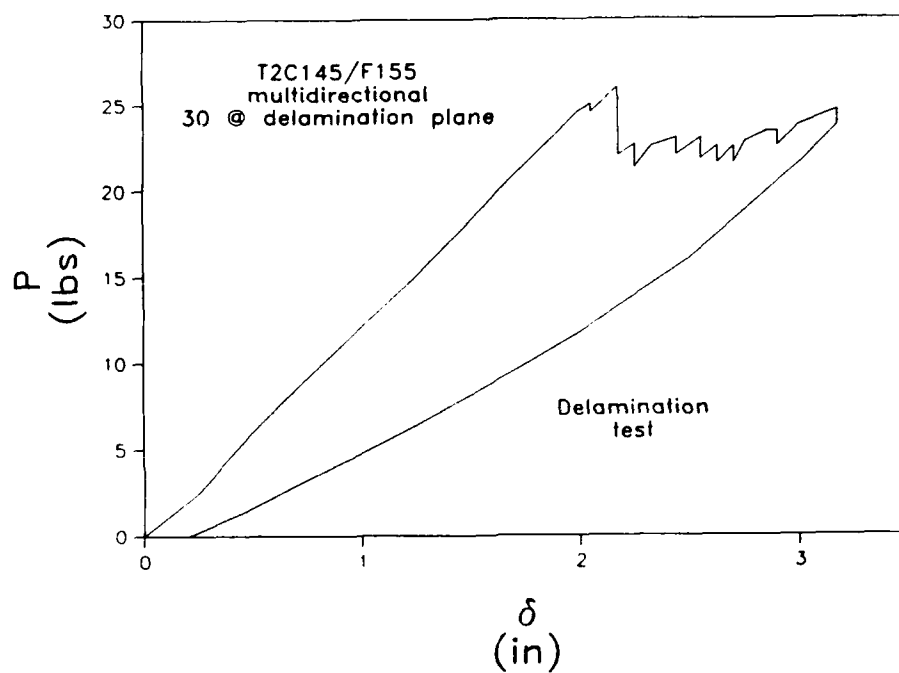
(a) Mode II delamination load-deflection record of multidirectional T2C145/F155 with 0° plies bounding the delamination plane
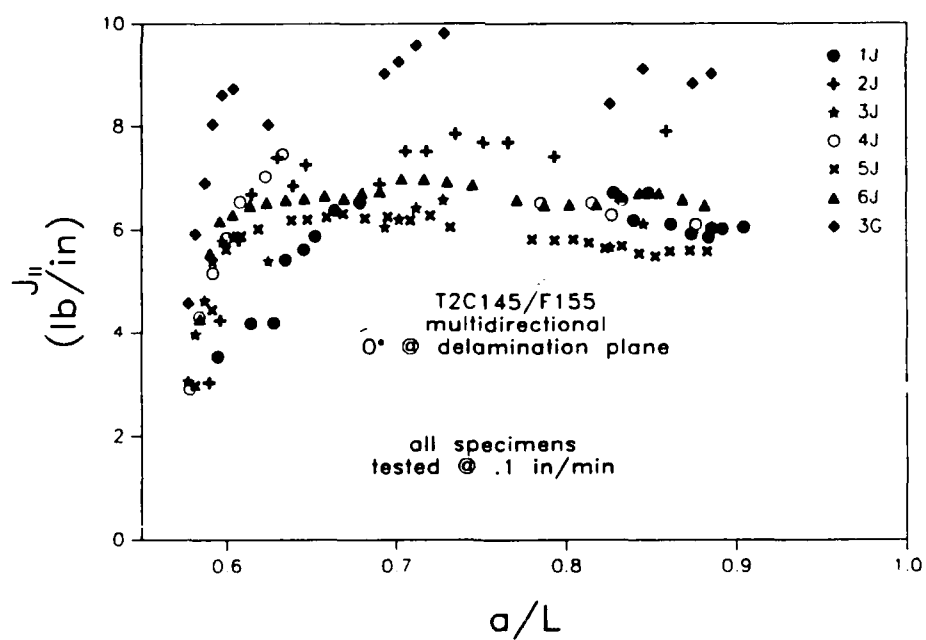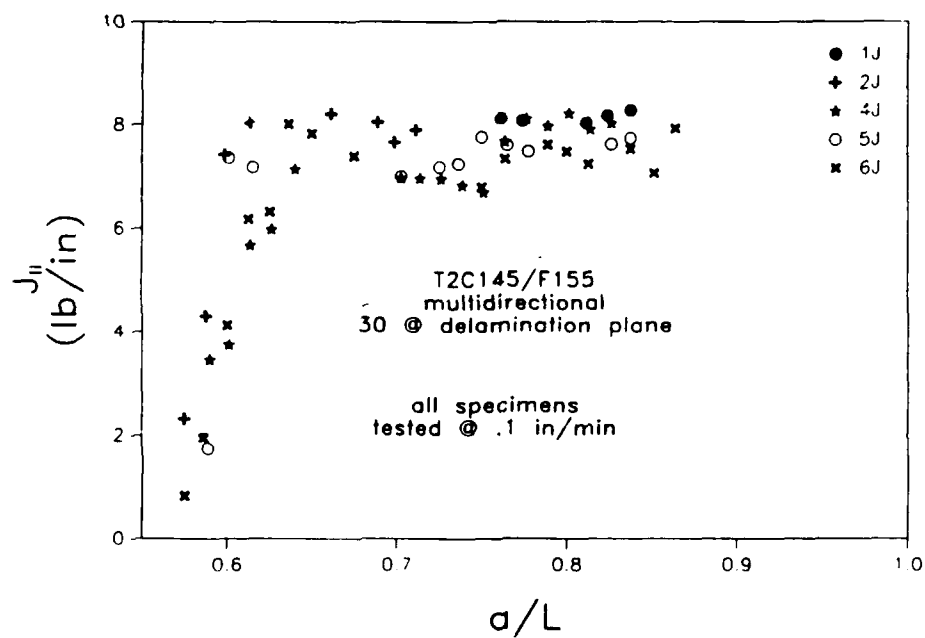

(b) J_{II}-a/L plot of multidirectional T2C145/F155 with 0° plies bounding the delamination plane

Figure 3.70

(a) Mode II delamination load-deflection record
of multidirectional T2C145/F155 with ±30° plies
bounding the delamination plane

(b) J_{II}-a/L plot of multidirectional T2C145/F155
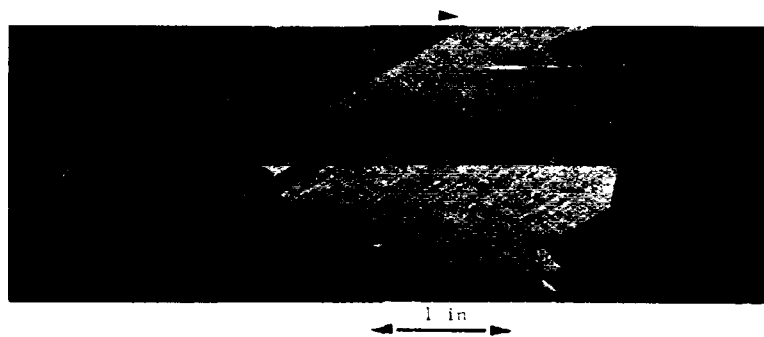with ±30° plies bounding the delamination plane

Figure 3.71

1 in

Figure 3.72   Fracture surface of multidirectional T2C145/F155
with ±30° plies bounding the delamination plane.

layups. Note also how upon mode II crack propagation, the fracture path progressively moves into the resin rich region between plies at the midplane. The crack then grows between plies (interply). Failure seems to occur in the resin rich region between plies and along the fiber/matrix interface. This is seen by the lighter and darker regions in the fracture surfaces, respectively (Fig. 3.72). At longer crack lengths, the fracture path changed again to be intraply and eventually migrated to different plies. J_{II} values for this crack region are note shown since they are artifically high due to the considerable ply jumping.

Ply jumping was also coupled with ply twisting at the longer crack lengths. In-situ delamination studies in the following Chapter will also confirm this findings. Loading at the crack tip is no longer limited to in-plane shear but has a significant component of out-of-plane shear as well.

The steady state J_{II} of this layup is between 7 and 8 lb/in. There seems to be a slight trend to increase from the unidirectional steady state toughness value which was in the range of 6-7 lb/in. This indicates that delamination resistance between unidirectional and multidirectional delamination planes is not necessarily the same similar. Unidirectional toughness seems to underestimate it for its multidirectional value. However, the difference seems to be small, at least between 0° and $\pm 30^o$ delamination planes and may be trivial in view of the scatter.

Crack growth when the crack front is between $\pm 45^o$ was also characterized by ply jumping and twisting at longer crack lengths. This feature is revealed in the load-deflection curve of this layup (Fig. 3.73). The load increases even as the crack propagates, when ply jumping and twisting take place. Considerably more far field damage is implied by the permanent deflection in the trace upon unloading and permanent set in the legs of the specimens. Fig. 3.56 supports this finding were the specimen used to evaluate the I_c-M_{tip} relationship for this layup showed a similar amount of permanent deformation to the ELS specimens. Crack growth was mostly stable and occurred at crack tip angles between 5° and 13° .

Initiation of delamination was at a value of J_{II} of 1 lb/in, similar to the $\pm 30^o$ layup. A steady state was reached at approximately 9-10 lb/in which was only maintained for a small range of crack growth. Resistance to crack propagation sharply increases at a/L rations of 0.7. This rising toughness is due to the development of extensive ply jumping and twisting observed during the test.

The fracture surface of one of the specimens with this layup is shown in Fig. 3.74. Similar to the $\pm 30^o$ layup, the mode I precrack forced the fracture path to be intraply. Then, upon mode II loading, the fracture path progressively migrated to the midplane. Finally, considerable ply jumping and twisting developed. These developments invalidate the J-integral analysis since considerable antisymmetry between the cracked legs is developing.

A comparison of crack growth resistance between 0° , $\pm 30^o$, and ± 45 delamination planes indicates a gradual increase from 7 lb/in for 0° to 8 lb/in for $\pm 30^o$ and 10 lb/in for $\pm 45^o$. Due to data scatter, these values may change but at least a definite increasing trend is revealed. Increases in mode II toughness of glass, carbon, and kevlar fabric reinforced composites have been observed as fiber orientation increases from 0°
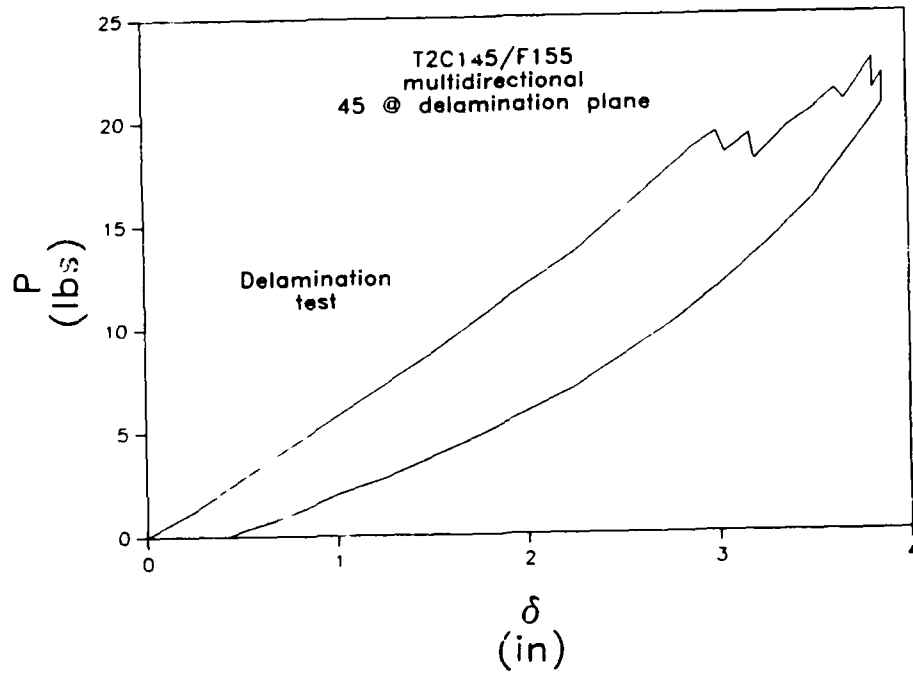
(a) Mode II delamination load-deflection record of multidirectional T2C145/F155 with ±45° plies bounding the delamination plane
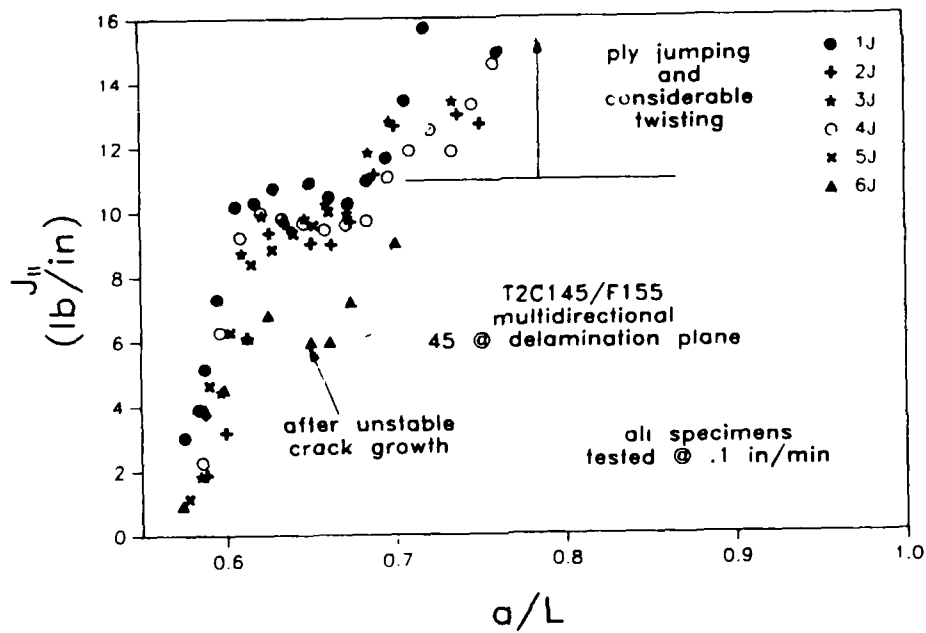
(b) J_{II}-a/L plot of multidirectional T2C145/F155 with ±45 plies bounding the delamination plane

Figure 3.73

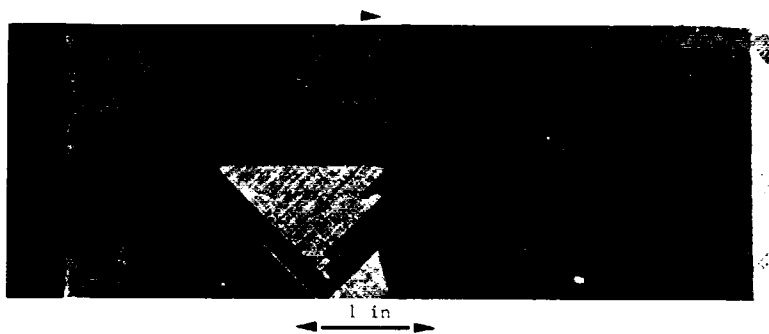Figure 3.74   Fracture surface of multidirectional T2C145/F155
with ±45° plies bounding the delamination plane.

to $\pm$ 45° at the delamination front [16]. However, their increase was considerably larger than the one observed for these fiber reinforced layups. Engineering assumptions of mode II toughness for unidirectional laminates may not be accurate for multidirectional layups. However, it appears that they may give a good lower bound value which would be adequate for engineering purposes.

With regard to the migration of the crack into the ply during mode I precracking, a possible way of sharpening the crack tip is to use considerable thinner teflon inserts instead. Such practice has been proven to be effective by other investigators [20].

The adequacy of the proposed J-integral to properly characterize steady state delamination in the presence of distributed damage is because steady state crack growth implies a constant crack tip moment during this stage. Therefore, as long as the paths to evaluate J are through material that had experienced the same maximum moment at the crack tip, the path independence of J is maintained. This was ceirtanly the case for the DCB. For the ELS configuration, the uncracked segment of the specimen experiences a higher moment than the maximum crack tip moment during crack growth. However, it is evident that since a steady state has been reached, this uncracked segment does not develop permanent damage and its behavior is mostly elastic. Unloading and loading paths are therefore the same. The development of damage occurs in the cracked segment as it has been previously demonstrated for these angle-ply layups.

3.3.7 Comparison Between Mode I and Mode II Delamination

When the mode I and mode II delamination results are compared, several important findings can be outlined with regard to the use of the J-integral to characterize delamination fracture toughness. First, for both mode I and mode II, the J-integral predicted similar values of toughness compared to G, (the energy release rate approach to fracture), for unidirectional layups that showed an essentially linear elastic response. In the case of the very tough composite under mode II loading (T6T145/F185), the J-integral approach was more appropriate to use than G, since the load-displacement behavior was not linear elastic. It was found that the J-integral predicted values on the order of 30% lower than G the tougher unidirectional composite studied (i.e., T6T145/F185)

Second, with regard to the fiber-dominated layups, the use of the J-integral is needed since mismatch between the flexural modulus in tension and in compression induced midplane compression. The J-integral analysis developed for both mode I and mode II delamination include midplane straining through the use of K^* rather than K, which for G, it is assumed to have a linear relationship with moment.

Third, in the case of angle-ply layups, significant damage development away from the crack tip indicated that the J-integral is necessary as well to properly characterize mode I and mode II delamination toughness. The use of G in these cases would greatly overestimate the energy required to induce delamination. This overestimation was 50% percent or higher in some cases.

With regard to delamination behavior for mode I and mode II loading, it was found that unidirectional composites had a discontinuous or unstable crack growth in both modes of failure. However, more stable crack growth behavior was found for the multidirectional layups for both modes of failure.

The mode I fracture toughness for angle-ply delamination planes was approximately 50% lower than the mode II fracture toughness of comparable delamination planes for T2C145/F155. Therefore, these findings arc similar to the relationships between mode I and mode II fracture toughness for unidirectional T2C155/F155 laminates.

DELAMINATION FRACTURE PHYSICS

The delamination behavior of multidirectional composites has been shown in the preceding discussion to be intimately associated with the fracture mechanisms which are evidenced by different surface morphologies. The most striking difference between the delamination behavior of unidirectional and multidirectional laminates is the much larger variety of mechanisms which the multidirectional composites exhibit. In this section the details of these mechanisms will be examined through the use of fractographs, micrographs of cross-sections, and in-situ observations of the fracture process. Also, strain field mapping around crack tips will be included. These measurements will provide quantitative information of delamination at the micromechanical level. Their usefulness will be discussed in terms of their potential to assess and develop mathematical models of delamination.

4.1 Procedures

4.1.1 Postmortem and In-situ Fractography

Portions of the fracture surfaces of DCB and ELS specimens were observed visually and under a JEOL-JSM-330A scanning electron microscope. Prior to SEM observations, the surfaces were coated with a 100-A-thick Au/Pd film to minimize charging effects associated with the non-conducting nature of the epoxy resins.

Mode I and mode II delamination fracture observations were made with 8 ply specimens in the case of mode II and approximately 10-12 plies for the mode I specimens. The latter one was ground from an original number of plies of 24. The mode I specimen was a $\pm 45^{\circ}$ angle-ply layup, while mode II specimens were unidirectional and multidirectional (their stacking sequence is shown in Table 2 in Chapter III). Also a mode I test was conducted on a compact tension (CT) specimen of a neat resin (F155) to compare the strain field ahead of the crack tip of the composites with the neat resin.

The mode I SEM delamination studies were accomplished by means of a special loading stage fixing one end of the specimen and driving a wedge into a pre-existing starter crack, as shown in Fig. 4.1a. The mode II studies were made with a specially designed three point bend fixture attached to a SEM tensile stage. See Fig. 4.1b. A small CT testing fixture was used with the SEM tensile stage to conduct the mode I fracture test on the neat resin. Figure 4.1c shows the CT configuration.

Prior to fracture in the SEM, the specimens were polished and coated with a 100 A Au/Pd coating. The purpose of the coating was, as described earlier, to minimize charging associated with the nonconducting nature of the resins. However, it is also used to place a dot pattern on the surface that allows the computation of displacements and strains on the surface.
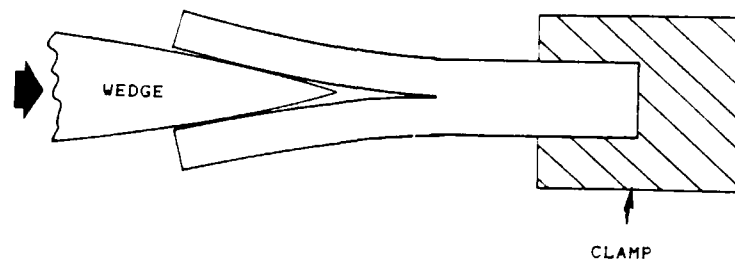
(a) Schematic of wedge loading for DCB
fracture studies in SEM
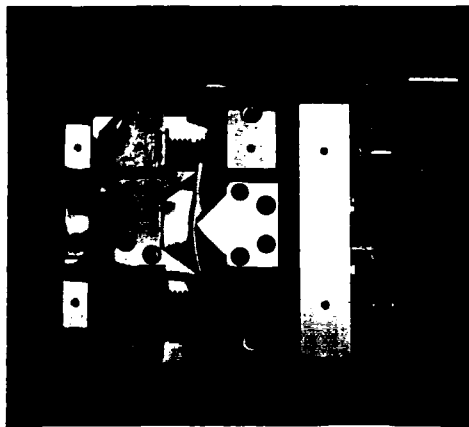
(b) Tensile stage used in SEM fracture studies.
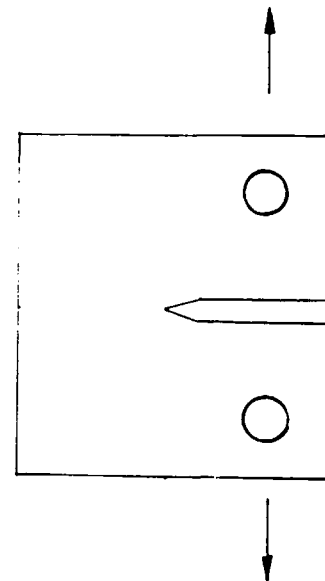
(c) Illustration of CT specimen

Figure 4.1

4.1.2 Strain Field Mapping

The strain field mapping technique used in this study consists of placing an array of dots on the surface of the specimen which serve as a deformation grid to measure displacements. The dot pattern is placed on the coating by means of the electron beam of the SEM. The procedure followed to accomplish this task was developed by Hibbs [83]. The arrays of approximately 1 μm diameter dots were placed ahead of the crack tip at a magnification of 720X. This provided a spacing between the dots of approximately 6 to 10 μm . Sometimes one or two additional arrays were placed adjacent to each other. The maps were placed prior to any load application to the specimen. The dot map placement was done automatically with a computer that controls the location of the electron beam. A beam voltage of 5 KV and a beam current of 300 picoamps were used with a 10 mm working distance. A typical array of dots is shown in Fig. 4.2a.

A refinement of the dot map technique is shown in Fig. 4.2b. This was accomplished by using an operating voltage of 20 KV instead of 5 KV, and reducing the beam current to less than 100 picoamps at the same working distance. The dot placement in this case was done at 20,000X. As it can be seen in Fig. 4.2b, the size and morphology of the dots is considerably different to the previous dot maps. In the former, a hole is burned in the gold-palladium coating with a very small center. The latter shows only a very small surface bubble which results from thermal expansion of surface contaminants that are deposited during sputter. This contamination is primarily diffusion pump oil. The size of the dots is in the order of 0.1 μm in diameter. Note the raised bubble appears as a white dot on the surface whereas the burned holes appear as black dots. This refinement of the technique was done to be able to study the interface. However, actual strain fields from interfaces was not investigated in this work. The advantage of this new dot morphology and size is that the resolution is greatly improved. Nonetheless, this is done at the expense of reducing the field of view, which is why it is less useful for studying strain fields around crack tips.

After the dot mapping was completed, micrographs were taken to record the undeformed configuration of the dots. The specimens were loaded in displacement increments until the crack grew into the dot maps. Micrographs were again taken that recorded the deformed configuration of the dots during crack advance. Standard 4x5 tri-x film was used for the micrographs.

4.1.3 Strain Field Measurements

The undeformed and deformed configuration micrographs obtained during in-situ fracture observations were used to measure normal and shear strains ahead of the crack tips. The 4x5 negatives containing this information were stored in a SEISS Image Analyser through a video camera. The (x,y) location of the dots in the undeformed and deformed configuration were digitized based on a 512x512 pixel digital image of the 4x5 negatives. The negatives were enclosed within this pixel area. The normal strains were computed using the (x,y) undeformed and (x,y)' deformed location of the dots and finite strain equations describing a two dimensional deformation field. The normal strain ϵ_{xx} is computed by means of
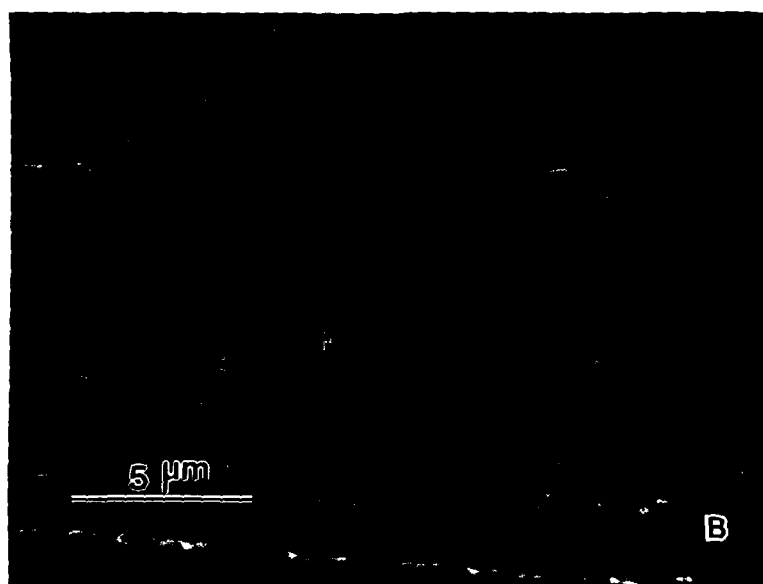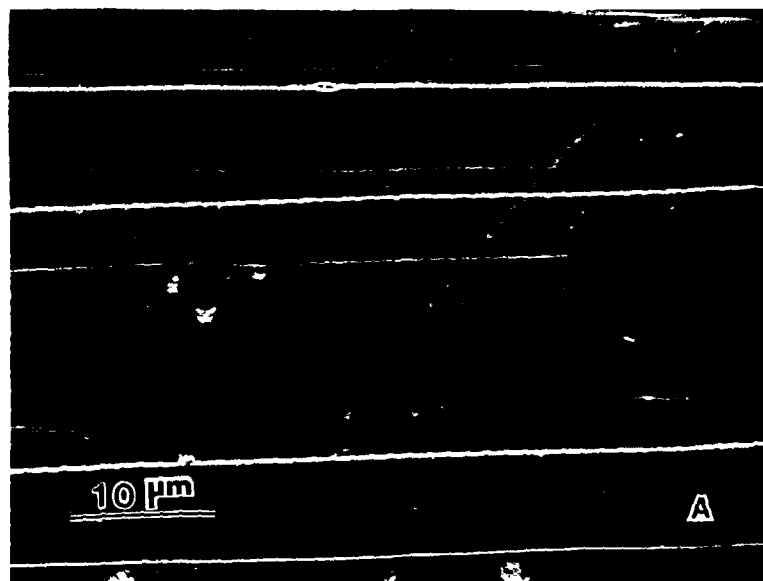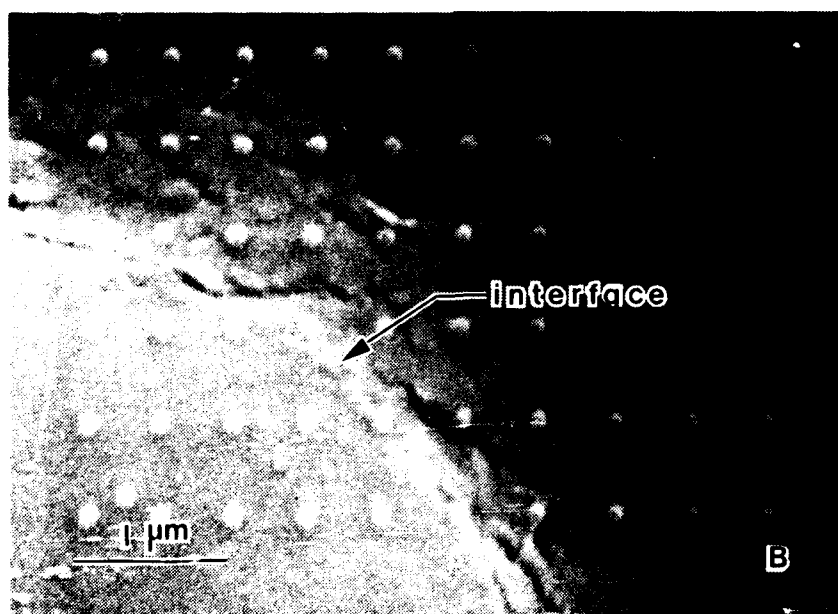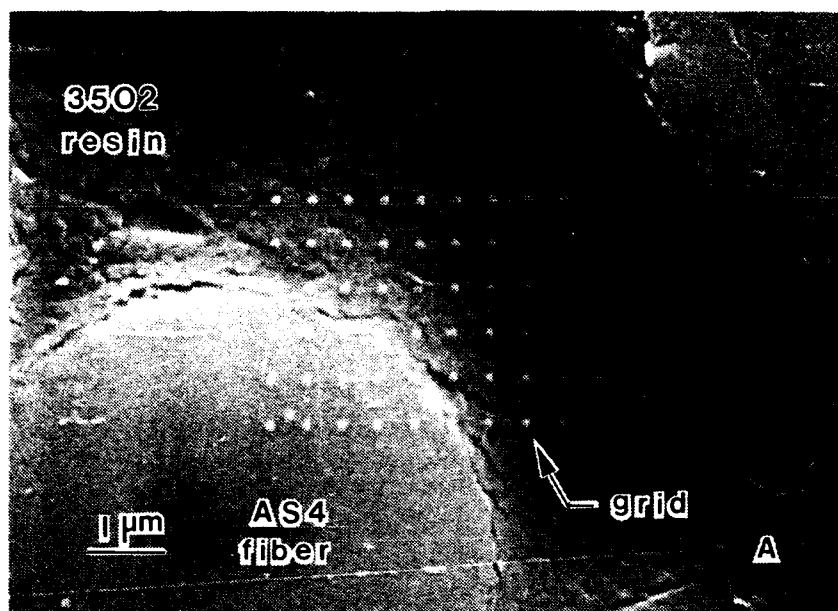
Figure 4.2 Sample dot maps

Figure 4.2 Continued

$$\epsilon_{xx} = \frac{\Delta x' - \Delta x}{\Delta x} \tag{4.1}$$

where $\Delta x'$ and Δx are the distance of the dots in the x direction after and before deformation, respectively. The normal strain ϵ_{yy} is given by

$$\epsilon_{yy} = \frac{\Delta y' - \Delta y}{\Delta y} \tag{4.2}$$

$\Delta y'$ and Δy are the distance between two dots in the y direction after and before deformation. The shear strain γ_{xy} can be computed from

$$\gamma_{xy} = \frac{\pi}{2} - \theta \tag{4.3}$$

where the angle γ_{xy} is shown in Fig. 4.3 and can be calculated from the $(x,y)'$ location of the dots arranged in the configuration shown in Fig. 4.3 using

$$\theta = cos^{-1}\left(\frac{\mathbf{AB}}{\mid \mathbf{A} \parallel \mathbf{B} \mid}\right) \tag{4.4}$$

The coordinate location of the resulting normal strains were assumed to be between the dots in the undeformed configuration. The coordinate location of the resulting shear strain is assumed to be the center of gravity of the triangle defined by the dots that were used to compute these strains.

The actual computation of the strains was done with a Vax computer system at Texas A&M University. The strain field were plotted using SURFER, a three dimensional computer program run on a PC computer.

4.1.4 Spatial Resolution and Measuring Accuracy of Strain Measurements

The spatial resolution of the strain field mapping technique depends on the dot spacing. As dot spacing is decreased, the spatial resolution increases. However, the dot size must be decreased to obtain good accuracy. As shown in Fig. 4.2b, the spacing between the dots is approximately 0.5 microns, an improvement in spatial resolution of one order of magnitude (compared to that in Fig. 4.2a). The size of the dots has been decreased from 1 μm to about 0.1 μm in diameter. A problem with decreasing the dot size can be that they become difficult to see after the deformation has occurred. Improvements in dot spacing are basically done by increasing the magnification at which the measurements are going to be made. However, this is done at the expense of losing the field of view by one half for every doubling in magnification.

The measuring accuracy of the technique is primarily affected by errors in the measurement of dot location and dot spacing. The former can be associated with the sensitivity of the digitizing device or technique and human errors such as difficulty in locating the center of the dots, particularly in the deformed configuration. Fig. 4.2a shows a 2x2 dot map placed at a magnification of 5000X, a dot size of approximately 0.5 μm , and a dot spacing of approximately 14 μm . The measuring accuracy under this conditions with the image analyser previously mentioned is $\pm$ 0.56% for the normal
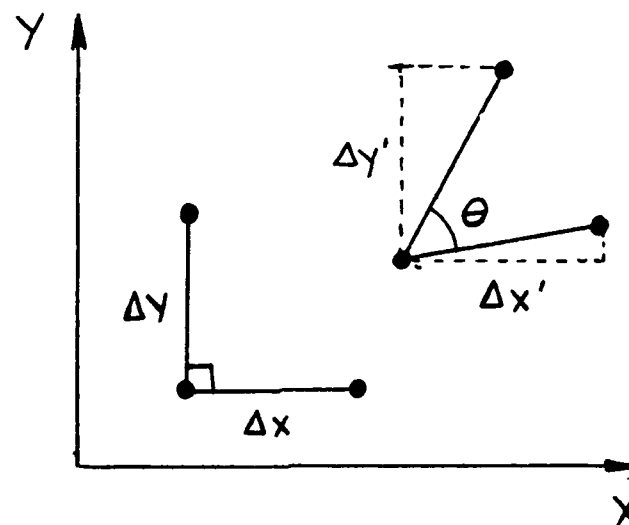
$$\varepsilon_{xx} = \frac{\Delta x' - \Delta x}{\Delta x} \qquad\qquad \varepsilon_{yy} = \frac{\Delta y' - \Delta y}{\Delta y}$$

$$\gamma_{xy} = \frac{\pi}{2} - \theta$$

Figure 4.3 Schematic showing dot in deformed and undeformed configuration and computation of strains

strains and $\pm\ 0.47^{\circ}$ for the shear strain. The distance between the dots in pixel units was 363. Using this information and equations (4.1-3), it can be seen that as the spatial resolution was improved (gage length between dots is decreased at a fixed magnification level) by a factor of two, the error associated with the measuring accuracy increased by a factor of two. This is shown in Table 4. Table 5 showns the limits in spatial resolution improvements obtained by magnification for a fixed level of measuring accuracy, provided that the ratio of dot spacing to dot size is maintained as the magnification is increased.

The measuring accuracy of the arrays placed at 720X with a dot spacing of approximately 6 μm , dot size of approximately 0.8-1 μm , and an array density such that the 512x512 pixel of the image analyser was completely covered with dots, was on the order of $\pm\ 10\%$ for the normal strains and about $\pm\ 5^{\circ}$ for the shear strains. Nevertheless, this very low measuring accuracy allows the digitization of a larger surface area. This was particularly advantageous to compute a large portion of the strain field ahead of the crack tip. It provided information regarding the trend of the field.

The measuring accuracy of the digitizing technique was improved to within $\pm\ 3\%$ normal strain and $\pm\ 2^{\circ}$ shear strain by digitizing an area composed of a much smaller dot density (4x4 as opposed to 15x25 for the low resolution). The 4x4 array area was enclosed within the 512x512 pixel area by focusing only this region during image storage. This effectively magnified the image several times. For the case of the neat resin fracture studies, an additional digitizing technique was used. In this case, the image was magnified using a standard copying machine. Then, a digital caliper with a resolution of $\pm\ 0.0001$ inches was used to digitize the data. The 4x5 micrographs were approximately doubled in size. The measuring accuracy in this case was improved to approximately $\pm\ 1.5\%$ in the case of the normal strains.

4.2 Results of Delamination Fracture Physics

4.2.1 Delamination Fracture Path

One feature of delamination of multidirectional composites which was noted in Chapter 3 is that the crack generally travels within a ply. The fracture path is typically intraply rather than truly interlaminar. That is, the crack travels within a ply rather than between plies. Furthermore, in the case of delamination under mode II loading, progressive ply jumping eventually led the fracture path significantly away from the midplane.

Figure 4.4 shows two micrographs of polished cross-sections of a unidirectional laminate. The first micrograph shows parts of five plies. The interlaminar regions are marked by the lines of resin. Although the plies are easily distinguishable, note the occasional ply interpenetration and nonuniform thickness of the plies. A few holes associated with gas trapped during the curing process are evident. Within the plies the distribution of the fibers is not completely uniform. Fig. 4.4b is a cross-section of a DCB fractured specimen showing the position of the crack plane. It does not pass through the resin-rich region between plies. Generally, the crack passes along the fiber-matrix interface, within the ply moving from fiber to fiber. Two implications for the mode I delamination of unidirectional T2C145/F155 are apparent. First, fiber nesting

Table 4.1

DOT SPACING (µm)	NORMAL STRAIN ERROR (%)	SHEAR STRAIN ERROR (DEG)
19.25 (512 PIX)	± 0.4	± 0.33
13.65 (363 PIX)	± 0.56	± 0.47
6.83 (182 PIX)	± 1.12	± 0.94
3.41 (91 PIX)	± 2.24	± 1.88
1.71 (45 PIX)	± 4.48	± 3.76
0.85 (23 PIX)	± 8.96	± 7.51

DOT SIZE = 0.5 µm
DIGITIZING (512 X 512 PIXEL)
MAG . 5000X

Table 4.2

NORMAL STRAIN ERROR	SHEAR STRAIN ERROR
±0.56 %	±0.33 °

FIXED PIXEL DISTANCE

363

MAGNIFICATION	DOT SPACING (µm) (RESOLUTION)
5000 X	13.65
10000 X	6.83
20000 X	3.41
40000 X	1.71

MEASURING FIELD DECREASES

DOT SIZE MUST DECREASE, TO AVOID
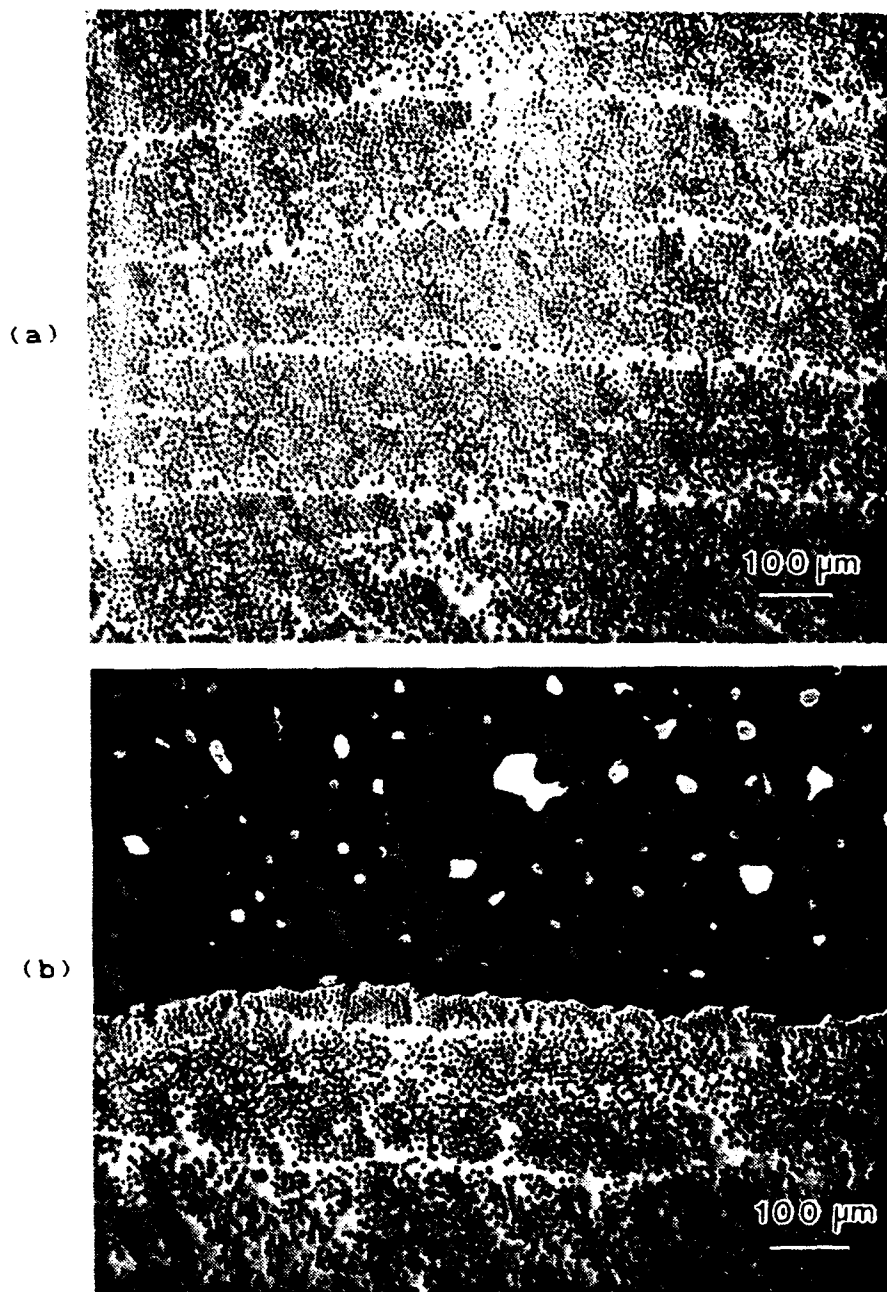GREATER PENALTY TO MEASURING ACCURACY

Figure 4.4 Micrographs of polished cross-sections of a
unidirectional DCB specimen. a) Fiber distribution and
resin-rich regions between plies. b) Fracture plane
passing within a ply. The mounting material is in the
top part of the photograph.

(from ply interpenetration) leading to a greater degree of fiber bridging is apparently rot a problem in T2C145/F155. Second, the potential dependence of toughness on the strength of the fiber-matrix interface and fiber volume fraction is suggested.

Cross-sections of the fracture path under mode II delamination are shown in Fig. 4.5. These cross-sections are from a unidirectional T2C145/F155 laminate and correspond to the initial stable crack growth region. The material seen between plies should not be confused with the resin rich region between plies. This is cold mount material used to mount the two fracture halves. While most of the "potting" material surrounds the two mating pieces of fracture surface, a small portion of the mounting found its way between the two pieces during potting. The fracture path is clearly seen to be on one edge of the resin rich region between plies, occasinally moving slightly into the ply and along the fiber-matrix interface. This is similar to the mode I case (Fig. 4.4b). However, this was not always the case. Fig. 4.6 shows a different fracture path, one that is observed to go in and out of the midplane into the ply. These micrographs represent the crack front after unstable crack extension of the same specimen of Fig. 4.5. Resin rich regions are obse ved between plies above and below the fracture plane (Fig 4.6a) with cracking occuring inply. The delamination toughness of this composite was observed to considerably decrease after this unstable crack growth, which is clearly due to the migration of the fracture path into the ply (see Figs 3.68b, 3.69a-b). It is evident that once crack propagation took place significantly into a ply, the decrease in local resin volume indicates there is not enough resin to absorb energy by resin shear deformation. Therefore, fracture toughness should decrease as the fracture path goes from interply to intraply mode.

It appears that given enough energy for the crack to jump from interply to intraply, the crack will try to follow the path of least resistance that is, intraply. An increase in local resistance due to a thicker resin rich region can increase loading requirements to a point were mode II failure intraply can begin. Since the energy required to propagate the crack along the interface is less than through the resin rich region, the extra available energy results in large unstable propagation that remains inply, since it is easier than in the resin rich region at the midplane. Apparently, this overshadows any increase in fracture toughness that would otherwise occur due to the additional surface that results from the sinusoidal fracture path seen in Fig 4.6.

Figure 4.7 is a micrograph of a cross-section of a $\pm$ 45° angle-ply specimen which was cut at 45° to the length of a DCB specimen. The two plies which are shown in part are therefore oriented perpendicular to the plane of the photograph and the ply shown in its entirely is oriented along its plane. The amount of resin in the interlaminar region is generally less than two fiber diameters thick. In some places the fibers from adjacent plies are almost touching. The plies are completely distinct. Most notably, the fracture path is several fiber diameters away from the interply region (resin rich region), again following the fiber-matrix interface. Fig. 4.8 also illustrates how the path is not in the resin rich region between plies. The plane of the micrographs is perpendicular to the length of the specimen, so the fibers appear as ovals. In both micrographs the crack has branched to form a double surface. In Figure 4.8b a bundle of fibers has been pulled away. It is attached to the specimen at another plane. Crack branching is one
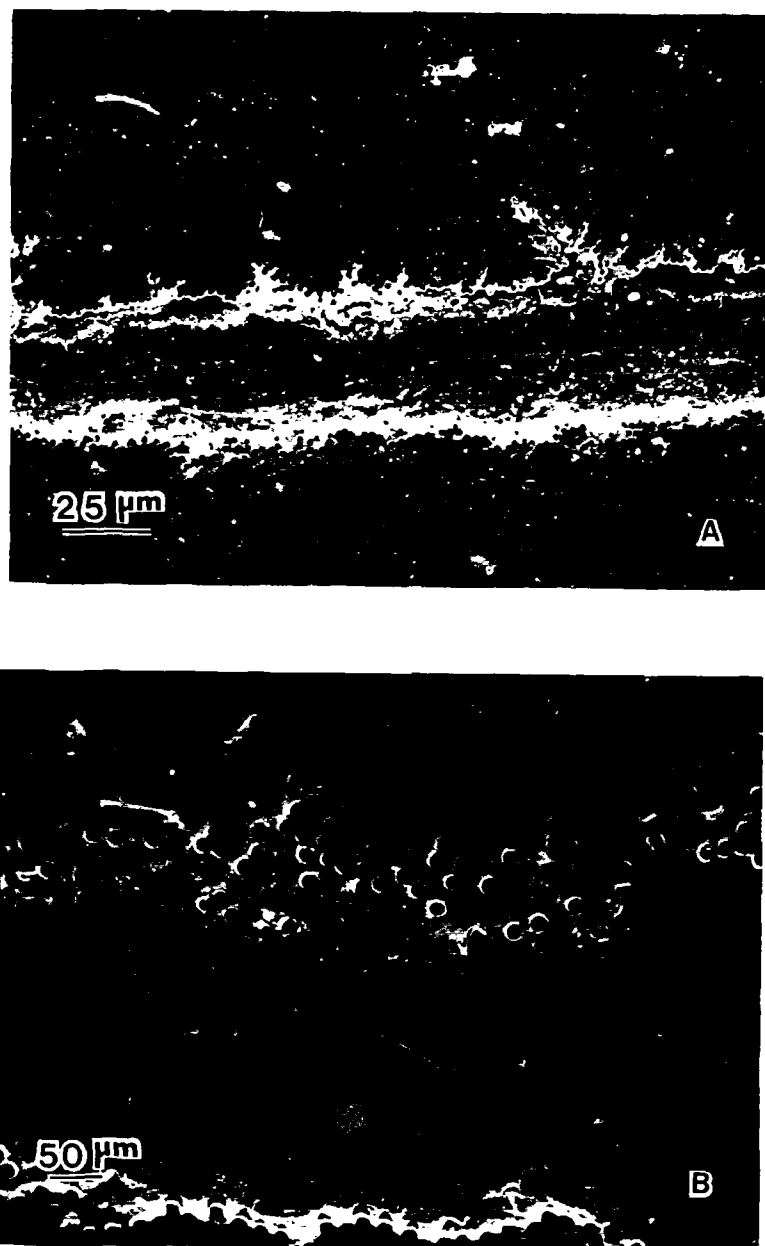
Figure 4.5 Cross-sections showing how fracture path is contained within the resin rich region between plies.
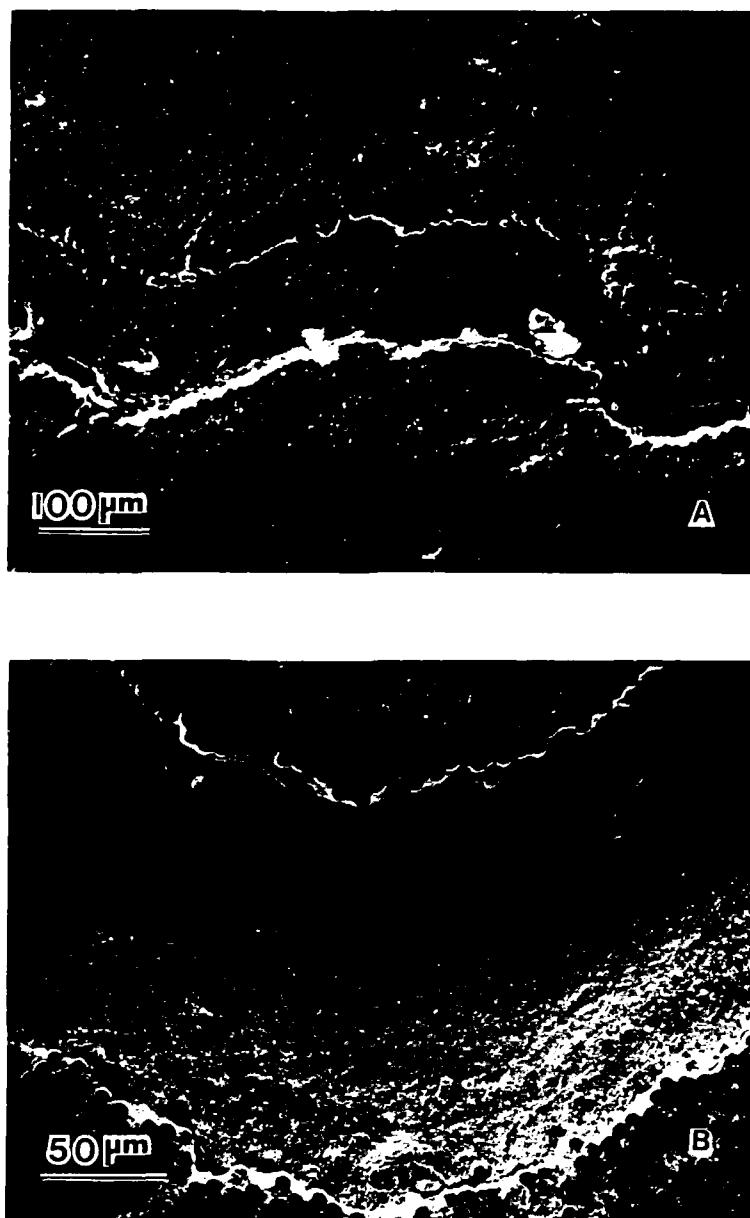
Figure 4.6 Cross-sections showing how fracture path is into the ply
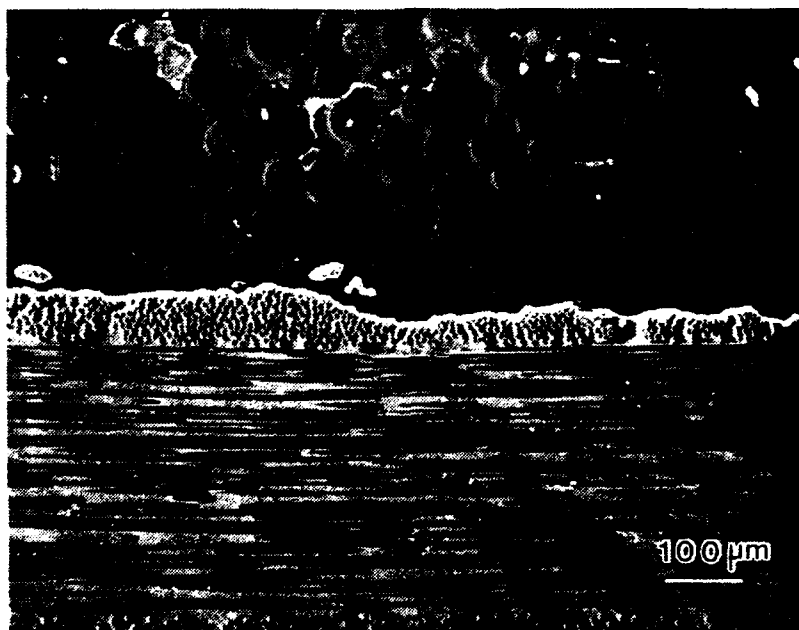
Figure 4.7 Micrograph of a polished cross-section of a +-45 angle-ply specimen showing intraply fracture. The section was made at 45° to the length of the specimen.

Figure 4.9 Fracture surface of a unidirectional DCB specimen

Figure 4.10 Fracture surface of a 10 fiber-dominated DCB showing transition from many steps to two plies.
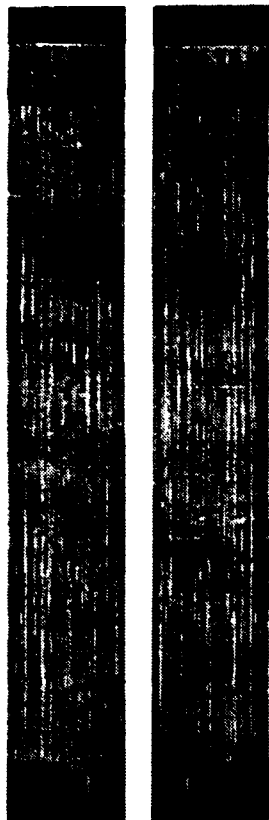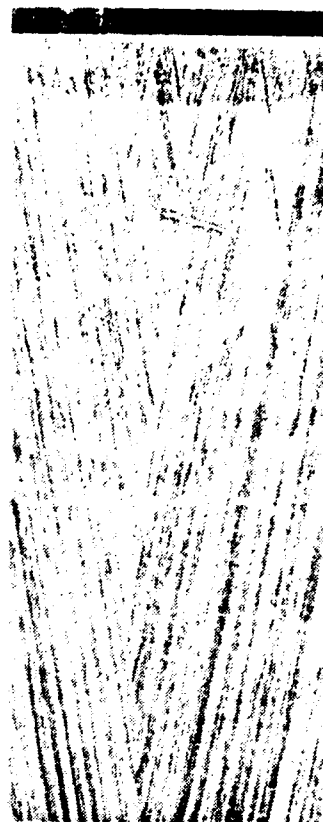

Figure 4.8. Cross-section of a +-45 angle-ply specimen. The section was made perpendicular to the length of the specimen

of the most commonly observed mechanisms for increasing surface roughness (which is associated with higher fracture energy).

4.2.2 Unidirectional versus Multidirectional Fracture Morphologies

Figures 4.9-10 show the fracture surface of unidirectional and multidirectional mode I specimens. The fracture surface of the unidirectional specimen is homogeneous. The fracture mechanism is essentially the same throughout the test, though the amount of fiber bridging and the rate of growth may vary. These variations lead to occasional sudden crack growth. Relative to muldirectional laminates, however, the fracture morphology is consistent. the fracture morphology of the multidirectional specimen is rather inhomogeneous. Several types of inhomogeneities can be found in multidirectional mode I fracture surfaces. The first one is multiplanar cracking which can be associated with a crack growth being initiated from a teflon insert. The multiplanar character of the initial growth is essentially a product of multiple initiation along the teflon insert. An example of a transition from many small steps to cracking on two plies is shown in Fig. 4.10. In view of the special complexities of early crack growth, one can expect the early crack growth during a DCB test to be unusual.

True interlaminar mode I crack growth can be seen in Fig. 4.11. These regions were found under the special conditions at the specimen edge (stress state, fiber ends, machining markds, etc). The precise cause of these edge regions is not known, but apparently they are associated with the special conditions near edges, since similar regions are not found away from the edge. The major significance of their existence is that they can form the beginning of a ply transition. Potentially they could play a part in establishing a width effect. Close inspection of the interior and edge regions of the fracture surfaces of two inch wide angle-ply specimen did not reveal any difference in appearance. One might expect a difference due to the difference in stress state (plane strain and plane stress).

Ply transitions along fibers under mode I delamination are seen in Fig. 4.12. Along the transition, fibers are broken leaving a step. The length of such transitions depends on the fiber angles and the specimen width. The length of the transition in turn affects the variation of the toughness with the crack length. This type of transition usually leads into another ply transition when it reaches the edge. The successive ply jumping lead to asymmetric legs which makes the analysis increasingly inaccurate.
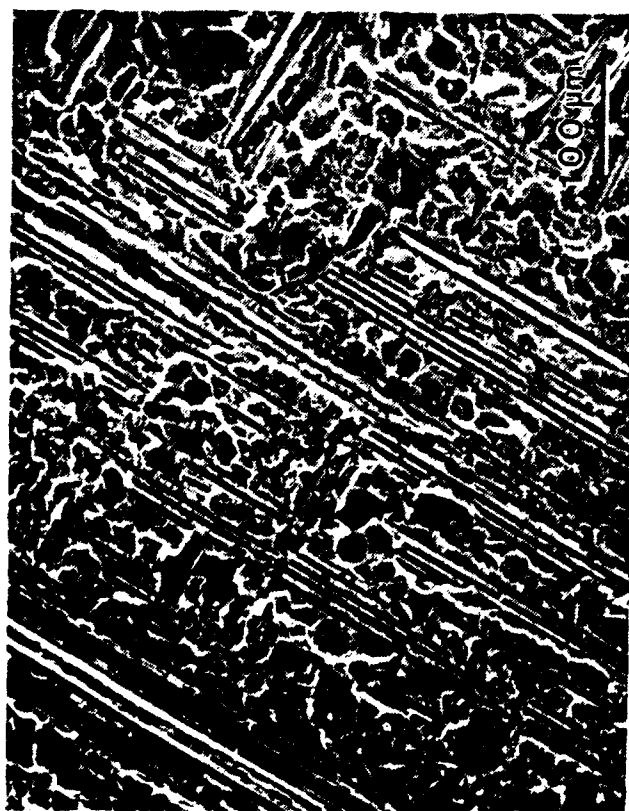
Figure 4.13 shows transverse cracks intersecting the mode I fracture plane. The interply resin region is quite thin; apparently fibers just below the surface act as stress concentrators, leading to periodic cracking. Such cracking was not typically seen.

Figures 4.14-17 show the mode II fracture surfaces of unidirectional and multidirectional ELS specimens. The arrows on the upper right hand corner of the micrographs reveal crack growth direction. The typical hackled surface of mode II delamination is seen for the unidirectinal specimen in Fig. 4.14. The formation of the hackles results from coalescence of microcracking that develop ahead of the crack tip and have been widely reported in the literature. The development of the hackles involves more energy dissipation, which explains the increase in toughness going from mode I to mode II delamination of unidirectional laminates. Mode I unidirectional fracture surfaces are characterized by fiber-matrix failures which require less energy than the hackled mode

Figure 4.12 Ply transition at an edge of a 2 inch
wide +- 45 angle-ply DCB specimen

(a)

(b)

Figure 4.11 Interlaminar cracking at the edge of a +-45
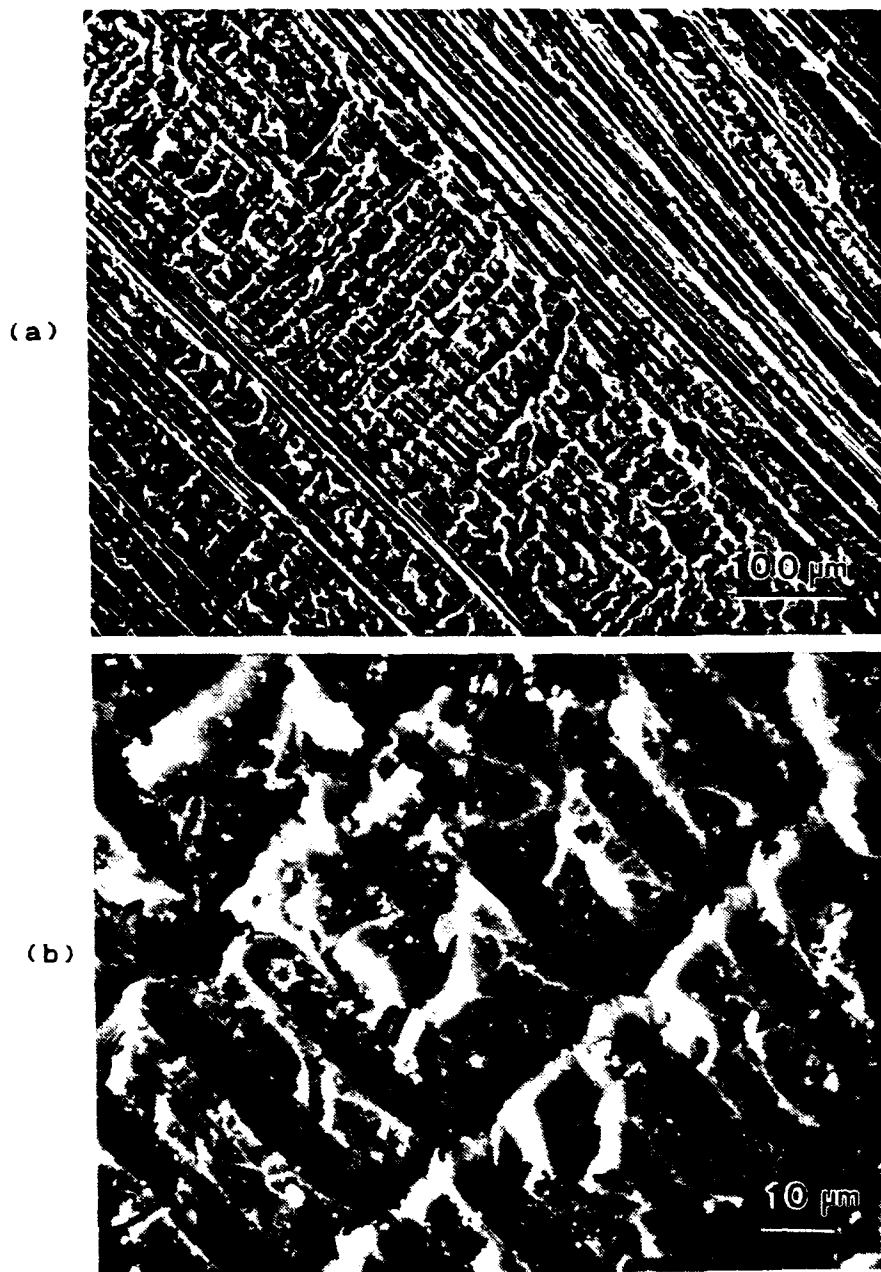angle-ply specimen. (a) Overview (b) Close-up
of the same area

(a)

(b)

Figure 4.13 Transverse cracks intersecting with the fracture plane.

Figure 4.15 Postmortem fractograph of T2C145/F155 sho-
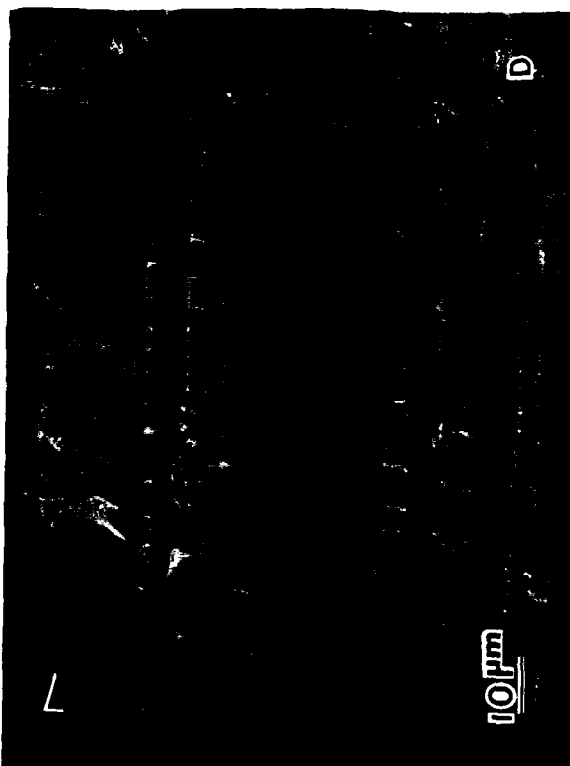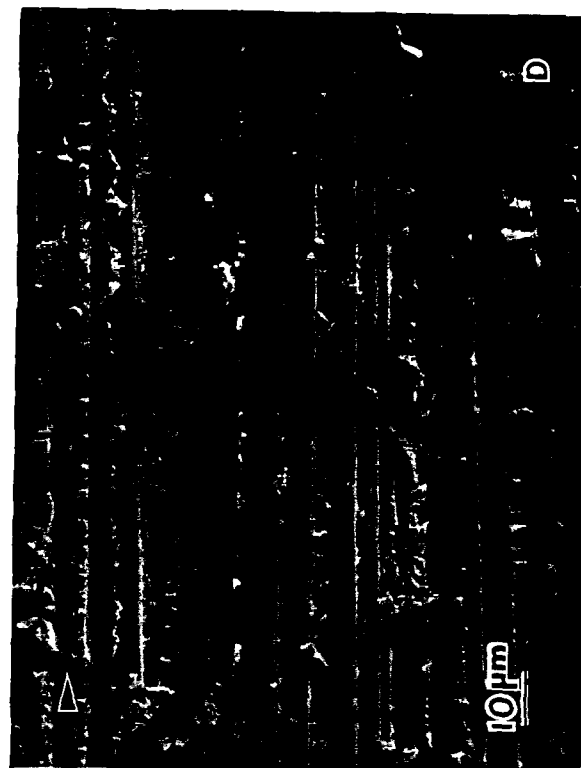wing an intralaminar fracture path

Figure 4.14 Postmortem fractograph of T2C145/F155 sho-
wing an interlaminar fracture path

II fracture surfaces. However, as it was shown in section 4.1.5, the mode fracture path was observed to move into the ply (intralaminar). The fracture surface for mode II intralaminar crack growth is seen in Fig. 4.15. Because the resin content in the ply is much smaller than between plies, little resin deformation by hackle formation is seen. This results in a decrease in toughness, as it has already been discussed.

The formation of hackles is mostly associated with brittle or low ductile resins. For composites with very tough resins, hackle formation is pre-emptied by extensive resin yielding. Corleto and Bradley have shown this when they compared mode II fracture surfaces of composites made with a brittle and a tough resin [52].

The fracture surface of multidirectional composites (Figs. 4.16-17) reveal a considerable more complex fracture surface compared to the unidirectional ones (Figs 4.14,4.15). Similar to the mode I fracture surfaces, multiplanar cracking is observed. The crack propagated into the ply and through the resin rich region between plies. This was also seen in Figs. 3.72,74. Multiplanar crack growth was developed as a mode I precrack was introduced to sharpen the original crack. It has been shown that mode I multiplanar cracking develops from delamination initiated from a teflon insert. The effect of multiplanar cracking was very significant in terms of the mode II toughness upon initial crack growth, as was discussed in the previous chapter. Extremely low toughness values were measured during initial crack growth compared to the steady state value.

The formation of hackles in the multidirectional mode II fracture surface can be seen in Figs 4.16-17 as well. However, these hackles are thinner than the ones seen on the unidirectional fracture surfaces. Also the density of hackles has increased as well. The hackles are seen in the areas were fracture was truly interlaminar and were not neccessarily found at the edges as was the case for interlaminar crack growth under mode I loading. Furthermore, evidence of the out-of-plane shear loading or tearing observed in the legs of the ELS specimens during the delamination tests can be seen by the slight twist of the hackles towards the direction of crack growth. Twisting is introduced locally by the off axis plies and it provides it indicates the crack front is straight and perpendicular to crack growth direction.

As it can be seen, the fracture morphologies of mode I and mode II fracture are significantly more complex in the case of multidirectional versus unidirectional composites. The significance of these findings in terms of resistance to delamination of these cases is that multidirectional toughness is higher than unidirectional toughness. This was in fact seen in the result discussed in the previous chapter. The more complex fracture surfaces indicate more energy dissipated than in more uniform ones. Also, the multiplicity or inhomogeneity of multidirectional fracture surfaces leads to a higher scatter in the delamination toughness values.

The same increasing trend in toughness going from unidirectional to multidirectional laminates can be seen when comparing mode I and mode II multidirectional toughness. The primary reason for this is similar to unidirectional composites, that mode II loading leads to hackle formation. Hackles are responsible for an increase in toughness from mode I to mode II loading.

113

Figure 4.17 Fracture surface of T2C145/F155 +-45 an-
gle-ply showing interlaminar and intrala-
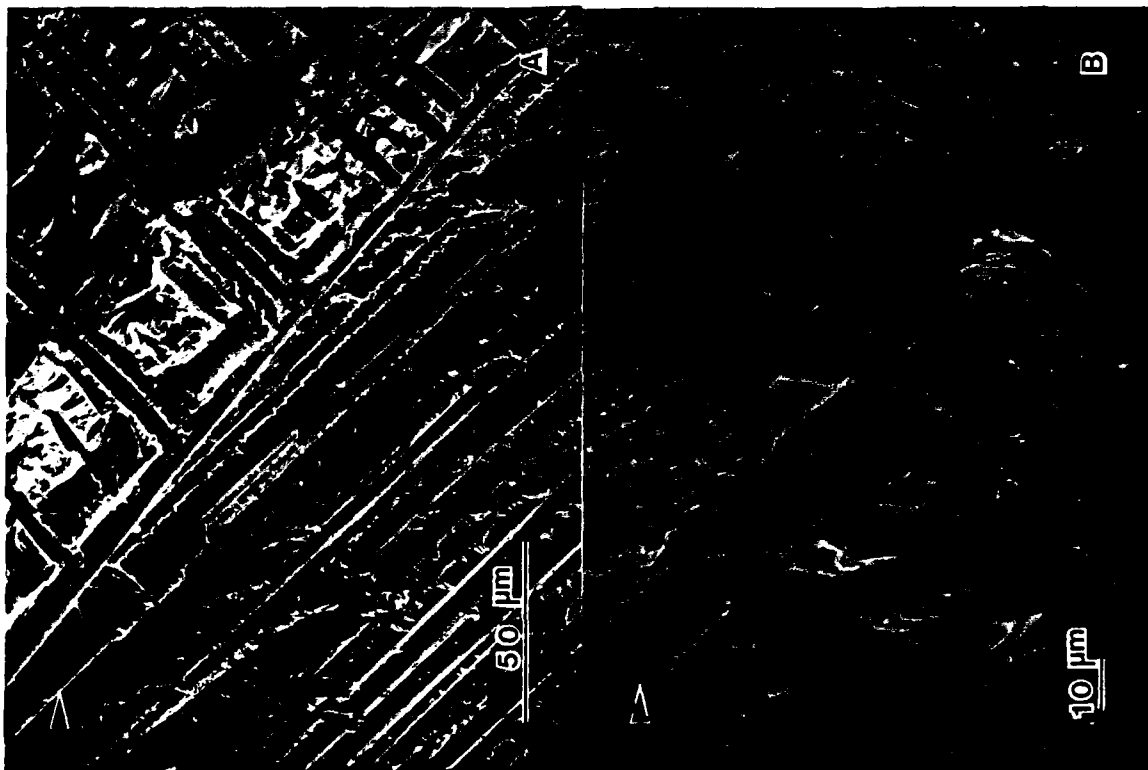minar crack growth. (a) 200X (b) 350X

Figure 4.16 Fracture surface of T2C145/F155 +-45 an-
gle-ply showing transition regions of
crack growth between interlaminar and
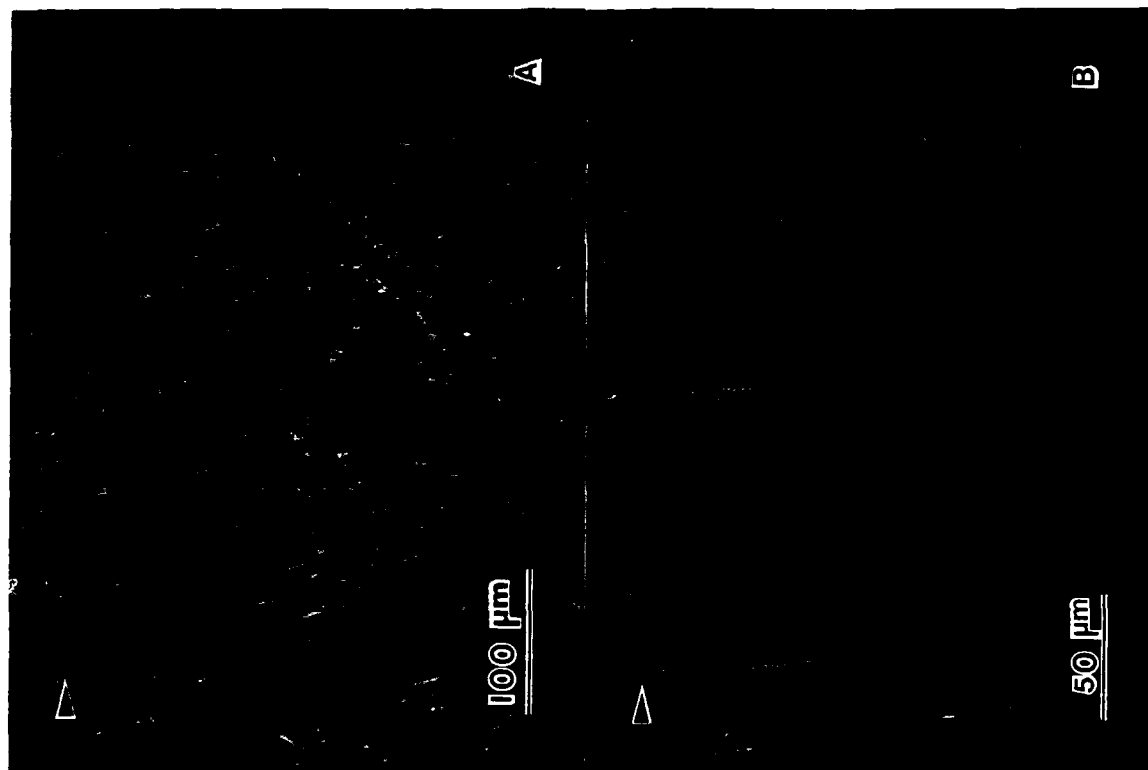intralaminar fracture paths (a) 500X
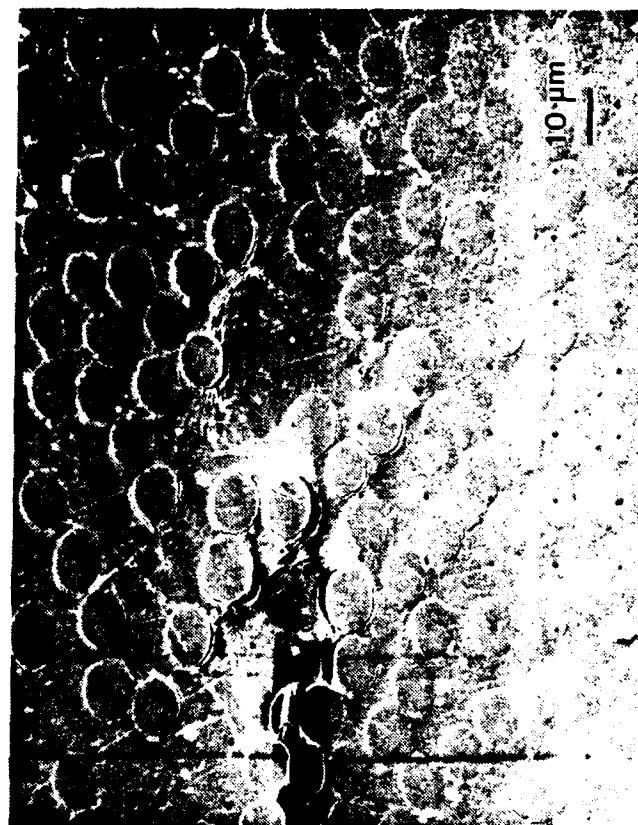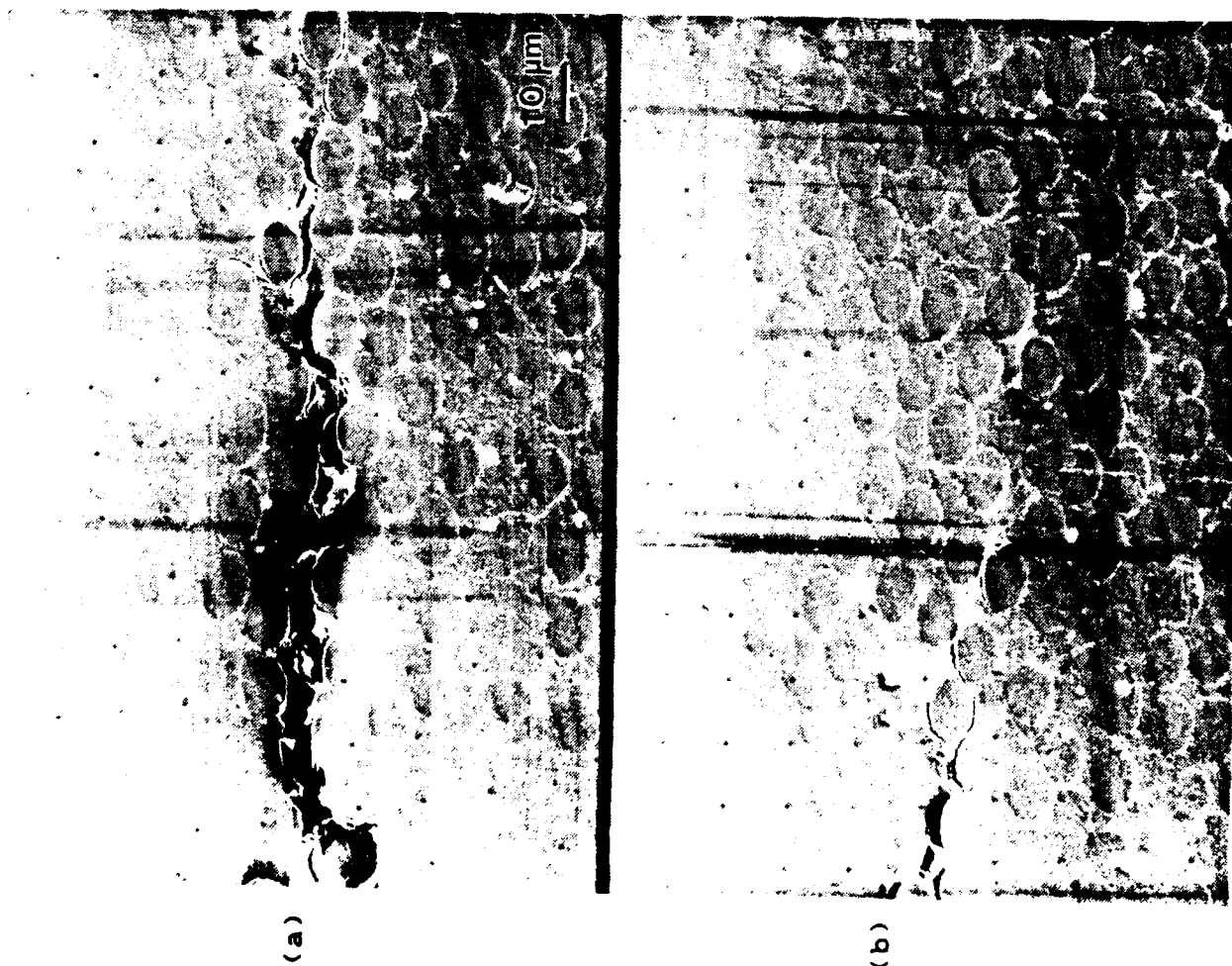(b) 750X

(c)

114

Figure 4.18 Micrographs of the edge of a DCB
specimen being fractured in the SEM

10 μm

(a)

10 μm

(b)

4.2.3 In-situ Fracture Observations

The progression of mode I crack growth along fiber-matrix interfaces can be seen by observing the edge of an angle-ply T2C145/F155 DCB a it is fractured in the SEM. Fig. 4.18a illustrates how the crack follows the fiber-matrix interface. Also note the microcracking in the resin between fibers. Fig. 4.18b shows the same crack which has advance slightly. In front of the crack tip there is fiber-matrix debonding. Debonding is seen well away from the apparent crack plane in Fig. 4.18c. Cracks not continuous with the original crack have initiated. Clearly debonding in the high strain fields ahead of the crack tip is determining both the location of the fracture plane and the character of the fracture surface.

The progression of mode II crack growth for an angle-ply with a $\pm 30°$ delamination plane can be observed in Fig. 4.19. Resin yielding, microcracking and out-of-plane fiber pullout are evidenced. The dots placed on the polished edge of the specimen by means of the electron beam of the SEM prior to the application of the load give an indication of the highly complex state of strain under load that results from the nominal mode II loading. Visual examination of the displacement of the dots seem to indicate that in addition to shear straining, opening and compressive strains seem to develop ahead of the crack front as well. Arrows in Fig. 4.19 show locations where the normal strains appear to develop.

The crack is seen to propagate in the resin rich region between plies although as seen in Fig. 4.19, it is propagating at the boundary of this region and lower ply. Furthermore, the resin rich region between plies is not uniform. The delamination tends to be along the edge of the resin rich region between plies were failure is facilitated by fiber/matrix interface failure. The fibers are apparently acting as stress raisers when they are in the fracture path.

One of the major characteristics of the fracture path for multidirectional delamination is the tendency for the crack to migrate or jump into the ply. This was particularly severe for mode II loading. Furthermore, this tendency increase going from $0°$ to $\pm 45°$ delamination planes. Fig. 4.20 provides evidence of this phenomenom. The micrographs are for crack growth originally intended to be along a $\pm 45°$ crack plane. The crack is propagating intraply. Note how once the crack is into the ply, it gradually continues to grow away from the resin rich region between plies were it started. Due to the proximity of the fibers in the ply, the stress concentration the fibers provide facilitates the fracture path to change toward the direction of principal opening stress and continually more into the portion of the beam under compression. It is very evident the crack path can move out of its path by an amount equal to one fiber radius at a time. This procedure will continue until given enough crack growth, the crack will considerably move away from the midplane. The tearing loading observed during the mode II delamination tests and seen in the hackles on the fracture surfaces are also corroborated by the out-of-plane displacement of the resin and fibers in Fig. 4.20

Crack propagation of a unidirectional specimen of T2C145/F155 under mode II loading can be seen in Fig. 4.21. Microcracking and continued resin deformation can be observed to have preceded fiber/matrix interface failure. Hackle formation can be seen as well. In comparison to the multidirectional case, the complex fracture path is not

Figure 4.20 Damage zone ahead of the crack tip of T2C145/F155 +-45 angle-ply. Note how fracture path is migrating into the ply
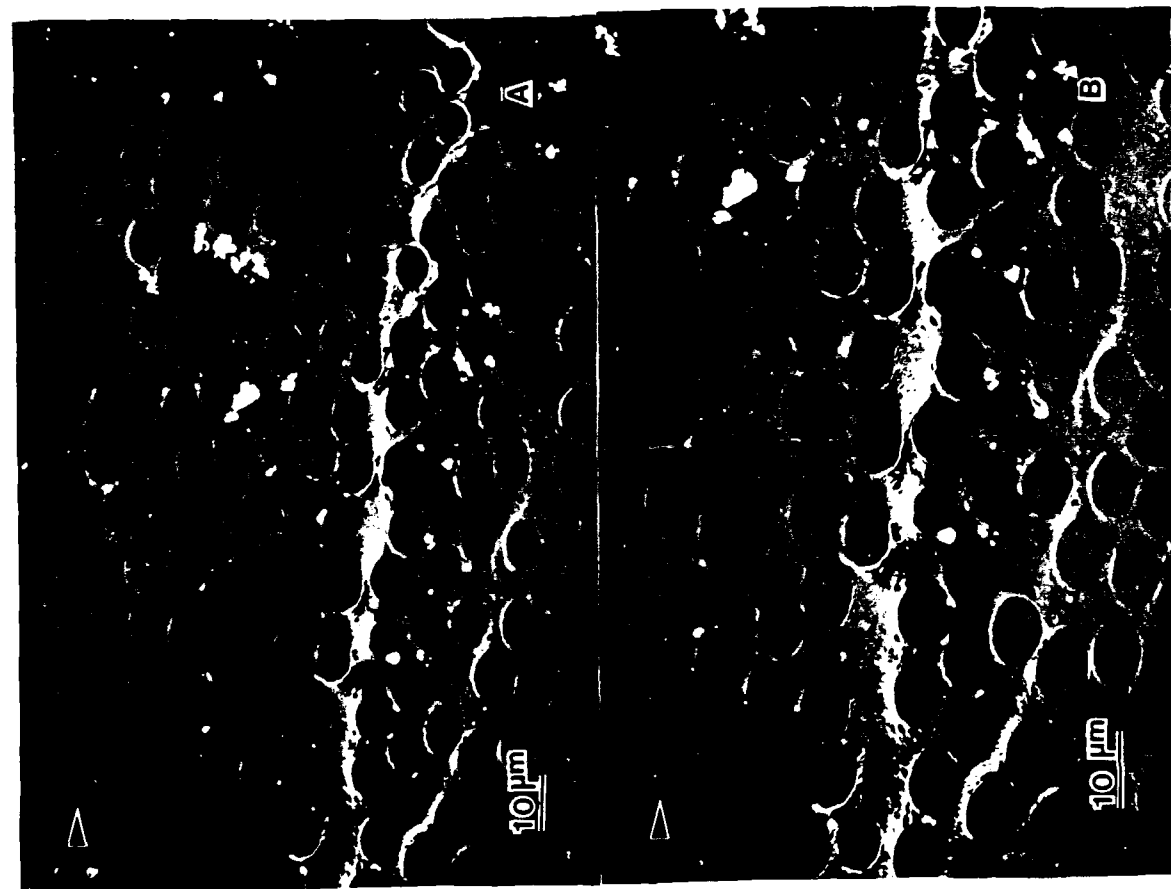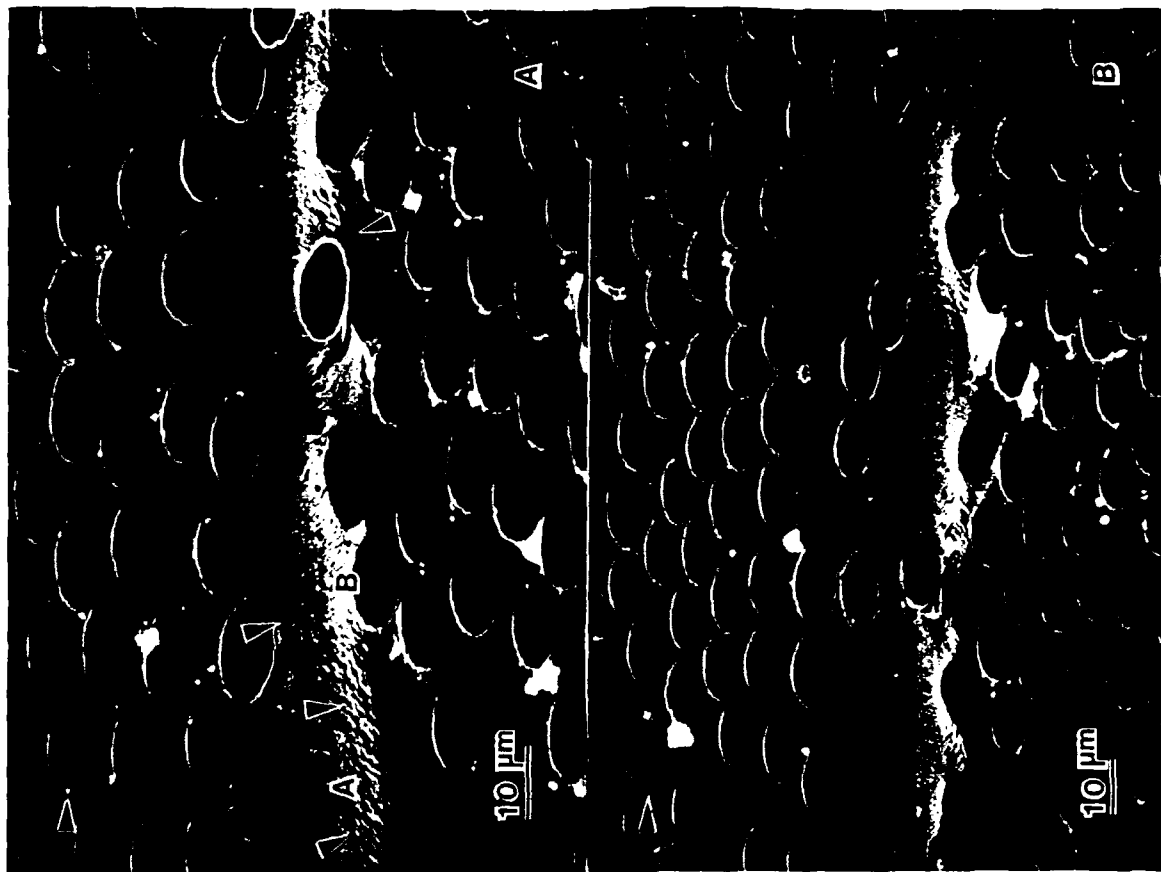

Figure 4.19 In-situ mode II delamination ahead of the crack tip of T2C145/F155 +-30 angle-ply showing the damage zone ahead of the crack tip
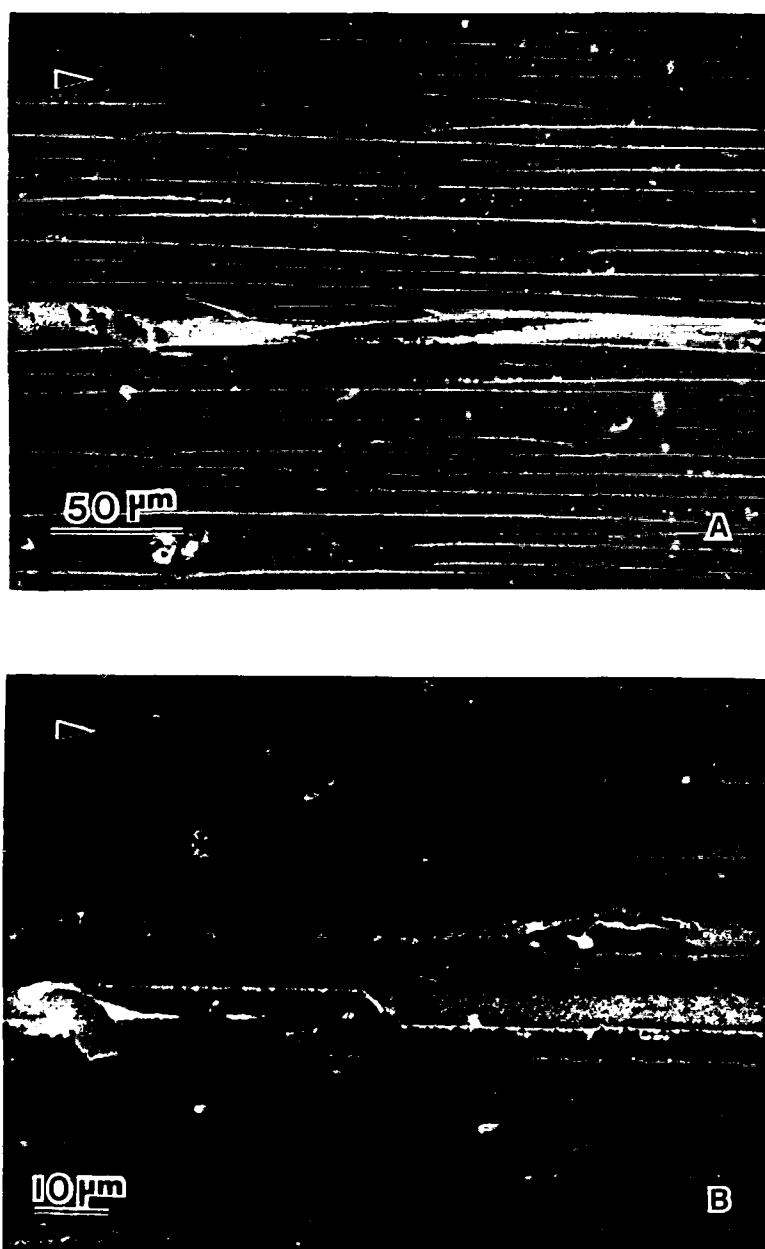
Figure 4.21 Insitu fractography of T2C145/F155 composite ahead of the crack tip during mode II delamination.

observed for the unidirectional case. However, the amount of resin deformation seems more uniform and to extend farther ahead of the crack tip than the multidirectional case.

4.3 Results of Crack Tip Strain Field Measurements

4.3.1 Neat Resin Crack Tip Strain Field

The deformation ahead of the crack tip of F155 neat resin under mode I loading is shown in Fig. 4.22a. Fig. 4.22b shows a three dimensional graph of the normal strain ϵ_{yy} distribution ahead of the crack tip. The maximum strain at the crack tip is in the order of 0.37 ± 0.015 The strain field is basically symmetric above and below the crack tip. As it can be seen in the contour map in Fig. 4.22c. the classical kidney shape is delineated. The size of the strain field can be seen to extend about 85 μm above and below the crack plane (y direction), and about 110 μm ahead of the crack tip (x direction).

The elongation of F155 measured in a tensile test is 5.2%, which is considerably smaller than the 37% measured at the tip of the crack of the CT specimen. Hibbs has also reported unexpectedly large normal strain levels ahead of the crack tip under mode I loading of 3501-6, a brittle resin [83]. He argues that a tensile test of a brittle resin will always fail at largest incipient flaw giving low nominal strain to failure, even though local strain at flow may be much larger. Thus, tensile tests will always result in an artificially low estimate of the materials true strain to failure. Therefore, the measurement of the local strain to failure at the crack tip gives a much more realistic estimate of a material capacity to deform prior to fracture. In addition, the gage length used in this study, approximately 10μm , is considerably smaller than the 2 inch gage length typically used in a tensile test. This will also affect the strain measurement at the crack tip where strain gradients are very steep.

Figure 4.23 shows the CT F155 specimen upon unloading, indicating most of the strain has been recovered (compare Fig. 4.22a and 4.23a). Therefore, very large viscoelastic strains are present at the crack tip. After subsequent annealing, essentially all the remaining strain was recovered, indicating that essentially all the crack tip strain that occurs prior to crack advance is viscoelastic.

The size of the "plastic zone" shown in Fig. 4.23 (nonlinear viscoelastic zone) is similar to the plastic zone shape predicted by Tuba [84], with the size approximately the same as well. The disagreement can be associated to the limits of the measuring accuracy of the strain field mapping technique, and the fact that it is uncertain if indeed the load level reached in Fig. 4.22 is the maximum load.

4.3.2 Mode II Delamination Strain Fields

Figure 4.24 shows a micrograph of the unidirectional AS4/3502 composite illustrating the failure zone or damage zone ahead of the crack tip sometime prior to mode II crack growth and the associated shear strain field γ_{zy} . The highly strained region is confined within the resin rich region at the midplane with microcracking defining the failure zone (some of the microcracking may be microcracking of the gold-palladium film used to minimize charging). The failure zone is approximately 180 μm long. Hibbs [83] has observed similar values of the failure zone size with another brittle composite,

(a)
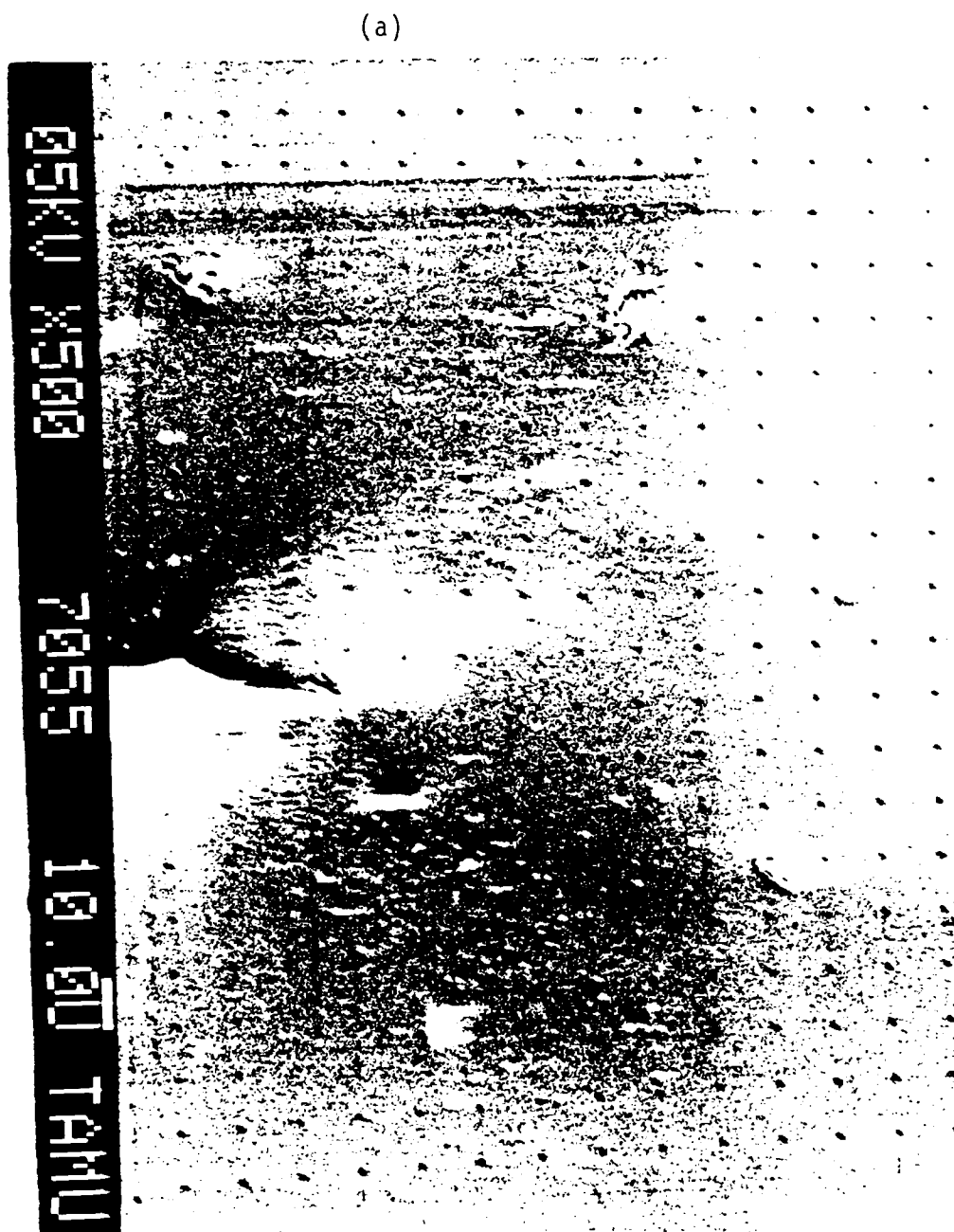
Figure 4.22 (a) mode I crack tip of F155 under the SEM during
fracture (b) Normal strain field in y direction
(c) contour plot of normal strain field

F155 EPOXY RESIN

(b)

MAX ε_{YY} = 0.37 ± 0.015

(c)
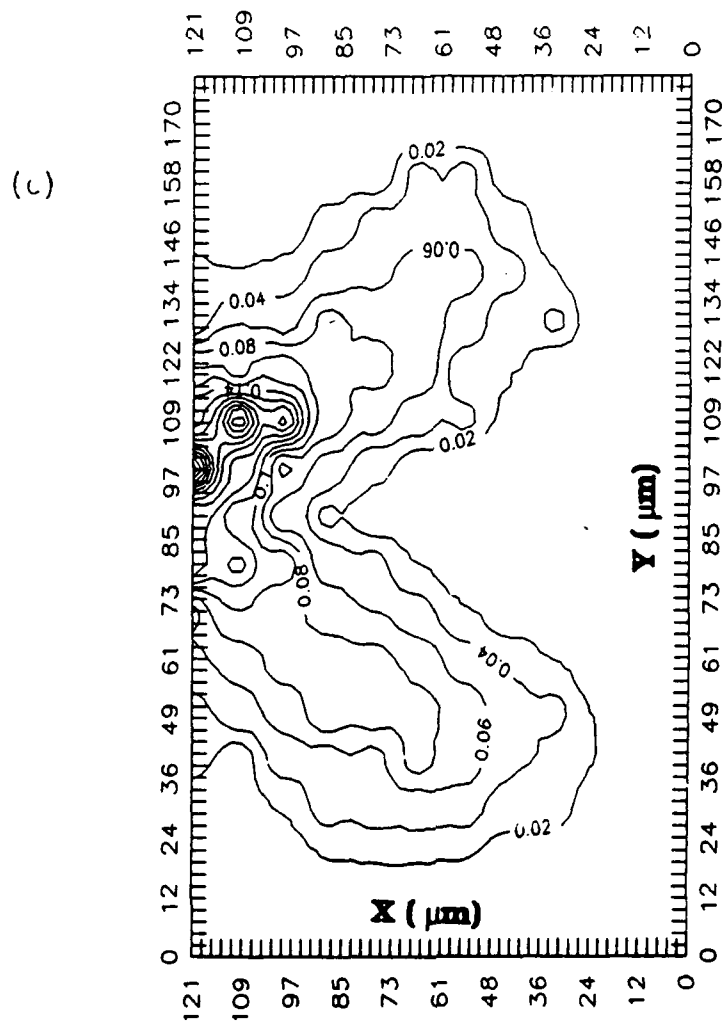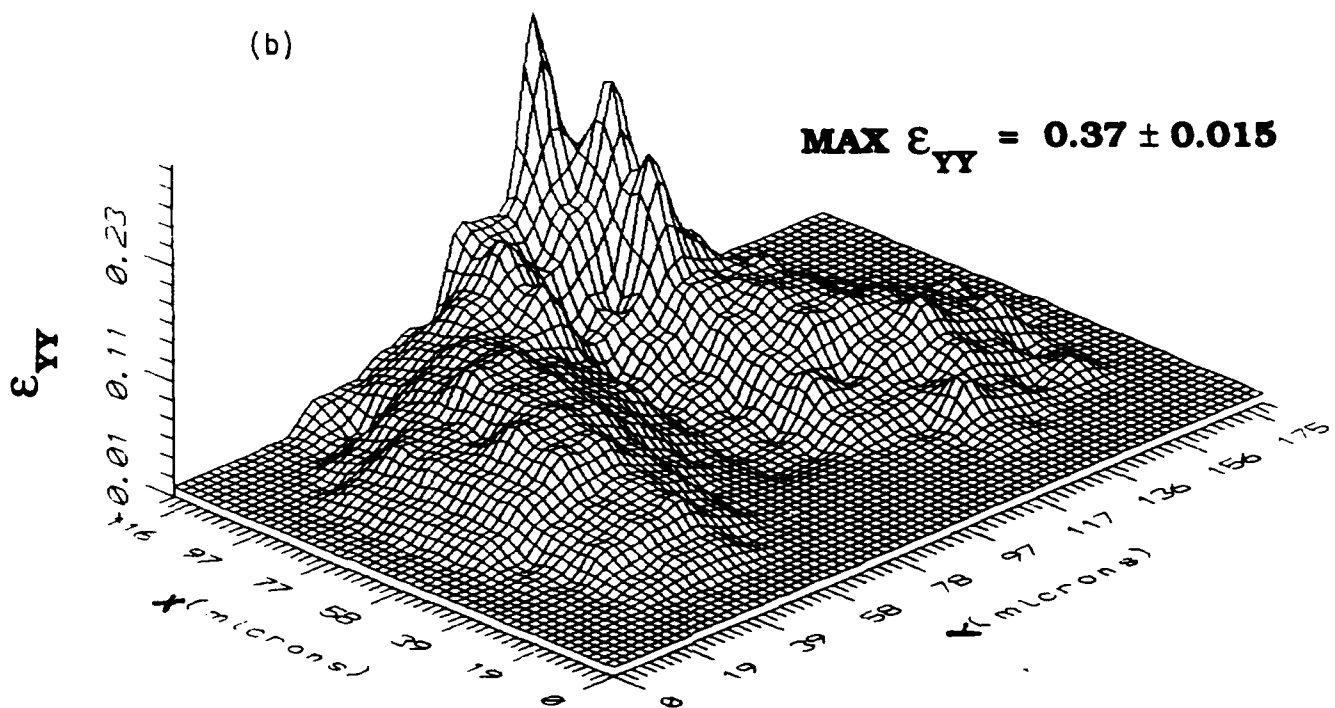
COUNTOUR PLOT

Figure 4.22
Continued

F155 EPOXY RESIN

AFTER UNLOADING

(a)

ε_{YY}

RESIDUAL ε_{YY} = 0.04 ±0.015

(b)

COUNTOUR PLOT

Figure 4.23 (a) Strain field of F155 after unloading
(b) Contour plot

AS4/3501-6. Definition of the exact location of the crack tip becomes difficult. The maximum shear strain is approximately 20° in the neighborhood of the crack tip. The measuring accuracy is approximately $\pm 5^o$ for this magnification. This low resolution is because of the large field of view that showed the extent of the damage zone. Corleto and Bradley [52] have noted that at the root of the hackles of this composite, large rotations are observed. Therefore, the γ_{xy} value of 20° affirms this observations. Also, this finding is in sharp contrast to the 1% elongation to failure reported from tensile tests of this resin [52]. However, this is not surprising since as discussed in the previous section, the F155 and 3501-6 resins (3501-6 is a similar resin as 3502) also showed significantly higher maximum crack tip strain prior to failure than the strain to failure measure from a tensile test.
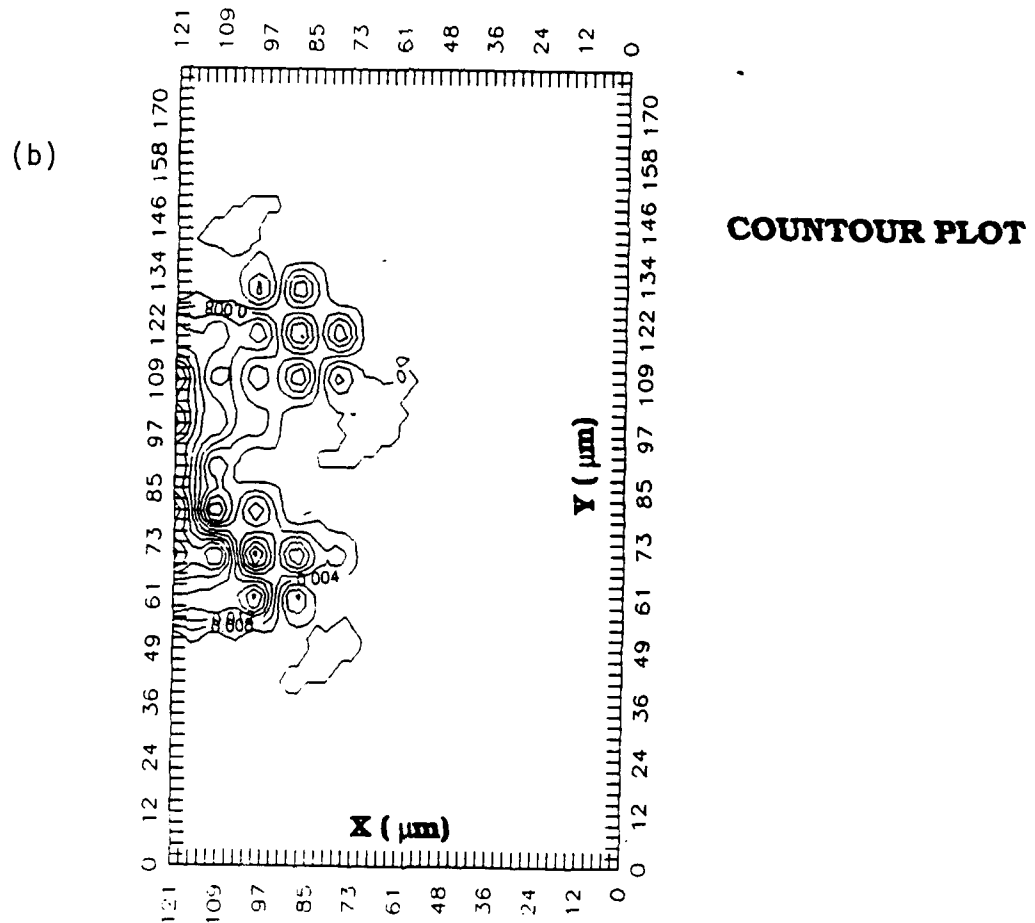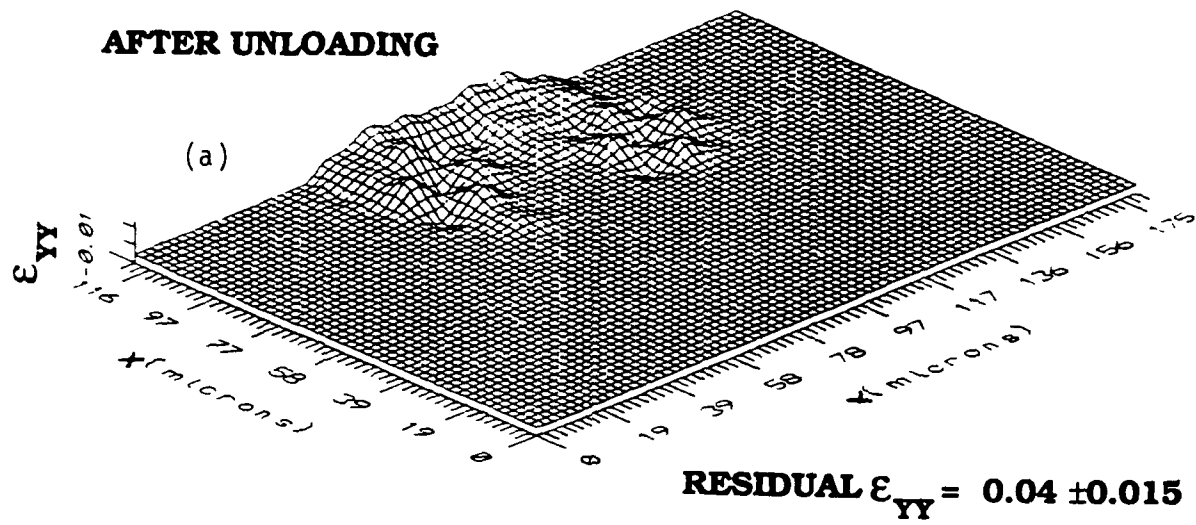
Because the failure zone is mostly defined by the formation of microcracks, the shear strains plotted in Fig 4.24 should be understood as an apparent (or pseudo) strains. That is, the strain is in a region of discontinuities and it represents displacement in a volume of material with microcracks. The displacements are not due to resin and/or fiber straining alone but include components resulting from microcracking.

Figure 4.25 shows the apparent normal strains ϵ_{xx} and ϵ_{yy} , and the shear strain γ_{xy} of region A indicated in Fig. 4.24 where hackles are in the process of rotation. The center region of this plot coincides with the crack plane where the hackles have been formed. Note how the value of ϵ_{xx} is practically negligible compared to ϵ_{yy} ; that is, in the order of 12%. γ_{xy} is approximately 16° . The measurement accuracy is $\pm 3\%$ for the normal strains, and $\pm 2^o$ for the shear strain. The improvement in accuracy was achieved by basically increasing the effective gauge length at which the measurements were made.

The strains measured are definitely surprisingly high. However, it should be kept in mind that they are apparent strains that reflect primarily displacements in the failure zone due to microcracking.

Figure 4.26 shows the mode II failure zone and corresponding shear strain field of T6T145/F185 unidirectional composite. A considerable amount of resin deformation and microcracking is observed. The failure zone is mostly contained in the resin rich region between plies, although microcracking and resin deformation are observed several fiber diameters away from it. Final hackle formation is not observed. This is consistent with the observations in [52] were extensive resin deformation overshadow hackle formation. The length of the failure zone is very long, and as previously reported [52], is greater than 1000 μm long. This damage zone is larger than the previous damage zones of less tough composites (Figs 4.21 and 4.24). In contrast to the strain field of AS4/3502, it does not drop off as fast ahead of the macroscopic crack. In fact, the strain seems to be approximately the same for a distance of at least 150 micron. This shear strain is approximately 50 ± 5° . The plot only included the highly deformed region in the resin rich region between plies (note how deformation is observed 2 to 4 fiber diameters away from the resin rich region between plies).

To have a better measure of the magnitude of the strains in the failure zone of T6T145/F185, strain measurements of region A indicated in the micrograph in Fig. 4.26 are presented in Fig. 4.27. ϵ_{xx} is seen to be in the order of $\pm 19\pm 3\%$. Note also

MODE II DELAMINATION
AS4/3502

Figure 4.24 Mode II delamination (a) damage zone ahead of the crack tip and (b) associated shear strain field of AS4/3502 (unidirectional)

MODE II DELAMINATION
AS4/3502

REGION A

Figure 4.25 Normal and shear strain of region A shown in Fig. 4.24

MODE II DELAMINATION
T6T145/F185
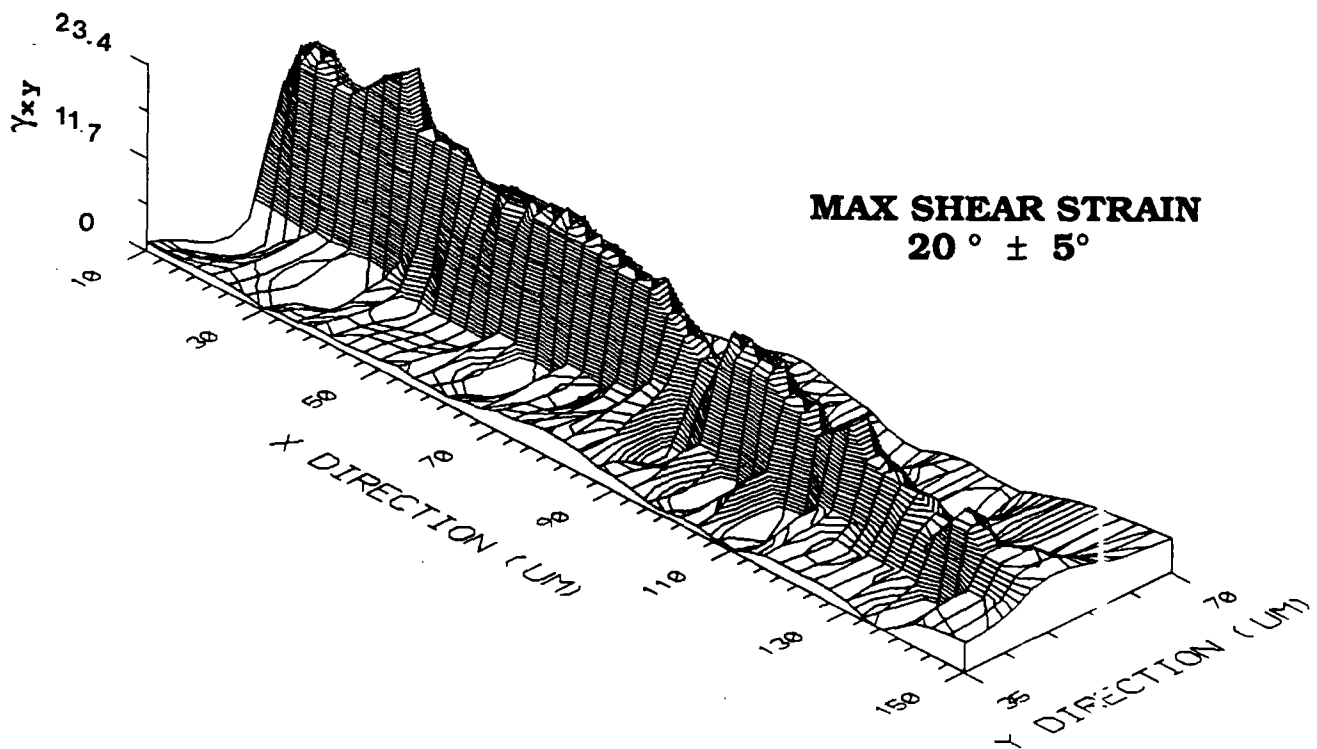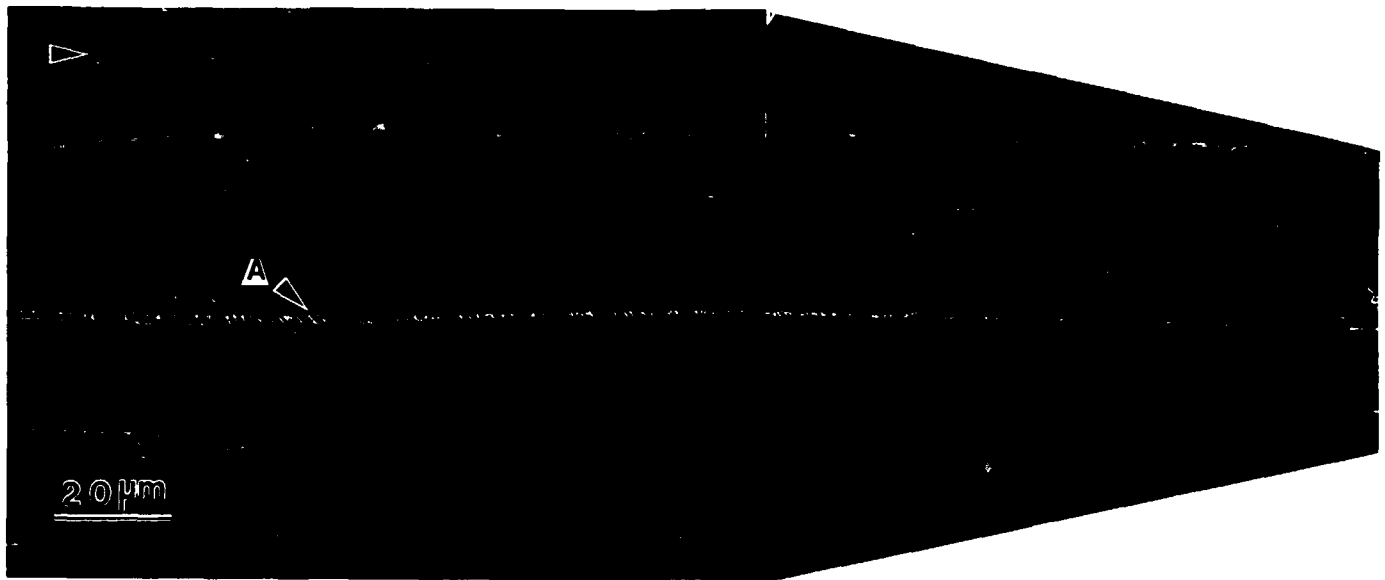

MAX SHEAR STRAIN
50 ° ± 5°

Figure 4.26 Mode II delamination (a) damage zone ahead of the crack tip
and (b) associated shear strain field of T6T145/F185
(unidrectional)
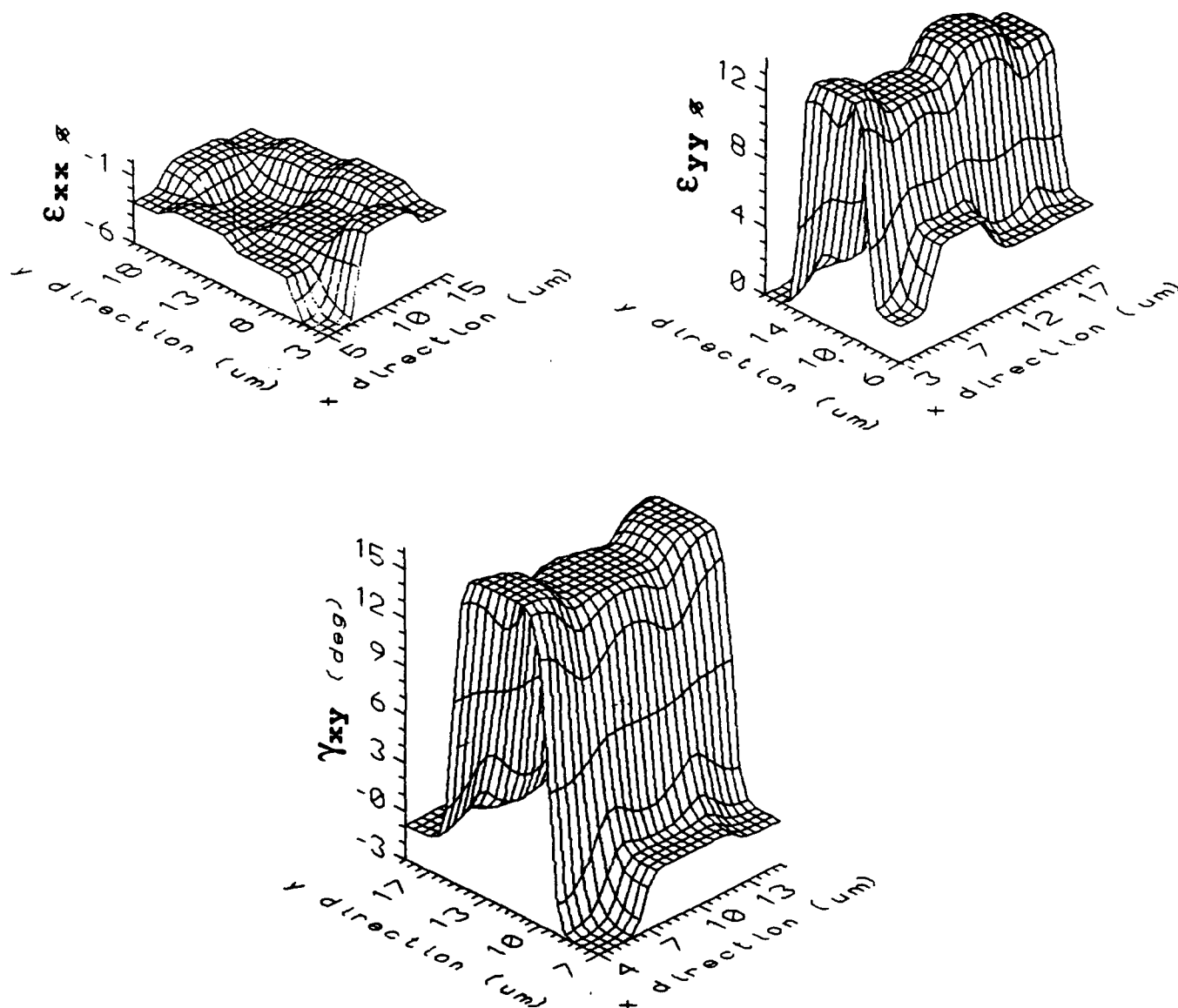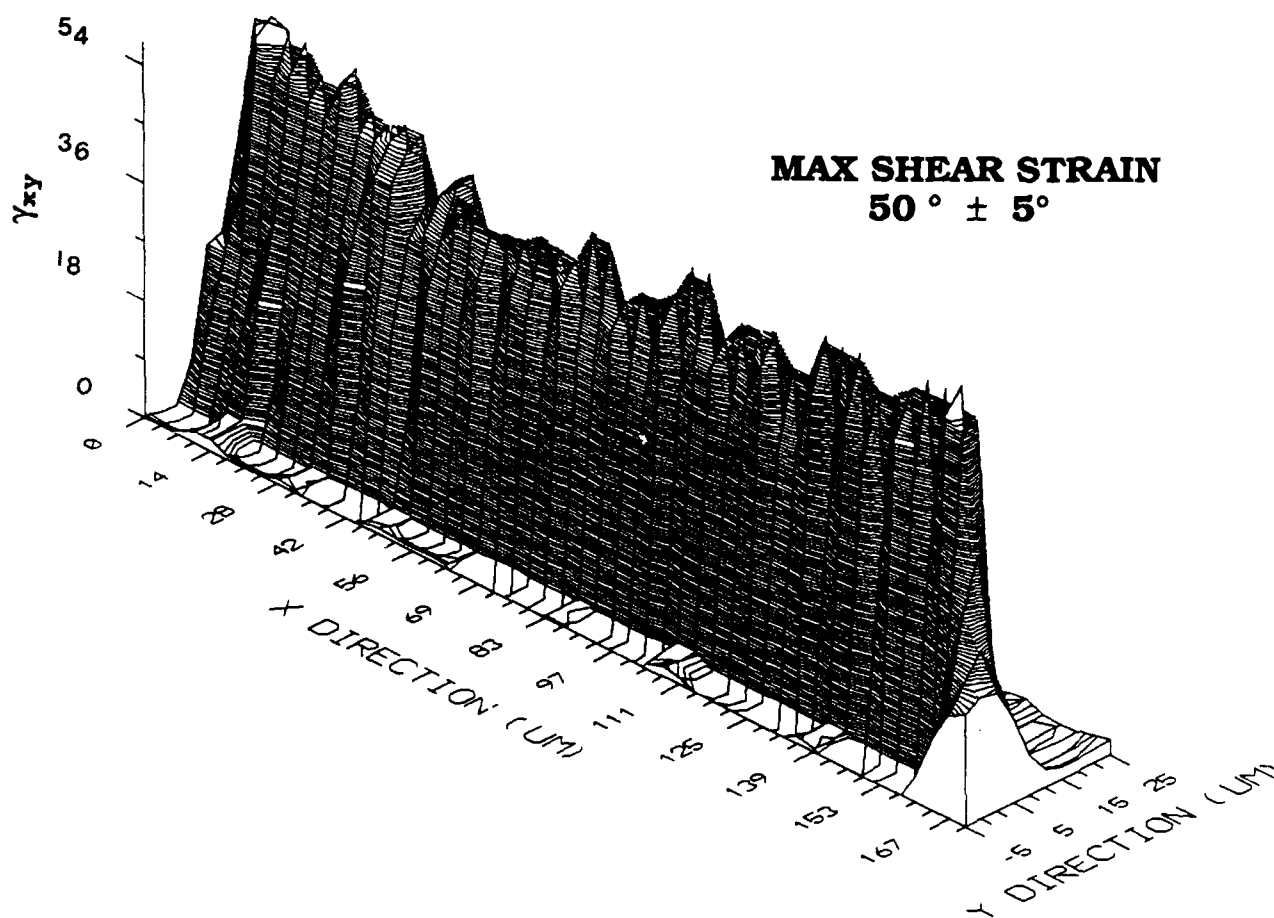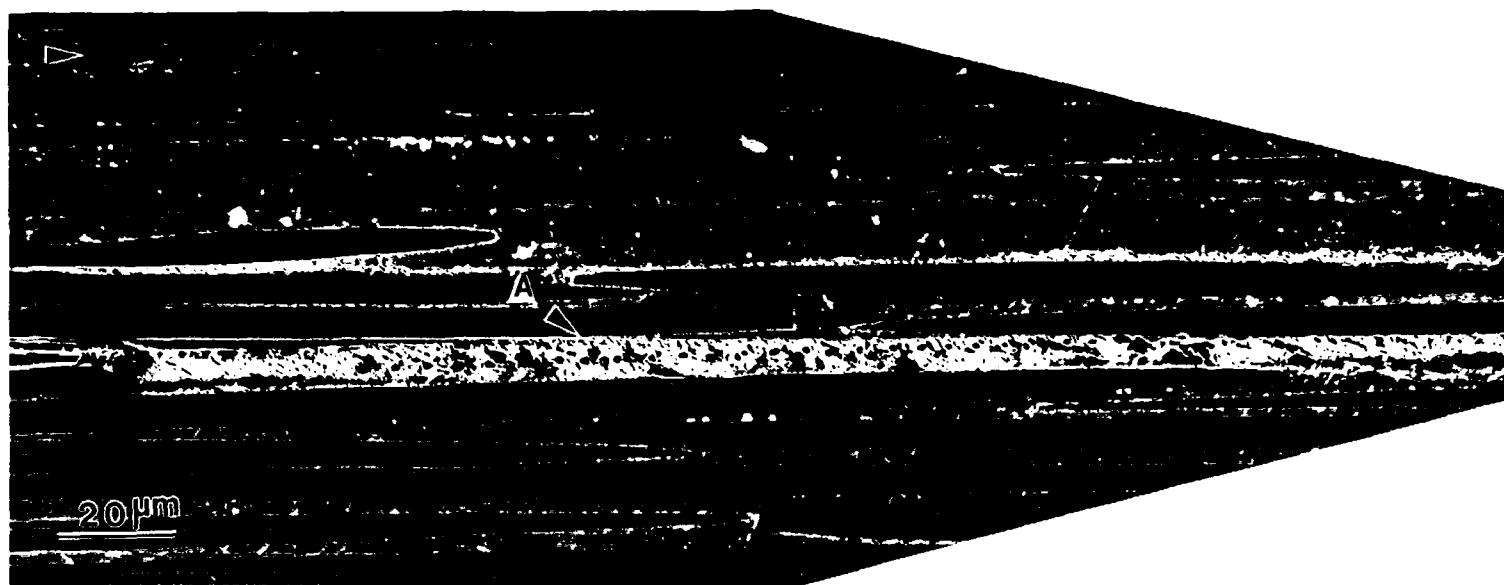
**MODE II DELAMINATION
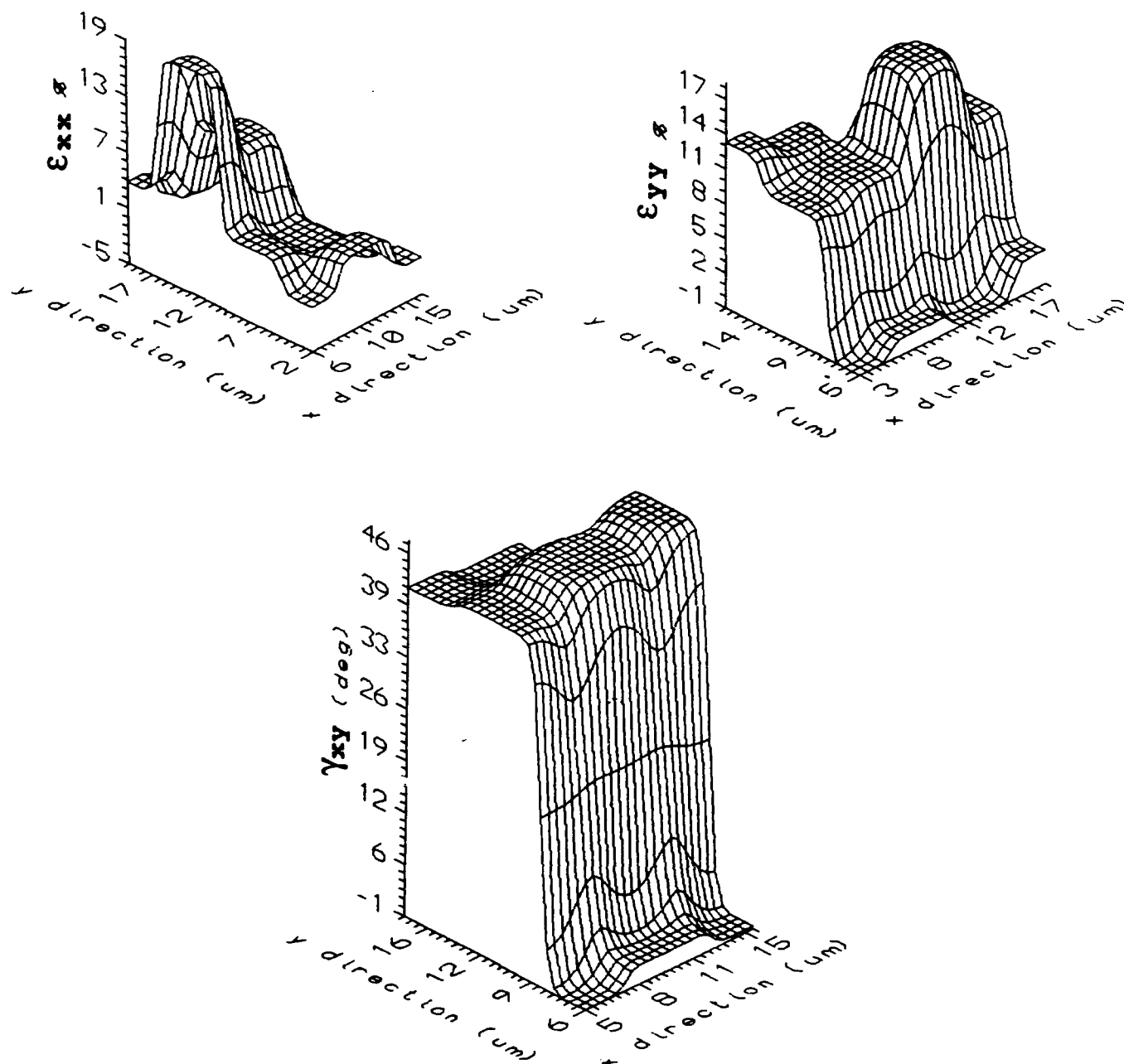T6T145/F185**

REGION A

Figure 4.27 Normal and shear strain of region A shown in Fig. 4.26

how heterogeneous is the strain field, being negligible where the fibers are but with a high degree of straining indicated in by the plastically deformed and microcracked region. In this case, the strain level measures not only the pseudo strain associated with microcracking but also a very significant component due to resin straining. This is expected since the F185 resin is much more ductile that the 3502 resin.

The apparent ϵ_{yy} is also high, in the order of 18± 3%, which is similar to that observed for ϵ_{xx} , although somewhat more uniform. With regard to γ_{xy} , it is considerably higher, in the order of 47± 2° . This seems surprisingly high if only the results of strain to failure from standard macroscopic tensile tests are considered. Strain to failure fo the F185 resin is reported to be 8% to 9% [52], although Chackachery [85] has reported 15% or greater values with failures occurring at incipient flaws. Therefore, since a tensile test provides a lower estimate of the strain to failure of resins, (it has been discussed already that even brittle resins show much higher tensile elongations from a mode I test than a macroscopic tensile test [52]), F185 should deform even more in this case.

As it can be seen for both composites, particularly for the brittle AS4/3502 composite, a considerable component of the strains measured are due to microcracking. However, it can be argued that as long as there is any load bearing capability in these microcrack regions (which seems to be the case), the composite is under an stress level that corresponds to the strain levels. A key question to address then is what are the constitutive properties in these damaged regions that relate these strains to corresponding stresses. This is particularly necessary in the development of analyses capable of predicting delamination fracture toughness. Possible approaches to determine the constitutive properties in these damage region could be by developing micromechanical models that include the formation of microcracks either implicitly in their effect on the constitutive properties, or explicitly in the model. Strain data as the one obtained in this investigation may be useful in the formulation and evaluation of such models. A microcrack density damage parameter as a function of normal and shear strains of a fiber reinforced composite has been proposed by Corleto and Bradley [86]. Their experimental assessment of this damage parameter indicates a linear relationship between growth of microcracks and normal and shear strains as shown in Fig. 4.28.

As it was found in Chapter 3, the toughness of T6T145/F185 was approximately 4 times that of AS4/3502. From the resutls of the damage zones and strain field of these composites, it is clearly evident that an increase in mode II delamination correlates well with an increase in damage zone size ahead of the crack tip and an increase in the critical crack tip strain level reached at fracture. The increased resistance is the result of an increased capability of the resin to deform, permitting load redistributions ahead of the crack tip. This process demands more energy to reach the critical strain at the crack tip for crack advance. The fibers also help with the load redistributions as well [87]. Further, due to the increase capabiltiy of tougher resins to deform, the critical strain at the crack tip for the composite increases as well.

It needs to be mentioned that the strain measurements shown depend on the thickness of the resin rich region between plies as all rotation occurs in the resin. Thus, to the extent that gage section includes fibers, real resin strain is underestimated.
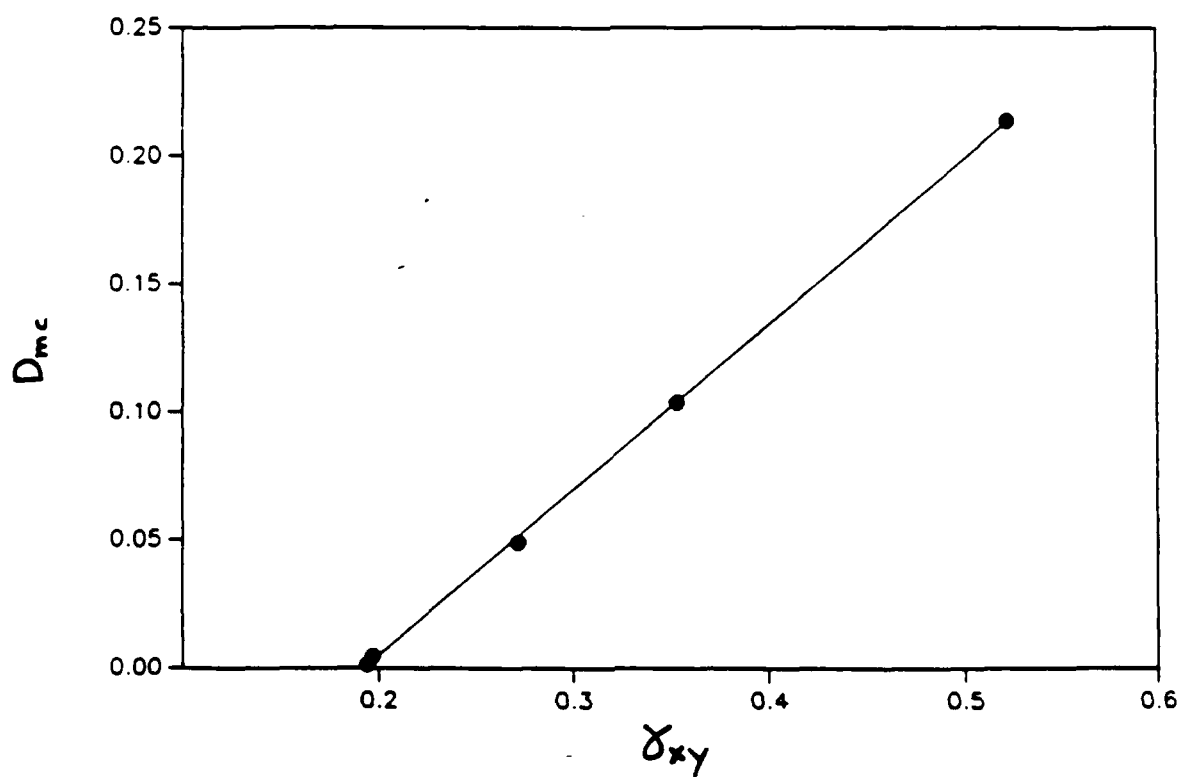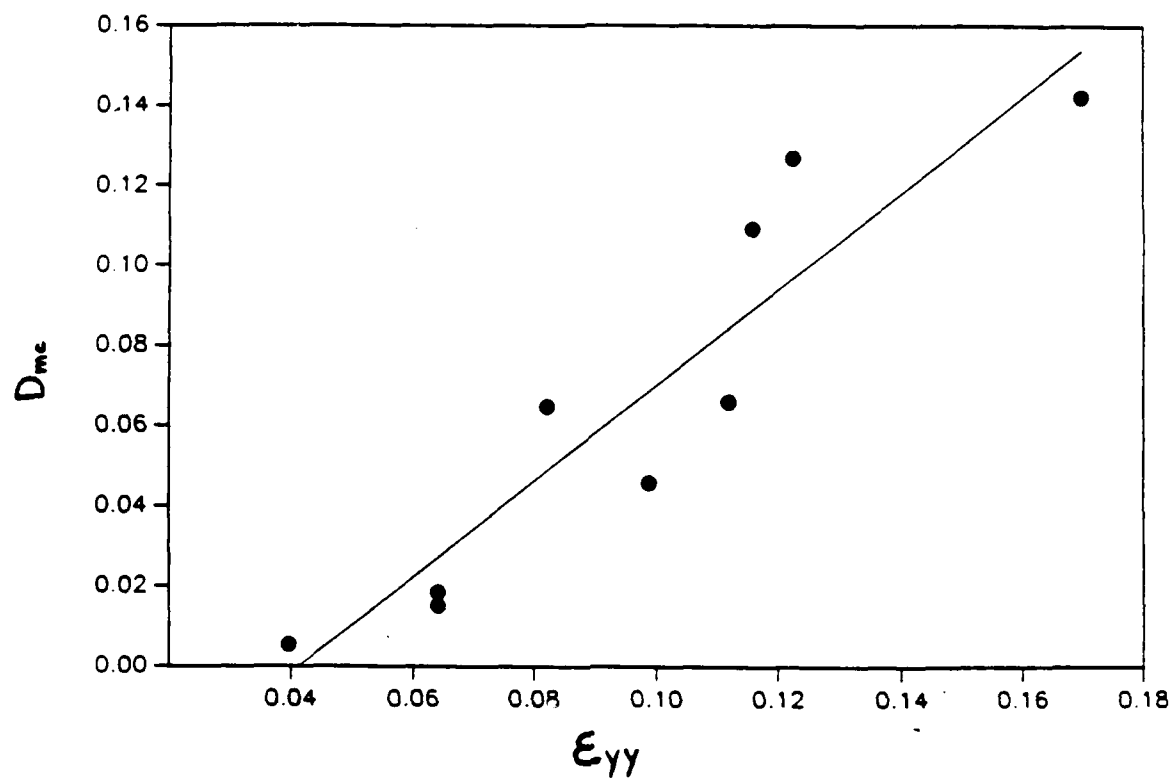
Figure 4.28 Damage parameter as a function of (a) normal strains and (b) shear strains.

Correlation of J_{II} with in-situ observations and strain measurements reveals the possibility of relating J_{II} with local parameters, namely the strain level at the crack tip and the size of the damage zone. Great similarity of the physics of mode II delamination with the Dugdale yield strip model of yielding in thin cracked metal sheets [88] indicates that idea that this model could be used to develop one for cracked orthotropic beams under mode II delamination. A relationship relating shear displacements at the crack tip, yield stress, crack length, and the length of the damage zone has already been developed using an edge dislocation theory model for isotropic cracked material undergoing mode II loading at the crack tip [89].

Further, steady state crack growth implies that there is a constant critical shear strain at the crack tip which is reached when the failure zone has also attained a critical value. This feature, together with a model relating J_{II} with local parameters, can be useful to define local stress parameters equivalent to yield stress in metals and polymers for the damage zone of the composite that would naturally include the effect of microcracking as well.

The other important task that would be valuable is the prediction of the damage/failure zone sizes and critical strains of the composite based on the properties of the fiber, resin, and very likely fiber/matrix interface properties. The strain measuring capabilities demonstrated would be very useful. Finally, successful developement of models like the ones outlined would provide a powerful tool to predict mode II delamination resistance of composites from the properties of the constituents.

In an attempt to have an indication for the strains that develop in an angle-ply delamination plane, normal and shear strains have been calculated from the dot map in the regions indicated in Fig. 4.19. In region A, the dot map from which the strains are calculated is contained within the resin rich region between plies and is shown in Fig. 4.29. The ϵ_{xx} strain field indicates compressive as well as tensile strains. However, they are much smaller compared to the ϵ_{yy} strains that have rapidly gone from -8$\pm$ 3% to 17$\pm$ 3%. The negative ϵ_{yy} is seen in the lower part of region A where the white corrugated lines are observed. The positive ϵ_{yy} strains are seen more in the upper part of region A where microcracking begins to form. Finally, the shear strain has reached a level of 29$\pm$ 2° and it is more uniform. It appears that the fibers tend to have a greater effect on the distribution of the normal strains than the shear strains.

The strains associated with region B are presented in Fig. 4.30. The strain distribution has changed dramatically for the normal strains. The shear strain has increased slighlty from that region A. In this case (Fig. 4.30), the effect of off-axis fibers on the strain field can be clearly seen. ϵ_{xx} has increased towards the positive direction indicating the stress intensity the fibers induce on ϵ_{xx} . On the other hand, the ϵ_{yy} strains have increased towards the negative side. This negative strain is somewhat surprising and seems to be due to the high heterogeneity the off-axis plies give to the crack front. However, due to the out-of-plane displacement in part of region B, these results need to be taken with caution.

The shear strain has been slightly increased as the fibers are approached. Apparently, the fibers shift the path where the maximum strain is developing towards areas where there is more resin and therefore allow deformation and microcracking to occur.

REGION A

T2C145/F155
(± 30°)
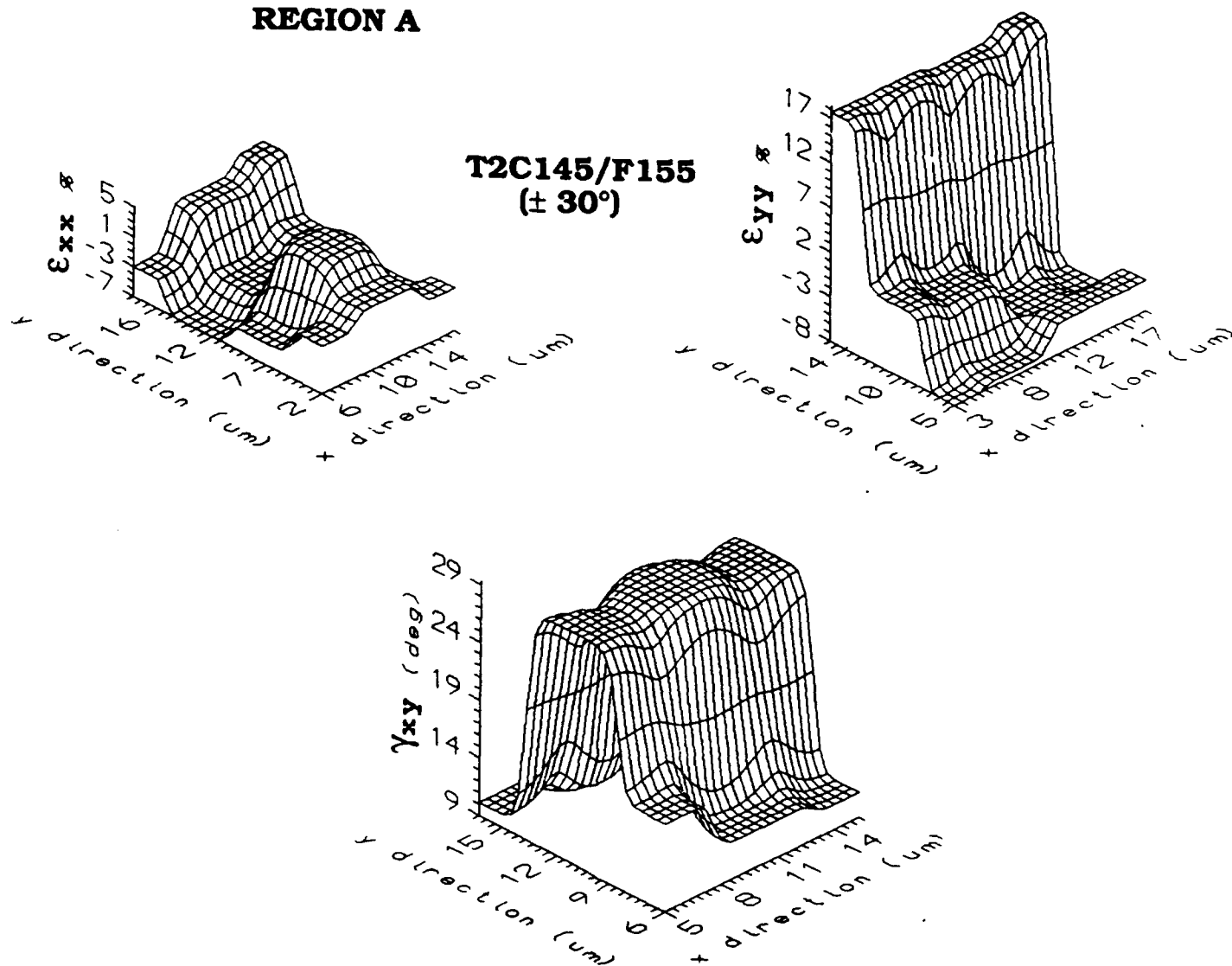
Figure 4.29   Normal and shear strain of region A shown in Fig. 4.20a
                of a +-30 angle-ply of T2C145/F155

MULTIDIRECTIONAL MODE II DELAMINATION

T2C145/F155
(±30°)

REGION B
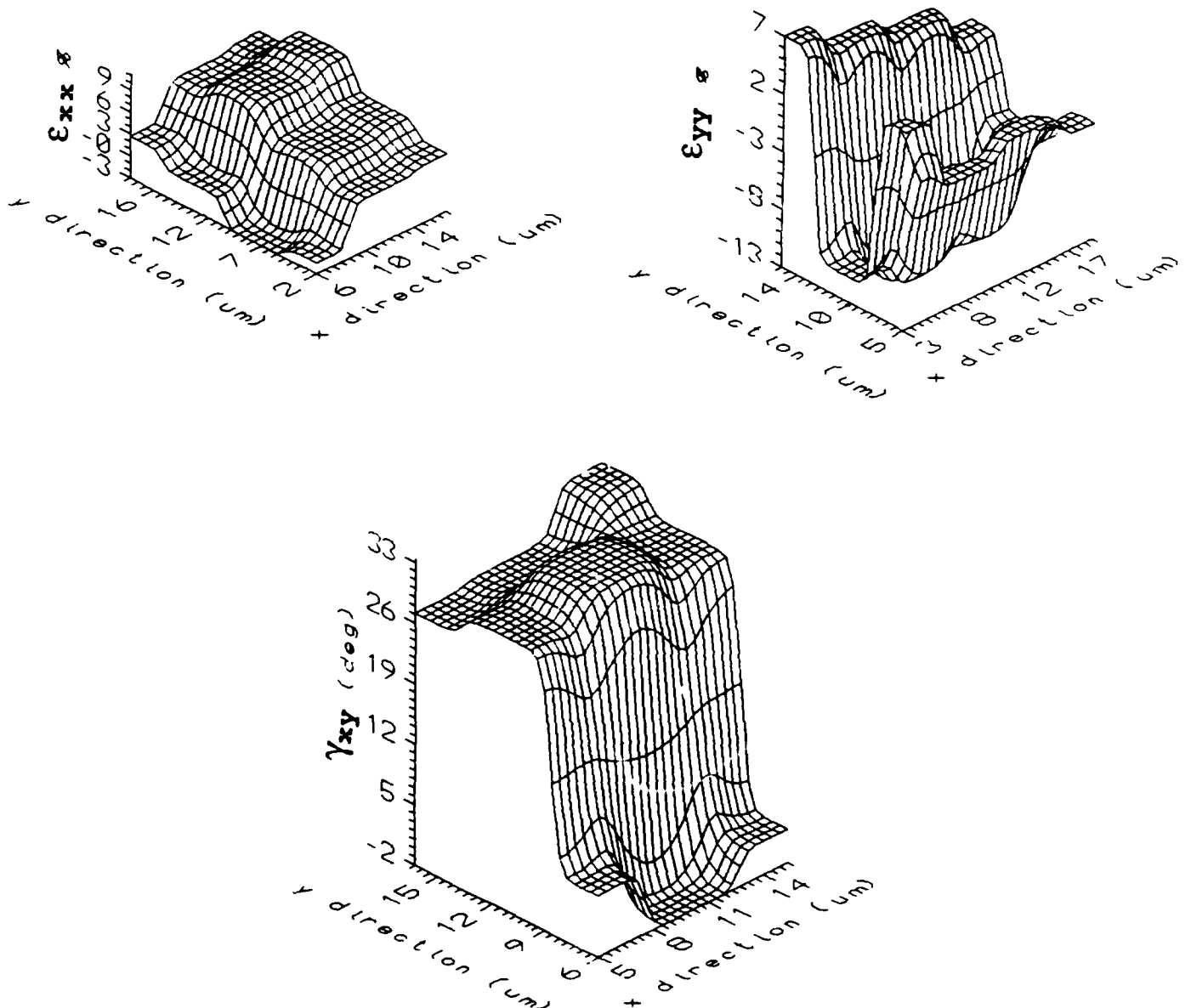
Figure 4.30 Normal and shear strain of region B shown in Fig. 4.20a of a +-30 angle-ply of T2C145/F155
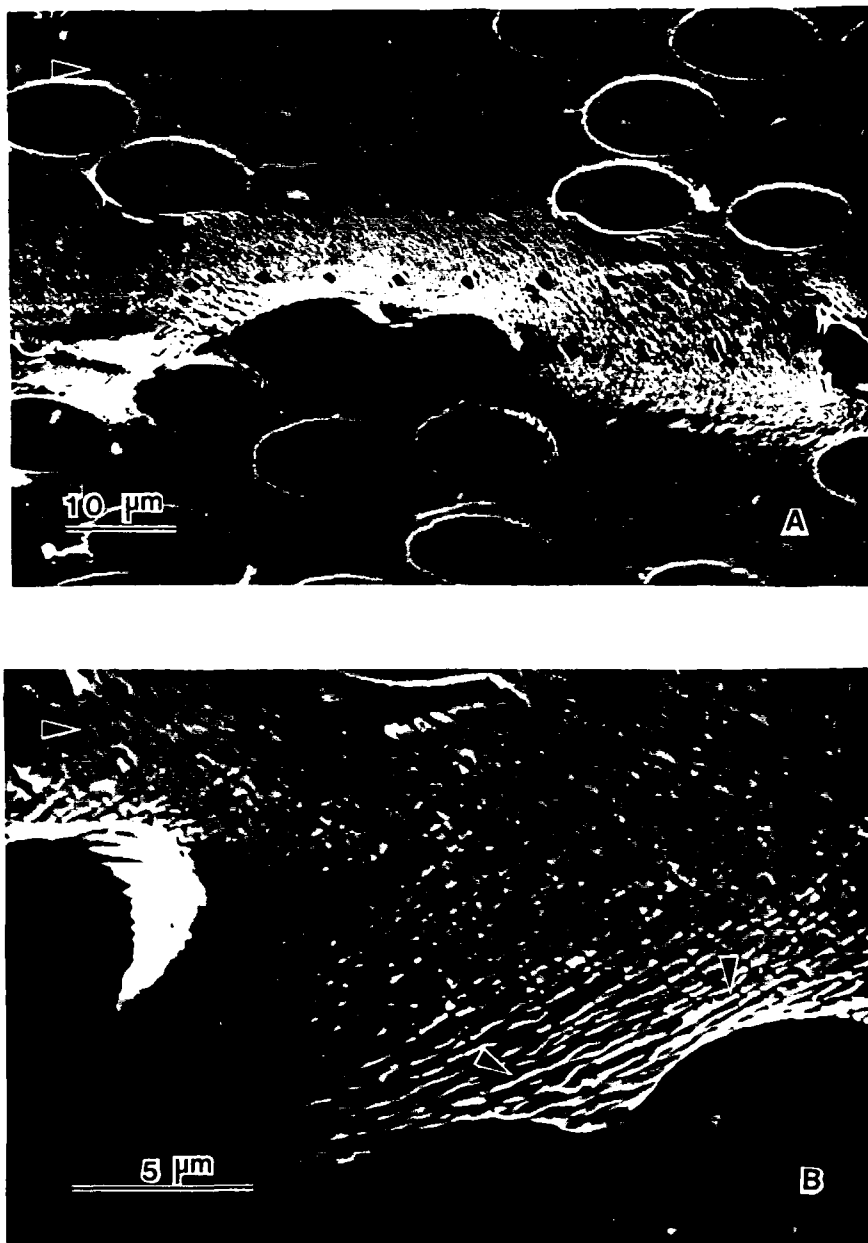
Figure 4.31   Fracture of a +-30 angle-ply in the SEM of T2C145/F155

The fibers are very stiff and will experience little to no deformation. In this shifting process forced by the fibers, normal strain are generated. This process will occur as long as the crack is within the resin rich region between plies.

Physical evidence that corroborates the opening and compressive strains that develop in the angle-ply delamination plane is shown Fig. 4.31. Ideally, under simple shear loading, the microcracks would form in the direction of the principal normal opening strain. Therefore, they should form oriented at 45° with respect to the plane of crack growth (x direction). However, the micrographs in Fig. 4.31 show the microcracks forming at variable orientations including nearly 90° , 45° , and 0° with respect to the plane of crack growth. This phenomenon indicates that normal stresses are developing. Basically, microcrack formation at angles greater than 45° but less or equal to 90° indicates a normal ϵ_{yy} strain component. If development is at 90° , the region of microcrack formation is only experiencing a normal ϵ_{yy} strain. Conversely, development at angles less than 45° but greater or equal to 0° provide evidence of ϵ_{xx} strains developing with only ϵ_{xx} acting when the microcracks form perpendicular to the crack growth plane (0°). The white corrugates lines indicate the direction of the principal compressive normal strains and are always perpendicualar to the principal opening normal strain.

SUMMARY

The mode I and mode II delamination of multi-directional composite laminates have been studied using a J-integral approach. The analytical and experimental formalism to apply the J-integral to delamination have been developed and verified on three different composite material systems with matrix toughness varying from very brittle to very tough. Large deflections and rotations, mid-plane straining and distributed damage are taken into account in the methodology. The experimental conditions under which a path independent J may be measured have been established. The effect of several variables including specimen geometry, stacking sequence, and material constitutive behavior on the J -Moment-at-the-crack-tip relationship have been determined.

Multidirectional composite laminates are both more susceptible to far field damage in the off-axis plies and less stiff that unidirectional laminates. These two factors cause a greater tendency to geometric and material nonlinearity in delamination testing. The use of a traditional G approach to characterize fracture behavior of such laminates gives artificially high indications of the delamination resistance. However, the use of the J approach developed in this research program satisfies in general the requirements of geometry independence. If the plies bounding the delamination plane are unidirectional, the mode I and mode II delamination resistance as measured by J are the same as that measured for delamination of a unidirectional composite laminate. The use of G for such a comparison gives the erroneous indication that delamination resistance for a multidirectional composite is greater than for a unidirectional composite.

Delamination of multidirectional laminates with off axis plies bounding the initial delamination starter crack always resulted in the growth of the delamination crack into th adjacent ply. For mode I delamination, the crack would move into the ply several fiber diameters and then grow at the same elevation thereafter. For mode II delamination, the crack tended to migrate further from the original delamination plane as it grew along the length of the specimen. For both mode I and mode II delamination, the critical J for crack growth was greater for multidirectional (delamination planes) laminates than for unidirectional laminates. In the case of mode I delamination, the delamination resistance did not seem to vary with fiber orientation whereas it monotonically increased with increasing fiber orientation for the mode II case. The use of a mode I induced precrack gave artificially low initial values for mode II delamination crack growth which soon increased to a steady-state value. Since fiber bridging does not play a significant role in mode II delamination, the R-curve like behavior is thought to be an artifact of the use of a mode I crack to begin mode II delamination, rather than representing some meaningful description of material behavior.

Strain field around the tip of growing cracks for neat resin, mode I delamination and mode II delamination have been made. The critical strain to failure at the crack tip is typically 3x to 10x the elongation observed in a tensile test. This indicates that tensile tests on brittle systems are truncated by propagation of incipient flaws. On ductile systems, tensile tests must have some significant degree of strain localization

prior to fracture. The large crack tip strain fields measured in brittle systems are exaggerated in part by the inclusion in the displacement, measures of microcracking induced displacements in addition to resin strain. A highly complex strain state has been measured for mode II delamination of multidirectional laminates.

REFERENCES

[1] Sela, N., and Ishai, O. **Comp.**, Vol. 20, No. 5, September 1989, pp. 423-435.

[2] Donaldson, S. L. **Proc. of 6th ICCM & 2nd ECCM**, July 1987, Vol. 3 London, United Kingdom, pp.3.274-3.283

[3] Ling, C. L., Mall, S., Donaldson, S. L. **Proc. of 4th Tech. Conf. of ASC**, October 1989, Blacksburg, Virginia, pp. 267-276

[4] Becht, G., and Gillespie, Jr, J. W. **Proc. of 2nd Tech. Conf. of ASC**, September 1987, Newark, Delaware, pp.9-18.

[5] Lamborn, M. J., "Deformation and Delamination of Inelastic Laminates Under Tensile and Torsional Loading". PhD. Dissertation, Civil Engineering, Texas A&M University (1989)

[6] Donaldson, S. L., "Mode III Interlaminar Fracture Characterization of Composite Materials". Master of Science Thesis, University of Dayton (1987)

[7] Ilcewicz, L. B., Keary, P. E., Trostle, J., "Interlaminar Fracture Toughness Testing of Composite Mode I and Mode II DCB Specimens". Boeing Commercial Airplane Company. Advanced Composites Development Program. Seattle, Washington

[8] O'Brien, T. K., Murri, G. B., Salpekar, S. A. **NASA Technical Memorandum 89157. USAAVSCOM Technical Memorandum 87-B-9**. NASA Langley Reseach Center, Hampton, Virginia 23665.

[9] Chapman, T. J., Smiley, A. J., and Pipes, R. B. **Proc. of 6th ICCM & 2nd ECCM**, Vol. 3, July 1987, London, United Kingdom, pp.3.295-3.304.

[10] Kenig, S., Moshonov, A., Shucrum, A., and Marom, G. **Int. J. of Adhesion and Adhesives**, Vol. 9, No. 1 (1989), pp.38-45

[11] Takeda, N., Tohdoh, M., and Takahashi, K. **Proc. of 4th Japan-U.S. Conference on Composite Materials**, Washington, Distric of Columbia, June 1988, pp.331-338.

[12] Huston, D. L., Moulton, R. J., Johnston, N. J., and Bascom, W. D., **ASTM STP 937**, (1987), pp. 74-94.

[13] Johnson, W.S., and Mangal G. **ASTM STP 937**, (1987), pp.295-315.

[14] Bradley, W. L., and Jordan, W. M. **Proc. of International Symposium on Composite Materials and Structures**, June 1986, Beijing, China, pp.445-450.

[15] Prel, V. J., Davies, P., Benzeggah, M. L., and de Charentenay, F. X. **ASTM STP 1012**, (1989), pp.251-269.

[16] Marom, G., Roman, I., Harel H., and Rosensaft, M. **Proc. of 6th ICCM and 2nd ECCM**, Vol. 3, July 1987, United Kingdom, pp.3.265-3.273.

[17] Lawrence, T. D., Rich, M. J., Shekhar, S. **Proc. of 3rd Tech. Conf. of ASC**, September 1988, Seattle, Washington, pp.217-222.

[18] Schwartz, H. S., Hartness, J. T., **ASTM STP 937**, (1987), pp.150-178.

[19] Jordan, W. M. **Proc. of 3rd Tech. Conf. of ASC**, September 1988, Seattle, Washington, pp.195-504.

[20] Martin, R. H., **Proc. of 3rd Tech. Conf. of ASC**, September 1988, Seattle, Washington, pp.688-700.

[21] Marom, G., Roman, I., Harel, H., Rosensaft, M., Kenig, S., and Moshonov, A., **Int. J. of Adhesion and Adhesives**, Vol. 8, (1988), pp.85-91.

[22] Goetz, D. P., "Determination of the Mode I Delamination Fracture Toughness of Multidirectional Composite Laminates". PhD. Dissertation, Texas A&M University, (1988).

[23] Jordan, W. M., and Bradley, W. L., **ASTM STP 937**, (1987), pp.74-94.

[24] Kanninen, M. F., Popelar, C. H., **Advance Fracture Mechanics**, Oxford UP (1985).

[25] Griffith, A. A., **Philosophical Transactions of the Royal Society**, A221, pp. 163-198, (1920).

[26] Jordan, W. M. "The effect of Resin Toguhness on the Delamination Fracture Behavior of Graphite/Epoxy Composites", Ph.D. Dissertation, Interdisciplinary Engineering, Texas A&M University (DEC. 1985).

[27] Tirosh, J., Mast, P, Becubien, L, Mulville, D, Sutton, S., and Wolock, I, **J. of Applied Mech.** 47 (1980) pp. 563-569.

[28] Kim, H. C., Yoon, K. J., Pickering, R., and Sherwood, P.J. **J. of Mater. Sci.** 20 (1985) pp. 3967-3975

[29] Agarwal, B. D, Patro, B .S. and Kumar, P, **Experimental Frac. Mech.** 19 (1984) pp. 675-684

[30] Keary, P. E., Ilcewicz, L. B., Shaar, C, and Trostle, **J. of Compos. Mater.** 19 (1985) pp. 154-177

[31] Newaz, G. M, **J. of Compos. Mater.** 19 (1985) pp. 276-286

[32] Carling, M. J., and Williams, J. G. in **Proc of 6th ICCM and 2nd ECCM**, ed. F. L. Matthews, N.C.R. Buskell, J. M. Hodgkinson and J. Morton, Elsevier Applied Science, London (1987) pp. 3.317-3.326.

[33] Tirosh, J. **J. of Applied Mechanics** 40 (1973) pp. 785-790

[34] Schapery, R. A. **Polymer Engineering and Science.** 27 (1987), pp.63-76.

[35] Eshelby, J. D. **Solid State Physics**, Vol. 3, (1956), pp.79-141.

[36] Rice, J. R. **J. of Applied Mechanics**, 35 (1968), pp.379-386.

[37] Schapery, R. A. **Int. J. of Fracture**, 25 (1984), pp. 195-223

[38] Bascom, W. D., Bullman, G. W., Hunston, D. L, and Jensen, R. M., in **Technology Vectors: Proceedings of the 29th National SAMPE Symposium and EXhibition**, Society of the Advancement of Material and Process Engineering, Covine, CA (1984) pp. 970-978.

[39] Guedra, D., Lang, D., Rouchon, J., Marais, C., and Sigety, P., in **Proc. of 6th ICCM and 2nd ECCM**, ed. F. L. Matthews, N. C. R. Buskell, J. M. Hodgkinson and J. Morton, Elsevier Applied Science, London (1987) pp.3.346-3.357

[40] Arcan, M. Hashin, Z., and Voloshin, A, **Experimental Mechanics** 18 (1978) 141-146.

[41] Turf, R. A. and Pipes, R. B., **J. of Compos. Mater.** 16 (1982) pp.386-394.

[42] Hashemi, S., Kinloch, A. J., and Williams, J. G., in **Proc. of 6th ICCM and 2nd ECCM**, ed. F. L. Matthews, N. C. R. Buskell, J. M. Hodgkinson and J. Morton, Elsevier Applied Science, London (1987) pp. 3.254-3.264.

[43] Wang, S, S., and Mandel, J. F. **NASA Technical Report** NASA-CR-135248 (1977).

[44] Vanderkeley, P. S., "Mode I-Mode II Delamination Fracture Toughness of a Unidirectional Graphite/Epoxy Composite", M. S. Thesis, Mechanical Engineering, Texas A&M University (Dec. 1981).

[45] O'Brien, T.K., Johnston, N. J.., Morris, D. H. and Simonds, R. A., **SAMPE Journal** 18 (1982) pp. 8-15.

[46] Whitney, J. M, Knight, M., in **Proc. of 6th ICCM and 2nd ECCM**, ed. F. L. Matthews, N. C. R. Buskell, J. M. Hodgkinson and J. Morton, Elsevier Applied Science, London (1987) pp. 3.358-3.367

[47] Carlsson, L. A., Gillespie, J. W., and Pipes, R. B., "On the Analysis and Design of the End-Notched Flexure (ENF) Test for Mode II Testing". Center for Composite Materials, College of Engineering, Univerisity of Delaware, Newark, Delaware

[48] Maikuma, H., Gillespie, J. W., Whitney, J. M., **J. of Compos. Mater.** 23 (1989) pp. 756-786.

[49] Carlsson, L. A., Gillespie, J. W., Trethewey, B. R., **J. of Reinforced Plastics and Composites** 5 July (1986) pp. 170-187.

[50] O'Brien, T. K., Murri, G. B., Salpekar, s. A., **ASTM STP 1012** (1989) pp. 222-250.

[51] Russell, A. J., and Street, K. N.m, **ASTM STP 937** (1087), pp. 275-294

[52] Corleto, C. R., and Bradley, W. L., **ASTM STP 1012** (1989) pp. 251-269.

[53] Hashemi, S., Kinloch, A. J., and Williams, J. G., "The Analysis of Interlaminar Fracture in Uniaxial Fibre Polymer Composites". Mechanical Engineering Department, Imperial College, London, UK.

[54] Hashemi, S., Kinloch, A. J. and Williams, J. G., in **Proc. of 6th ICCM and 2nd ECCM**, ed. F. L. Matthews, N. C. R. Buskell, J. M. Hodgkinson and J. Morton, Elsevier Applied Science, London (1987) pp. 3.254-3.264

[55] Whitney, J. M., Gillespie, J. W., Carlsson, L. A., in **Proc. of 2nd Tech. Conf. of ASC**, (1987) Newark, Delaware, pp. 291-398.

[56] Whitney, J. M., Browning, C. E. and Hoogsteden, W., **J. of Reinforced Plastics and Composites** 1 (1982) 297-313.

[57] Hine, P. J., Brew, B., Duckett, R. A., and Ward, I. M., in **Proc. of 6th ICCM and 2nd ECCM**, ed. F. L. Matthews, N. C. R. Buskell, J. M. Hodgkinson and J. Morton, Elsevier Applied Science, London (1987) pp. 3.397-3.404.

[58] Devitt, D. F., Schapery, R. A., and Bradley, w. L., **J. of Compos. Mater.** 14 (1980) 270-285.

[59] Williams, J. G., **J. of Compos. Mater.** 21 (1987) pp. 330-341.

[60] Wang, S. S., Suemascu, H. and Zahlan, N. M. **J. of Compos. Mater.** 18 (1984) pp. 574-594

[61] Hibbs, M. F., Tse, M. K., and Bradley, W. L., **ASTM STP 937** (1987) pp. 115-130.

[62] Begley, J. A., and Landes, J. D., **ASTM STP 514** (1972) pp. 24.

[63] Landes, J. D., and Begley, J. A., in **ASTM STP 514** (1972) p. 1.

[64] Hunston, D. L., Moulton, R. J., Johnston, N. J. and Bascom, W. D., **ASTM STP 937** (1987) pp. 74-94.

[65] Russel, A. J. and Street, K. N., in **Progress in Science and Engineering of Composites**, ed. T. Hayashi, K. Kawata and s. Umekawa, 4th ICCM, Japan Society for Composite Materials, Tokyo (1982) pp. 279-286.

[66] Chai, H. **Composites** 15 (1984) pp. 277-290.

[67] Nicholls, d. J. and Gallagher, J. P., **J. of Reinforced Plastics and Composites** 2 (1983) pp. 2-17.

[68] Marom, G., Roman, I, Harel, H., Rosensaft, M., Kenig, S., Moshonow, M., **Proc. of 6th ICCM and 2nd ECCM**, ed. F. L. Matthews, N. C. R. Buskell, J. M. Hodgkinson and J. Morton, Elsevier Applied Science, London (1987) pp. 3.265-3.273.

[69] Schapery, R. A., Jordan, W. M., and Goetz, D. P., in **Proc. of the Int. Sympos. on Compos. Mater and Struc.** ed T. T. Loo and C. T. Sun, Technomic Publishing, Lancaster, PA (1986) pp. 543-549.

[70] Mittelman, A., Harel, H., Roman, I., Marom, G., **J. of Material Science Letters**, 4 (1985) pp. 1361-1363.

[71] Bradley, W. L., and Corleto, C. R., "The Significance of Hackles in the Failure Analysis of Graphite/Epoxy Composite Materials". A final report, Mechanical Ebngineering Division of the Texas Engineering Experiment Station, Texas A&M University, (1985).

[72] Bradley, W. L. , and Hibbs, M. F., Annual Report, AFOSR Grant No. 84-0064, Texas A&M University, (1986).

[73] Lankford, J., Davidson, D. ., and Williams, D. R., **Experimental Mechanics**, 20 (1980) pp. 134-139.

[74] Hibbs, M. F., Bradley, W. L., and Burghart, R., "Crack Tip Strain Field Measurements Determined In-situ in Scanning Electron Microscope for Mode I Crack Extension in a Polymeric Material", to be submitted to **Experimental Mechanics**.

[75] Corleto, C. R. "Mode II Delamination Fracture Characterization of Fiber Reinforced Composite Materials", A Ph.D. Dissertation, Mechanical Engineering, Texas A&M Univeristy (1990)

[76] Davidson, B. D., and Schapery, R. A., **J. of Compos. Mater.** 22 (1988) pp. 640-656.

[77] Frassine, R. Texas A&M Mechanics and Materials Center Report MM-9045-88-12 (1988)

[78] Johnson, W. S., Mangalgiri, P. D., NASA Technical Memorandum 87716 (1986) pp. 1-19.

[79] Bradley, W. L., Corleto, C. R., Goetz, D. P., Texas A&M Mechanics and Materials Center Report MM-5021-87-12 (1987).

[80] Brown, J., "Optimization of Composite Mode I Delamination Fracture Specimens", M. S. Thesis, Civil Engineering, Texas A&M University (Aug. 1988).

[81] Davidson, B. D., "Two New Techniques for Predicting Delamination Growth in Laminate Plates" Ph.D. Dissertation, Aerospace Engineering, Texas A&M University (Dec. 1988).

[82] Poursartip, A., Ashby, M. F., and Beaumont, P.W.R., **Composites Science and Technology** 25 (1986) pp. 193-218.

[83] Hibbs, M. H. "Microscopic Delamination Processes and the Resulting Crack Tip Strain Fields of Graphite/Epoxy Composites". Ph.D. Dissertation, Interdisciplinary Engineering, Texas A&M University, (1988).

[84] Tuba, I.S. **J. of Strain Analysis** 1 (1966) pp.115-122.

[85] Chakachery, E. A. "Deformation and Micromechanisms in Polymeric Matrices and Carbon Fibre Reinforced Composites". Ph.D. Dissertation, Mechanical Engineering, Texas A&M Univerisity, (1989).

[86] Corleto, C. R., and Bradley, W. L., in **Proc. of 4th Tech. Conf. of ASC, Blacksburg, Virginia, (1989) pp.782-790.**

[87] Bradley, W. L., "Role of Matrix Properties on Toughness of Thermoplastic Composites". To appear in **Composite Materials Series**, 7 ed. Leif Carlsson, Elsevier Publishing (1990).

[88] Kanninen, M. F. and Popelar, C. H., "Advance Fracture Mechanics". Oxford University Press, (1985).

[89] Bilby, B. A., Cottrell, A. H., and Swinden, K. H., in **Proc. of the Royal Society Series A**, 272, (1963) pp. 304-314.

III. ORAL AND WRITTEN PRESENTATIONS

1. Journal Articles and Conference Proceedings

"Microcrack Density Damage Parameter as a Function of Normal and Shear Strain of a Fiber Reinforced Composite Material," Proceedings of American Society for Composites: 4th Technical Session, October, 1989, pp. 782-790. (with Corleto).

"The Role of Matrix Properties on the Toughness of Thermoplastic Composites," Thermoplastic Composite Materials, R. Byron Pipes (ed.), Elsevier Science Publishers, to appear in 1990.

"Fracture Toughness of Polymer Matrices in Relation to Interlaminar Fracture Toughness," Chapter 8 in Application of Fracture Mechanics to Composite Materials, editor K. Friedrich, Elsevier Book Series on Composite Materials, accepted for publication in 1990.

"The Relationship Between Resin Mechanical Properties and Mode I Delamination Fracture Toughness," Journal of Composite Materials, Vol. 23, PP. 923-943, September, 1989. (with Jordan).

"Understanding the Translation of Neat Resin Toughness into Delamination Toughness in Composites, chapter in Interlaminar Fracture in Composites, editor, E. A. Armanios, (Aedermannsdorf, Switzerland: Trans Tech publications), 1989, pp. 161-198.

"Mode II Delamination Fracture Toughness of Unidirectional Graphite/Epoxy Composites," Composite Materials: Fatigue and Fracture, ASTM STP 1012, Paul A. Legace, Ed., American Society for Testing and Materials, Philadelphia, 1989, pp. 201-221. (with Corleto).

"Relating Resin Mechanical Properties to Composite Delamination Fracture Toughness," Journal of Materials Science, Vol. 7 (1988), pp. 1362-1364. (with Jordan).

"New Techniques in Strain Field Mapping Around Crack Tips," Proceedings of Annual Society of Experimental Mechanics, Savannah, Georgia, 1987. (with Hibbs).

"Correspondence Between Stress Fields and Damage Zones Ahead of Crack tip of Composites Under Mode I and Mode II Delamination Loading," accepted for publication in Proceedings of Sixth International Conference on Composite Materials, London, July, 1987, 3.378-3.388. (with Corleto and Henriksen).

"A Comparison of Crack Tip Damage Zone for Fracture of Hexcel F185 neat Resin and T6T145/F185 Composite material," <u>Polymer Science and Engineering</u>, Vol. 27, Nol 1, (1987), pp. 33-40. (with Chakachery).

"Correlations Between Micromechanical Failure Processes and Delamination Fracture Toughness of Graphite/Epoxy Composites," in ASTM STP on <u>Fractography of Modern Engineering Materials</u>, 1987, pp. 68-97. (with Hibbs).

"Micromechanisms of Fracture in Toughened Graphite-Epoxy Laminates," ASTM-STP 937, <u>Toughened Composites</u>, 1987, pp.115-130. (with Hibbs and Tse).

"The Relationship Between Resin Ductility and Composite Delamination Fracture Toughness," <u>Proceedings of International Conference on Composite Materials</u>, June, 1986., Beijing, China, pp. 445-451. (with Jordan).

"The Meaning and Significance of Hackles in Composite Materials," International Conference on Post Failure Analysis Technique for Fiber Reinforced Composites, Dayton, Ohio, July, 1985, pp. 17-1 to 17-18.

"Matrix Deformation and Fracture in Graphite Reinforced Epoxies," <u>Delamination and Debonding of Materials</u>, ASTM STP 876, W.S. Johnson, Ed., American Society for Testing and Materials, Philadelphia, 1985, pp. 389-410.

"In-Situ Delamination Fracture Studies of T6T145/F185 Composite Materials," <u>Proceedings of International Fracture Conference IX</u>. New Delhi, India, December, 1984, Chakachery.

2. <u>Oral Presentations</u>

"Use of Composites in Marine Applications," American Association for the Advancement of Science Annual Meeting, New Orleans, Feb, 1990 (invited).

"Effect of Seawater on Graphitic Composites," <u>Proceedings of Ocean and Marine Engineering Conference</u>, Houston, Feb, 1990.

"Failure Analysis in Engineering Design," Monterrey Tech, Monterrey, Mexico, March, 1990 (invited).

"Effect of Resin Toughness on Delamination Toughness," Technological Institute, Leningrad, Russia, June, 1990 (invited).

"Strain Field Mapping Around Crack Tips," Annual Meeting of Society of Experimental Mechanics," June, 1990,, Albuquerque, NM (invited).

"Factors Affecting Compression Strength in Composite Materials," University of

Delaware, Nov., 1989 (invited).

"Measurement of Crack Tip Strain Fields for Delamination in Composite Materials," Gordon Research Conference on Composite Materials, Venture, CA, January, 1989.

"The Relationship of Resin Toughness to Delamination Toughness in Composites," European Fracture Conference, Budapest, Hungary, Sept., 1988, (invited).

"A Study of the Micromechanisms of Delamination Fracture in Composite Materials," Rice university, March, 1988, (invited).

"Recent Advances in Strain Field Mapping in Composites During Delamination," Rockwell International, Thousand Oaks, CA, Feb., 1988, (invited).

"Mechanisms of Failure in Composites," invited presentation for American Society for Metals Symposium, Los Angeles, CA, November, 1987, (invited).

"Micromechanisms of Fracture in Delaminating Composites," presentation for Corporate R&D, 3M Corporation, Minneapolis, October, 1987 (invited).

"New Techniques in Strain Field Mapping Round Crack Tips," invited presentation to Society of Experimental Mechanics Annual Meeting, Savannah, Georgia, October, 1987.

"Strain Field Mapping for Growing Crack in Composites," presentation for DOD Composite Materials Review, Bal Harbour, Florida, October, 1987 (invited).

"Correspondence Between Stress Fields and Damage Zones Ahead of Crack Tip of Composites Under Mode I and Mode II Delamination," Sixth International Conference on Composite Materials, London, England, July, 1987.

"Fracture Studies in Neat and Fiber Reinforced Thermoset Resins," keynote presentation for Gordon Research Conference on Thermosetting Plastics, New London, New Hampshire, June, 1987 (invited).

"Micromechanics of Compressive Failures in Composite Laminates," with Gail Guynn, and Mode II Delamination Fracture Toughness of Unidirectional Graphite/Epoxy Composites," with Carlos Corleto, ASTM Symposium of Fatigue and Fracture in Composite Materials, Cincinnati, Ohio, April, 1987.

"Failure Analysis of Airport Roof Collapse," and "Use of Fracture Mechanics in Pipeline Failure Analysis," International Conference on Fatigue, Corrosion Cracking, Fracture Mechanics and Failure Analysis, Salt Lake City, Utah, December, 1986, (invited).

"Relationship Between Neat Resin Fracture Toughness and Delamination Fracture Toughness of Composite Materials," presented to Phillips Petroleum Corporate Research and Development, Bartlesville, Oklahoma, November, 1986 (invited).

"The Relationship Between Resin Ductility and Composite Delamination Fracture Toughness," International Symposium on Composite Materials, Beijing, China, June, 1986, (invited).

"On Mode II Delamination Fracture Toughness measurements in Composite Materials," ASTM Annual Meeting, Charleston, SC, March, 1986, (invited).

"Direct Observation of Fracture in Composites," lecture for Gordon Research Conference on Composites, Santa Barbara, CA, January, 1986, (invited).

"Correlations Between Micromechanical Failure Processes and Delamination Fracture Toughness of Graphite/Epoxy Composites," ASTM Symposium on Fractography of Modern Engineering Materials, Nashville, November, 1985, (invited).

"A Comparison of the Crack Tip Damage Zone for Fracture of Hexcel F185 Neat Resin and T6T145/F185 Composite Material," International Symposium on Nonlinear Deformation, Fracture and Fatigue of Polymeric Materials, Chicago, September, 1985 (invited).

"The Meaning and Significance of Hackles in Composite Materials," International Conference: Post Failure Analysis Technique for Fiber Reinforced Composites, Dayton, Ohio, July, 1985.

"Micromechanisms of Fracture in Toughened Graphite/Epoxy Laminates," ASTM Symposium on Toughened Composites, Houston, TX, March, 1985.

"Delamination Fracture Studies of Some Toughened Graphite/Epoxy Composites, Including Real-Time Fracture Observations in Scanning Electron Microscope," ASTM Symposium on Toughened Composites, Houston, TX, March, 1985.

"Delamination Fracture Behavior of Graphite/Thermoplastic Composite Systems," invited, NASA Langley, Hampton, VA, February, 1985.

"Micromechanics Modelling of Delamination Fracture in Graphite/Epoxy Composites," Gordon Conference on Composite Materials, Santa Barbara, CA, Jan., 1985, (invited).

"In Situ Delamination Studies of TBT 145/F185 Composite Materials," presented at 6th International Fracture Symposium, New Delhi, India, December, 1984.

"In Situ Studies in Delamination of Graphite/Epoxy; Recent Results," Air Force Composite Materials Review, Dayton, Ohio, October, 1984, (invited).

"In Situ SEM Studies of Fracture of Plastics and Fiber Reinforced Plastics," Dow Chemical, Research Center, Freeport, TX, July, 1984, (invited).

IV. PROFESSIONAL PERSONNEL INFORMATION

1. List of Professional Personnel

Walter L. Bradley, Principal Investigator
Douglas Goetz, Graduate Research Assistant
Carlos Corleto, Graduate Research Assistant
William Jordan, Graduate Research Assistant
Michael Hibbs, Graduate Research Assistant
Sun Yongqi, Visiting Scholar/Research Associate
Elizabeth Chakachery, Technician
Robert Jones, Technician

2. Degrees Awarded

William Jordan, Ph.D. in Mechanical Engineering, Dec., 1985
Michael Hibbs, Ph.D. in Mechanics and Materials, May, 1987
Douglas Goetz, Ph.D. in Mechanical Engineering, Dec., 1988
Carlos Corleto, Ph.D. in Mechanical Engineering, May, 1990